SEALING OF BOREHOLES AND SHAFTS IN TUFF

QUARTERLY PROGRESS REPORT

March 1, 1989 - May 31, 1989

Contract No. NRC-04-86-113
FIN: D1192

prepared by:

K. Fuenkajorn
S. Ouyang
H. Akgun
R.C. Armstrong
D.R. Crouthamel
C.J. Sharpe

and

J.J.K. Daemen
Principal Investigator

Department of Mining and
Geological Engineering

University of Arizona

Tucson, AZ 85721

prepared for:

Division of Engineering
Office of Nuclear Regulatory Research
U.S. Nuclear Regulatory Commission
Washington, DC 20555

TABLE OF CONTENTS

TABLE OF CONTENTS--Continued

TABLE OF CONTENTS--Continued

LIST OF FIGURES

LIST OF FIGURES--Continued

LIST OF FIGURES--Continued

LIST OF FIGURES--Continued

LIST OF TABLES

LIST OF TABLES--Continued

CHAPTER ONE

INTRODUCTION

This quarterly report describes the work performed during the period March - May 1989. This introductory chapter briefly summarizes the work reported on in each chapter.

Material characterization testing is presented in Chapter Two, which deals with tuff characterization. It has been reported previously that extreme variability in mechanical properties appears to be fairly characteristic for Apache Leap tuff. Some complementary testing carried out during this quarterly period has been aimed specifically at identifying the possible influence of some test variables on rock properties. The most immediate observation during this additional testing is the great difficulty encountered in satisfying ASTM sample preparation requirements due to the extreme heterogeneity of the samples, and in particular due to the presence of voids, vesicles and inclusions along the surfaces to be prepared. The main conclusion from uniaxial compression testing, for cylinders with different length to diameter ratios, tested over a range of strain rates, and for Brazilian disk tensile tests remains that the rock appears to be intrinsically extremely variable. It has not been possible as yet to determine any statistically significant relations, e.g. with respect to sample size, or strain rate. Even though substantially larger samples have been tested during this quarter, the seemingly intrinsic variability of the rock properties continues to overwhelm any size-related strength variations, and raises serious questions as to the scale on which testing might be required in order to determine size effects. It is readily apparent from the tabulated results that density (or, conversely, porosity) does not appear to be a discriminatory independent variable. Results of some uniaxial compression test series suggest that the ISRM-recommended L/D (length to diameter) test specimen ratio of 2.5 to 3.0 may be preferable to the ASTM-recommended ratio of 2.0 to 2.5.

Two radial permeameter tests are continuing on rock bridges left in place in tuff cylinders (Chapter Three). The main reason for continuing these already long-term (one-month) flow tests is the surprisingly low hydraulic conductivity measured in these tests. Present results suggest hydraulic conductivities in the 10^{-10} to 10^{-12} cm/s range. These results are based on outflow only. Leakage in the injection system has prevented establishing reliable inflow measurements, and hence determination of a mass balance.

Appendix 3.A gives the experimental procedure for performing radial permeameter tests. Radial permeameter tests allow testing of borehole plugs emplaced in rock cylinders under a relatively wide range of (axisymmetric) external loading conditions.

Chapter Four describes ongoing flow testing of bentonite and of bentonite/crushed tuff sealants. Samples containing 25 or 35 percent bentonite (by weight) have been tested at 207 and at 345 kPa injection pressure, after previously having been tested at up to 690 kPa. The permeabilities have decreased measurably (by a factor of 2 to 4), presumably as a result of the preceding application of higher pressures. Initial (room temperature) flow test results are presented on crushed tuff/bentonite plugs designed and installed for elevated temperature testing. Also given are initial flow test results on crushed tuff/bentonite samples in which the crushed tuff is graded according to the Fuller-Thompson curve in order to provide maximum crushed tuff packing. Permeability to air is being tested for four bentonite plugs. Swelling tests on bentonite have been initiated.

The first part of Chapter Five presents an analysis of the influence of cylinder stiffness on the radial contact stress along the plug/rock interface of a push-out test. The main incentive for performing this analysis was to evaluate whether the tested cylinders are of sufficient wall thickness, and to allow extrapolation of the results, if warranted, to in-situ conditions (i.e. infinitely thick "cylinders"). The second part of Chapter Five gives results for 16 additional push-out tests. For data analysis purposes these results are combined with those for the 85 tests reported on previously. The bond strength shows a marked decrease with increasing plug diameter. These results need to be analyzed in terms of cylinder stiffness before drawing firm conclusions from this observation. A pronounced strength loss is observed at 90°C, but not consistently at 70°C. No sensitivity to degree of saturation is observed, but this may be due to the relatively short curing and storage duration (typically 8 days) prior to testing.

Fracture grouting progress is reported in Chapter Six. This includes fracture flow testing, grout characterization, and a description of procedures that will be used for fracture surface characterization.

The results of uniaxial and biaxial compression tests on a rectangular Topopah Spring tuff parallelepiped are given in Chapter Seven. Stiffness analysis of the results may be reported in the future. Some uncertainty exists as to the validity of these results, which will be investigated in more detail.

Field work is presented in Chapter Eight, which describes in-situ permeability testing of three inclined holes and coring and videologging of three vertical holes, intended for plug emplacement and plug testing. The hydraulic conductivity along most of the inclined holes exceeds 10^{-5} m/s, making these sections virtually useless for the purpose of testing low permeability plugs. Along each hole some sections have been located in which the hydraulic conductivity is below 2×10^{-8} cm/s. Plug testing will be feasible in such sections. Of the three vertical holes (A,B,C), only C appears highly promising for in-situ plug testing, based on core and hole videolog information. Appendices 8.A, 8.B and 8.C give the core logs for the vertical holes.

CHAPTER TWO

MATERIAL CHARACTERIZATION TESTING

2.1 Tuff Characterization Testing

This section describes the results of characterization experiments of the welded tuff used in this sealing research. Daemen et al. (1988a, Ch. 2) give the work plan and test schedule. The rocks used are Apache Leap tuff, A-Mountain tuff and Topopah Spring tuff. The rock properties to be determined are divided into mechanical, hydrological and petrographical property groups.

Apache Leap tuff gives large variations of the mechanical properties (Daemen et al., 1988b,c, Section 2.1). The variability probably is caused by the effects of inclusions, flow layers, porosity and degree of welding of the rock. Daemen et al. (1989, Section 2.1) describe the effect of the tuff characteristics on the rock properties, as well as the future research needs to improve the representativeness of the test results.

The work in this quarter involves determination of the effect of some test parameters on the mechanical properties of Apache Leap tuff. The specific objective of this effort is to determine a suitable set of test parameters (scale, shape, boundary loading rate) to minimize the influence of test variables on the variations of the mechanical properties of the rock. The experimental work is divided into five tasks: (1) determination of the length-to-diameter ratio effect on the compressive strength, (2) determination of the loading rate effect on the compressive strength and elastic parameters, (3) determination of the size effect on the Brazilian tensile strength, (4) determination of the influence of cyclic loading on the compressive strength, and (5) determination of the size effect on the compressive strength. In this chapter, results of the first three tasks are reported.

2.1.1 Effect of Length to Diameter Ratio on Uniaxial Compressive Strength

The purpose of this study is to determine the effect of the length-to-diameter ratio of specimens on the uniaxial compressive strength of Apache Leap tuff. The L/D ratio used here covers the range suggested by the ISRM (Bieniawski, 1978) test method (i.e. L/D = 2.5 to 3.0), as well as the range recommended by ASTM D2938 (L/D = 2.0 to 2.5).

2.1.1.1 Rock Sample and Test Method

Fifteen cylindrical specimens with a diameter of 50.2 mm are cut from core drilled normal to flow layers from an Apache Leap tuff block (no. AP40). The specimens have nominal length-to-diameter ratios of 2.0, 2.5 and 3.0 (five samples for each ratio). Both end surfaces of the cylinders are ground flat and parallel. Smoothness and perpendicu-

larity of each sample are measured in accordance with the ASTM (D2938) standard practice. Table 2.1 gives the results of these measurements. Only four samples satisfy both perpendicularity and smoothness requirements. Most samples do not satisfy the ASTM requirements due to the presence of voids, vesicles and inclusions on the rock surfaces. Density of the samples averages 2.45 $\pm$ 0.01 g/cc.

All rock cylinders are axially loaded to failure at an axial strain rate of 100 microstrains per second. An SBEL (CT 500) load frame with a servocontroller is used in the experiment. Failure load, test duration and failure mode are recorded. The compressive strength is calculated by assuming that the cross-sectional area remains constant during loading.

2.1.1.2 Test Results

Table 2.2 summarizes the results of uniaxial compressive strength tests of Apache Leap tuff cylinders with various length/diameter (L/D) ratios. The uniaxial compressive strengths of rock cylinders having L/D ratios of 2.0, 2.5 and 3.0 are 91.18 $\pm$ 25.08, 99.70 $\pm$ 19.30 and 107.04 $\pm$ 3.56, respectively. Figure 2.1 gives the compressive strengths as a function of L/D ratio. Linear regression analysis suggests that the strength (C_o) increases as the L/D ratio increases: $C_o = 62.1 + 14.81(L/D)$, for $2 \leq L/D \leq 3$. This result is in conflict with the usual observation that the uniaxial compressive strength decreases with increasing L/D ratio (e.g. Jaeger and Cook, 1979, Section 6.2). Coefficients of variation of the strength (Table 2.2) tend to decrease with increasing L/D ratio. This implies that more consistent strength results of tuff can be obtained by testing samples with large L/D ratios (about 3). This might be explained by the fact that large L/D ratios minimize the end effect (i.e. friction between loading platens and sample end surfaces) which may cause the variation of test results, or that the tuff samples failed in shear (observed from long specimens) yield more consistent failure stresses than do the ones failed in tensile splitting (observed from short specimens). These conclusions and implications suggest that the L/D ratio of 2.5 to 3.0 recommended by the ISRM (Bieniawski et al., 1978) may be more appropriate for tuff testing than the ASTM-recommended L/D ratio of 2.0 to 2.5. More specimens need to be tested to confirm this conclusion, as well as to establish relations, if any, between strength and cylinder length. The shear failure planes have an angle of approximately 30° with the core axis.

2.1.2 Effect of Strain Rate on Compressive Strength

The purpose of this test is to determine the effect of the axial strain rate on the uniaxial compressive strength of Apache Leap tuff. The strain rate used here ranges from 0.022×10^{-6} to 96×10^{-6} second^{-1}.

2.1.2.1 Rock Samples and Test Method

Ten cylindrical samples with L/D ratios of 2 were prepared from Apache

Table 2.1 Perpendicularity and Smoothness of Apache Leap Tuff Cylinders Compared with ASTM Requirements

Sample Number	Side Smoothness (< 0.02 in)	Perpendicularity (< 0.005 in) Top	Perpendicularity (< 0.005 in) Bottom	End Smoothness (degree)
AP40-10b-2-UN1	0.012 ✔	0.006	0.025	0.17 ✔
AP40-4-2-UN2	0.020 ✔	0.023	0.010	0.67
AP40-8-2-UN3	0.007 ✔	0.003 ✔	0.005 ✔	0.14 ✔
AP40-6a-2-UN4	0.019 ✔	0.003 ✔	0.004 ✔	0.12 ✔
AP40-9a-2-UN5	0.010 ✔	0.004 ✔	0.007	0.20 ✔
AP40-10a-2.5-UN6	0.022	0.011	0.002 ✔	0.32
AP40-9a-2.5-UN7	0.009 ✔	0.003 ✔	0.006	0.17 ✔
AP40-9b-2.5-UN8	0.039	0.004 ✔	0.023	0.67
AP40-10-2.5-UN10	0.019 ✔	0.016	0.003 ✔	0.46
AP40-5-2.5-UN11	0.036	0.008	0.007	0.23 ✔
AP40-7a-3-UN9	0.009 ✔	0.005 ✔	0.004 ✔	0.14 ✔
AP40-7b-3-UN12	0.039	0.008	0.007	0.23 ✔
AP40-3b-3-UN13	0.010 ✔	0.005 ✔	0.004 ✔	0.14 ✔
AP40-4a-3-UN14	0.013 ✔	0.008	0.012	0.38
AP40-4b-3-UN15	0.028	0.038	0.012	1.10

✔ indicates that the measurement meets ASTM Standard D2938 requirements

Table 2.2 Results of Uniaxial Compression Test of Apache Leap Tuff Cylinders with Different L/D Ratios

Sample Number	Length (mm)	Diameter (mm)	Density (g/cc)	L/D Ratio	Test Duration (min:s)	Failure Stress (MPa)
AP40-10b-2-UN1	101.4	50.2	2.45	2.02	3:10	65.08
AP40-4-2-UN2	98.9	50.2	2.43	1.97	3:15	67.33
AP40-8-2-UN3	101.0	50.2	2.44	2.01	3:18	92.11
AP40-6a-2-UN4	100.0	50.2	2.46	1.99	3:33	121.31
AP40-9a-2-UN5	99.9	50.2	2.45	1.99	4:09	110.08
Mean ± Standard Deviation				2.00 ± 0.02		91.18 ± 25.08
Coefficient of Variation				1%		28%
AP40-10a-2.5-UN6	128.1	50.2	2.44	2.55	4:26	114.35
AP40-9a-2.5-UN7	124.1	50.2	2.46	2.47	4:18	112.32
AP40-9a-2.5-UN8	124.4	50.2	2.46	2.48	3:51	114.68
AP40-10-2.5-UN10	125.9	50.2	2.45	2.51	5:38	78.70
AP40-5-2.5-UN11	127.2	50.2	2.45	2.53	3:26	78.47
Mean ± Standard Deviation				2.51 ± 0.03		99.70 ± 19.30
Coefficient of Variation				1%		19%
AP40-7a-3-UN9	152.5	50.3	2.46	3.03	4:14	109.65
AP40-7b-3-UN12	154.6	50.2	2.46	3.08	4:49	100.99
AP40-3b-3-UN13	150.9	50.2	2.46	3.00	4:22	107.73
AP40-4a-3-UN14	152.8	50.3	2.47	3.04	4.23	109.65
AP40-4b-3-UN15	150.2	50.3	2.46	2.98	4:01	107.20
Mean ± Standard Deviation				3.03 ± 0.04		107.04 ± 3.56
Coefficient of Variation				1%		3%

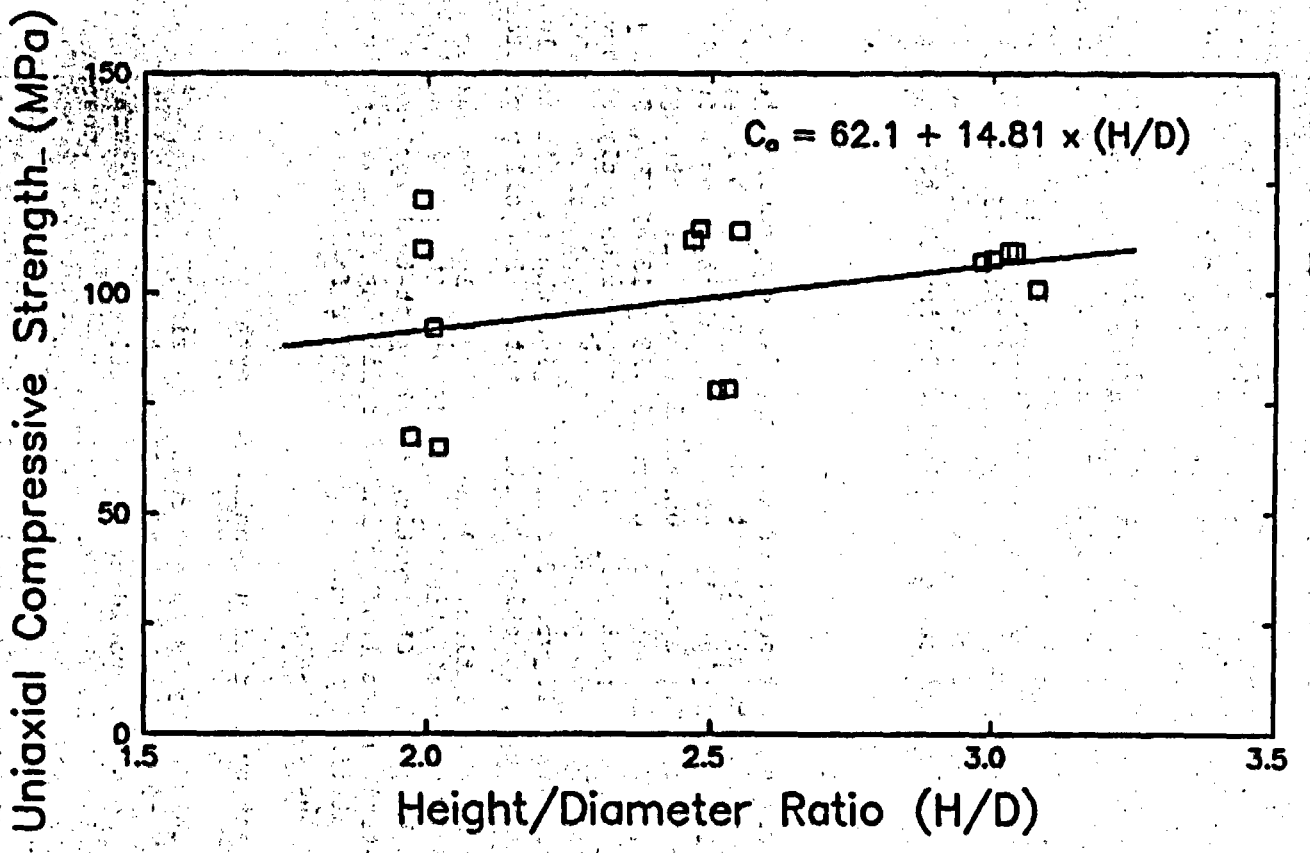

Figure 2.1 Uniaxial compressive strength as a function of length-to-diameter ratio. Test data (points) and linear regression results (line).

Leap tuff. Five samples were cut from 95 mm diameter core drilled from tuff block no. AP21. Five samples having a diameter of 101 mm were obtained from tuff block no. APSHFT6. The sample axis is perpendicular to flow layers. Smoothness and perpendicularity of the samples are measured in accordance with the ASTM (D2938) standard practice. Table 2.3 summarizes the results of measurements. Only four samples satisfy the side smoothness requirement. None satisfies the end perpendicularity requirement. This is due to the presence of voids and inclusions on the rock surfaces. Density of samples averages 2.47 g/cc.

An SBEL (CT 500) load frame with servocontroller is used to apply axial load to the samples at constant strain rates. The axial strain rates range from 0.022×10^{-6} to 96×10^{-6} second^{-1}. The axial and lateral displacements are measured by means of electrical strain gages. The strain gages are installed at the midsection of the cylinder. All samples are loaded to failure. The axial load-displacement curve and axial-lateral displacement curve are plotted during the test using an X-Y plotter.

2.1.2.2 Test Results

Table 2.4 summarizes the results of the uniaxial compression tests. For each sample size, the strength tends to increase with increasing strain rate. Figure 2.2 gives the compressive strength as a function of axial strain rate. The average uniaxial compressive strength, elastic modulus, and Poisson's ratio are 126.19 $\pm$ 13.42 MPa, 34.3 $\pm$ 1.5 GPa, and 0.21 $\pm$ 0.02, respectively. Linear regression analyses have been performed on the three parameters for both sample sizes. Table 2.5 gives the results. Figures 2.3 and 2.4 give the elastic modulus and Poisson's ratio as a function of strain rate. For all parameters, the coefficient of correlation (R^2) is strikingly low. The number of tests performed is not statistically significant; therefore, no firm conclusions can be drawn. Observation on the post-test specimens shows that the high strain rates tend to induce splitting tensile fractures, whereas the low strain rates tend to induce shear failure, at an angle of about 30° to the core axis.

2.1.3 Size Effect on Brazilian Tensile Strength

The purpose of this study is to determine the size effect on Brazilian tensile strength of Apache Leap tuff. The test results would indicate appropriate sample sizes providing representative strength results (i.e. low variation). Daemen et al. (1988c, Section 2.1) give some results of the Brazilian tension test on Apache Leap tuff. In this quarter, Brazilian tensile strength tests have been performed on larger samples (180 mm diameter). Testing large specimens may reduce the effect of inclusions on the tensile strength. An attempt at measuring the elastic modulus and Poisson's ratio of the rock disk has been made.

2.1.3.1 Rock Samples and Test Method

Five Brazilian disks have been prepared from a core (AP42-2A-7) of Apache Leap tuff. The core was drilled perpendicular to flow layers

Table 2.3 Dimensions of Apache Leap Tuff Specimens Used in Strain Rate Effect Study

Sample Number	Diameter (mm)	Length (mm)	Density (g/cc)	ASTM D2938 Specification: Side Smoothness	ASTM D2938 Specification: End Perpendicularity
AP21-5-SNUN1	95.3	192.7	2.42	✓	X
AP21-3-SNUN2	95.4	190.3	2.42	✓	X
AP21-4-SNUN3	95.4	187.5	2.42	X	X
AP21-6-SNUN5	95.3	190.1	2.42	X	X
AP21-7-SNUN4	95.3	191.8	2.42	X	X
APSHFT6-5-SNUN6	102.1	200.7	2.53	X	X
APSHFT6-4-SNUN7	102.0	197.0	2.53	X	X
APSHFT6-3-SNUN8	101.9	197.1	2.53	✓	X
APSHFT6-2-SNUN9	102.0	197.2	2.53	✓	X
APSHFT6-1-SNUN10	101.9	197.3	2.53	X	X

✓: complies with the ASTM standard
X: does not comply with the ASTM standard

Table 2.4 Uniaxial Compressive Strength of Apache Leap Tuff Determined at Various Axial Strain Rates

Number	Axial Strain Rate (x 10^{-6} s^{-1})	Uniaxial Compressive Strength (MPa)	Elastic Modulus (GPa)	Poisson's Ratio
AP21-5-SNUN1	1.1	130.8	33.7	0.24
AP21-3-SNUN2	18	124.6	34.0	0.19
AP21-4-SNUN3	96	131.9	32.5	0.21
AP21-6-SNUN5	2.6	125.4	33.6	0.24
AP21-7-SNUN4	0.55	109.1	32.1	0.17
APSHFT6-5-SNUN6	4.9	137.9	35.9	0.21
APSHFT6-4-SNUN7	0.098	142.5	33.8	0.19
APSHFT6-3-SNUN8	0.045	124.3	37.2	0.22
APSHFT6-2-SNUN9	0.022	98.7	34.7	0.21
APSHFT6-1-SNUN10	0.022	136.7	35.3	0.22
Mean ± Standard Deviation		126.19 ± 13.42	34.3 ± 1.5	0.21 ± 0.02
Coefficient of Variation		11%	4%	11%

NOTE: The elastic modulus and Poisson's ratio are determined at 50% failure stress.

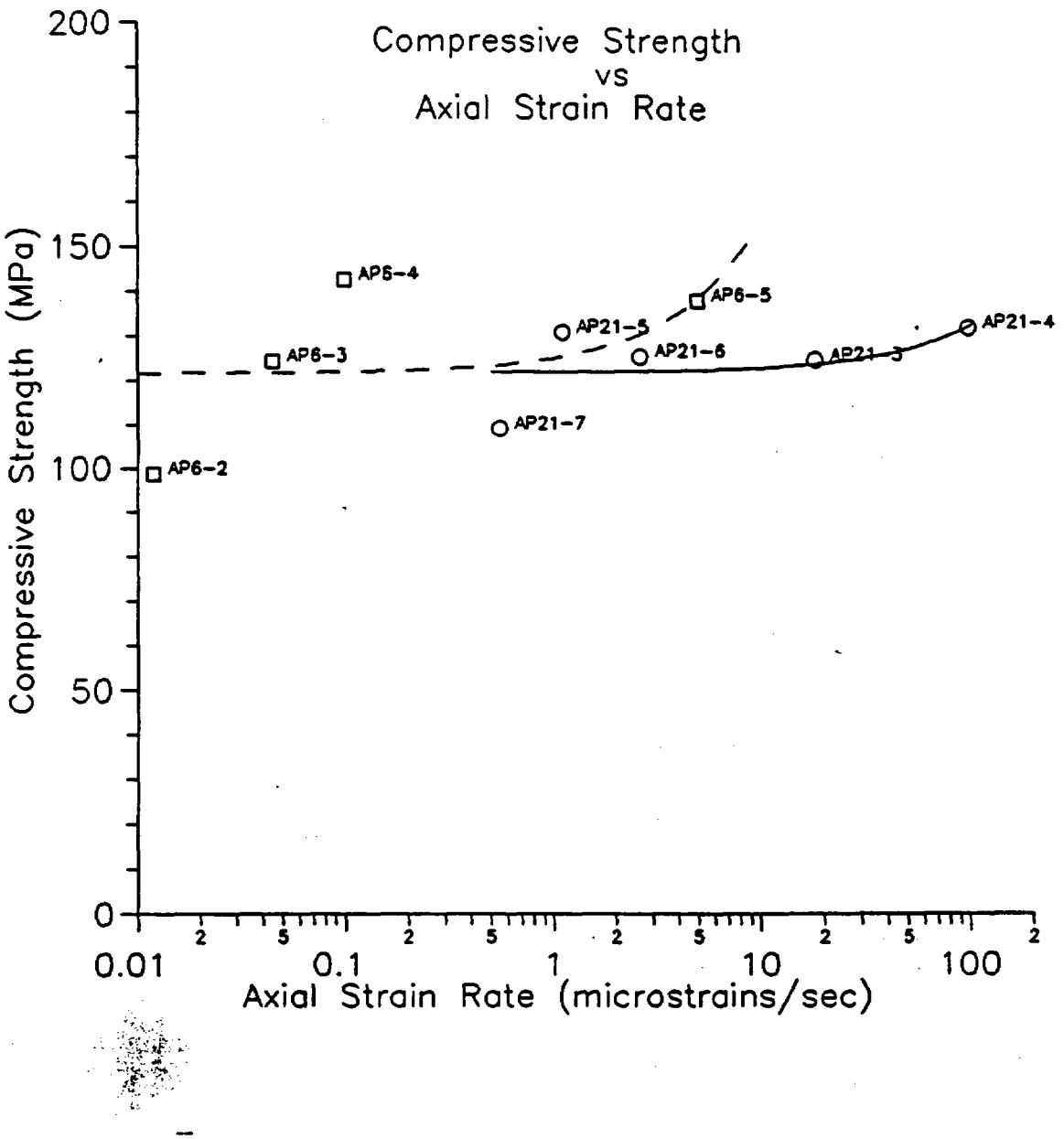

Figure 2.2 **Uniaxial compressive strength as a function of axial strain rate. A linear fit applied to each data set indicates an increase of strength with increasing strain rate.**

circles = 95 mm diameter samples
squares = 101 mm diameter samples

Table 2.5 Results of Linear Regression Analysis; Uniaxial Test on Apache Leap Tuff

Uniaxial Compressive Strength:	$C_o = a\dot{\varepsilon}_R + b$
For 95 mm samples:	$C_o = 0.108\dot{\varepsilon}_R + 120.3$ MPa; $R^2 = 0.237$
For 101 mm samples:	$C_o = 3.419\dot{\varepsilon}_R + 121.5$ MPa; $R^2 = 0.177$
Elastic Modulus:	$E = d\dot{\varepsilon}_R + f$
For 95 mm samples:	$E = -0.007\dot{\varepsilon}_R + 33.3$ GPa; $R^2 = 0.119$
For 101 mm samples:	$E = 0.056\dot{\varepsilon}_R + 36.6$ GPa; $R^2 = 0.014$
Poisson's Ratio:	$\nu = i\dot{\varepsilon}_R + j$
For 95 mm samples	$\nu = 0.21$; $R^2 = 0.003$
For 101 mm samples	$\nu = -0.003\dot{\varepsilon}_R + 0.18$; $R^2 = 0.102$

where $\dot{\varepsilon}_R$ = strain rate in microstrains per second
a,d,i = slope of the curve
b,f,j = intercept.

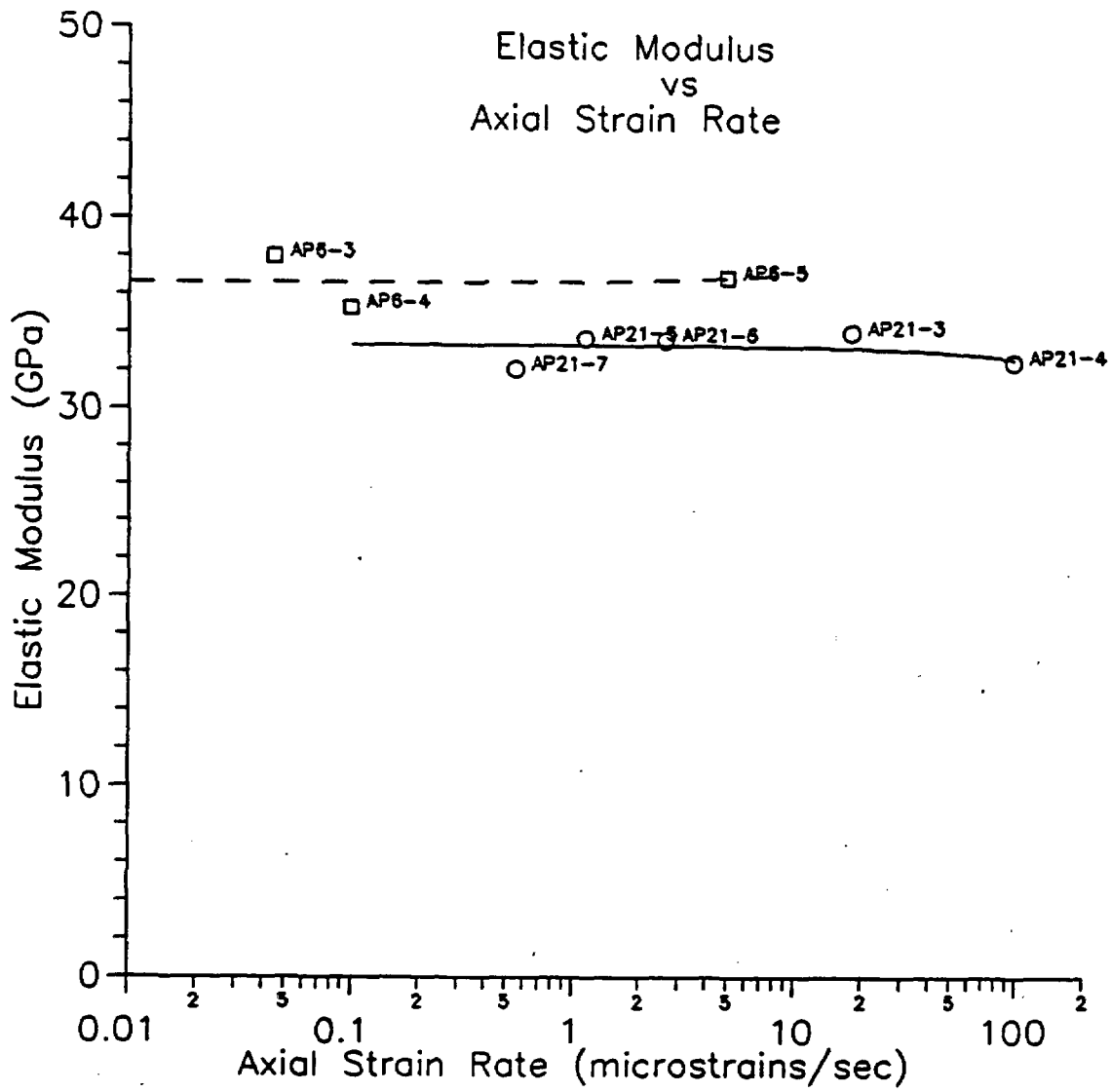

Figure 2.3 **Elastic modulus as a function of axial strain rate. A linear fit is applied to both data sets.**

circles = 95 mm diameter samples
squares = 101 mm diameter samples

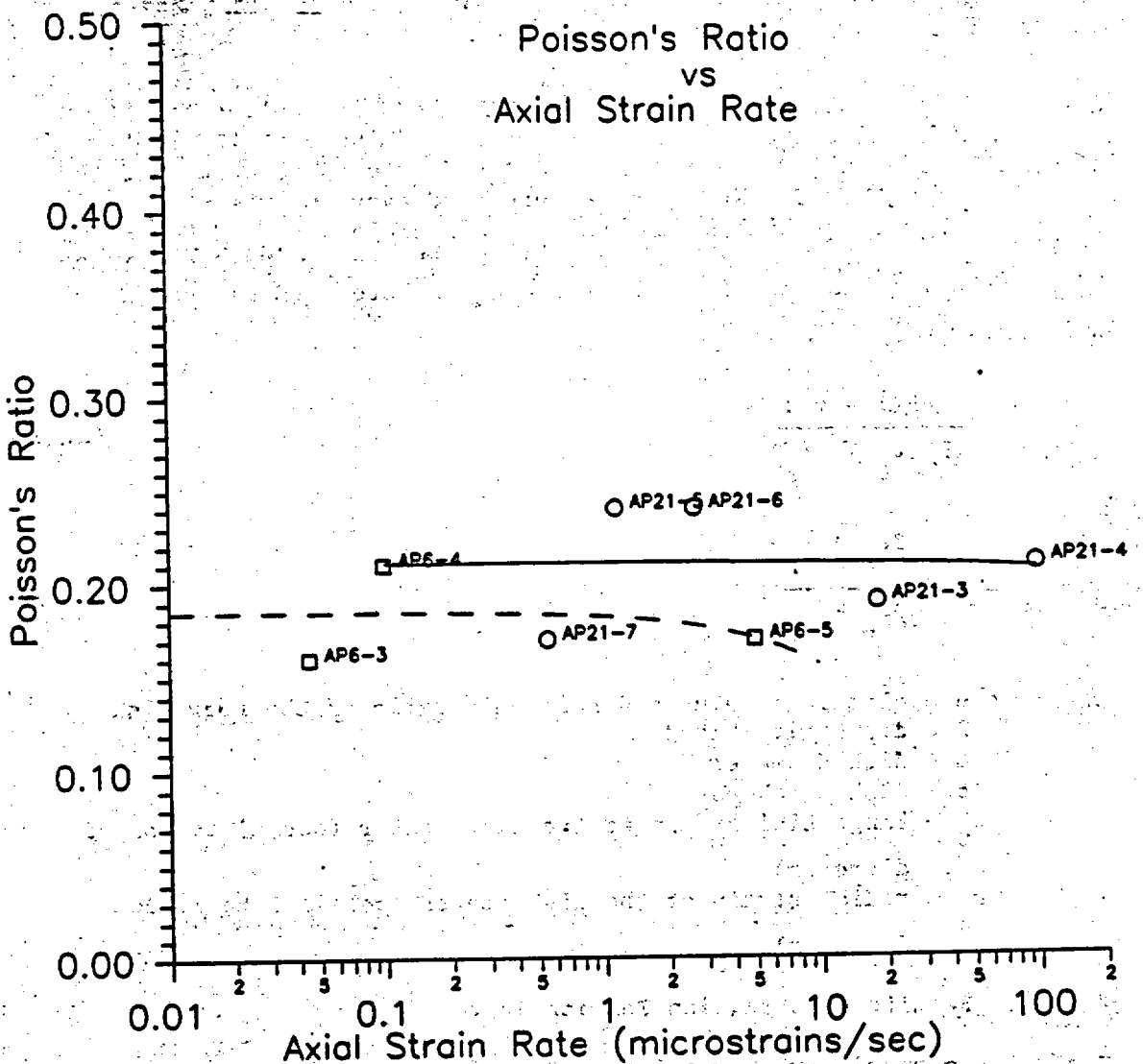

Figure 2.4 Poisson's ratio as a function of axial strain rate. A linear fit is applied to both data sets.

circles = 95 mm diameter samples
squares = 101 mm diameter samples

of tuff block no. AP42. The disk samples have a nominal diameter of 180 mm and a length-to-diameter ratio of 0.5. Electrical resistance strain gages are installed at the center of the disk. The gages are used to measure tangential strain (normal to loading diameter) and radial strain (parallel to loading diameter). The strain gages are connected to a strain indicator and a switch-and-balance unit.

All rock samples are diametrically loaded to failure using an SBEL (CT 500) load frame with servocontroller. The load is applied to obtain a tangential tensile stress rate of about 3 kPa/minute at the center of the disk. The failure load is recorded and is used to calculate the tensile strength. The strain gages are read every minute until failure. The tangential strain and radial strain are used to calculate the elastic modulus and Poisson's ratio of the rock. Hondros (1959) gives solutions to calculate the elastic parameters (E,ν) from a Brazilian test specimen as:

$$E = \frac{6P(1 - \nu^2)}{\pi Dt(\varepsilon_\theta + \nu\varepsilon_r)} \qquad (2.1)$$

$$\nu = -\left(\frac{3\varepsilon_\theta + \varepsilon_r}{3\varepsilon_r + \varepsilon_\theta}\right) \qquad (2.2)$$

where E,ν = elastic modulus and Poisson's ratio of the rock disk
P = diametrical load
D = disk diameter
t = disk thickness
ε_θ = tangential strain at the disk center (normal to loaded diameter)
ε_r = radial strain at the disk center (parallel to loaded diameter)

2.1.3.2 Results of Brazilian Tension Test

Table 2.6 summarizes the results of Brazilian tension test on 180 mm diameter disks of Apache Leap tuff. The average Brazilian tensile strength is 6.16 ± 1.36 MPa. The coefficient of variation is 22%. All samples fail in tension along the loading diameter. Table 2.7 gives the elastic modulus and Poisson's ratio calculated from the tangential and radial strains at the disk center. The elastic parameters are calculated at 10% and at 50% of the tensile strengths. The Poisson's ratio calculation gives physically meaningless values, except for samples AP41-2A-7-B23 and AP42-2A-7-B25. This is probably caused by nonhomogeneity of the rock disk due to the presence of flow layers, vesicles (voids) and inclusions, which induces a complex strainfield along the loaded diameter.

Figure 2.5 gives the Brazilian tensile strength of Apache Leap tuff as a function of sample size (disk diameter). The experiments on 24.5,

Table 2.6 Results of Brazilian Test on Apache Leap Tuff

Sample Number	Average Diameter (mm)	Average Length (mm)	Brazilian Tensile Strength (MPa)
AP42-2A-7-BZ1	181.5	86.3	5.06
AP42-2A-7-BZ2	181.4	93.1	5.36
AP42-2A-7-BZ3	181.2	86.5	5.60
AP42-2A-7-BZ4	181.5	86.3	6.33
AP42-2A-7-BZ5	181.7	94.3	8.43
Mean ± Standard Deviation			6.16 ± 1.36
Coefficient of Variation			22%

Table 2.7 Elastic Modulus and Poisson's Ratio of Apache Leap Tuff, Obtained from Brazilian Test Specimens

Sample Number	Poisson's Ratio Measured at 10% Strength	Poisson's Ratio Measured at 50% Strength	Elastic Modulus (GPa) Measured at 10% Strength	Elastic Modulus (GPa) Measured at 50% Strength
AP42-2A-7-BZ1	1.304	1.661	142.08	173.06
AP42-2A-7-BZ2	-0.106	-0.062	29.30	41.63
AP42-2A-7-BZ3	0.418	0.418	63.25	55.03
AP42-2A-7-BZ4	0.662	0.874	151.10	269.54
AP42-2A-7-BZ5	0.186	0.081	176.83	96.15

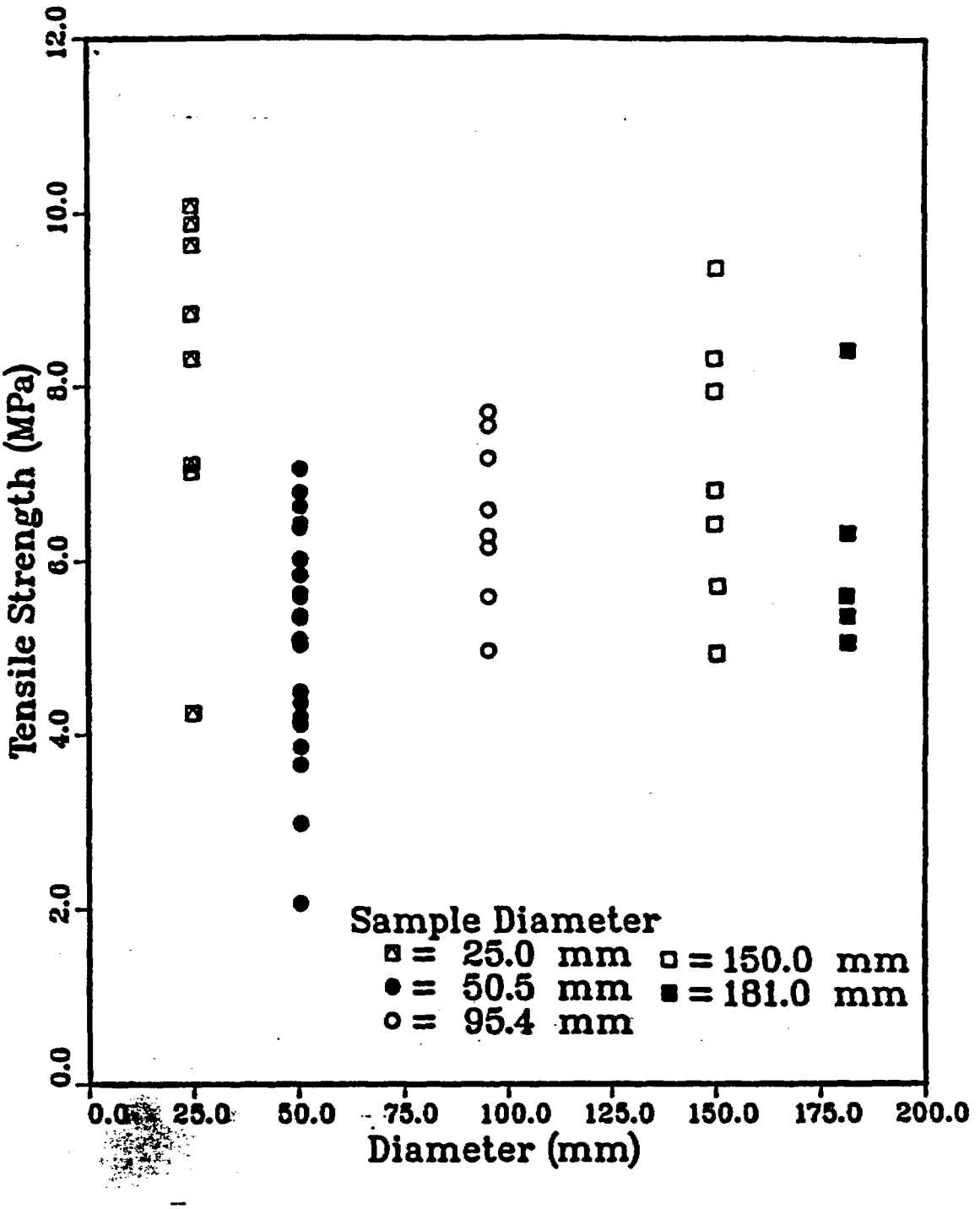

Figure 2.5 Brazilian tensile strength of Apache Leap tuff, obtained from different sample sizes.

50.5 (ASTM D3967), 94.5 and 150.0 mm diameter disks have been reported earlier by Daemen et al. (1988c, Section 2.1). In order to determine a mathematical relationship between strength and size, Evans' power law and Lundborg's logarithmic expression (Jaeger and Cook, 1979, pp. 196-199) are used in linear regression analysis. Table 2.8 gives the results of the regression. Both criteria show a low coefficient of correlation (R^2). Mathematically, the strength decreases as sample size increases. The size effect criteria (Evans' law and Lundborg's expression) do not fit the experimental data. A large coefficient of variation is obtained from all sample sizes. More experimental data are needed which may reduce the variation of the strength results. To extrapolate the tensile strength to a larger scale (i.e. toward in-situ conditions), samples having diameters larger than 180 mm should be tested.

2.3 References

ASTM D2938-79, "Standard Test Method for Unconfined Compressive Strength of Intact Rock Core Specimens," Annual Book of ASTM Standards, Section 4, Construction, Vol. 04.08, Soil and Rock; Building Stones, American Society for Testing and Materials, Philadelphia, PA (also standardized as ANSI/ASTM D2938-79).

ASTM D3967-81, "Standard Test Method for Splitting Tensile Strength of Intact Rock Core Specimens," Annual Book of ASTM Standards, Section 4, Construction, Vol. 04.08, Soil and Rock; Building Stones, American Society for Testing and Materials, Philadelphia, PA.

Bieniawski, Z.T. et al., 1978, "Suggested Methods for Determining the Uniaxial Compressive Strength and Deformability of Rock Materials," Committee on Laboratory Tests, International Society for Rock Mechanics Commission on Standardization of Laboratory and Field Tests; also pp. 111-116 in E.T. Brown, ed., 1988, Rock Characterization Testing and Monitoring, Pergamon Press, Oxford.

Daemen, J.J.K., K. Fuenkajorn, S. Ouyang, and H. Akgun, 1988a, "Sealing of Boreholes and Shafts in Tuff: Quarterly Progress Report, March 1 - May 31, 1988," Contract NRC-04-86-113, prepared for the U.S. Nuclear Regulatory Commission, Office of Nuclear Regulatory Research, Division of Engineering, by the Department of Mining and Geological Engineering, University of Arizona, Tucson.

Daemen, J.J.K., K. Fuenkajorn, S. Ouyang, H. Akgun, and R. Armstrong, 1988b, "Sealing of Boreholes and Shafts in Tuff: Quarterly Progress Report, June 1 - Aug. 31, 1988," Contract NRC-04-86-113, prepared for the U.S. Nuclear Regulatory Commission, Office of Nuclear Regulatory Research, Division of Engineering, by the Department of Mining and Geological Engineering, University of Arizona, Tucson.

Table 2.8 Results of Size Effect Calculation of Brazilian Tensile Strength of Apache Leap Tuff

Evans' Power Law: $\sigma_B = kD^{-\infty}$

Apache Leap Tuff: $\sigma_B = 8.521D^{-0.0627}$; $R^2 = 0.305$

Lunborg's Expression: $\ln\sigma_B = A - (1/m)\ln V$

Apache Leap Tuff: $\ln\sigma_B = 1.979 - (1/47.79)\ln V$; $R^2 = 0.303$

where σ_B = Brazilian tensile strength in MPa
D = sample diameter in mm
k, ∞, A, m = empirical constants
V = sample volume in cc
R^2 = coefficient of correlation

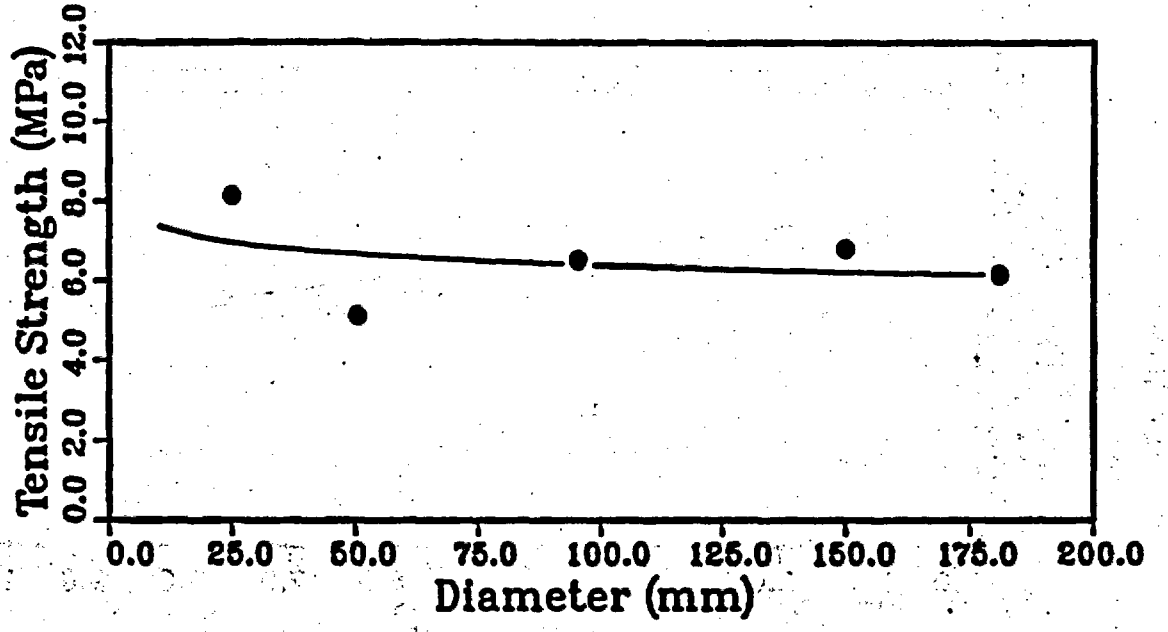

Figure 2.6 Evans' power law fit to Brazilian tensile strength data as a function of disk diameter. Each data point represents an average tensile strength of 5 to 20 tests.

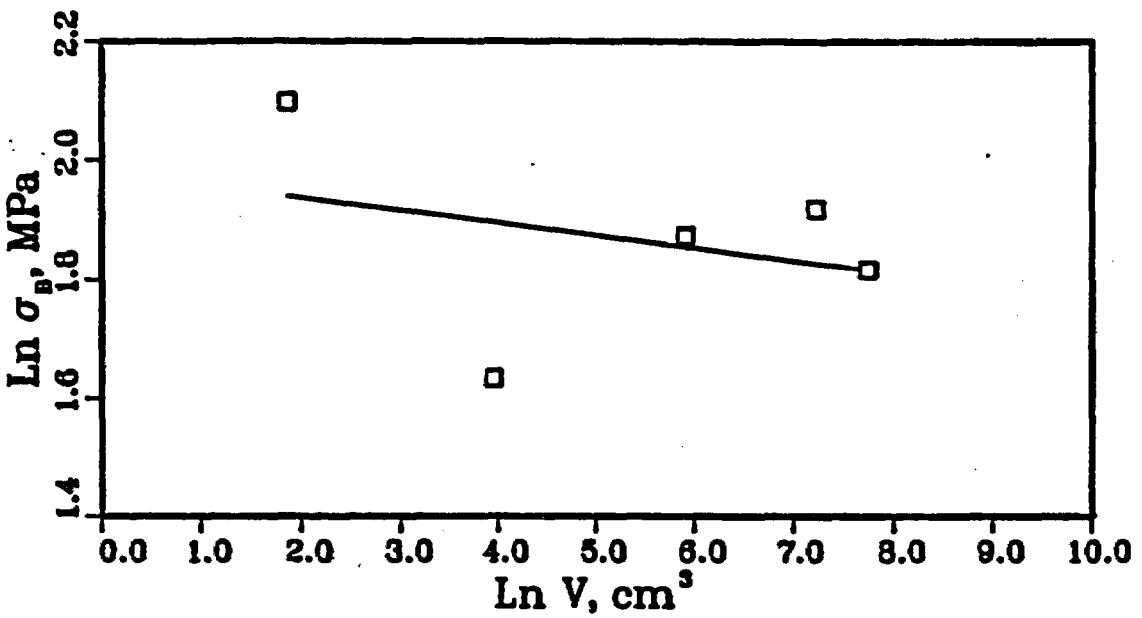

Figure 2.7 Lundborg's logarithmic expression fit to Brazilian tensile strength data as a function of disk diameter. Each data point represents the average tensile strength of 5 to 20 tests.

Daemen, J.J.K., K. Fuenkajorn, S. Ouyang, H. Akgun, and R. Armstrong, 1988c, "Sealing of Boreholes and Shafts in Tuff: Quarterly Progress Report, Sept. 1 - Nov. 31, 1988," Contract NRC-04-86-113, prepared for the U.S. Nuclear Regulatory Commission, Office of Nuclear Regulatory Research, Division of Engineering, by the Department of Mining and Geological Engineering, University of Arizona, Tucson.

Daemen, J.J.K., K. Fuenkajorn, S. Ouyang, H. Akgun, R. Armstrong, D.S. Crouthamel, and C.J. Sharpe, 1989, "Sealing of Boreholes and Shafts in Tuff: Quarterly Progress Report, Dec. 1, 1988 - Feb. 28, 1989," Contract NRC-04-86-113, prepared for the U.S. Nuclear Regulatory Commission, Office of Nuclear Regulatory Research, Division of Engineering, by the Department of Mining and Geological Engineering, University of Arizona, Tucson.

Hondros, G., 1959, "The Evaluation of Poisson's Ratio and Young's Modulus of Materials of a Low Tensile Resistance by the Brazilian (Indirect Tensile) Test with Particular Reference to Concrete," Australian Journal of Applied Sciences, Vol. 6, No. 1, pp. 243-268.

Jaeger, J.C. and N.W.G. Cook, 1979, Fundamentals of Rock Mechanics, Third Edition, Chapman and Hall, London.

CHAPTER THREE

RADIAL PERMEAMETER TESTING

3.1 Introduction

Radial permeameter testing allows application of simulated in-situ stress states to rock cylinders within which borehole plugs are emplaced for flow testing. As such, it represents a test configuration corresponding more closely to in-situ conditions than flow testing on unloaded cylinders. Moreover, by changing the stresses applied to the cylinder, i.e. by reducing them, very severe interface test conditions can be exerted. Experimental procedures are described in Appendix 3.A.

Apache Leap tuff has been used for rock samples. Daemen et al. (1988a, Ch. 3, pp. 11-14) give the work plan and nominal test schedule. Daemen et al. (1988b, Ch. 3, Section 3.2) give specifications of the samples.

Appendix 3.A gives the test procedure for radial permeameter testing. This chapter gives results of rock bridge testing under high confining pressure.

3.2 Rock Bridge Testing under High Confining Pressure

Samples APX-C-6-RP2 and AP10-4-6-RP3 have been subjected to axial and lateral pressures of 13 and 12 MPa, respectively. A constant injection pressure of 6 MPa has been applied to the top of the samples. The bottom hole is connected to a high-precision pipette ($\pm$ 0.001 cc). An identical pipette is used to measure the evaporation in the testing room. The measurements have been made daily. The temperature of the testing room has been maintained at 22 $\pm$ 1°C.

3.3 Flow Test Results

Tables 3.1 and 3.2 give the results of flow tests of samples APX-C-6-RP2 and AP10-4-6RP3, respectively. The water inflow and outflow have been measured and are used to calculate hydraulic conductivity of the rock. The calculation assumes that the flow is one-dimensional(through the rock bridge only), the rock is saturated, the flow is laminar, and Darcy's law is valid. For both rock cylinders, length and cross-sectional area of the rock bridge are 3.175 cm and 5.305 cm^2, respectively. The calculation is made for each time interval. The evaporation rate of water collected in the pipette is 0.030 to 0.035 cc per day.

Sample APX-C-6-RP2 gives the hydraulic conductivities calculated from the outflow (k_o) ranging from 10^{-12} to 10^{-11} cm/s and the hydraulic conductivities from the inflow (k_I) as 10^{-10} to 10^{-9} cm/s. It has been

found that the injection water leaks through a seal between the piston and the cylinder of the pressure intensifier. This indicates that the measured inflow rates and the inflow-conductivities (k_I) overestimate the actual values. Since the leakage is small and the injection pressure can be maintained constant, the test is being continued.

The inflow hydraulic conductivities of samples AP10-4-6-RP3 range from 10^{-10} to 10^{-9} cm/s. The outflow conductivities are 10^{-11} to 10^{-10} cm/s. The measured inflow rates are approximately an order of magnitude higher than the outflow rates. Comparison of the outflow hydraulic conductivities shows that the permeability of sample AP10-4-6-RP3 is one order of magnitude higher than those of sample APC-C-6-RP2.

A more accurate calculation of the hydraulic conductivities can be obtained by performing a numerical (finite element) analysis (South and Daemen, 1986, pp. 180-184; Fuenkajorn and Daemen, 1986, pp. 154-157). The calculation can take the water flow through the rock cylinder (bypass to the rock bridge) into account.

3.4 References

Daemen, J.J.K., K. Fuenkajorn, S. Ouyang, and H. Akgun, 1988a, "Sealing Boreholes and Shafts in Tuff, Quarterly Progress Report, March 1 - May 31, 1988," Contract NRC-04-86-113, prepared for the U.S. Nuclear Regulatory Commission, by the Department of Mining and Geological Engineering, University of Arizona, Tucson.

Daemen, J.J.K., K. Fuenkajorn, S. Ouyang, H. Akgun, and R. Armstrong, 1988b, "Sealing Boreholes and Shafts in Tuff, Quarterly Progress Report, June 1 - Aug. 31, 1988," Contract NRC-04-86-113, prepared for the U.S. Nuclear Regulatory Commission, by the Department of Mining and Geological Engineering, University of Arizona, Tucson.

Fuenkajorn, K. and J.J.K. Daemen, 1986, "Experimental Assessment of Borehole Wall Drilling Damage in Basaltic Rocks," NUREG/CR-4641, prepared for the U.S. Nuclear Regulatory Commission, by the Department of Mining and Geological Engineering, University of Arizona, Tucson.

South, D.L. and J.J.K. Daemen, 1986, "Permeameter Studies of Water Flow Through Cement and Clay Borehole Seals in Granite, Basalt, and Tuff," NUREG/CR-4748, Technical Report prepared for U.S. Nuclear Regulatory Commission, by the Department of Mining and Geological Engineering, University of Arizona, Tucson.

Table 3.1 Results of Rock Bridge Testing on Sample APX-C-6-RP2. σ_{lat} = 12 MPa, σ_{ax} = 13 MPa, P_i = 6 MPa.

Date	Time	Time Interval hr:min	Outflow (cc)	Outflow Rate ($\times 10^{-5}$ cc/min)	k_o ($\times 10^{-12}$ cm/s)	Inflow (cc)	Inflow Rate ($\times 10^{-4}$ cc/min)	k_I ($\times 10^{-10}$ cm/s)
3/24	11:30							
3/25	11:36	24:06	0.028	1.94	3.30	13.75	95.1	16.21
3/26	16:25	28:49	0.042	2.43	4.14	5.57	32.22	5.49
	19:25	3:00	-0.001	-0.55	-	0.880	48.9	8.33
3/27	10:25	15:00	0	0	0	3.670	40.8	6.95
	16:30	6:05	-0.018	-4.93	-	1.631	44.7	7.62
3/28	13:00	20:30	0	0	0	3.447	28.02	4.78
	17:00	4:00	0.010	4.17	7.10	0.432	18.00	3.07
3/29	10:00	17:00	0.013	1.27	2.17	3.214	31.51	5.37
	16:00	6:00	0.023	6.39	10.90	0.877	24.36	4.15
3/30	13:00	21:00	0.065	5.16	8.79	2.089	16.58	2.82
	16:00	3:00	0	0	0	1.632	90.67	15.45
3/31	13:05	21:05	0.010	0.79	1.35	5.939	46.95	8.00
4/3	9:20	68:15	0.055	1.34	2.29	11.748	28.66	4.88
	16:40	7:20	0.020	4.55	7.75	-	-	-
4/4	16:00	23:20	0.020	1.43	2.43	-	-	-
4/5	16:50	24:50	0.021	1.41	2.40	4.920	33.02	5.63
4/6	16:50	24:00	0.025	1.74	2.96	5.402	37.51	6.39
4/7	11:05	19:15	0.010	0.87	1.48	2.173	18.73	3.19
4/8	16:05	22:50	0.029	2.12	3.61	1.310	9.56	1.63
4/9	17:15	22:10	0.029	1.92	3.27	4.030	30.30	5.16
4/10	16:05	22:50	0.031	2.26	3.86	4.264	31.12	5.30
4/11	16:20	24:15	0.035	2.38	4.06	4.264	29.31	4.99
4/12	15:50	23:30	0.025	1.77	3.02	3.140	22.27	3.79
4/13	16:40	24:50	0.010	0.67	1.14	5.241	35.17	5.99

Table 3.1 Results of Rock Bridge Testing on Sample APX-C-6-RP2. σ_{lat} = 12 MPa, σ_{ax} = 13 MPa, P_i = 6 MPa--Continued.

Date	Time	Time Interval hr:min	Outflow (cc)	Outflow Rate ($\times 10^{-5}$ cc/min)	k_o ($\times 10^{-12}$ cm/s)	Inflow (cc)	Inflow Rate ($\times 10^{-4}$ cc/min)	k_I ($\times 10^{-10}$ cm/s)
4/14	16:40	24:00	0.025	1.74	2.96	5.414	37.60	6.41
4/16	16:40	48:00	0.070	2.43	4.18	7.453	25.88	4.41
4/17	15:55	23:15	0.009	0.65	1.10	3.090	22.15	3.78
4/18	15:50	23:55	0.035	2.44	4.16	2.707	18.86	3.22
4/19	15:50	24:00	0.030	2.08	3.55	4.030	27.99	4.77
4/20	15:50	24:00	0.035	2.43	4.14	3.758	26.10	4.45
4/21	17:50	26:00	0.036	2.31	3.93	4.203	26.94	4.59
4/22	15:55	22:05	0.028	2.11	3.60	3.374	25.46	4.34
4/23	19:30	27:35	0.025	1.52	2.59	4.598	27.78	4.74
4/24	16:50	21:20	0.028	2.19	3.73	3.486	27.23	4.64
4/25	16:20	23:30	0.0020	1.42	2.42	–	–	–
4/26	16:17	23:57	0.015	1.04	1.78	3.721	25.89	4.41
4/27	15:55	23:48	0.010	0.70	1.19	5.340	37.39	6.37
4/28	16:30	24:35	0.015	1.02	1.73	4.402	27.40	4.67
4/29	18:15	25:45	0.040	2.59	4.41	3.399	22.00	3.75
4/30	15:20	21:05	0.015	1.19	2.02	1.607	12.70	2.17
5/1	15:43	24:23	0.031	2.12	3.61	4.808	32.86	5.60
5/2	16:05	24:22	0.027	1.85	3.15	2.040	13.95	2.37
5/3	15:24	23:19	0.040	2.86	4.87	3.090	22.09	3.76
5/4	16:15	24:51	0.047	3.15	5.37	2.410	16.16	2.76
5/5	16:45	24:30	0.061	4.15	7.07	–	–	–
5/6	15:10	22:25	0	0	0	3.276	24.36	4.15
5/7	15:45	24:35	0.045	3.051	5.20	3.646	24.72	4.21
5/8	15:22	23:37	0.040	2.82	4.81	3.337	23.55	4.01
5/9	16:11	23:49	0.039	2.73	4.65	3.869	27.07	4.61

Table 3.1 Results of Rock Bridge Testing on Sample APX-C-6-RP2. σ_{lat} = 12 MPa, σ_{ax} = 13 MPa, P_i = 6 MPa--Continued.

Date	Time	Time Interval hr:min	Outflow (cc)	Outflow Rate ($\times 10^{-5}$ cc/min)	k_o ($\times 10^{-12}$ cm/s)	Inflow (cc)	Inflow Rate ($\times 10^{-4}$ cc/min)	k_I ($\times 10^{-10}$ cm/s)
5/10	15:28	23:17	0.029	2.08	3.54	3.288	23.54	4.01
5/11	15:02	23:34	0.030	2.12	3.62	3.622	25.62	4.37
5/12	15:06	24:04	0.015	1.04	1.77	4.116	28.50	4.86
5/13	12:30	21:24	0.026	2.02	3.45	2.682	20.89	3.56
5/14	12:06	23:36	0.029	2.05	3.49	4.645	32.80	5.59
Mean ± Standard Deviation:					3.71 ± 1.98			5.12 ± 2.61
Coefficient of Variation:					53%			51%

NOTE: k_o = hydraulic conductivity calculated from outflow

k_I = hydraulic conductivity calculated from inflow

The inflow is affected by a pump seal leak, which results in an erroneous (excessive) apparent inflow, and hence permeability.

Table 3.2 Results of Rock Bridge Testing on Sample AP10-4-6-RP3. σ_{lat} = 12 MPa, σ_{ax} = 13 MPa, P_i = 6 MPa.

Date	Time	Time Interval hr:min	Outflow (cc)	Outflow Rate ($\times 10^{-4}$ cc/min)	k_o ($\times 10^{-11}$ cm/s)	Inflow (cc)	Inflow Rate ($\times 10^{-3}$ cc/min)	k_I ($\times 10^{-11}$ cm/s)
4/22	15:55							
4/23	19:30	27:35	-0.070	-0.423	-	2.188	1.322	22.53
4/24	16:50	21:20	0.035	0.273	0.466	7.107	5.552	94.62
4/25	16:20	23:30	-0.010	-0.071	-	0	0	0
4/26	17:17	23:57	0.020	0.139	0.237	0.906	0.631	10.74
4/27	15:55	23:48	0.150	1.05	1.79	0.519	0.363	6.194
4/28	16:30	24:35	0.185	1.25	2.14	0.606	0.411	7.002
5/3	15:50	-	-	-	-	-	-	-
5/4	16:15	24:51	-0.135	-0.905	-	4.005	2.686	45.78
5/4	16:20	0:05	0	0	0	0.012	2.40	40.90
5/5	16:17	23:57	0.915	6.37	10.85	5.414	3.768	64.21
5/6	15:10	22:53	0.400	2.913	4.97	9.765	7.112	121.2
5/8	15:22	-	-	-	-	-	-	-
5/9	11:56	23:49	-0.050	-0.035	-	-	-	-
5/9	16:11	4:15	0.070	2.75	4.68	3.646	32.85	560.0
5/10	15:28	23:17	0.650	4.65	7.93	7.342	5.256	89.57
5/11	15:04	23:34	0.550	3.89	6.63	3.491	2.469	42.07
5/12	15:06	24:04	0.960	6.65	11.13	2.151	1.490	25.39
Mean ± Standard Deviation:					5.08 ± 4.0 x 10^{-11}			86.9 ± 140 x 10^{-11}

NOTE: k_o = hydraulic conductivity calculated from outflow

k_I = hydraulic conductivity calculated from inflow

APPENDIX 3.A

Radial Permeameter Test

Test Procedure

Department of Mining and
Geological Engineering
University of Arizona
Tucson, AZ 85721

Contract No. NRC-04-86-113
FIN: D1192
PI: J. Daemen
(602)621-2501

Draft 1, Revision 1

Test Procedure written by:	K. Fuenkajorn	Date: 9-29-86
reviewed by:	J. Daemen	Date: 12-3-86
revised by:	K. Fuenkajorn	Date: 5-3-89
revision reviewed by:	J. Daemen	Date: 6-6-89

1. Objective

The objective of the radial permeameter test is to assess the sealing performance of borehole plugs (cement, bentonite and crushed rock) under a variety of stress conditions applied to a plugged rock cylinder. Changing the stress conditions sequentially makes it possible to impose severe conditions on the plug-rock interface. The applied stressfield makes it feasible to operate at high differential pressures across the plug, as well as to simulate in-situ stress states.

The instrumentation and test method used for the radial permeameter test are described by South and Daemen (1986, Sections 3.2, 3.3).

2. Experimental Apparatus

A permeameter and a constant pressure pump were designed and four each were constructed by the Central Machine Shop, University of Arizona Instrument Shops. A data acquisition system was assembled and software written to collect the required data. Design and construction was performed using English units, and English units will be cited in this section where appropriate (South and Daemen, 1986, Ch. 3).

2.1. Permeameter Design

An assembly drawing of the permeameter design is shown in Figure 1; small black rectangles indicate O-ring seals. The permeameter is designed to accept a 15.24 cm (6 inch) diameter, 30.48 cm (12 inch) long cylindrical rock specimen with a 1 inch diameter hole drilled at both ends along the longitudinal cylinder axis. There is enough travel in the piston to accept samples between 27.94 cm (11 inches) and 31.12 cm (12 1/4 inches) long, using a 6.35 mm (1/4 inch) thick platen at the bottom of the pressure cell. Shorter specimens require

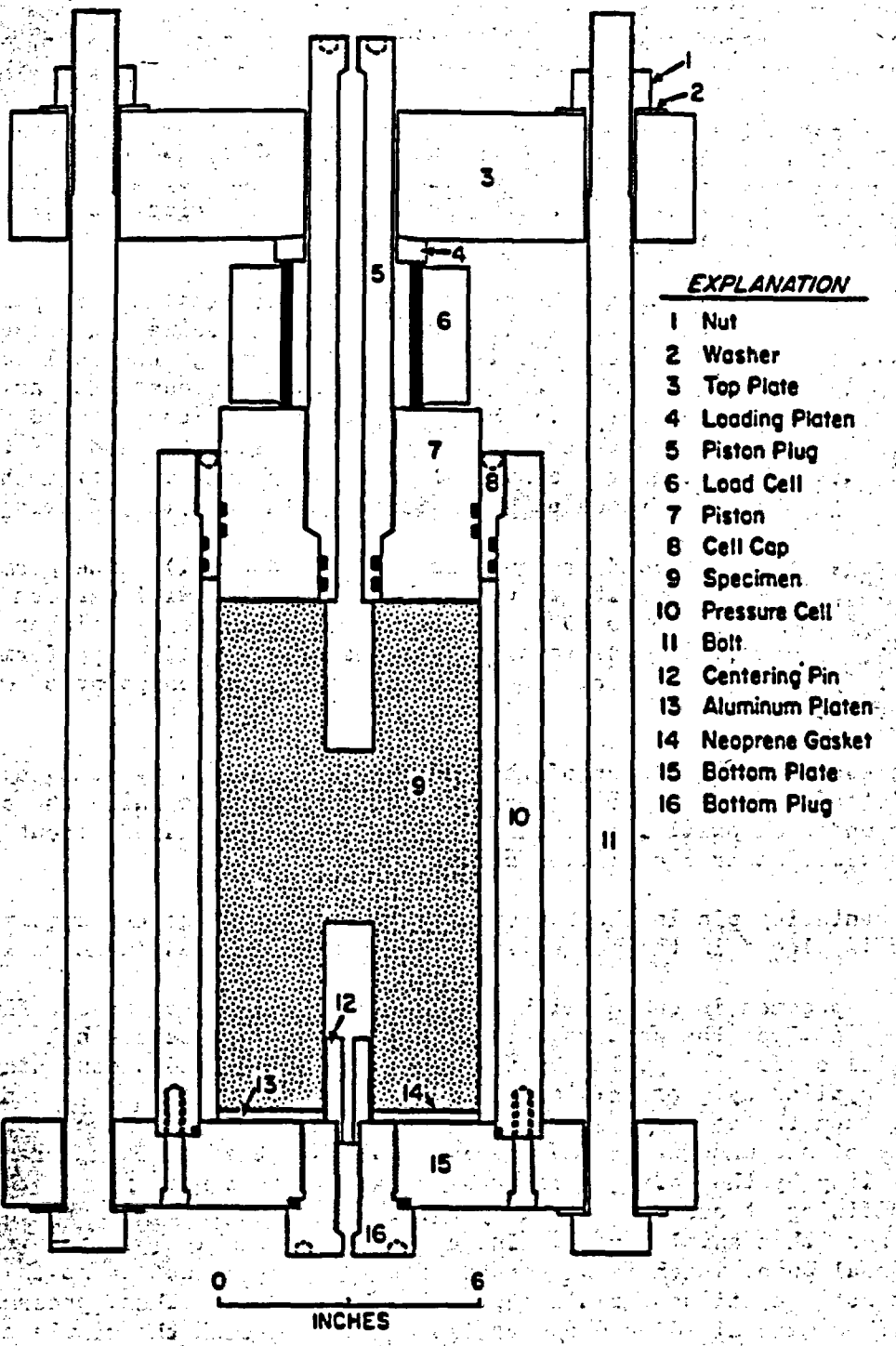

Figure 1 Radial permeameter assembly drawing. Small black rectangles indicate O-ring seals.

(from South and Daemen, 1986, Figure 3.9, p. 78)

a thicker platen or multiple platens. Longer specimens may interfere with the cell cap. The specimen diameter should be as close to 15.24 cm (6 inches) as possible to match the diameter of the piston. Aluminum platens, as indicated on Figure 1, are usually closer to the stiffness properties of rock; stainless steel platens are used for most of this work, however, because they are more chemically inert.

A nominal axial stress of up to 21 MPa (3000 psi) may be applied to the rock cylinder by tightening the bolts. The load thus applied is measured with a load cell. A loading platen on top of the load cell has a hemispherical top which matches a hemispherical seat in the bottom of the top plate.

Fluid (distilled water, brine, oil or nitrogen gas) may be pumped into the top hole, the bottom hole, and the annulus between the rock cylinder and the pressure cell. (Fittings through the cell to the annulus are not shown on the assembly drawing because they are out of the plane of the section.) Neoprene gaskets are cut as needed from a 0.16 cm (1/16 inch) thick sheet and used to seal the ends of the rock cylinder, isolating the annulus from the top hole and bottom hole. These gaskets are shown as heavy lines on the assembly drawing.

Nominal maximum fluid pressure is 21 MPa (3000 psi). The permeameter was designed to operate at room temperature, but will perform at temperatures of up to 80°C. It may be possible to use higher temperatures, but additional safety analyses should be performed, particularly if temperatures above the vaporization point of water are involved.

Access to the interior of the specimen is provided by removing the piston plug and the bottom plug. This may be done while the specimen is under an axial stress and, if pressure is maintained about the annulus, under a confining stress.

A centering pin in the bottom plug is used to align the specimen when it is placed in the permeameter; the pin is removed during testing.

The specimen is coated with epoxy on the outside to prevent fluid seepage from the annulus through the rock to the center hole. An axial stress is applied by tightening the bolts and a confining stress is applied by pressurizing water, brine, oil, or gas in the annulus between the specimen and the pressure cell. The neoprene gaskets on top of and underneath the specimen maintain the confining pressure. Sealing by the gaskets requires an axial stress higher than the confining stress. It is not possible to maintain a higher confining stress than axial stress. The confining stress is applied with a manual pump, which is disconnected after pressurization so that there is not a continuous fluid supply to the annulus. Thus, pressure is either maintained or drops as fluid leaks through the sample and seals. A pressure drop of 0.01 MPa corresponds to a leakage of about 0.007 cc of water through the end seals.

Good sealing can be obtained only if the ends of the specimen are parallel. Care must be taken to ensure parallelism when specimens are prepared, as discussed under sample preparation techniques.

The permeameter AISI* 4140 steel has a tensile strength of 1000 MPa (145,000 psi) and a yield point of 900 MPa (131,000 psi). The bolts were heat-treated to obtain a tensile strength of 1310 MPa (190,000 psi). No other pieces were heat-treated. SAE Grade 8, 2.54 cm (1 inch) diameter, 14 thread-per-inch nuts are used on the bolts. These have a minimum tensile strength of 1035 MPa (150,000 psi) (Baumeister and Marks, 1967, pp. 8-35, Table 30) and were purchased commercially. The bolts are made by threading a nut on one end of a piece of 1-inch round stock and welding it in place. The other end is then threaded and the bolt heat treated.

Table 1 lists the parts necessary to assemble one permeameter. Flareless tube fittings and 3.2 mm (1/8 inch) diameter high-strength stainless steel tubing are used to connect the permeameter to other equipment. For this work, Hoke Gyrolok brand fittings and needle valves (D3712G2Y) were used. The tubing was 3.2 mm (1/8 inch) O.D. seamless, annealed 316 stainless steel tubing with an allowable working stress of 87 MPa (12,641 psi) (ASTM A-213). Tubing with a higher working stress than necessary for safety was used to make the system as rigid as possible (that is, to minimize expansion of the tubing as pressure is applied).

The pressure cell has an outside diameter of 17.15 cm (6 3/4 inches), 2.54 cm (1 inch) thick walls, and an overall length of 40.64 cm (16 inches).

The O-ring seals must hold 21 MPa (3000 psi) water pressure. The top plug, bottom plug, and pressure cell were tapped to accept 1/8-inch NPT (National Pipe Thread) fittings. The bolts were threaded to fit the commercially purchased nuts. All other threads were 10 threads per inch. Holes were tapped in the top plug, the bottom plug, and the cell cap to accept a spanner wrench. In the case of the cell cap a spanner wrench was made from a piece of pipe. The outside of each permeameter was painted for corrosion resistance. Engine paint resistant to temperatures up to 315°C was used. Parts not painted were cadmium plated.

Steel pallets were constructed on which to place the permeameters, and a pallet truck is used to move them about. Holes for lifting are tapped on the top plate for drop-forged eyebolts. The weight of the assembly is about 230 kg (500 lbs), and access to the bottom is obtained by turning the entire permeameter over when it is assembled, using an overhead crane.

2.2. Pump Design

Testing fluid (distilled water, nitrogen gas, brine or oil) must be supplied to a specimen in the permeameter at a constant pressure and a very slow rate. To be able to compare experiments it is desirable to

---

*American Iron and Steel Institute

Table 1 Radial Permeameter Parts List
(from South and Daemen, 1986, Table 3.7, p. 80)

Part	Number Needed	Made From
SAE Grade 8 1" Nuts	18	Purchase commercially
1" Washers	12	Purchase commercially
Bolts	6	1" round stock
Top Plate	1	15-1/4" diameter, 3" thick piece
Bottom Plate	1	15-1/4" diameter, 2" thick piece
Loading Platen	1	1-1/4" thick, 3-1/2" diameter piece
50 Ton Load Cell	1	Purchase commercially
Piston Plug	1	2-1/4" round stock
Piston	1	6-1/4" round stock
Cell Cap	1	7-1/4" O.D. tubing, 0.875" wall
Pressure Cell	1	8-3/4" O.D. tubing, 1-1/4" wall
Bottom plug	1	3" round stock
A-320 O-Ring (for Piston Plug)	2	Purchase commercially
A-331 O-Ring (for Bottom Plug)	1	Purchase commercially
A-358 O-Ring (for Piston)	2	Purchase commercially
A-362 O-Ring (for Cell Cap)	2	Purchase commercially
A-363 O-Ring (for Bottom Plate)	1	Purchase commercially

NOTE: Material used is to be AISI-4140 steel. Parts may be made from any available stock, but stock purchased must be sufficiently over the final dimensions to allow for clean-up and machining. Dimensions given in this table are stock dimensions, not final dimensions.

set the pressure and let flow rates be controlled by the permeability of the rock/plug system, as opposed to injecting fluid at a constant rate and letting pressure fall where it may. The injection pressure is read by means of a pressure gage.

A constant pressure pump was designed and four were constructed by the Central Machine Shop, University of Arizona Instrument Shops. Figure 2 is an assembly drawing of the pump. Compressed nitrogen is supplied to a large diameter cylinder, forcing a piston downward. A smaller piston is thus forced into a cylinder containing liquid, forcing liquid out of the bottom of the small cylinder at constant pressure. The fitting connected to the bottom of the liquid cylinder is connected with tubing to a fitting on the permeameter (Figure 3).

Pressure intensification is approximately 11.5. The gas cylinder and water cylinder are connected by eight 1.91 cm (3/4 inch) diameter rods through flanges welded to the cylinder ends. The other end of each cylinder is capped by a round plate held on with cap screws. The capping plates are drilled and tapped for 1/8-inch NPT fittings and use an O-ring to provide a static seal. At the flange end of the cylinders sliding seals are necessary as the pistons must slide back and forth. Two O-rings, separated by spacers, and a packing nut provide these seals. In the case of the gas cylinder "Bal Seal" brand teflon O-rings are used. Standard teflon O-rings are used to provide the seal on the liquid cylinder to avoid the use of grease, which could contaminate the liquid.

The main pump limitation is that pressures below about 1 MPa (150 psi) cannot be maintained constant because of O-ring friction. O-ring friction is responsible for pressure fluctuations of 0.1 to 0.2 MPa (10 to 20 psi) at higher pressures as well.

The volume of liquid pumped must be measured precisely. The piston has a stroke of 25.40 cm (10 inches) and a diameter of 2.49 cm (0.980 inches). A travel of 0.003 cm (0.001 inch) corresponds to a volume of 0.0124 cc. Piston travel is measured using a linear encoder interfaced with the microcomputer controlled data acquisition system.

Provision is made on the pumps for mounting a long-range displacement dial gage which measures to the nearest 0.003 cm (0.001 inch).

2.3. Data Acquisition System

To provide a redundant measurement, pressure transducers and LVDT (linear variable displacement transducer) may be used to measure the top and bottom hole pressures and the displacement of the piston in the intensifier, respectively.

Data are collected using an automatic data logging system. A Model PC-100B microcomputer made by Applied Microtechnology, Tucson, Arizona, monitors transducers and records pressures and intensifier piston displacements.

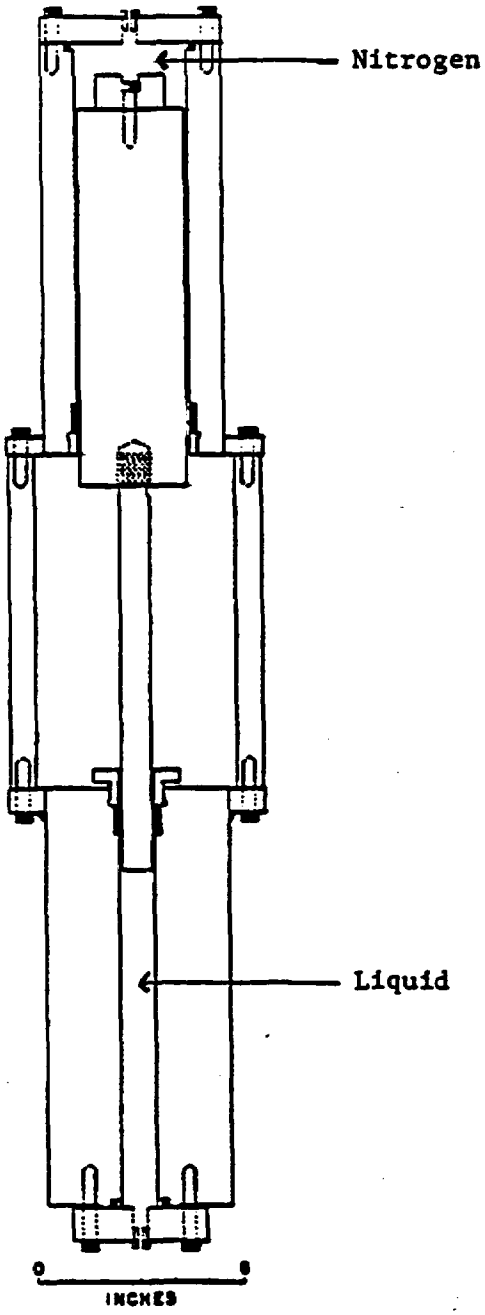

Figure 2 Constant pressure pump assembly drawing. Gas admitted to the top cylinder forces the large piston down, pressurizing liquid in the bottom cylinder. Pressure intensification is 11½.

(from South and Daemen, 1986, Figure 3.10, p. 83)

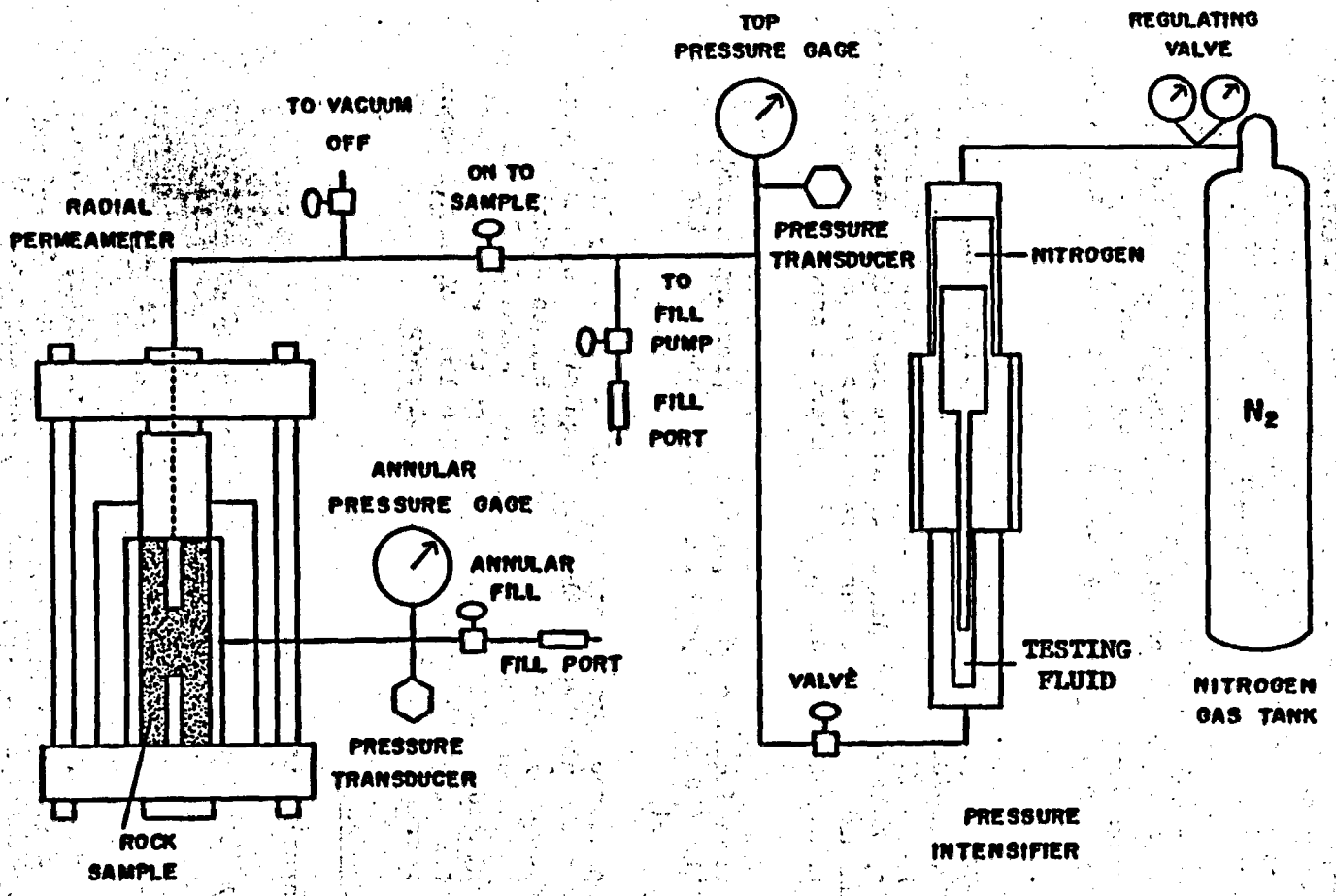

Figure 3 Laboratory arrangement for radial permeameter testing.

The volume of liquid pumped into a sample is measured by monitoring the pump piston displacement with a Heidenhain Pos-Econ Model 501 linear encoder connected to a circuit card designed by Applied Microtechnology.

The liquid flowing out of the sample can be collected in a flask which sits on a Gould Model UC-3 force transducer. This analog device is connected to an analog-to-digital voltage converter card in the microcomputer. Reading the force transducer yields the amount of liquid which has flowed out of the sample. Alternatively, the outflow can be collected in a high-precision pipette. An identical pipette is used in parallel to monitor evaporation. Evaporation is controlled by a thin layer of vacuum pump oil on top of the collected fluid. Chemical composition and pH of the inflow and outflow fluids should be determined.

Fluid pressure is measured using National semiconductor Model LX-1450AF and LX-1460AF pressure transducers. The Model LX-1450AF has a range of 0-14 MPa (0-2000 psi) and the Model LX-1460AF a range of 0-21 MPa (0-3000 psi). The lower pressure range is used to measure pressure in the top hole and the higher pressure range to measure pressure in the annulus. The pressure transducers are analog devices connected to the analog-to-digital voltage converter card.

As connected, the linear encoder has an accuracy of 0.0020 cm (0.0008 inch), the force transducers of 0.02 gm, and the pressure transducers of 0.07 and 0.10 MPa (10 and 15 psi) for the LX-1450AF and the LX-1460AF, respectively.

Axial stress is monitored using fifty ton (455 kN) capacity load cells. These are not connected to the data acquisition system. Each load cell is connected by a cable and a junction box to a strain indicator unit which, when read, allows the total axial load on a sample to be calculated. Axial stress depends on the exact sample diameter. Loads are accurate to about 400 N (90 lb). This equipment was furnished by Terrametrics, Inc., Golden, Colorado.

3. Experimental Procedure

3.1. Sample Preparation and Loading

15.24 cm (6 inch) diameter samples are obtained either by laboratory coring of blocks collected from the field or directly by field coring. The cylinders are cut to length, typically 30.48 cm (12 inches) with a diamond saw. The ends are ground flat and parallel.

Grinding is important. Flat, parallel ends are necessary to obtain good seals and to insure a uniform stress distribution. Sample ends are prepared to specifications recommended by the International Society for Rock Mechanics (Bieniawski et al., 1978) for preparing samples for uniaxial compressive strength testing. This specification states that the ends shall be flat to 0.02 mm and shall be parallel to within 0.10 mm in 50 mm. Samples are prepared and flatness and parallelism checked with a dial gage.

Next, 2.54 cm (1 inch) diameter holes are drilled along the sample axis from each end to a depth of one-third the total sample length. Centering is aided by means of a jig made for this purpose. The holes are drilled with a core drill. When the desired depth is reached the core drill is withdrawn and the core broken off. A 2.54 cm diameter blind bit is then used to flatten the bottom of the hole.

In order to prevent seepage of confining fluid into the sides and ends of the sample, several coats of epoxy (Scotch Weld Structural Adhesive 2216) are applied to the external surfaces of the sample. Next, the sample is placed in the permeameter and a small axial load is applied to keep the top plate secure. The permeameter is turned over, the bottom plug removed, and the bottom hole filled with testing liquid. Enough liquid is poured into the bottom hole so that when the bottom plug is replaced, liquid is forced from the valve, ensuring that no air is entrapped.

The testing fluid needs to be specified . Unless otherwise indicated, the testing liquid will be deaired distilled water.

The permeameter is righted and connected to a pump, ready for saturation and testing.

3.2. Testing

The sample is first tested with a rock bridge in place. Axial and confining stresses are applied to the sample. A vacuum is applied to the top hole. At this time the bottom hole is filled with liquid and its valve is closed. The vacuum draws the air from the top hole and from the sample's pore space. Once the sample has been saturated, which is assumed to be evidenced by liquid flowing from the top hole at the same rate as it is injected, testing liquid is injected into the top hole through a manifold which allows the liquid to be injected without admitting air to the top hole.*

Liquid flows through the sample to the bottom hole, which is at zero or at some controlled pressure. Flow from the bottom hole is collected in a flask or in a high-precision pipette and weighed; flow into the top hole is measured by pump piston displacement. pH of inflow and outflow fluid should be monitored or measured regularly.

---

* It is recognized that this procedure does not guarantee sample saturation.

It can readily be visualized (e.g. South and Daemen, 1986, Figs. 8-10, pp. 12-14) that the flowpath does not significantly affect the corners of the rock cylinder. It is assumed here that the flowpaths are sufficiently similar over the full range of tests to warrant neglecting any corner effects. A desirable but time-consuming alternate, used on occasion, is to saturate the cylinder by radial flow, alternating convergent and divergent flow. This saturation procedure must precede sample coating.

During the test, axial stress is maintained by the permeameter bolts and confining stress is maintained by fluid pressure in the annulus. No pump is permanently connected to the annulus. Any leakage results in a drop in annular pressure and is detected by this pressure drop. Annular pressure is kept higher than top and bottom hole pressure.

Following tests at three different top hole injection pressures, the rock bridge is cored from the sample. Axial and confining stress are maintained during this operation. A plug of cement, bentonite or crushed rock is then placed. The cement grout is mixed according to American Petroleum Institute specifications (American Petroleum Institute, 1986, pp. 14-19). Bentonite plug or crushed rock plug preparation are subject to a separate experimental procedure write-up. A rubber stopper is placed at the location of the bottom of the rock bridge. Cement grout is placed on top of the rubber stopper, by pouring a measured quantity of grout through a funnel, avoiding splashing and turbulence. The cement grout is then covered with water and allowed to cure. Following curing the rubber stopper is removed and the same series of tests performed on the rock bridge is performed on the cement plug. Flow through the plug will thus be directly comparable with flow through the intact rock.

3.3. Loading the Radial Permeameter

a. Start with permeameter completely disassembled.

b. Put in bottom plug with centering pin (see Figure 1).

c. Place neoprene gasket on the bottom. This should be a 15-cm (6-inch) diameter gasket with a 5- or 7-cm (2- or 3-inch) diameter hole in the center. Normally 2-mm (1/16-inch) thick gasket material is used. When the axial stress is applied, the gasket material squeezes toward the center hole and the annulus.

d. Put stainless steel platen on top of gasket.

e. Put in another gasket.

f. Place sample in permeameter, inserting centering pin in bottom hole of sample.

g. Put a neoprene gasket on top of the sample.

h. Screw in cell cap until about 6 mm (1/4 in) from sample top.

i. Fill annulus with water. Annular valve should be open at first to let air out of lines; let water drip from valve for a while, then shut the valve. Bottom plug must be capped.

j. Insert piston into cell cap. This works best if the piston plug is screwed into the piston and used to lower the piston into the cell cap. Lower the piston straight down, being careful not to get it tilted, cocked and stuck in the cell cap.

k. Put on the load cell and the hemispherical seat. Piston plug should still be screwed into the piston.

l. Take out to crane. Put on the top plate using the crane. Be careful not to damage the bolt threads.

m. Tighten bolts, being careful to keep load cell, hemispherical seat, and top plate centered. Using a wrench about a foot long, tighten the bolts as tightly as possible. At this point it is a good idea to check whether the annulus will hold water pressure by connecting the Ruska pump and putting about 1 MPa (145 psi) water pressure on the annulus. The cell should maintain the pressure fairly well (i.e. pressure drop should not exceed 10 psi/day). Also check that the piston plug can be removed.

n. Turn the permeameter over, using the crane and the chains and straps. Remove bottom plug. Remove centering pin. Fill bottom with water. Replace bottom plug with a valve. Be sure water runs out the valve as the plug is tightened.

o. Turn permeameter right side up.

p. Take the permeameter back into the test lab. Connect load cell to strain indicator. Record the initial strain reading.

q. Tighten bolts with torque wrench to desired axial stress. Figure 4 gives the calibration curves for the four cells (axial load as a function of strain). Apply desired confining stress to annulus. These stresses will relax somewhat over the first few hours and some readjustment will be necessary.

r. Bottom valve should be closed and the bottom full of water. Apply vacuum to the top hole, which should be empty of water. Apply a few hundred psi water pressure to bottom hole. Evacuate for a minimum of 24 hrs to remove air from the pore space of the sample.

s. Once sample has been evacuated (as evidenced by water flowing from the bottom hole into the top hole), close vacuum valve and fill top hole with water from the Ruska pump. Do not re-admit air to the top hole.

t. Ready to test. Connect the top hole of the sample to the pressure intensifier. Supply water at constant pressure to top hole and collect water from bottom hole. It will probably take some time - possibly days - for the mass balance to reach a reasonable value. What constitutes a reasonable mass balance is a difficult judgment call for the individual researcher, who should be guided by previous experience and analysis (e.g. South and Daemen, 1986).

4. References

American Petroleum Institute, 1986, Specifications for Materials and Testing for Well Cements, Third Edition, American Petroleum Institute, Production Department, Dallas, TX.

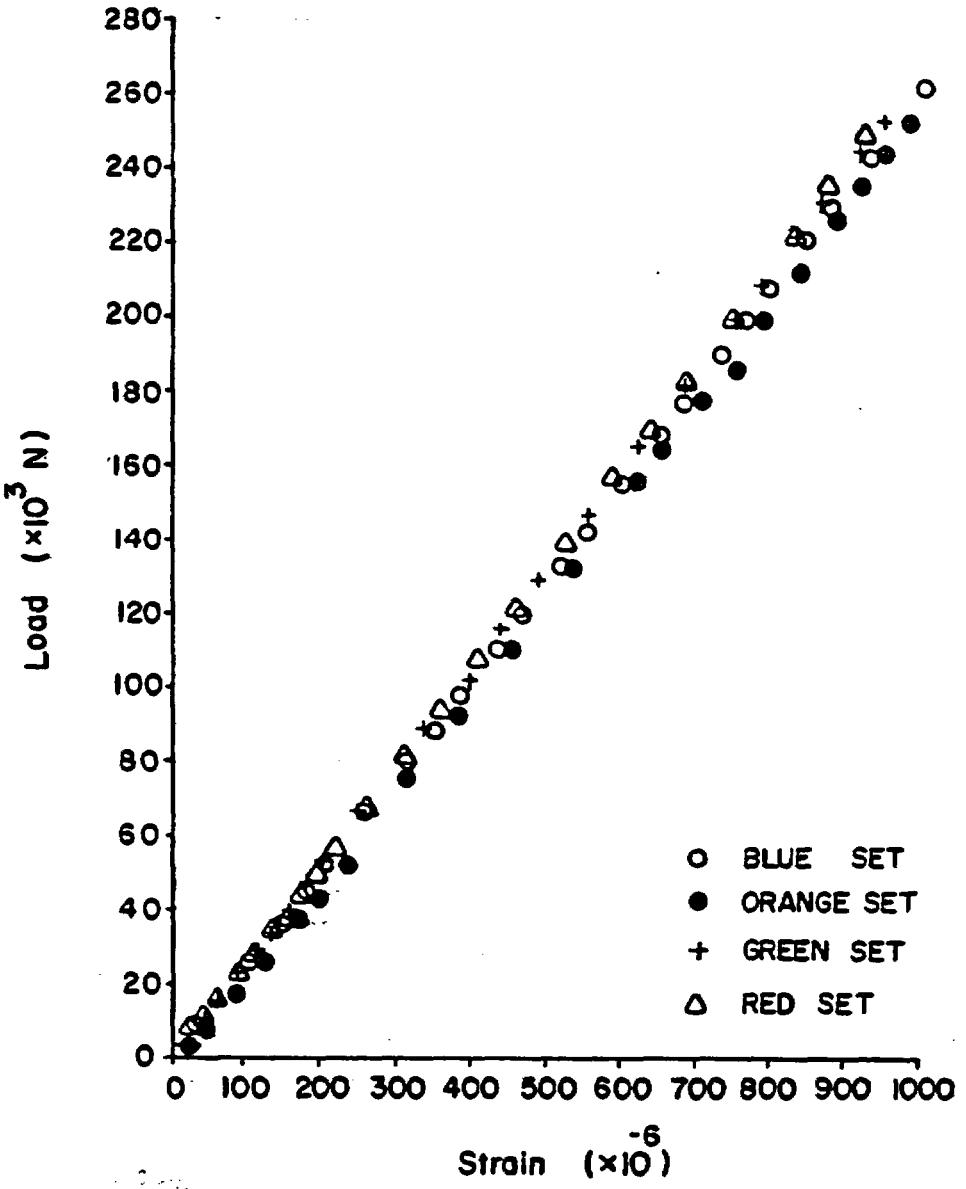

Figure 4 Calibration curves of load cells used in four radial permeameters. Axial load applied to the sample as a function of strain read from strain indicator.

Baumeister, T. and L.S. Mark, eds., 1967, Standard Handbook for Mechanical Engineers, 7th Edition: McGraw-Hill Book Company, San Francisco.

Bieniawski, Z.T., et al., 1978, "Suggested Methods for Determining the Uniaxial Compressive Strength and Deformability of Rock Materials," International Society for Rock Mechanics, Commission on Standardization of Laboratory and Field Tests, Committee on Laboratory Tests, September, published in International Journal of Rock Mechanics and Mining Sciences and Geomechanics Abstracts, Vol. 16, No. 2, pp. 135-140 (1979). Also in Rock Characterization Testing and Monitoring, ISRM Suggested Methods, pp. 111-116, E.T. Brown, ed., Pergamon Press, Oxford, 1981.

South, D.L. and J.J.K. Daemen, 1986, "Permeameter Studies of Water Flow Through Cement and Borehole Seals in Granite, Basalt and Tuff," Technical Report to the U.S. Nuclear Regulatory Commission, Division of Radiation Programs and Earth Sciences, Contract No. NRC-04-78-271, by the Department of Mining and Geological Engineering, University of Arizona, Tucson.

Spotts, M.F., 1971, Design of Machine Elements, Prentice-Hall, Englewood Cliffs, New Jersey.

CHAPTER FOUR

FLOW TESTING OF BENTONITE AND BENTONITE/CRUSHED TUFF SEALANTS

4.1 Introduction

This chapter gives the results of flow tests on bentonite and on bentonite/Apache Leap crushed tuff plugs.

The mixture samples containing 25 or 35 bentonite weight percent were tested again using injection pressures of 207 and 345 kPa (30 and 50 psi) after having been subjected to a series of flow tests at injection pressures of up to 690 kPa (100 psi). During the present flow test stage, the amount of solids carried in the outflows was carefully measured to allow for the assessment of the deterioration of the sealing performance. The time needed for the loss of 10 weight percent of bentonite was estimated, assuming that the flow rates obtained under the given injection pressures remain constant. The permeabilities measured appear to be 2 to 4 times lower than the results acquired earlier for similar injection pressures. Also included are preliminary results of the reversed flow tests (upward permeation). Six samples are undergoing reversed flow testing, at higher injection pressures.

Based on the results of the Schedule A flow tests for the mixture samples (Daemen et al., 1989, Ch. 4, Section 4.5), crushed tuff gradation type A and 25 and 35 bentonite weight percent were chosen for high-temperature and high-injection pressure flow testing in stainless steel permeameters (101.6 and 203.2 mm in diameter) (flow test Schedule B). The permeabilities of four such samples, measured at room temperature, are presented. Also reported are the results of flow tests performed on four additional samples installed in 101.6 mm diameter PVC permeameters. The crushed tuff of these four samples has a Fuller-Thompson size distribution curve, an ideal grading in which the particles fit together in the densest possible state of packing (Winterkorn, 1975; Head, 1980, p. 150). Fifteen and twenty-five bentonite weight percent was used in the sample preparation.

Four bentonite samples for high-temperature and high-injection pressure flow testing (test Schedule B for bentonite plugs) have been installed in stainless steel permeameters of 25.4, 34.9, 60.3 and 101.6 mm (1, 1 3/8, 2 3/8, and 4 in) diameter, respectively. Due to the prolonged saturation process, only preliminary room-temperature permeability results are included here. Additionally, the permeability to air has been determined for four compacted bentonite plugs installed in 25.4 mm diameter plexiglass permeameters. These samples are to be permeated with de-aired distilled water.

4.2 Flow Testing of Bentonite/Apache Leap Crushed Tuff Plugs

4.2.1 Flow Testing of Mixture Samples in PVC Permeameters

Reported in this section are the flow test results of six previously tested compacted bentonite/Apache Leap crushed tuff plugs. These samples have been emplaced with either 25 or 35% bentonite by weight. After being subjected to injection pressures up to 690 kPa (100 psi), they were tested again at lowered injection pressures of 207 and 345 kPa (30 and 50 psi). The permeability results are shown in Figures 4.1 through 4.3. Figures 4.4 to 4.9 depict the cumulative inflow and outflow for each sample.

The amount of solids carried in the outflows was carefully measured and the solid concentrations were calculated in grams per 100 cc. Based on the concentrations and average flow rate measured, a computation was performed to estimate the time possibly required for the loss of 10 weight percent bentonite, given the conditions of continuous permeation and constant flow rate. The results are summarized in Table 4.1. Also included in the table are the pH values of the outflows measured at the end of the flow testing at 345 kPa injection pressure. The pH values of the outflows collected from Samples B/AL-C-4-25/B, B/AL-C-4-25/C and B/AL-C-4-35/B appear to be lower than those for the other samples. The low pH values seem to be associated with high flow rates. The de-aired distilled water yields a pH value of 6.36, which increases to 7.31 when measured at room temperature after the water has been boiled in the presence of crushed tuff. Crushed tuff particles used in the boiling range from 12.7 to 19.05 mm in size. The boiling was maintained for 30 minutes, at room pressure.

The permeability results shown in Figures 4.1 to 4.3 are compared with the results obtained earlier under the same injection pressures in Figures 4.10 through 4.15. Except for Sample B/AL-C-4-25/B, the newly obtained permeabilities (second run) appear to be consistently 2 to 4 times lower than the results reported previously (first run). This suggests that irreversible changes in sample structure may have occurred. The contrasting behavior of B/AL-C-4-25/B (Figure 4.11) is believed to indicate sealing performance deterioration resulting from piping. The outflow collected from this sample has remained cloudy throughout the testing.

In the subsequent flow testing, the flow direction was reversed (to the upward direction) to study the sealing performance under the action of an upward seepage force. Sample B/AL-C-4-25/B, however, was omitted from this test series due to the rapid depletion of its inflow reservoir. Limited results (for injection pressures up to 69 kPa) are shown in Figures 4.16 and 4.17 for the samples with 25 and 35 bentonite weight percent, respectively. The permeability tends to increase as injection pressure increases. Upon incrementing the pressure from 35 kPa (5 psi) to 69 kpa (10 psi), cracks were seen to develop around the coarse portions (which contain less bentonite) close to the bottom of Sample B/AL-C-4-25/C. This may be due to insufficient confinement during installation of the sample, or due to particle migration or rearrangement.

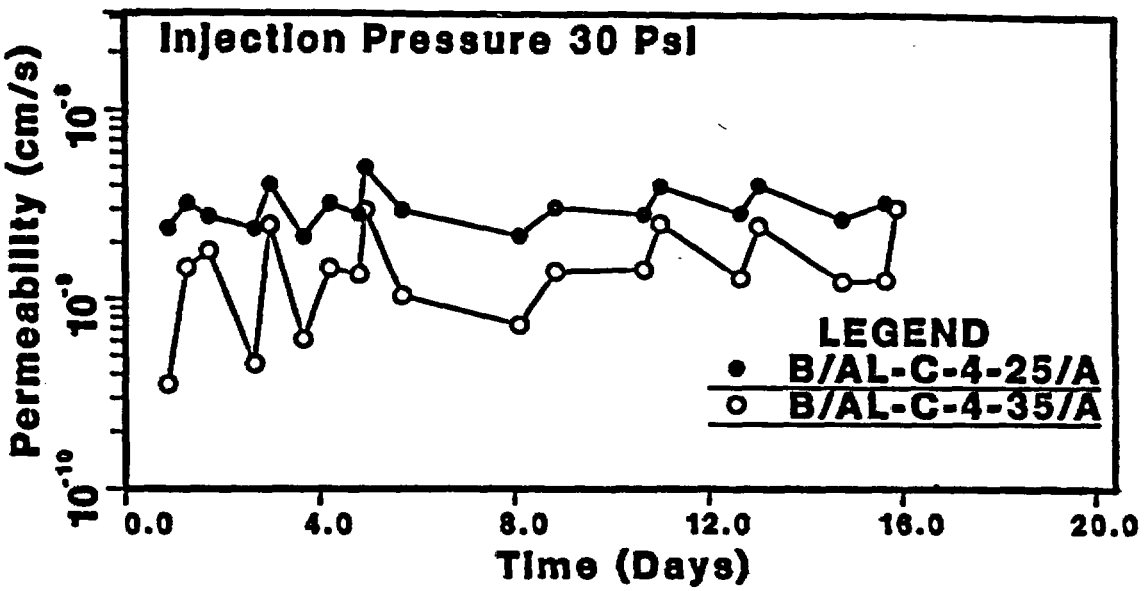

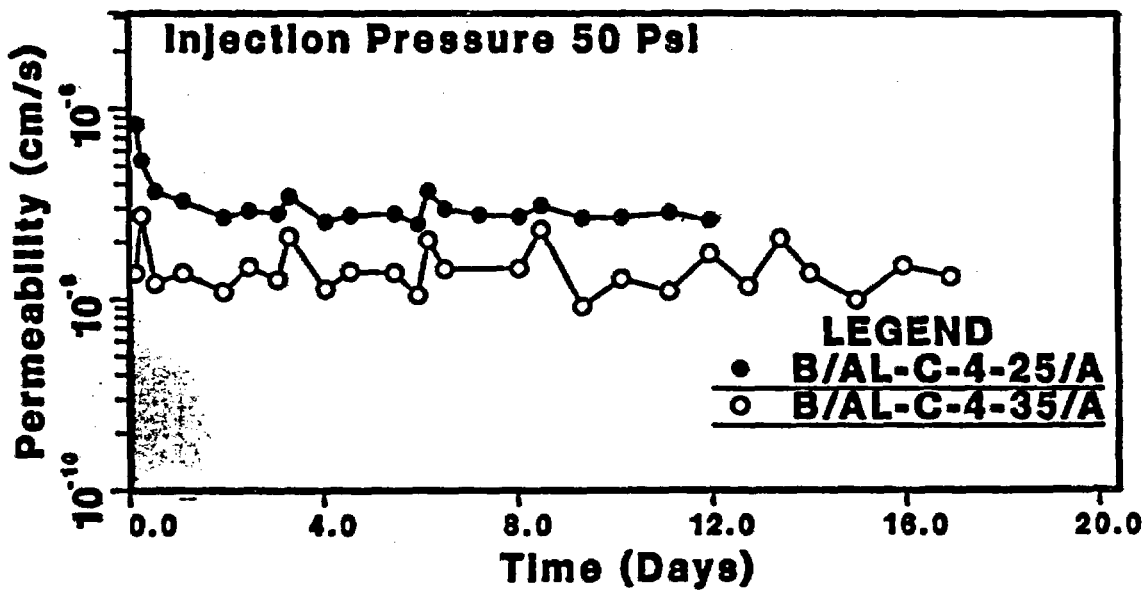

Figure 4.1 Permeability results of samples B/AL-C-4-25/A and B/AL-C-4-35/A at injection pressures of 207 and 345 kPa (30 and 50 psi). Hydraulic gradient: 200 to 208 for the former injection pressure, 333 to 347 for the latter.

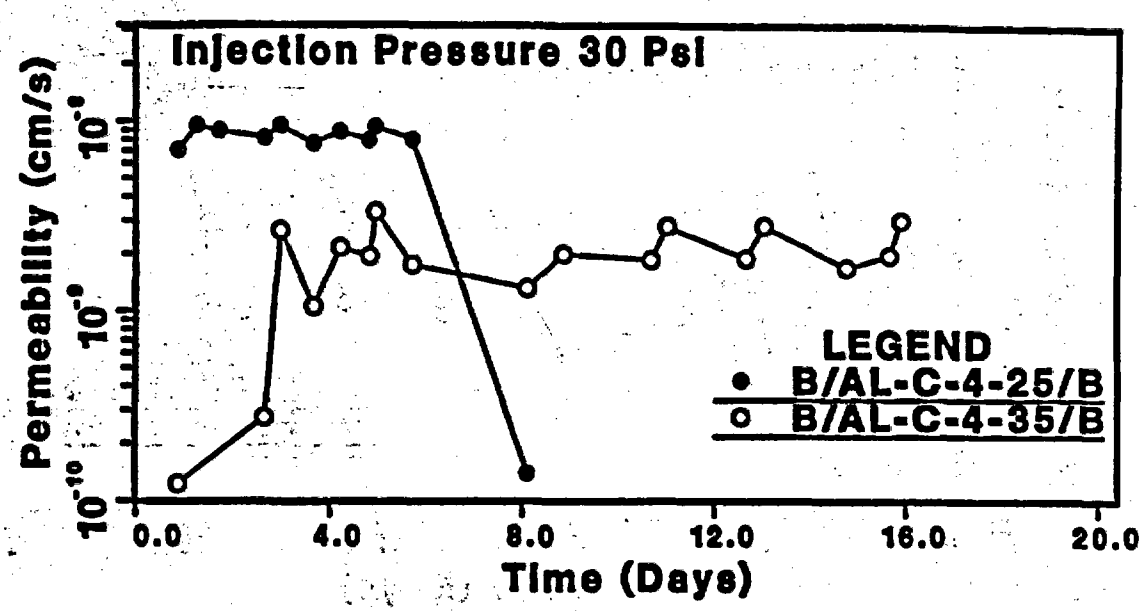

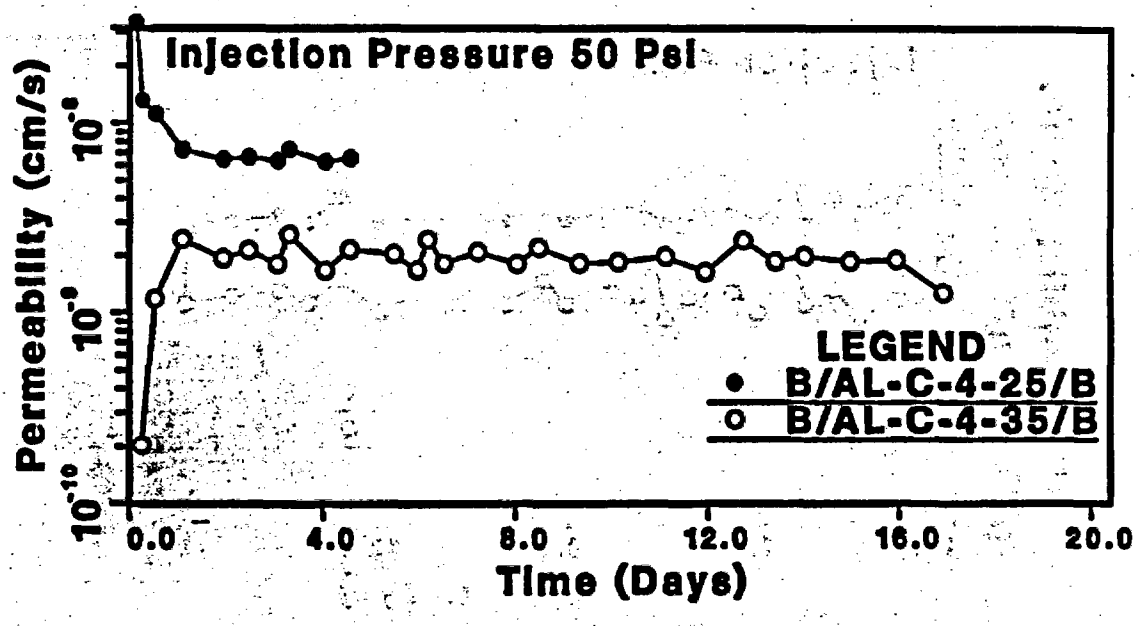

Figure 4.2 Permeability results of samples B/AL-C-4-25/B and B/AL-C-4-35/B at injection pressures of 207 and 345 kPa (30 and 50 psi). Hydraulic gradient: 193 to 211 for the former injection pressure, 321 to 351 for the latter.

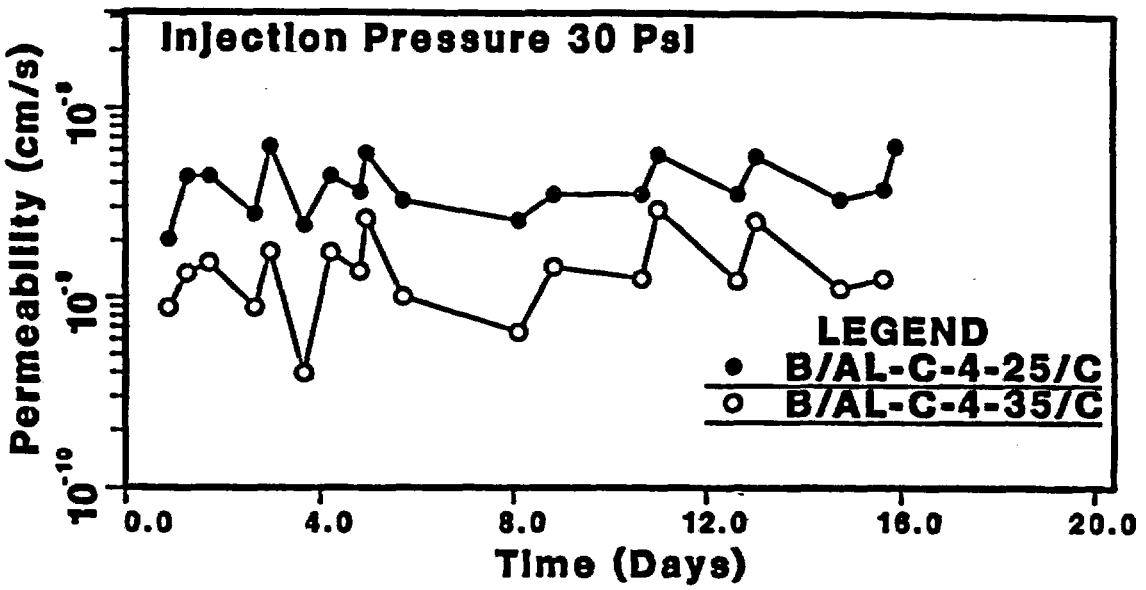

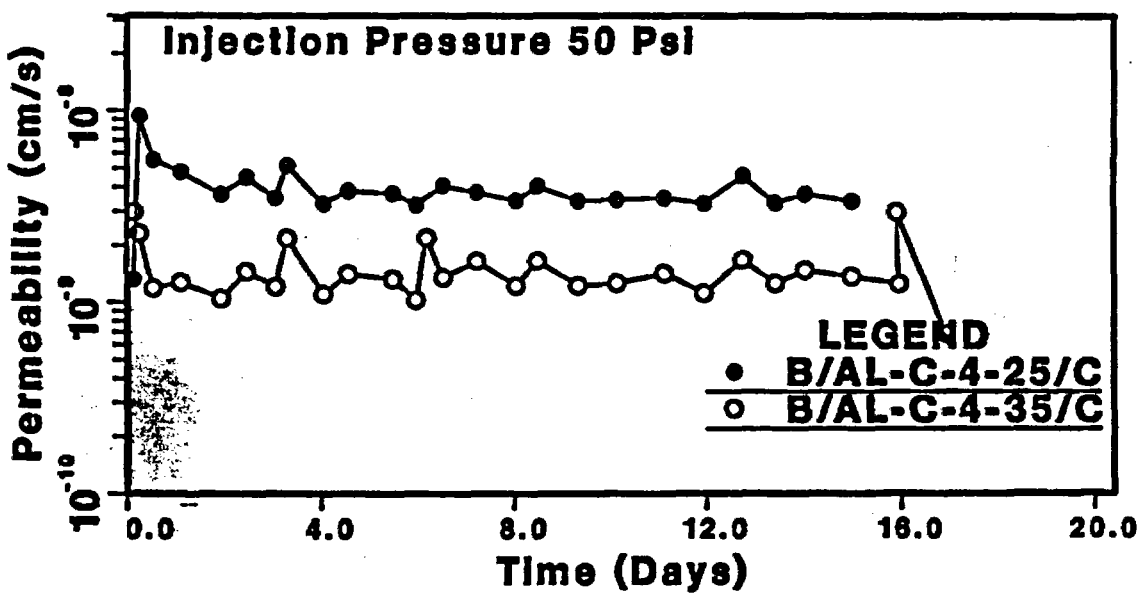

Figure 4.3 Permeability results of samples B/AL-C-4-25/C and B/AL-C-4-35/C at injection pressures of 207 and 345 kPa (30 and 50 psi). Hydraulic gradient: 186 to 208 for the former injection pressure, 310 to 347 for the latter.

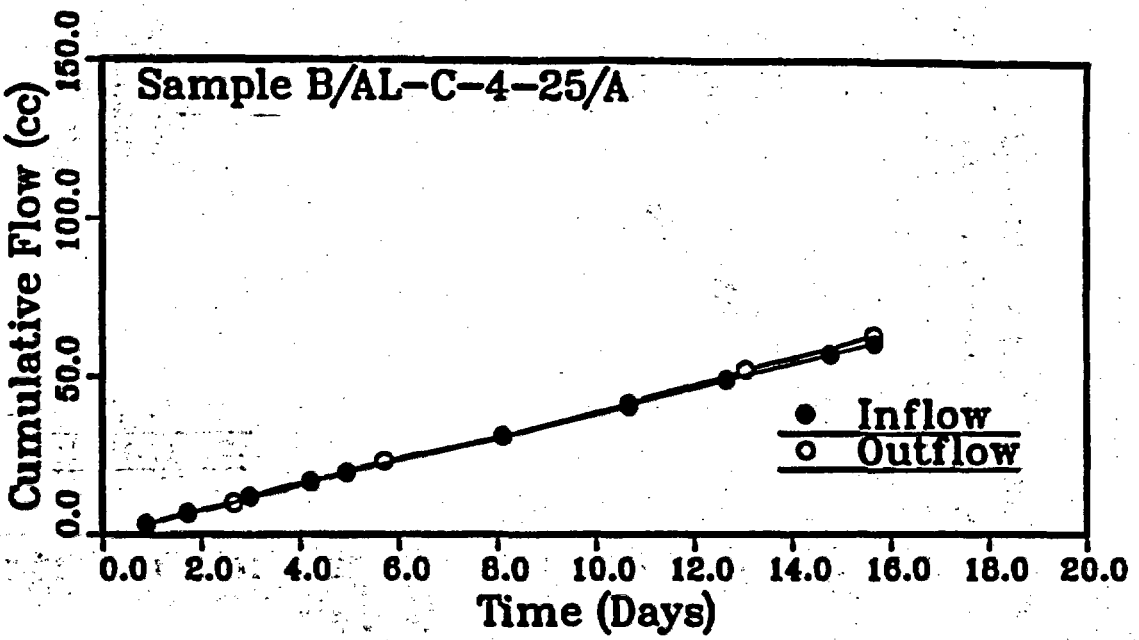

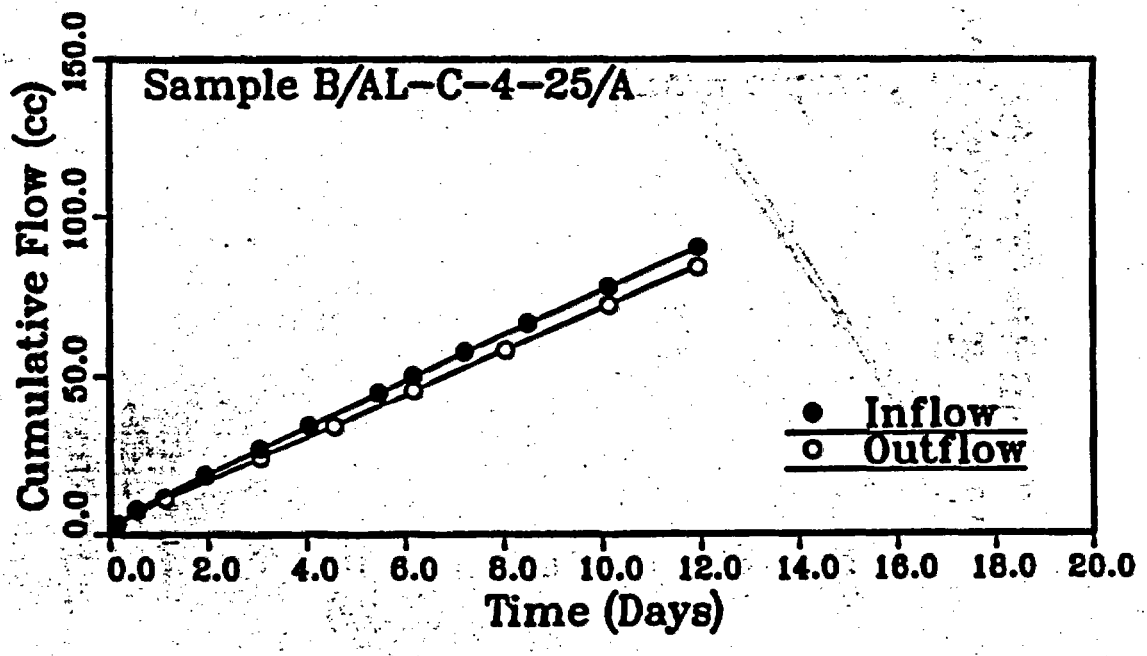

Figure 4.4 Cumulative inflow and outflow vs. time for sample B/AL-C-4-25/A (top: injection pressure = 207 kPa; bottom: injection pressure = 345 kPa).

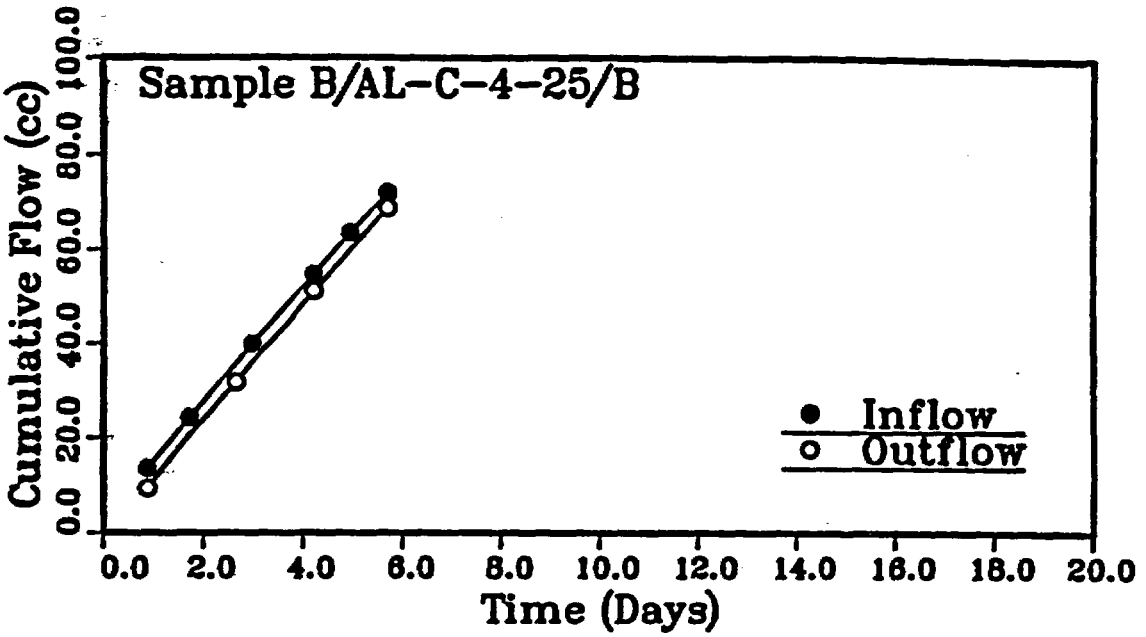

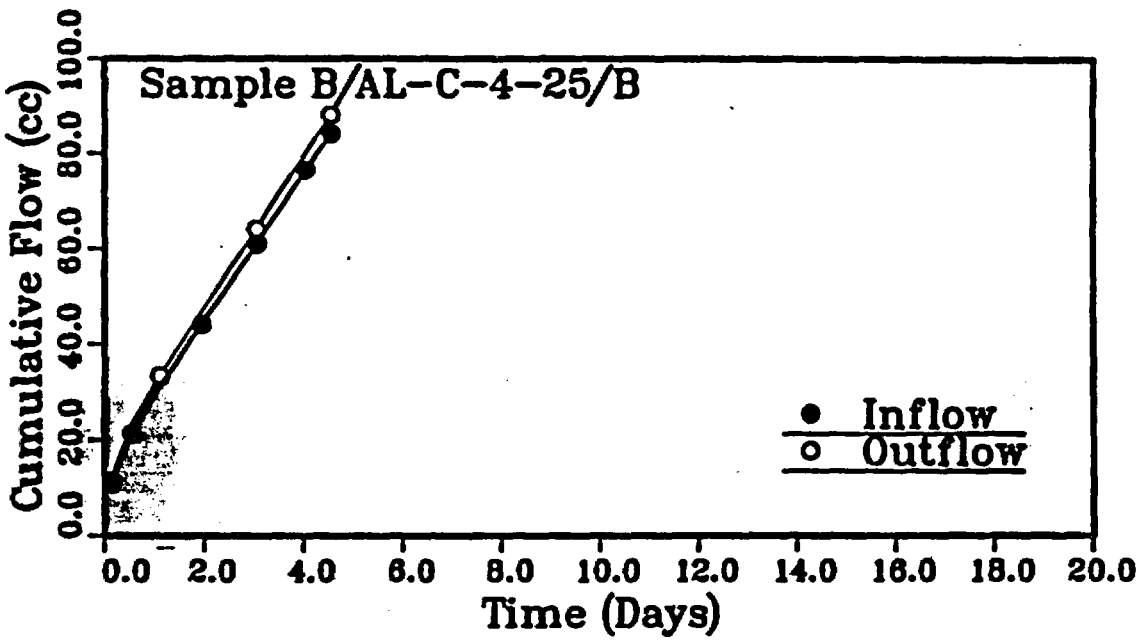

Figure 4.5 Cumulative inflow and outflow vs. time for sample B/AL-C-4-25/B (top: injection pressure = 207 kPa; bottom: injection pressure = 345 kPa).

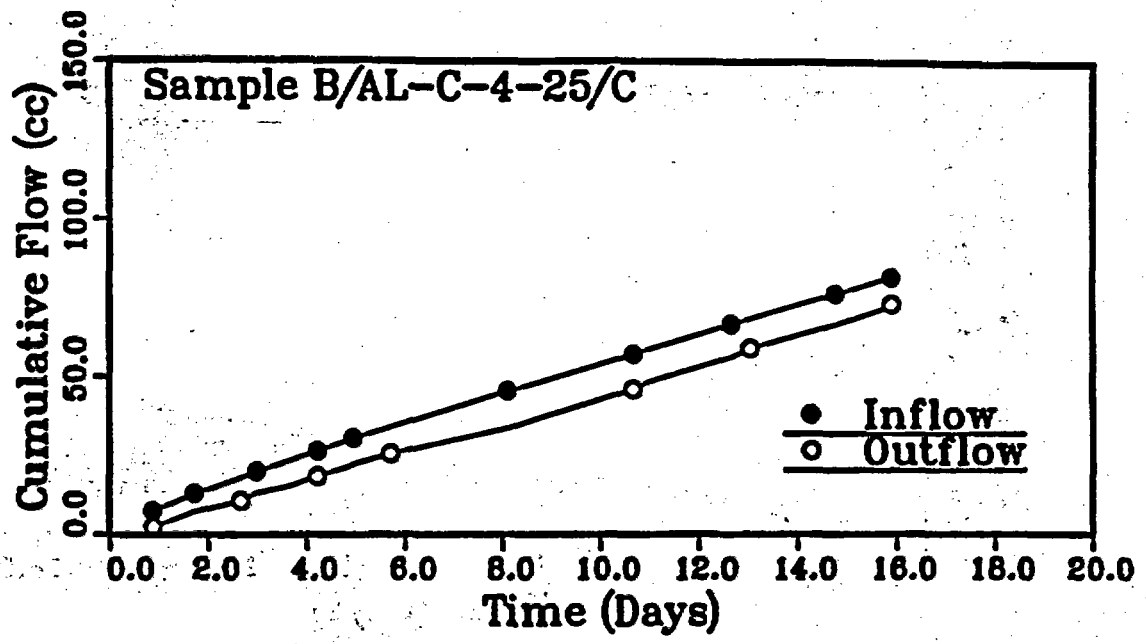

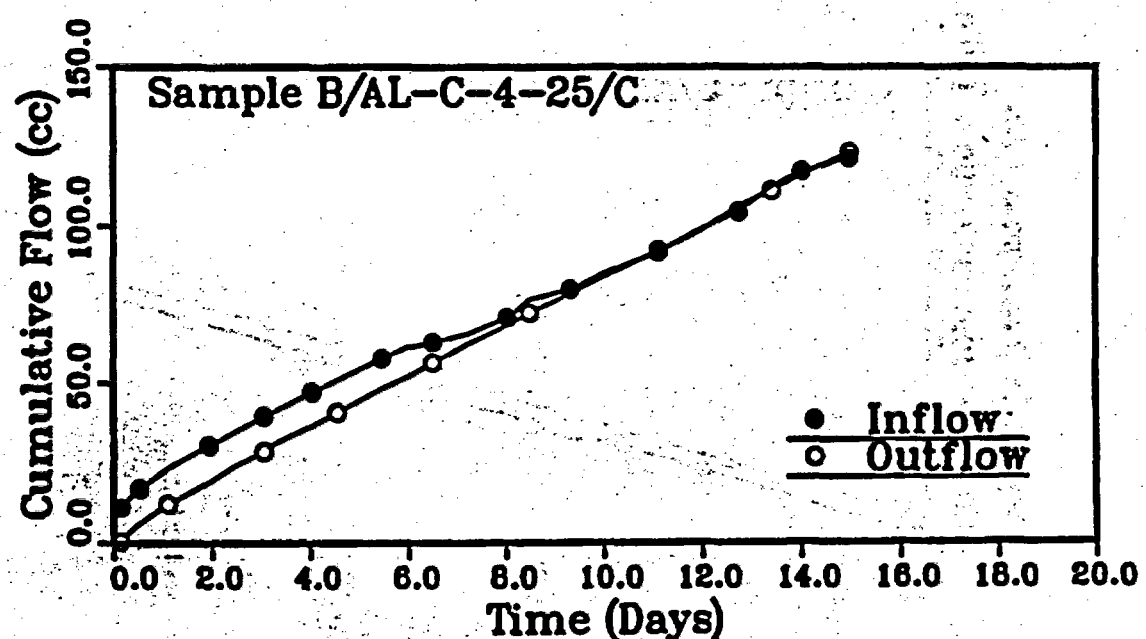

Figure 4.6 Cumulative inflow and outflow vs. time for sample B/AL-C-4-25/C (top: injection pressure = 207 kPa; bottom: injection pressure = 345 kPa).

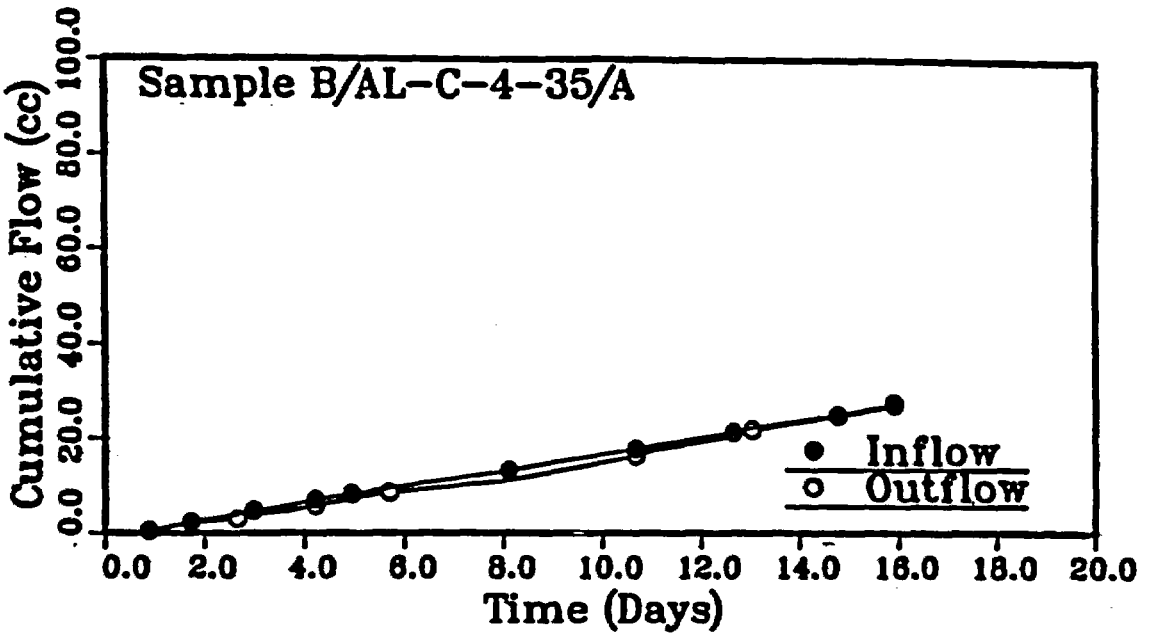

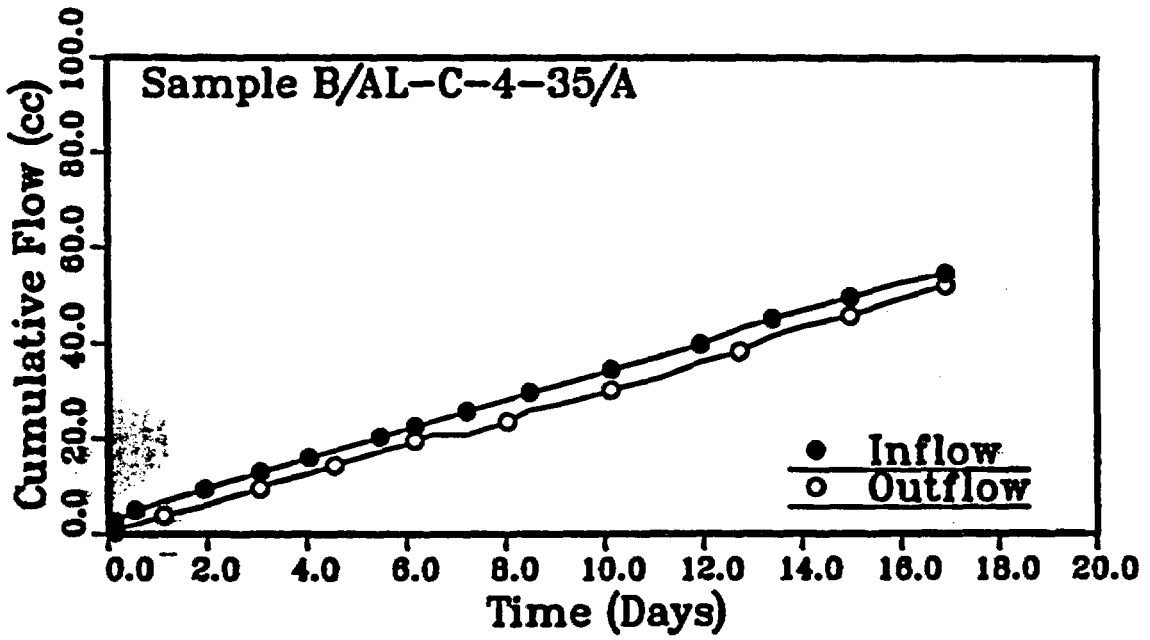

Figure 4.7 Cumulative inflow and outflow vs. time for sample B/AL-C-4-35/A (top: injection pressure = 207 kPa; bottom: injection pressure = 345 kPa).

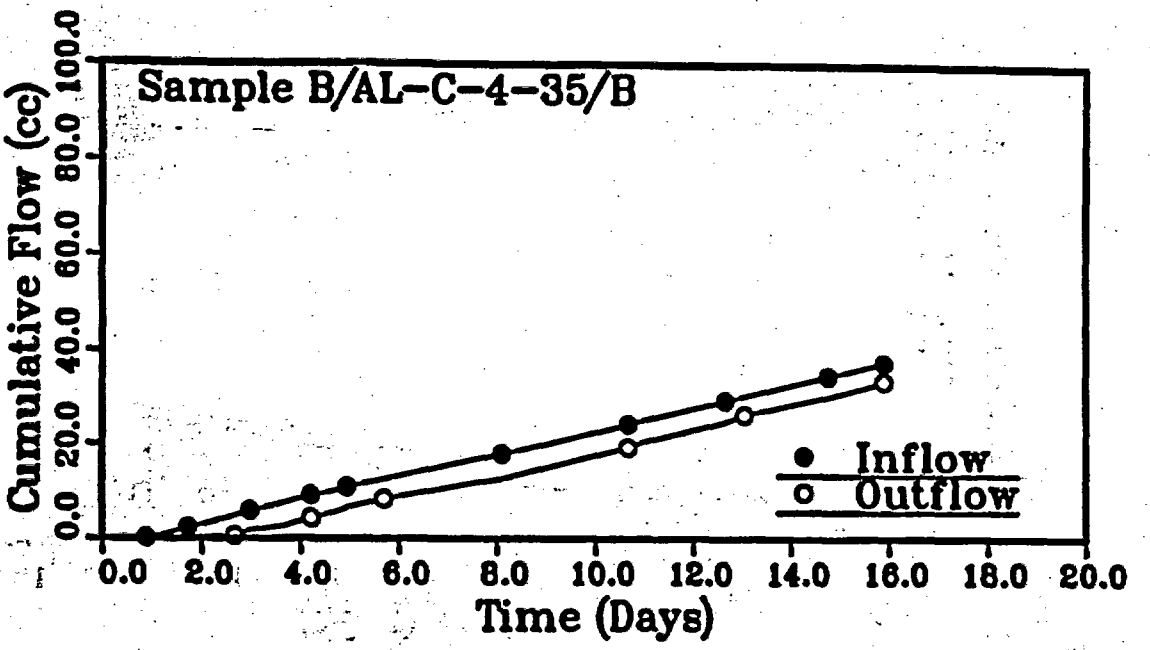

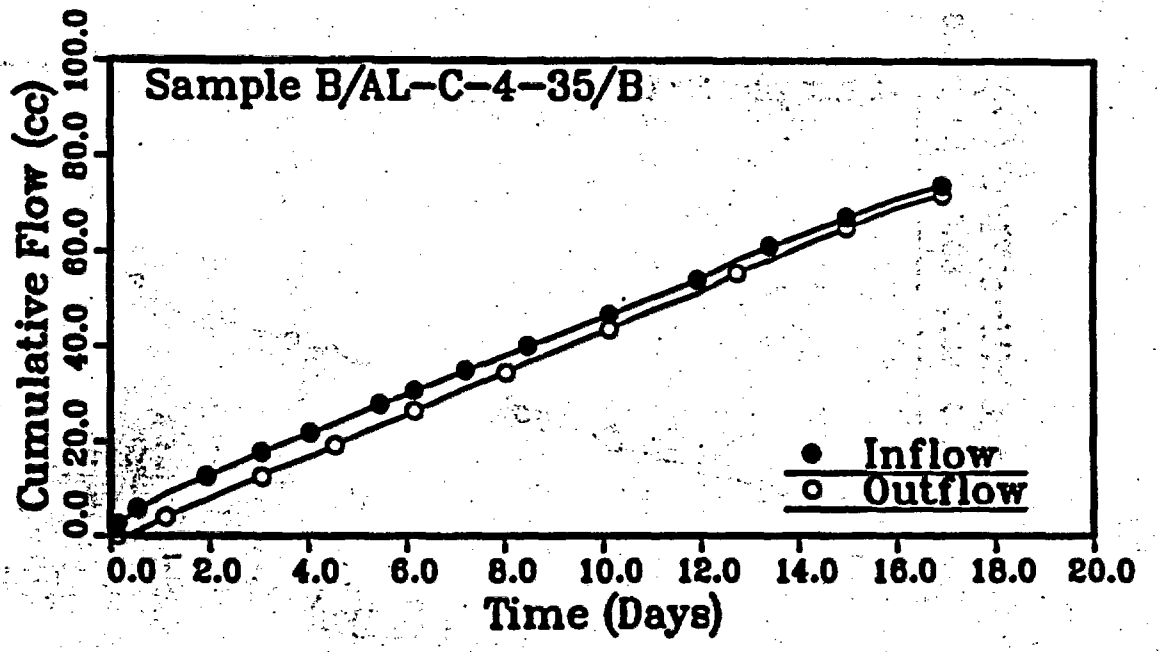

Figure 4.8 Cumulative inflow and outflow vs. time for sample B/AL-C-4-35/B (top: injection pressure = 207 kPa; bottom: injection pressure = 345 kPa).

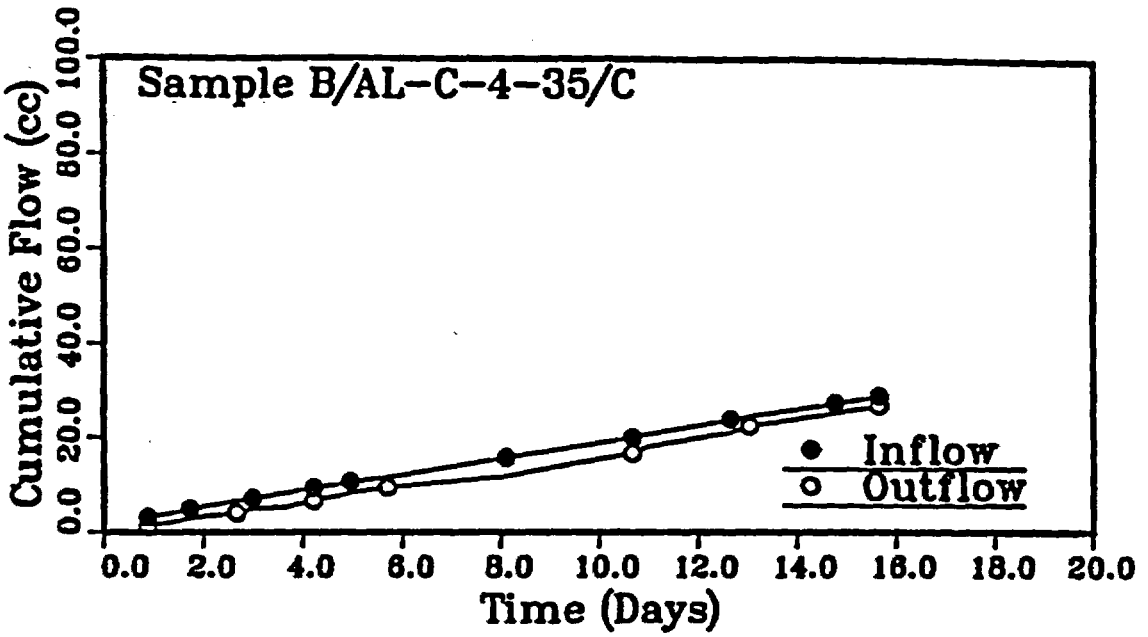

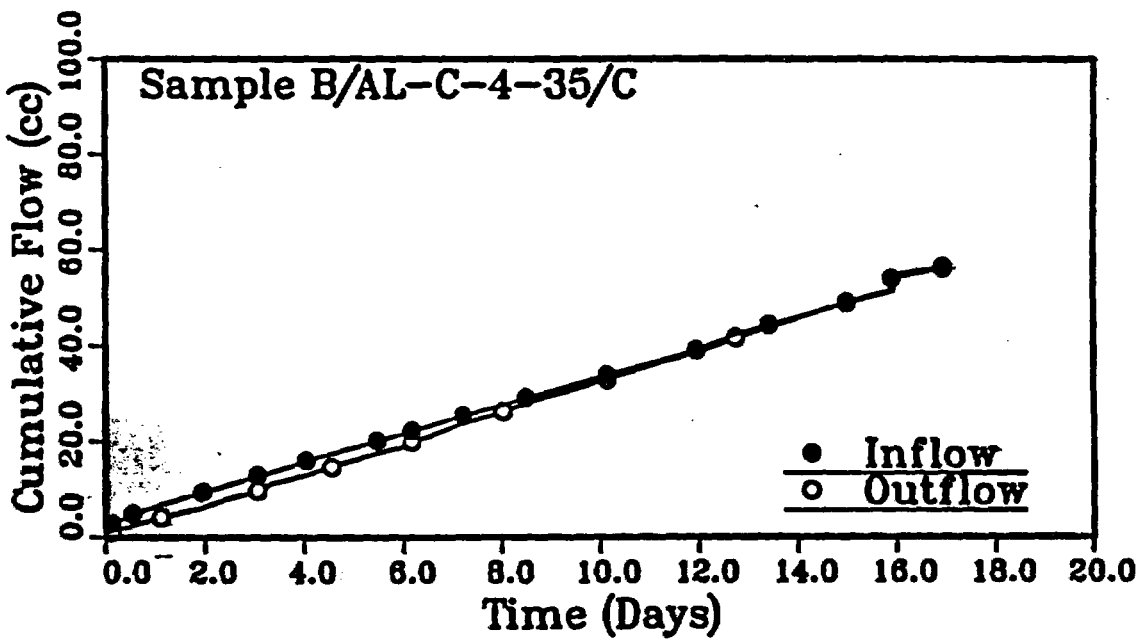

Figure 4.9 Cumulative inflow and outflow vs. time for sample B/AL-C-4-35/C (top: injection pressure = 207 kPa; bottom: injection pressure = 345 kPa).

Table 4.1 Flow Rates and Solids Carried in the Outflows of Mixed Samples Installed with 25% and 35% Bentonite by Weight

Sample Number	Hydraulic Gradient	Flow Rate ($\times 10^{-4}$ cc/s) Mean $\pm$ S.D.*	Solids in Outflow (g per 100 cc)	Estimated Time (yrs) for Loss of Bentonite to 15%	25%	pH
B/AL-C-4-25/A	343-347	0.818 $\pm$ 0.102	0.09	57.3		
			0.08	64.5		
			0.075	68.8		
			0.036	143.3		9.23
B/AL-C-4-25/B	209-211	1.445 $\pm$ 0.142	0.26	11.2		
			0.30	9.8		
			0.12	24.4		
			0.24	12.1		
	349-351	2.245 $\pm$ 0.723	0.24	7.9		
			0.17	11.1		
			0.18	10.5		
			0.15	12.5		
			0.08	23.5		
			0.082	22.9		
			0.075	25.1		
			0.088	21.3		
			0.12	15.6		8.89
B/AL-C-4-25/C	310-314	0.977 $\pm$ 0.167	0.076	56.8		
			0.083	52.0		
			0.083	52.0		
			0.081	53.3		9.06
B/AL-C-4-35/A	333-337	0.401 $\pm$ 0.122	0.087		137.1	
			0.08		149.1	9.25

Table 4.1 Flow Rates and Solids Carried in the Outflows of Mixed Samples Installed with 25% and 35% Bentonite by Weight

Sample Number	Hydraulic Gradient	Flow Rate ($\times 10^{-4}$ cc/s) Mean $\pm$ S.D.*	Solids in Outflow (g per 100 cc)	Estimated Time (yrs) for Loss of Bentonite to 15%	25%	pH
B/AL-C-4-35/B	321-325	0.508 $\pm$ 0.087	0.091		103.5	
			0.082		114.8	9.03
B/AL-C-4-35/C	342-347	0.404 $\pm$ 0.133	0.086		137.6	
			0.081		146.1	9.15

*S.D. = Standard Deviation

NOTES:

1) The first three samples consist of 312.5 g (air-dried) bentonite and crushed tuff. The latter three samples consist of 437.5 g bentonite and 812.5 g crushed tuff. The last letter shown in the sample number designation indicates the type of crushed tuff gradation used for mixing.

2) The air-dried bentonite has a moisture content of 9.5%.

3) The calculation of time required for loss of bentonite to the next lower bentonite percentage (i.e. 15% or 25%) is based on the assumption that the flow rate and the rate of bentonite removal remain constant.

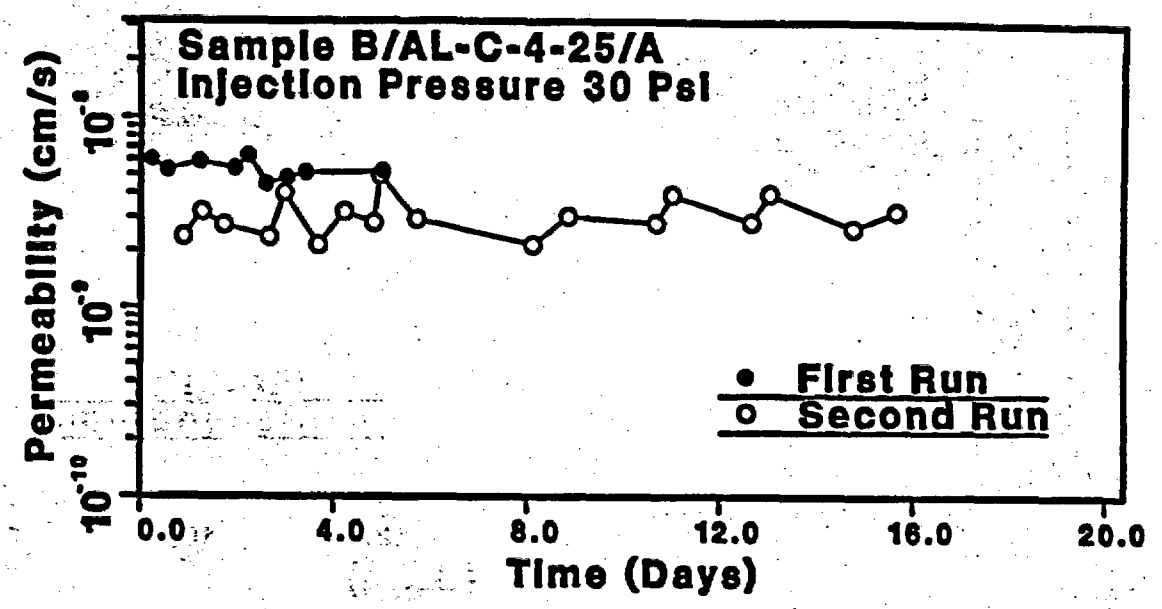

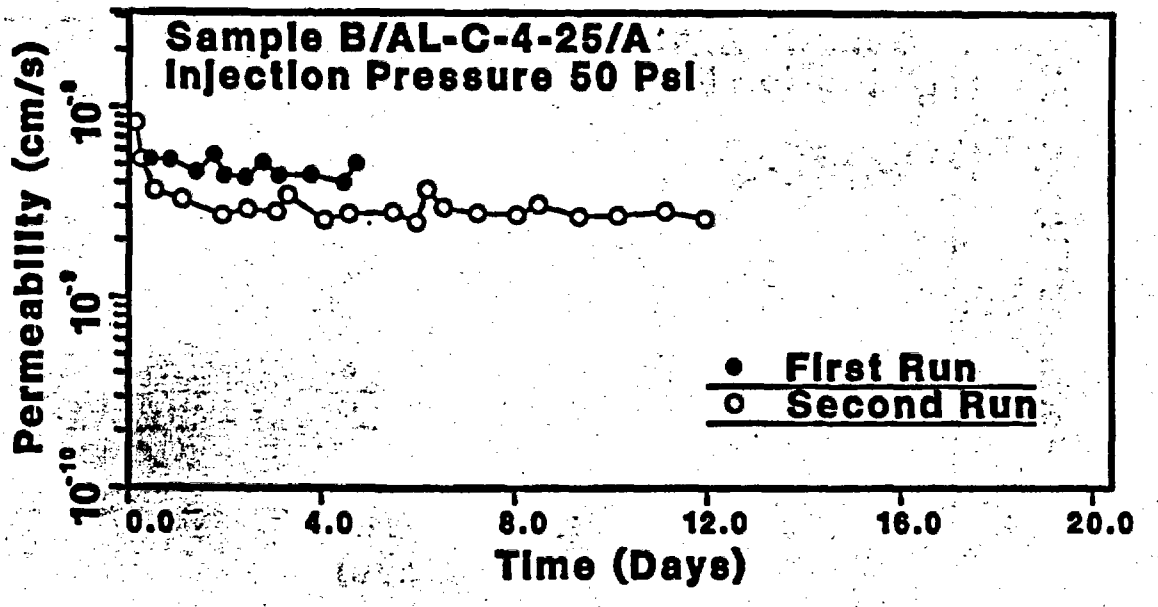

Figure 4.10 Comparison between first-run and second-run permeability results of Sample B/AL-C-4-25/A at injection pressures of 207 and 345 kPa (30 and 50 psi). Second run was after injection pressure of 690 kPa (100 psi) had been applied.

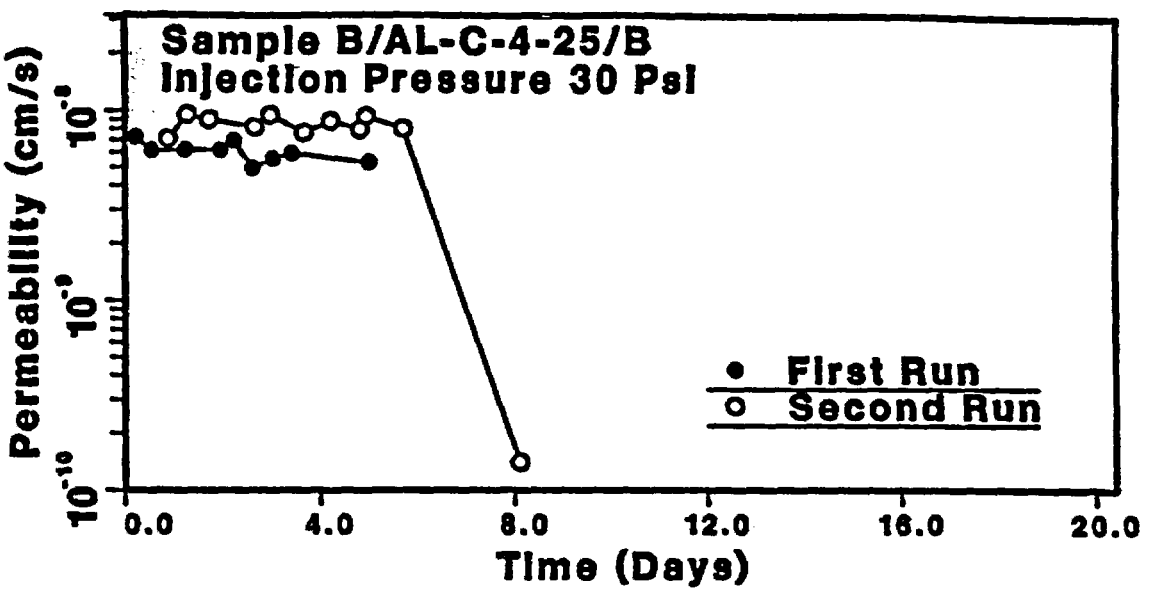

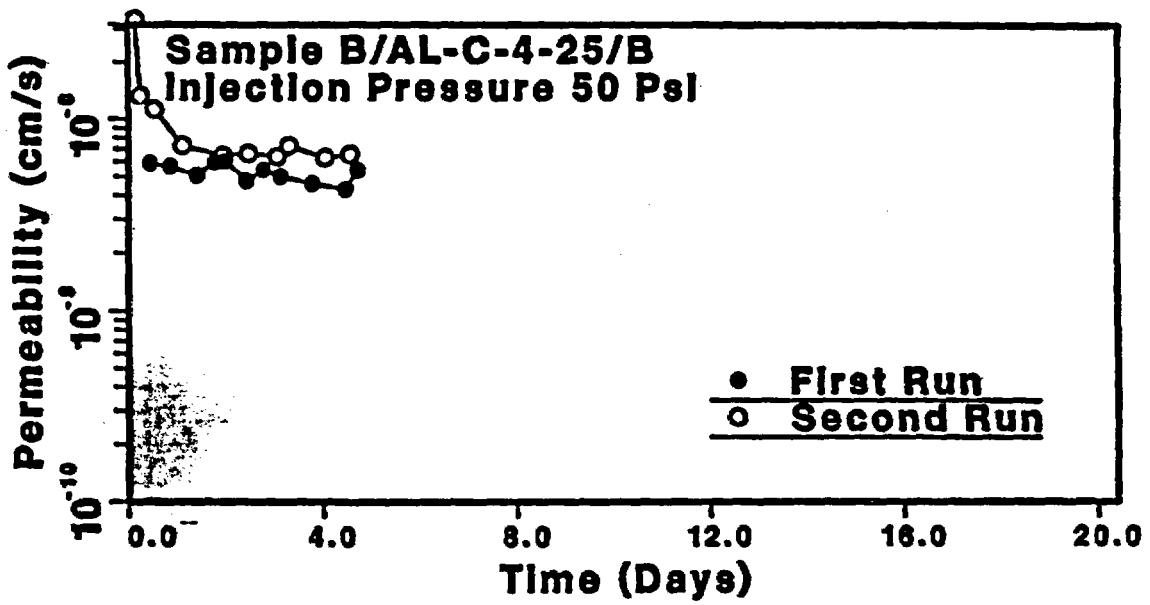

Figure 4.11 Comparison between first-run and second-run permeability results of Sample B/AL-C-4-25/B at injection pressures of 207 and 345 kPa (30 and 50 psi). Second run was after injection pressure of 690 kPa (100 psi) had been applied.

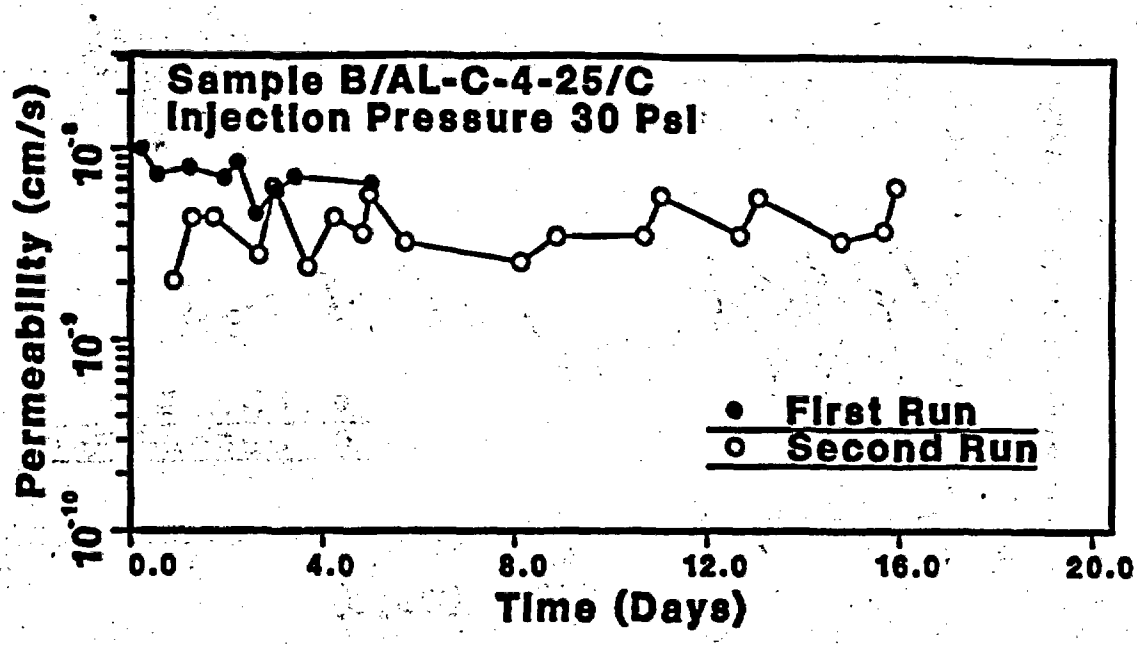

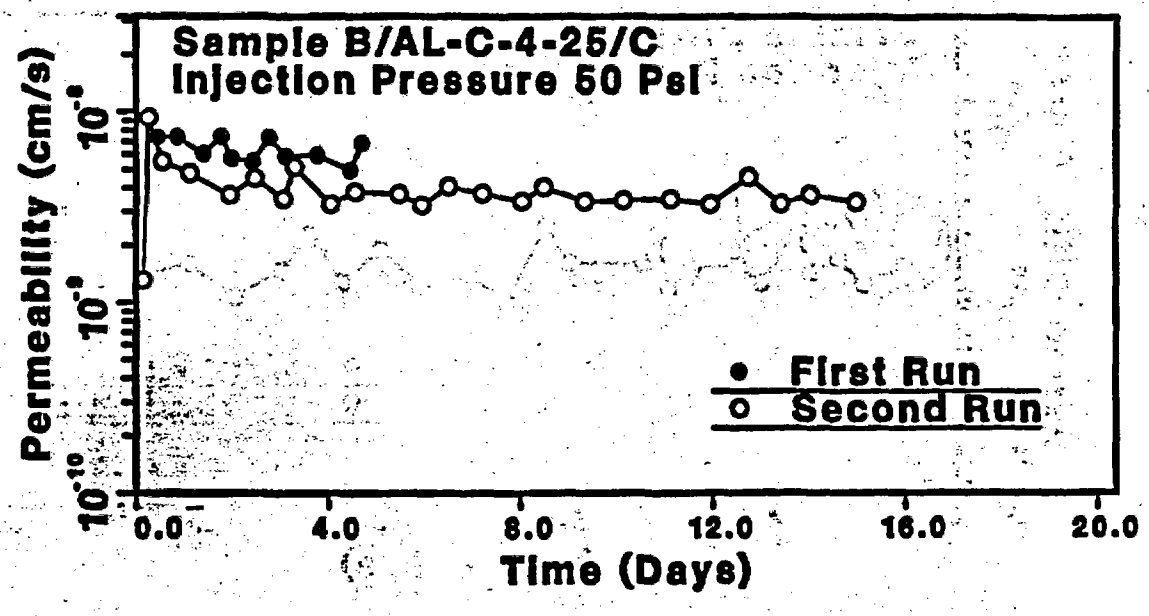

Figure 4.12 Comparison between first-run and second-run permeability results of Sample B/AL-C-4-25/C at injection pressures of 207 and 345 kPa (30 and 50 psi). Second run was after injection pressure of 690 kPa (100 psi) had been applied.

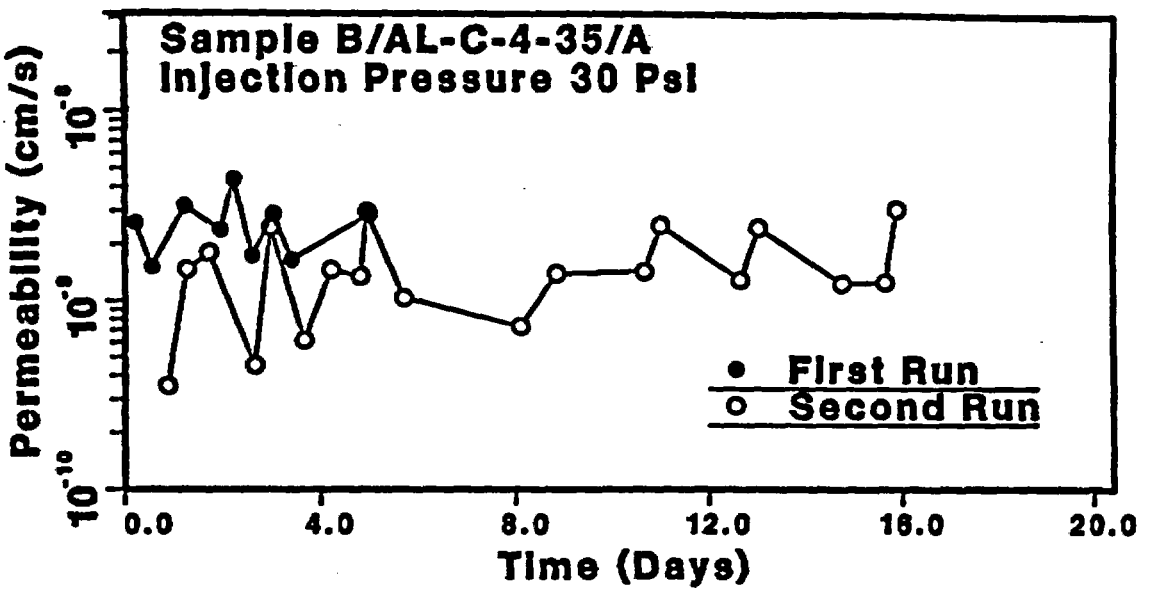

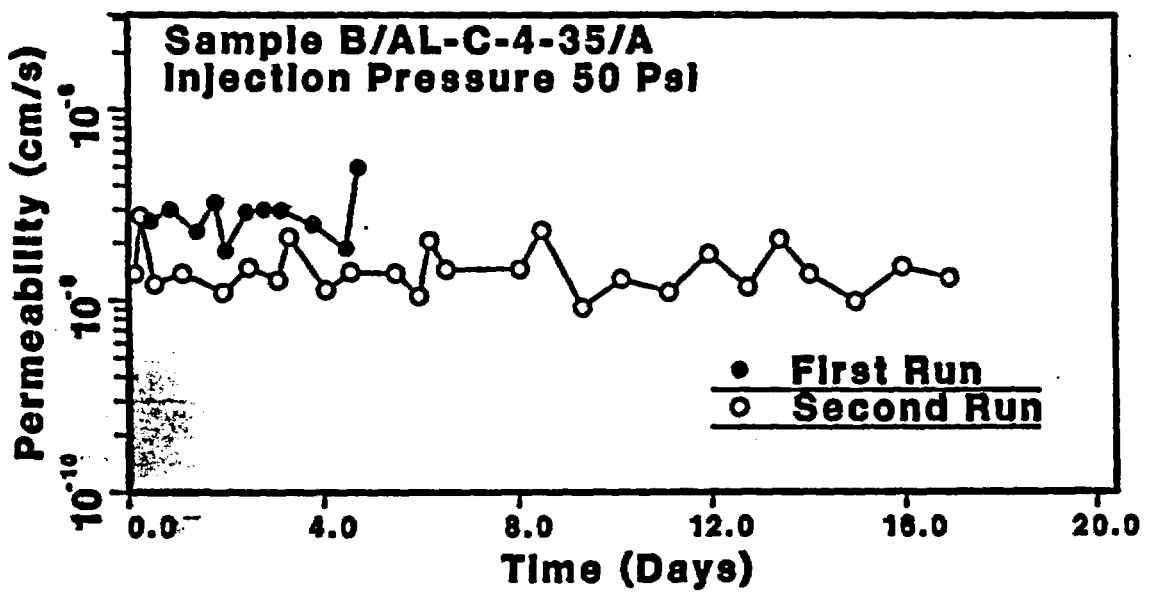

Figure 4.13 Comparison between first-run and second-run permeability results of Sample B/AL-C-4-35/A at injection pressures of 207 and 345 kPa (30 and 50 psi). Second run was after injection pressure of 690 kPa (100 psi) had been applied.

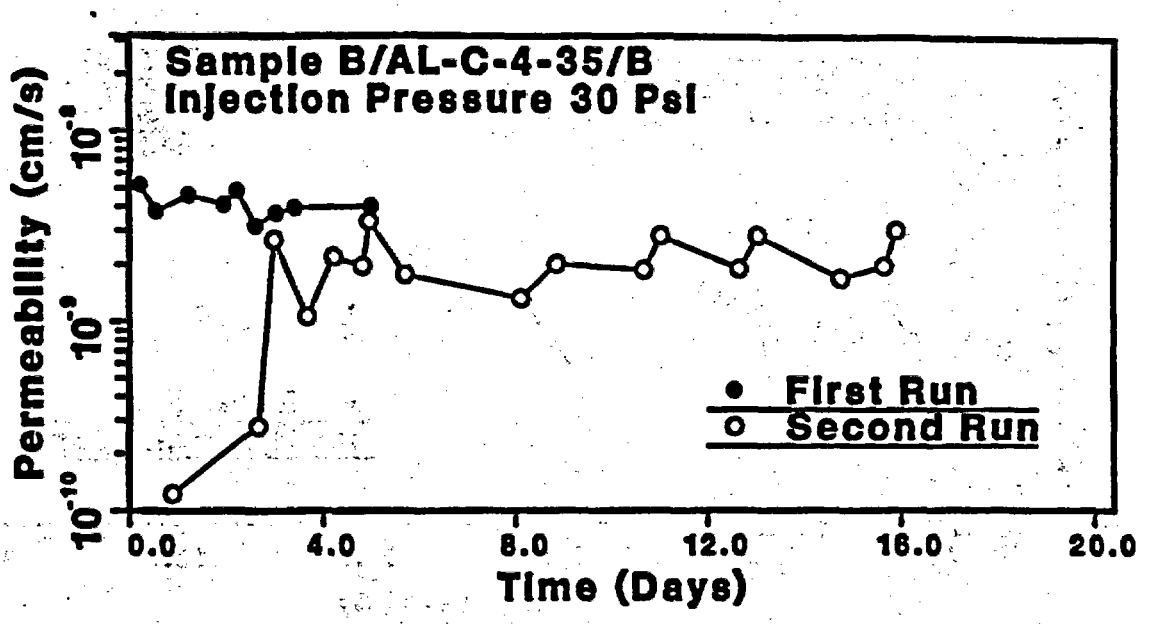

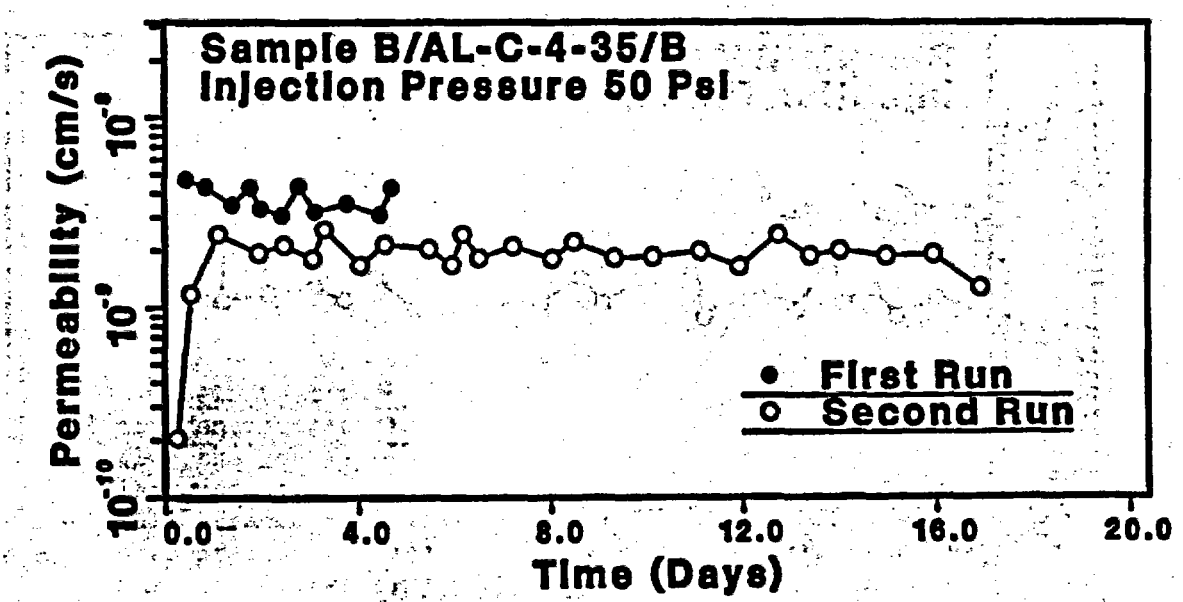

Figure 4.14 Comparison between first-run and second-run permeability results of Sample B/AL-C-4-35/B at injection pressures of 207 and 345 kPa (30 and 50 psi). Second run was after injection pressure of 690 kPa (100 psi) had been applied.

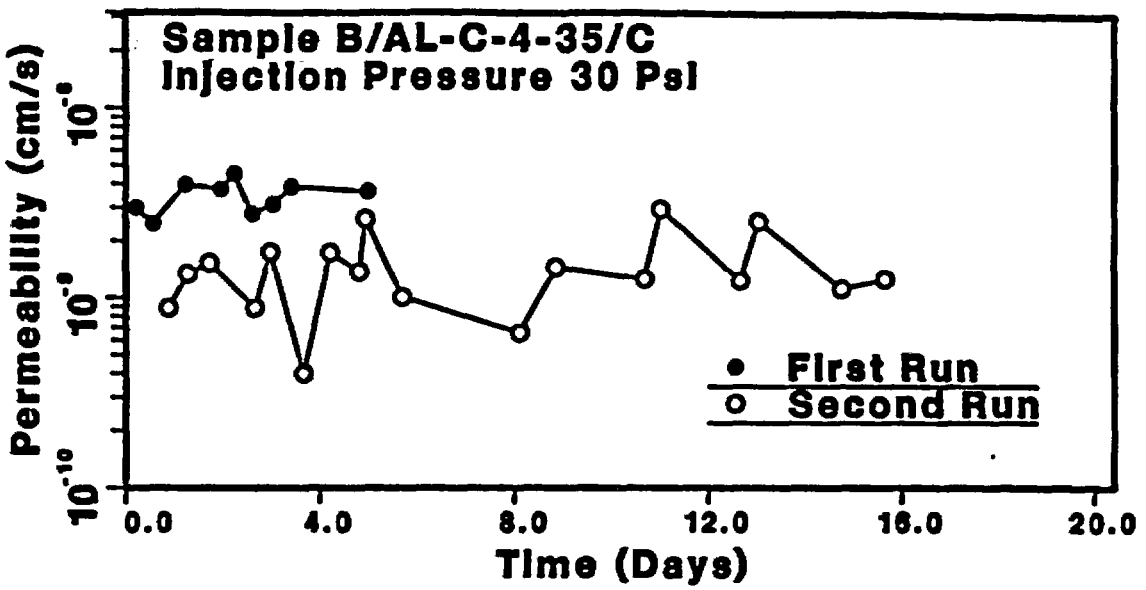

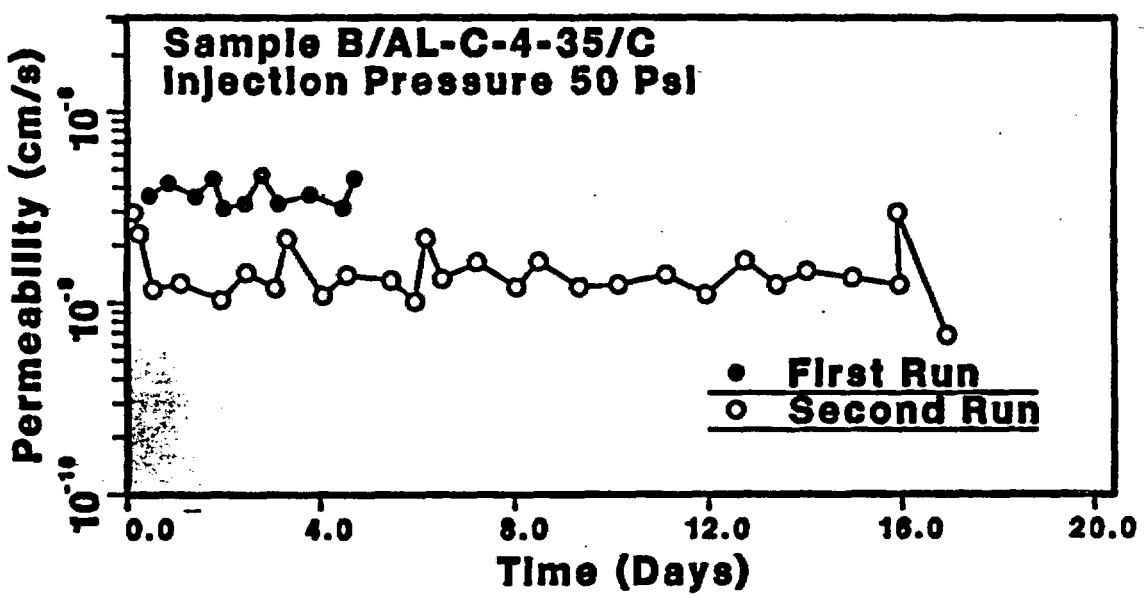

Figure 4.15 Comparison between first-run and second-run permeability results of Sample B/AL-C-4-35/C at injection pressures of 207 and 345 kPa (30 and 50 psi). Second run was after injection pressure of 690 kPa (100 psi) had been applied.

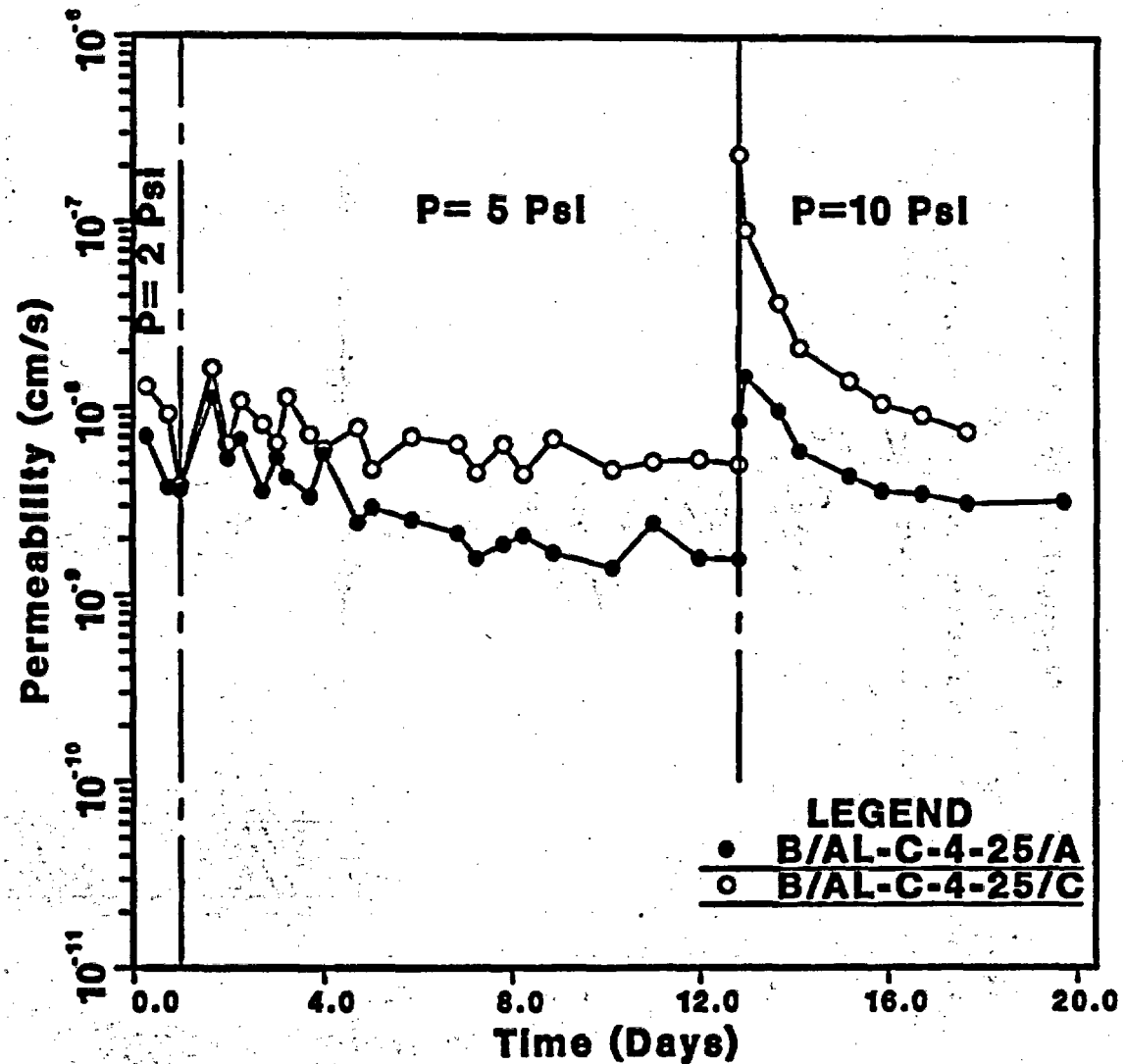

Figure 4.16 Permeability results of the mixture samples containing 25% bentonite by weight (measured in the upward permeation). Injection pressure p = 13.8, 34.5 and 69 kPa (2, 5 and 10 psi). Hydraulic gradient: 12-16, 30-35 and 63-70, respectively.

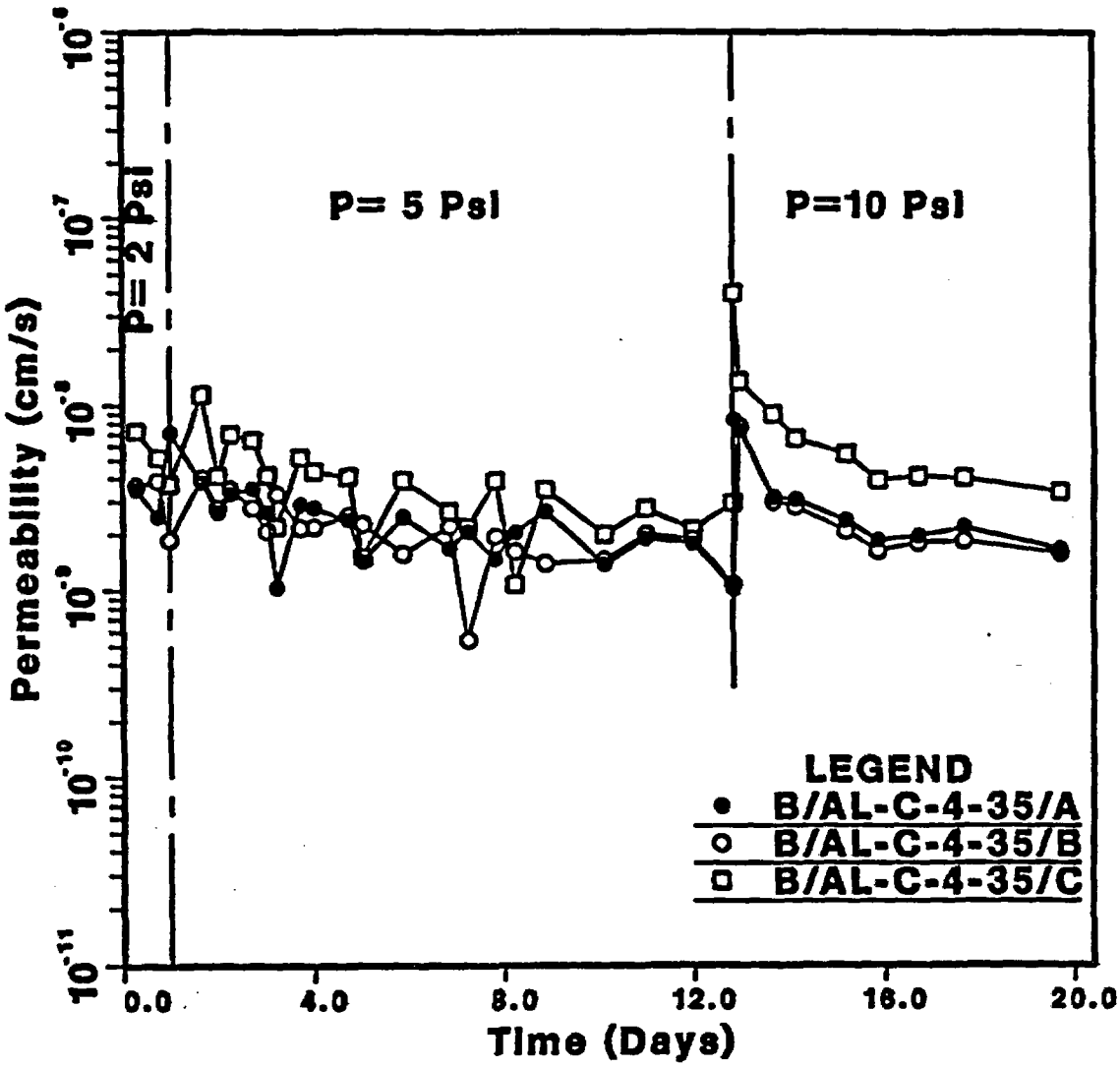

Figure 4.17 Permeability results of the mixture samples containing 35% bentonite by weight (measured in the upward permeation). Injection pressure p = 13.8, 34.5 and 69 kPa (2, 5 and 10 psi). Hydraulic gradient: 12-16, 31-35 and 65-71, respectively.

4.2.2 Flow Testing of Mixture Samples in Stainless Steel Permeameters

Crushed tuff of gradation type A and with 25 and 35 bentonite weight percent was selected to prepare four samples in stainless steel permeameters for high-temperature and high-injection pressure flow testing. Compactive efforts equivalent to the Standard Proctor method were applied to the samples, i.e. 25 blows per layer for the 101.6 mm (4 in) samples and 100 blows per layer for the 203.2 mm (8 in) samples. After inserting piston and capping plate, the samples were subjected to a 2.5 m water head from the bottom port for saturation. The saturation process was aided intermittently by applying vacuum from the top port, at a vacuum of 103.5 kPa (15 psi) for 30 to 45 minutes. During the saturation, the pistons gradually moved upward, responding to the swelling of samples. Such movements were minimized by filling the remaining space between piston and top cap plate with water.

The flow test results are presented in Figures 4.18 and 4.19. The four samples are tested at room temperature using the double-pipette falling head method. The inflow and outflow measurements are shown in Figures 4.20 and 4.21. Sample dimensions and bulk densities before and after saturation are summarized in Table 4.2.

Among the four samples, B/AL-C-8-25/A-S had the lowest bulk density, 1.582 g/cm^3 and exhibited comparatively high permeability, on the order of 10^{-8} cm/s. It was noted that, while compacting this sample (203.2 mm in diameter), the material in the vicinity of the contact zone heaved with each impact. Lateral movements of particles also were associated with the heaving. The compactor has a rammer of 50.8 mm (2 in) in diameter and is in accordance with the specifications of ASTM standard D698-78. For samples of 101.6 mm (4 in) in diameter, each impact of the rammer covers 1/4 of the cross-sectional area. The same rammer covers only 1/16 of the sample area when compacting 203.2 mm (8 in) plugs. The same compaction procedure had been applied to the other 203.2 mm sample which contains 35 bentonite weight percent (Sample B/AL-C-8-35A-S). In this case, the heaving and the lateral movements of particles seemed to be minimal and the coarse material appeared to be anchored in the fine particles during the compaction. After compaction this sample yielded a bulk density of 1.74 g/cm^3.

For the same bentonite percent, the 203.2 mm (8 in) samples have higher permeability than the 101.6 mm (4 in) samples. This suggests the possible existence of a size effect. Additional tests are needed to confirm the statistical validity of the observation of a size effect. Especially if such size effect observations are confirmed, flow tests on larger diameter samples are warranted.

The break in the curves shown in Figures 4.20 and 4.21 corresponds to the refilling of the inflow pipette preceded by vacuuming the sample at a vacuum of 103.5 kPa for 30 to 45 minutes. After the vacuuming, the permeability of sample B/AL-C-4-25/A-S appears to increase, while that of sample B/AL-C-8-35/A-S seems to decrease. The corresponding changes in permeability can be seen in Figures 4.18 and 4.19.

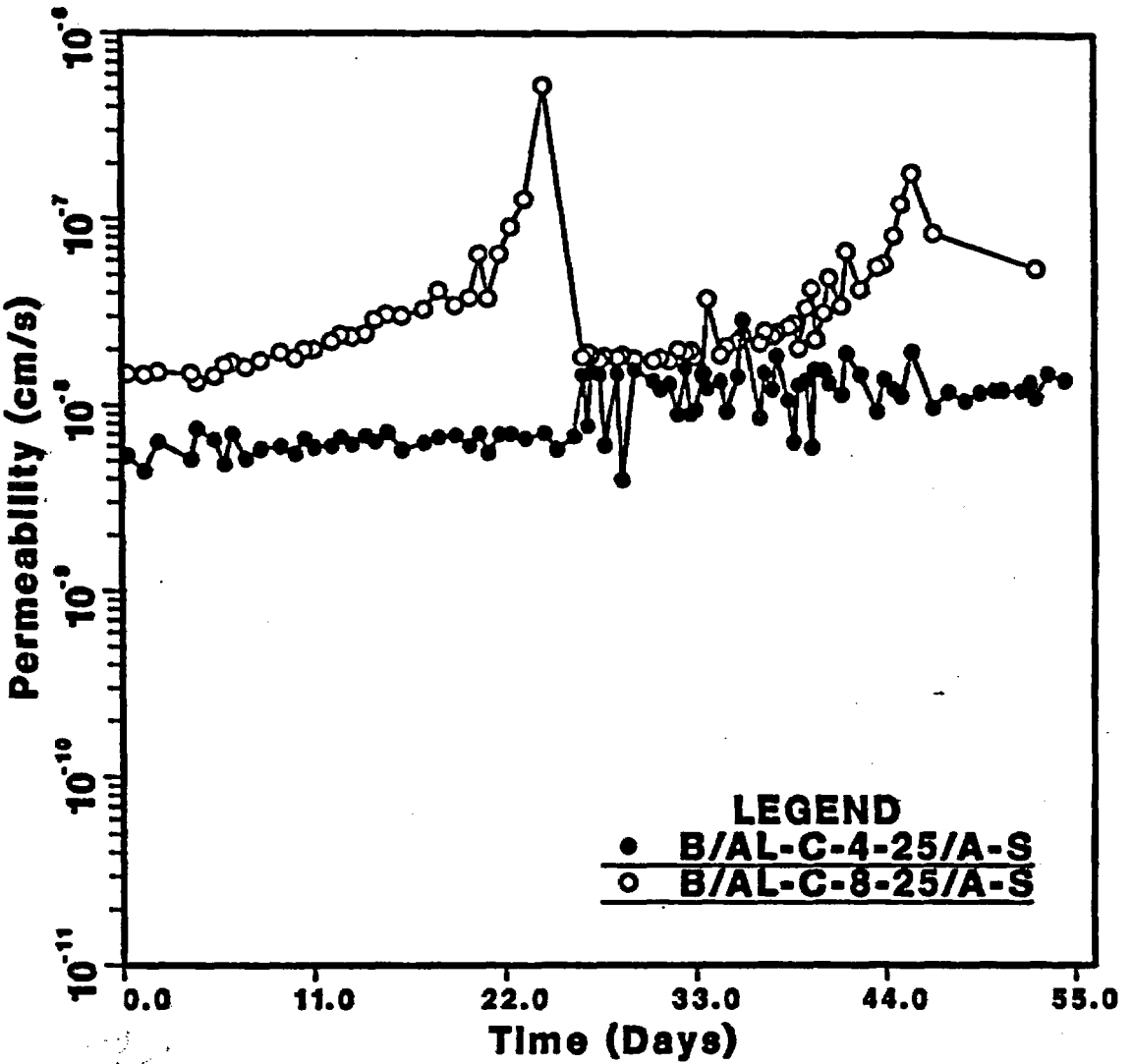

Figure 4.18 Permeability results of the mixture samples installed in stainless steel permeameters (25% bentonite by weight). Hydraulic gradient: 6-9.75 for B/AL-C-4-25/A-S and 0.1-6.5 for B/AL-C-8-25/A-S.

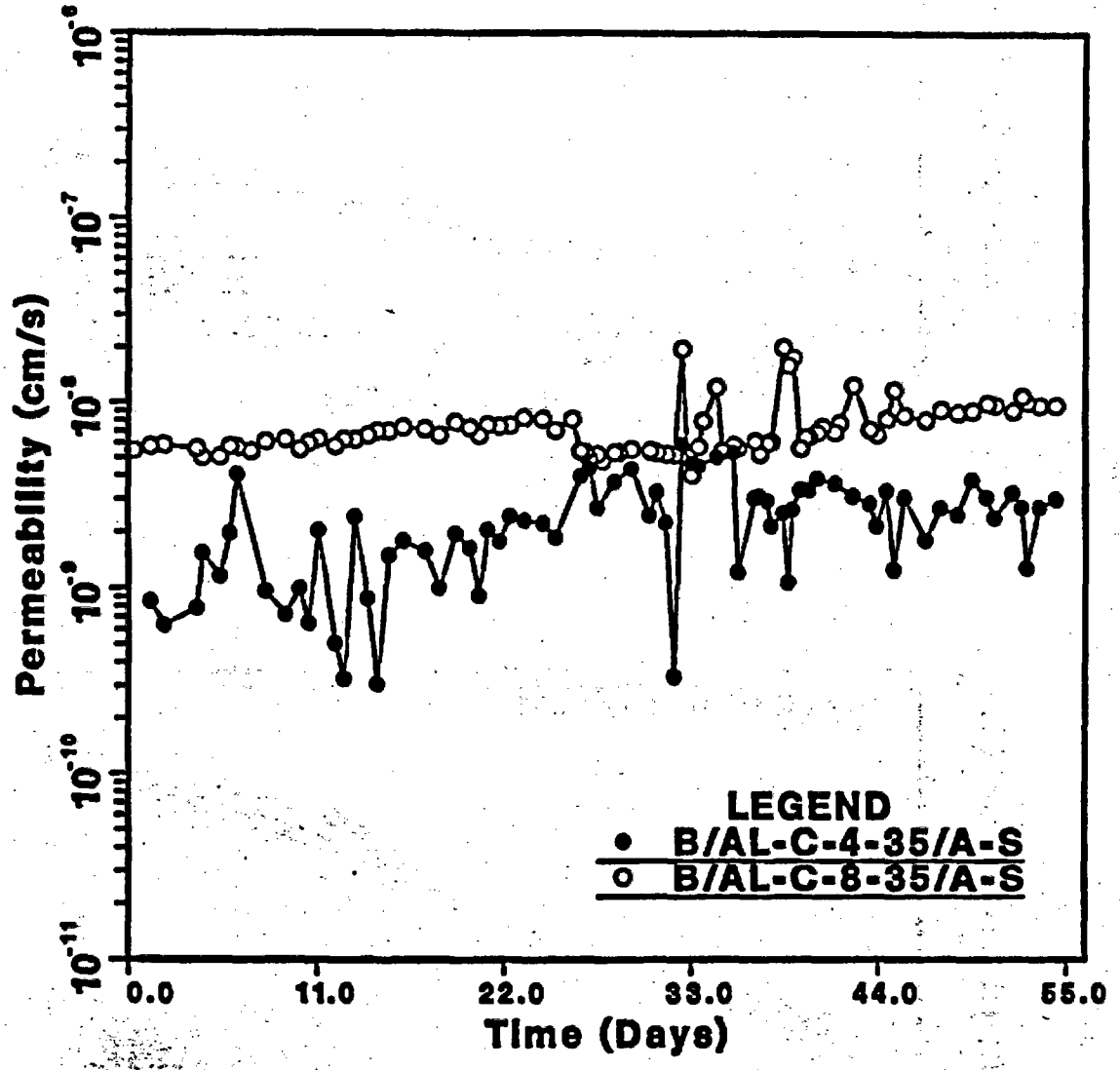

Figure 4.19 Permeability results of the mixture samples installed in stainless steel permeameters (35% bentonite by weight). Hydraulic gradient: 9.5-10.6 for B/AL-C-4-35/A-S and 1.5-6 for B/AL-C-8-35/A-S.

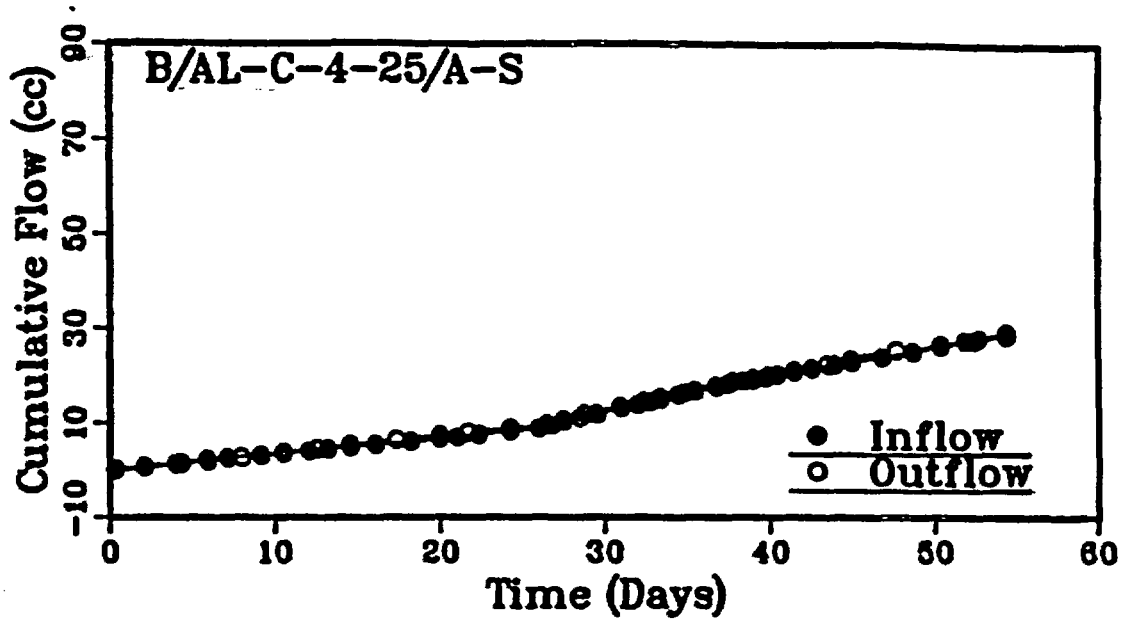

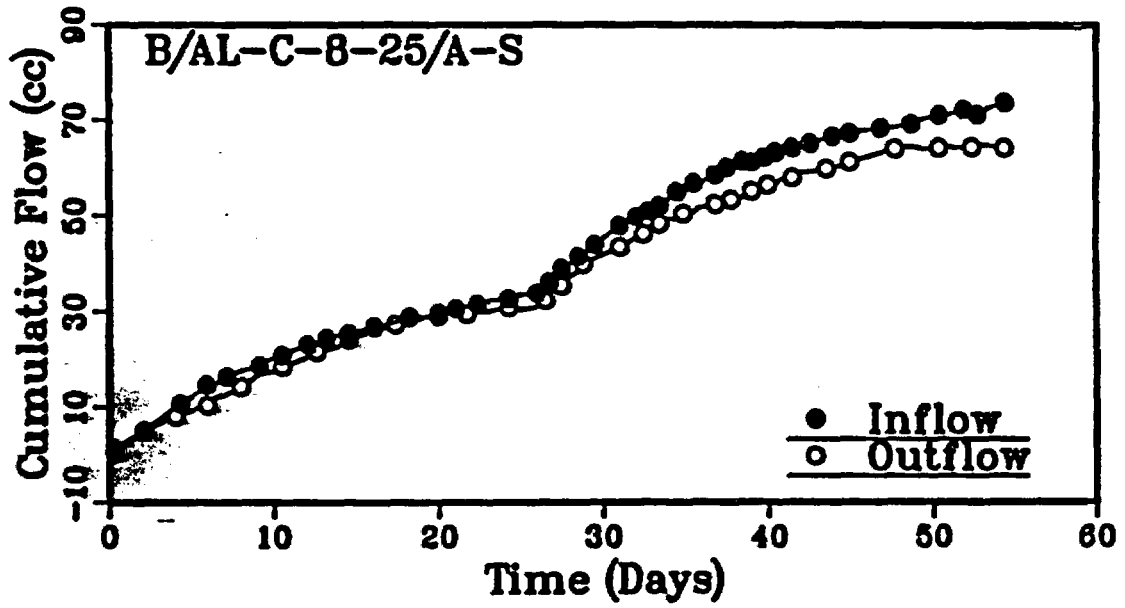

Figure 4.20 Cumulative inflow and outflow vs. time for samples B/AL-C-4-25/A-S and B/AL-C-8-25/A-S. The break in the curves corresponds to the refilling of inflow pipette preceded by vacuuming samples at a vacuum of 103.5 kPa for 30 to 45 minutes.

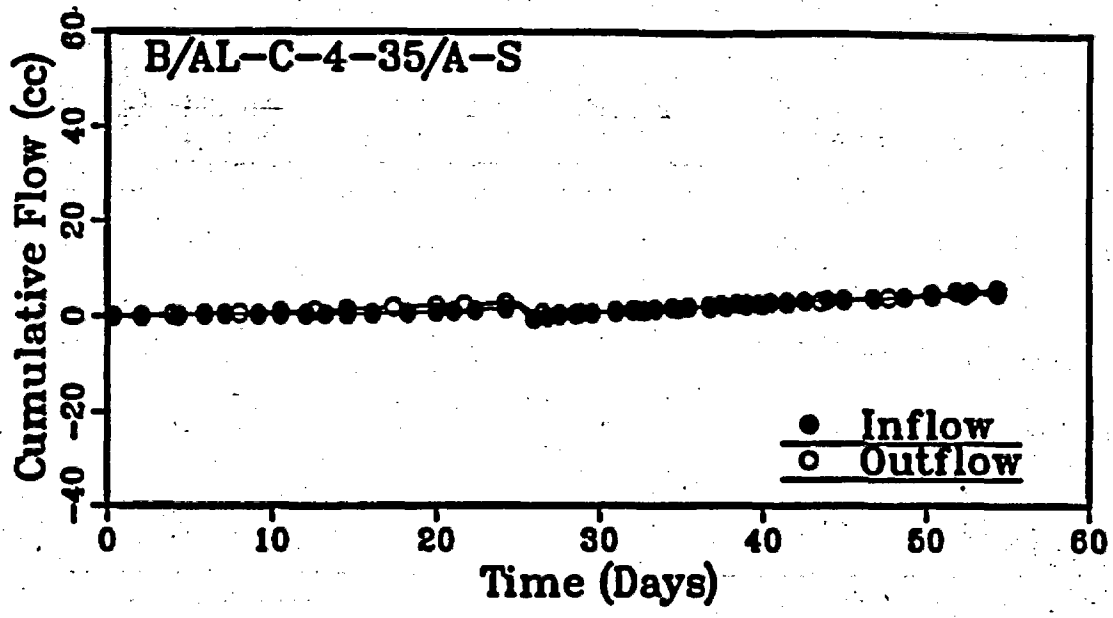

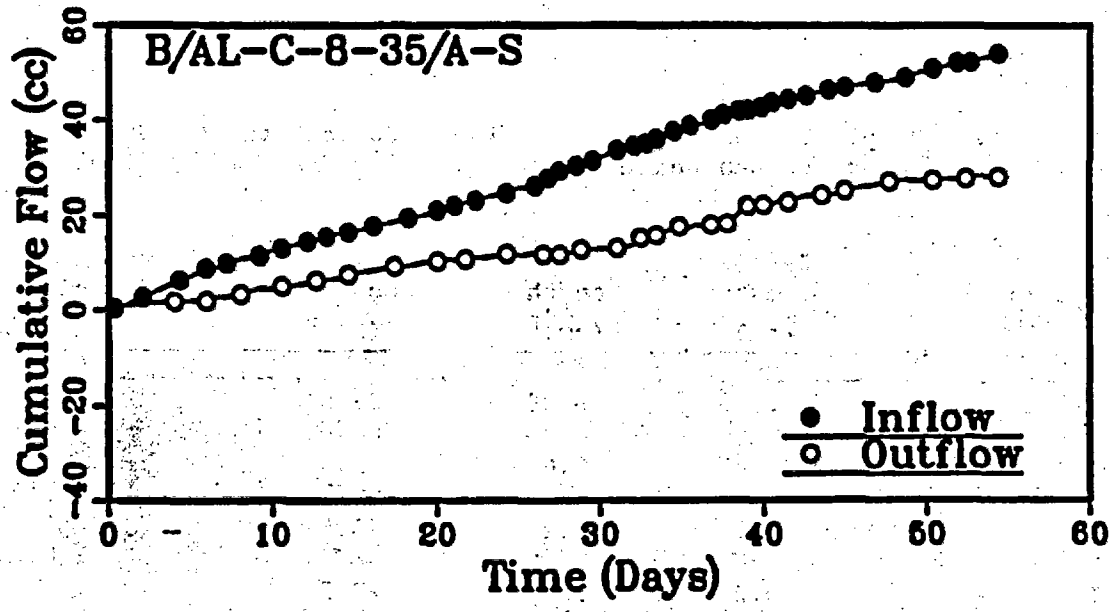

Figure 4.21 Cumulative inflow and outflow vs. time for samples B/AL-C-4-35/A-S and B/AL-C-8-35/A-S. The break in the curves corresponds to the refilling of inflow pipette preceded by vacuuming samples at a vacuum of 103.5 kPa for 30 to 45 minutes.

Table 4.2 Sample Dimensions and Bulk Density of Mixed Samples Installed in Stainless Steel Permeameters

Sample Number	Sample Diameter (cm)	Sample Length (cm)		Bulk Density (g/cm^3)	
		Before Saturation	After Saturation	Before Saturation	After Saturation
B/AL-C-4 -25/A-S	10.24	10.8	11.05	1.633	1.596
B/AL-C-8 -25/A-S	20.65	11.0	10.90	1.582	1.597
B/AL-C-4 -35/A-S	10.25	10.8	11.25	1.644	1.579
B/AL-C-8 -35/A-S	20.65	10.05	10.65	1.740	1.642

Table 4.3 Sample Dimensions, Initial Water Content and Dry Density of Compacted Bentonite Plugs

Sample Number	Sample Diameter (cm)	Sample Length (cm)	Initial Water Content (%)	Initial Dry Density (g/cm^3)
B-C-1-A-S	2.65	8.89	23.5	1.094
B-C-1 3/8-A-S	3.47	9.62	32.0	0.816
B-C-2 3/8-A-S	6.01	14.95	23.5	1.058
B-C-4-A-S	10.25	13.12	23.5	1.038

4.2.3 Flow Testing of Mixture Samples Having Ideal Crushed Tuff Gradation

Flow tests were conducted on four mixture samples to explore further the effect of grain size gradation on the sealing performance. Instead of gradation types A, B and C used earlier, the Fuller-Thompson curve was adopted to prepare the crushed tuff portion. The Fuller-Thompson grading curve is considered to be an ideal grading which may result in the densest possible state of packing (Winterkorn, 1975; Head, 1980, p. 150). The grading curve is described by:

$$P_w = 100\ (d/D)^n \qquad (4.1)$$

where P_w = weight percent passing sieve aperture d,
D = maximum particle size,
n = exponent.

The U.S. Bureau of Public Roads (USBPR, 1962; as cited by Winterkorn, 1975) recommends 0.45 for n as the best overall value. Head (1980, p. 150) suggests an n value of 0.5. The Fuller-Thompson curve has been used in formulating backfill material for a nuclear waste disposal vault (Pusch and Altermark, 1985; Yong et al., 1986).

The crushed tuff used in the preparation of the four samples follows a grading curve obtained using D = 9.42 mm and n = 0.5. The four mixture samples include two each of 15 and of 25 bentonite weight percent. The flow tests were performed downward. The results are shown in Figure 4.22. The cumulative inflow-outflow balances of Samples B/AL-C-4-15/FA-A and B/AL-C-4-15/FA-B are given in Figure 4.23. These two samples were tested using the double-pipette falling head method. The constant head method furnished with the compressed gas (helium) pressurization system (Lambe, 1951, p. 58) was employed to test Samples B/AL-C-4-25/FA-A and B/AL-C-4-25/FA-B which contain 25% bentonite by weight.

As shown in Figure 4.22, the permeability values obtained for each pair of samples are consistent. The conformity may indicate the quality control of the sample preparation, installation and test procedures. The sharp jumps of permeability observed for Samples B/AL-C-4-15/FA-A and B/AL-C-4-15/FA-B correspond to the refilling of the inflow pipette. A similar phenomenon has been reported earlier (Daemen et al., 1988). Considering the good inflow-outflow balance recorded (Figure 4.23), the sudden increase of permeability after the refilling is most likely due to hydraulic fracturing. The localized fluctuations of permeability in Figure 4.22 are found to correlate with room temperature variations, as illustrated in Figures 4.24 and 4.25. The room temperature record is designated by an open square in the two figures. Using the same data, the permeabilities were recalculated on a time-interval basis such that the temperatures at two ends of each interval were equal or approximately the same. Such a correction generally removes most of the local permeability fluctuations. The corrected permeabilities are represented by open circles in Figures 4.24 and 4.25.

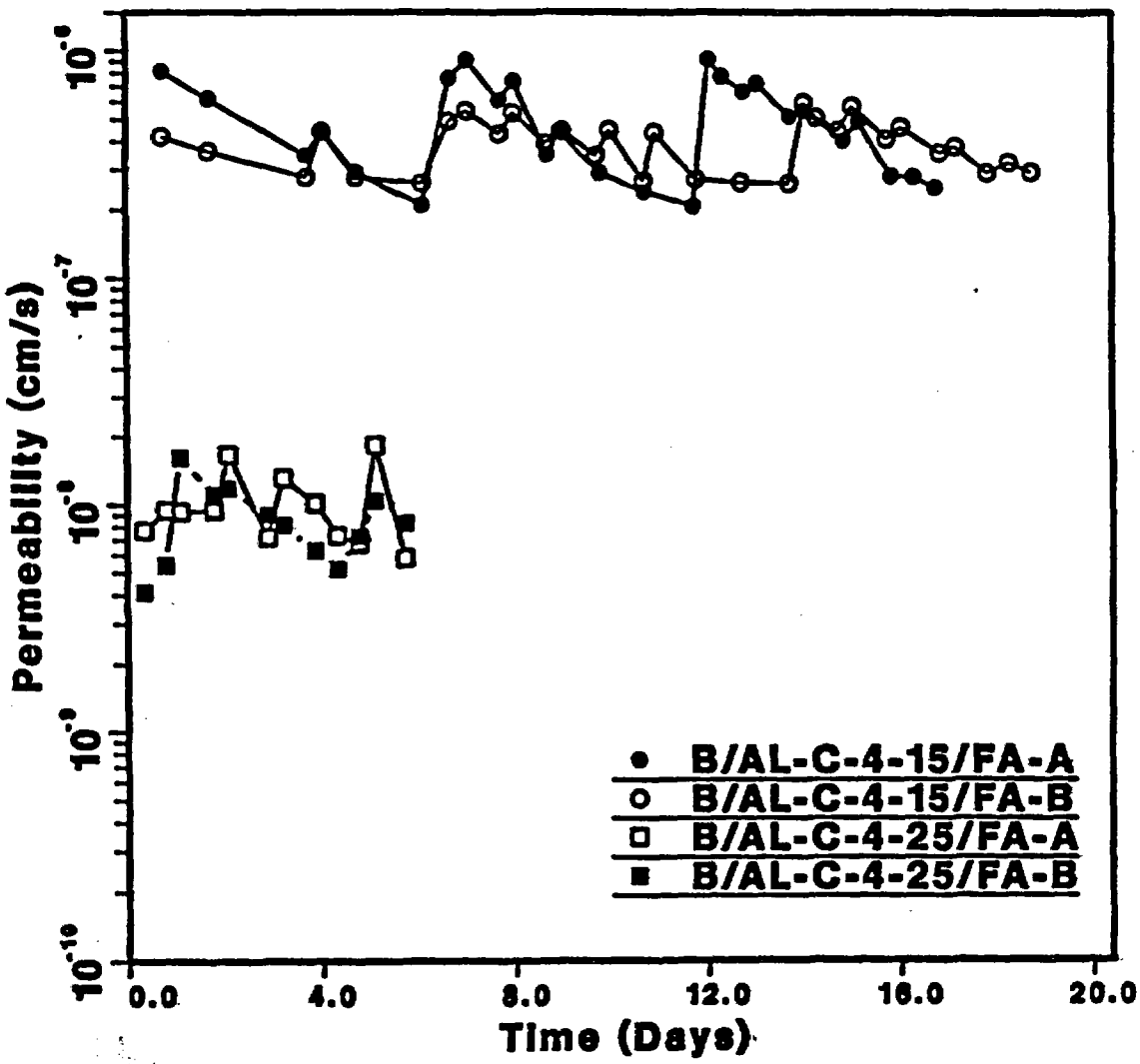

Figure 4.22 Permeability results of Samples B/AL-C-4-15/FA-A, B/AL-C-4-15/FA-B, B/AL-C-4-25/FA-A and B/AL-C-4-25/FA-B. The grading of crushed tuff constituents follows the Fuller-Thompson curve. Hydraulic gradient: 1-7, 3-7, 18-22 and 17-21, respectively.

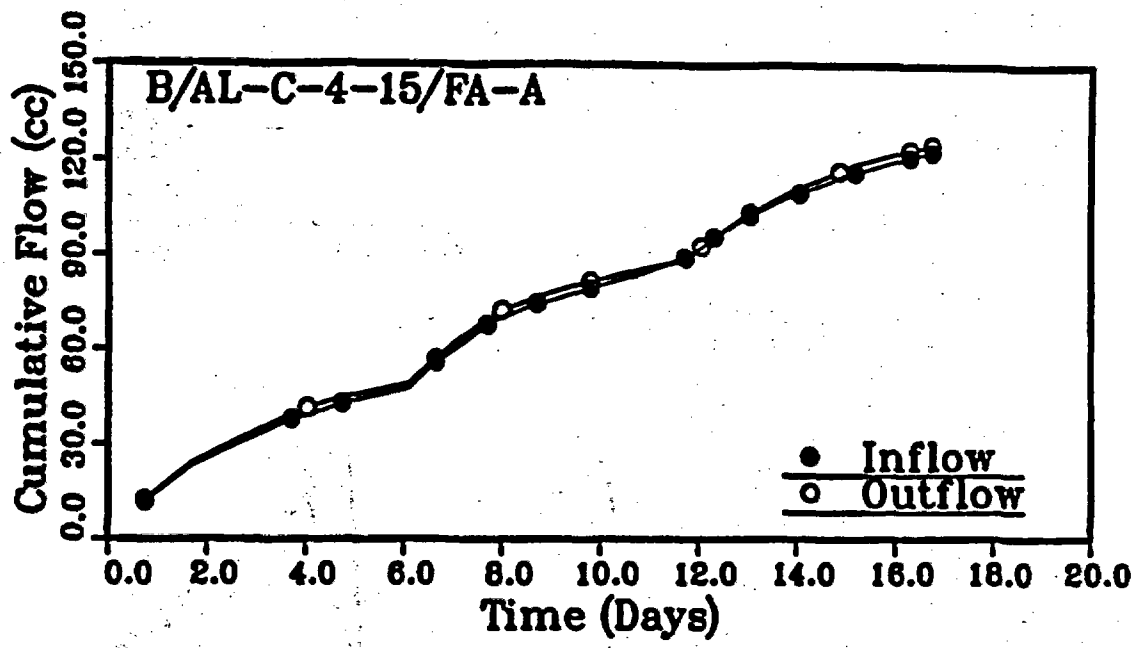

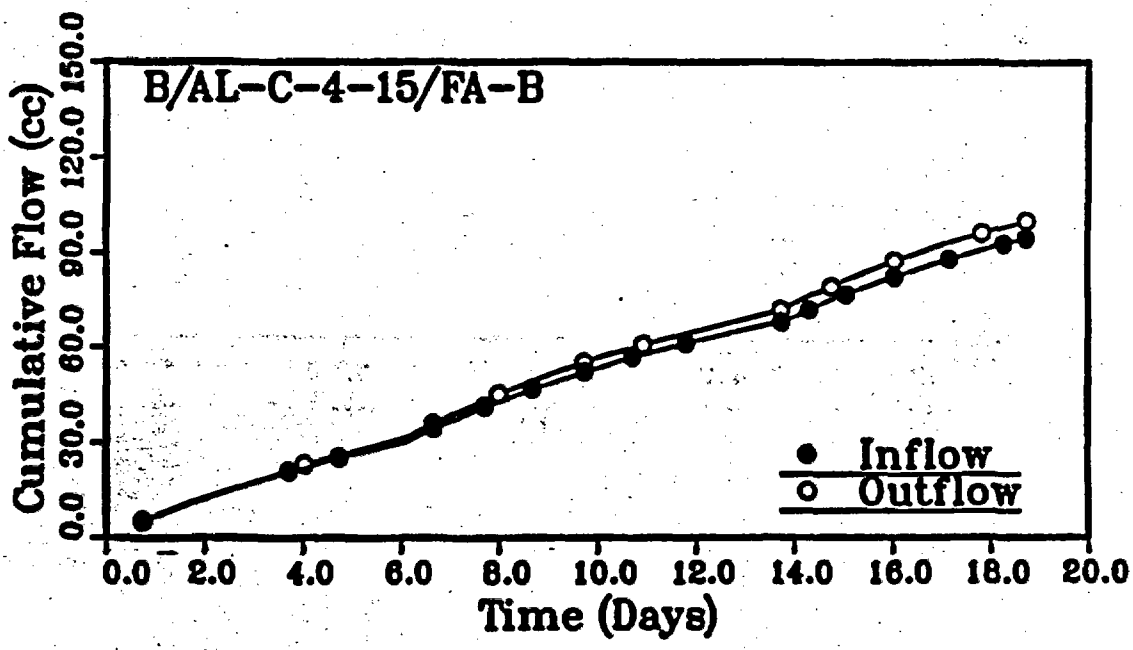

Figure 4.23 Cumulative inflow and outflow vs. time for Samples B/AL-C-4-15/FA-A and B/AL-C-4-15/FA-B.

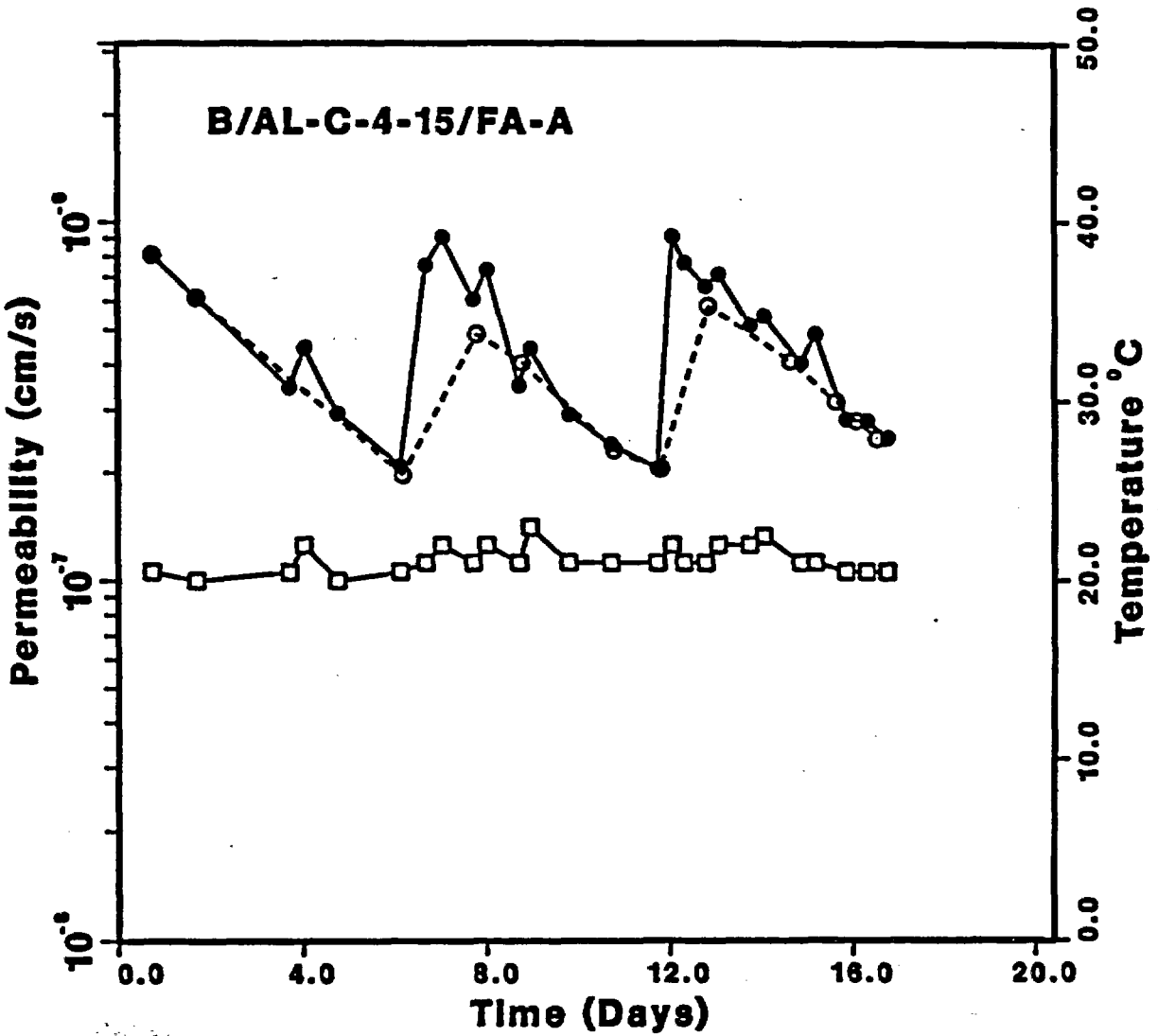

Figure 4.24 Room temperature effect on the permeability measurement of sample B/AL-C-4-15/FA-A. Solid circle: original data point; open circle: corrected data point; open square: temperature.

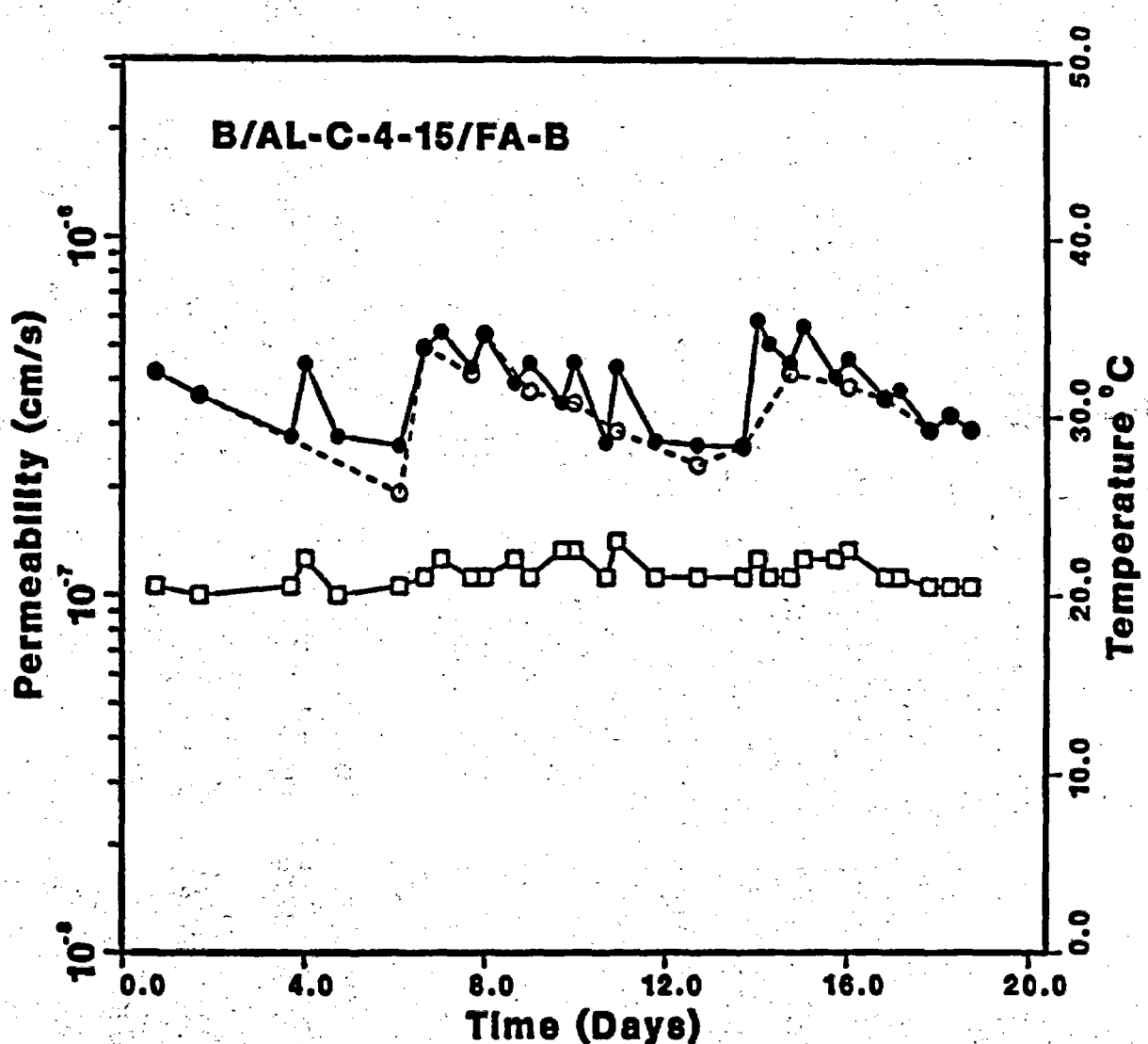

Figure 4.25 Room temperature effect on the permeability measurement of sample B/AL-C-4-15/FA-B. Solid circle: original data point; open circle: corrected data point; open square: temperature.

4.3 Flow Testing of Bentonite Plugs

4.3.1 Flow Testing of Bentonite Plugs in Stainless Steel Permeameters

This experimental series includes flow tests of Samples B-C-1-A-S, B-C-1 3/8-A-S, B-C-2 3/8-A-S, and B-C-4-A-S. The numeric in the sample number designation represents the nominal plug diameter in inches while the S stands for stainless steel permeameter. Sample dimensions, initial water content and dry density are given in Table 4.3.

Before flow testing, the samples were subjected to an injection water pressure of 345 kPa (50 psi) for about two months, and intermittently to vacuuming at the top. The double-pipette falling head method was then used to determine permeabilities. With approximately 1.2 m of water head difference across the samples, the flow testing continued for more than a month and no positive outflows were discerned. The samples were again subjected to vacuum and the test set up was replaced with the the constant-head method driven by a compressed helium pressurization system. The outflow was monitored by observing the movement of an injected air bubble in a horizontal pipette. Preliminary permeability results (the upward permeation) obtained under an injection pressure of 34.5 kPa (5 psi) are shown in Figure 4.26. No outflow was detected for Sample B-C-1 3/8-A-S.

4.3.2 Flow Testing of Bentonite Samples in Plexiglass Permeameters

The seals to be placed in a nuclear waste repository are required to prevent significant amounts of water from reaching waste. They may be required additionally to prevent significant amounts of gaseous radionuclides from escaping through shafts, ramps, and boreholes (Gupta et al., 1989). Prior to permeating with water, four bentonite samples of 25.4 mm (1 in) in diameter installed in plexiglass permeameters were tested to determine the permeability to air. The test procedure followed ASTM Standard D4525.

Nine tests were performed on the four samples. Each sample contains a different initial water content. Various dry densities were achieved by changing the number of layers compacted. The rammer weight and drop height used for compaction are 0.053 kg (1.15 lbs) and 0.27 m (10.62 in). The permeability results (expressed in m^2, 1 m^2 = 10^{12} Darcy) are plotted against the reciprocal of the mean pressure in Figure 4.27. The legend in Figure 4.27 indicates, in order, the water content, the number of layers compacted, and the number of blows per layer. Figure 4.28 shows the permeability results as a function of dry density.

The permeability to air of the compacted samples ranges from 10^{-11} to 10^{-17} m^2. It appears that the permeability to air first decreases and then starts to increase. The decrease may be explained by pore clogging due to particle migration. The increase in permeability that occurs later can be, at least in part, accounted for by pore enlarging resulting from loss of moisture. For the samples of high water contents (e.g. 28 and 41.3%), the loss of moisture to the percolating

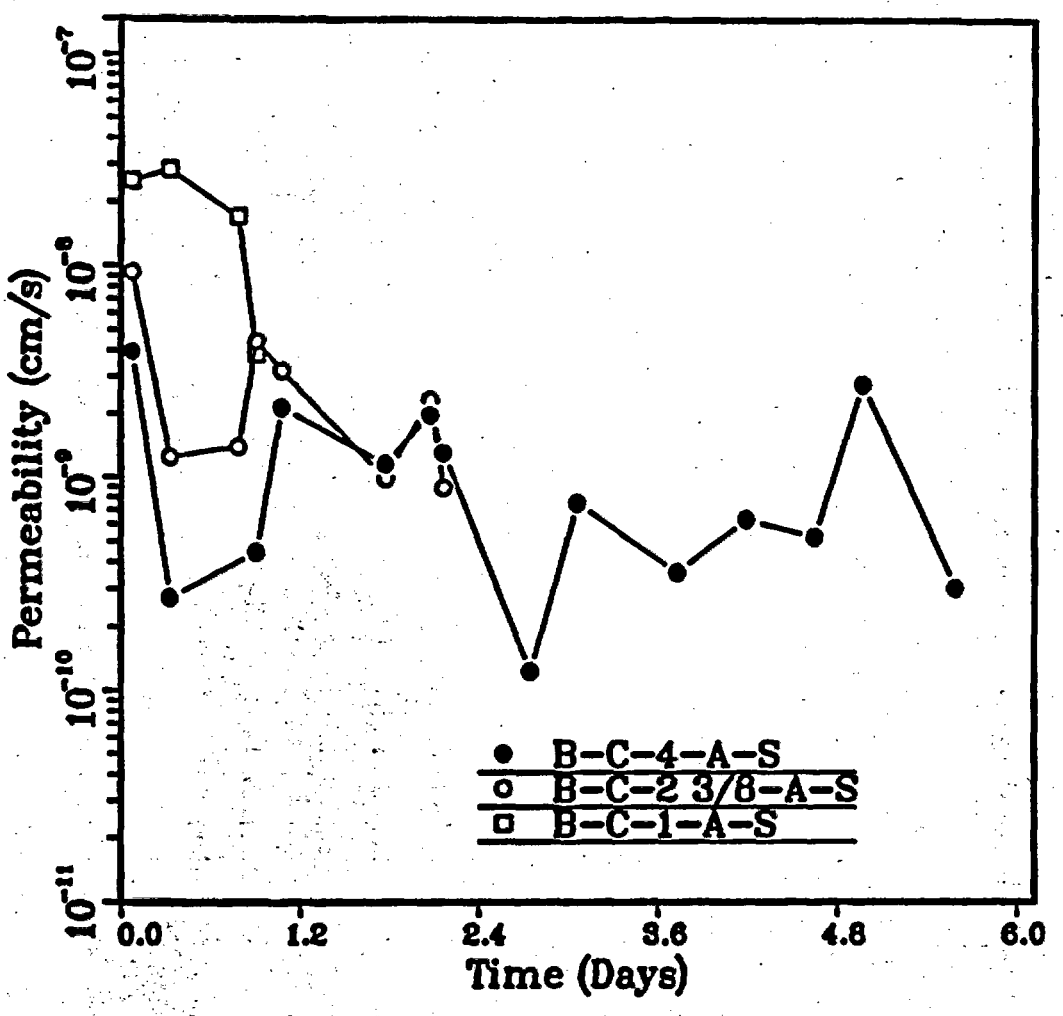

Figure 4.26 Preliminary permeability results of compacted bentonite samples installed in stainless steel permeameters. Hydraulic gradient: 43-45 for B-C-1-A-S, 25.5-26.7 for B-C-2 3/8-A-S, and 29-31.3 for B-C-4-A-S.

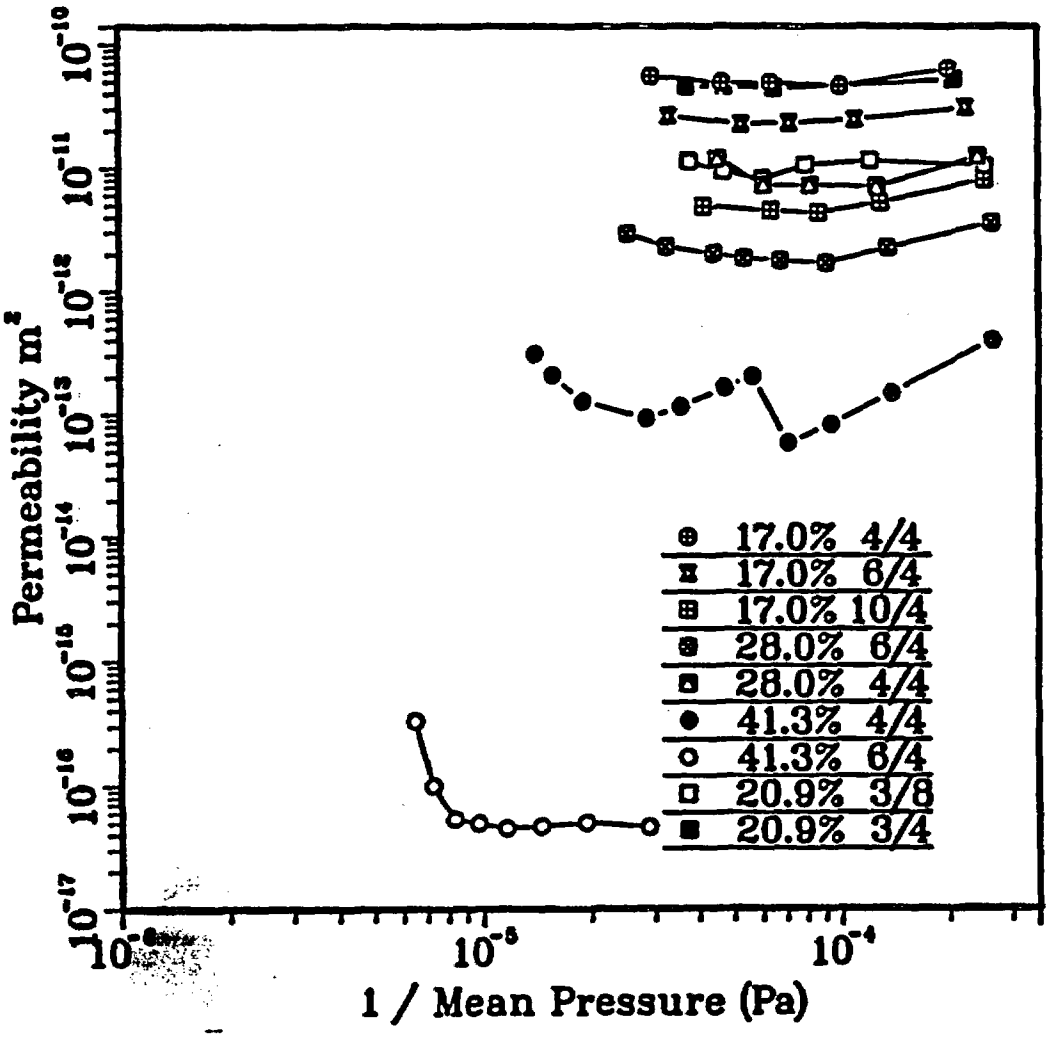

Figure 4.27 Permeability to air of compacted bentonite samples installed in plexiglass permeameters of 25.4 mm in diameter.

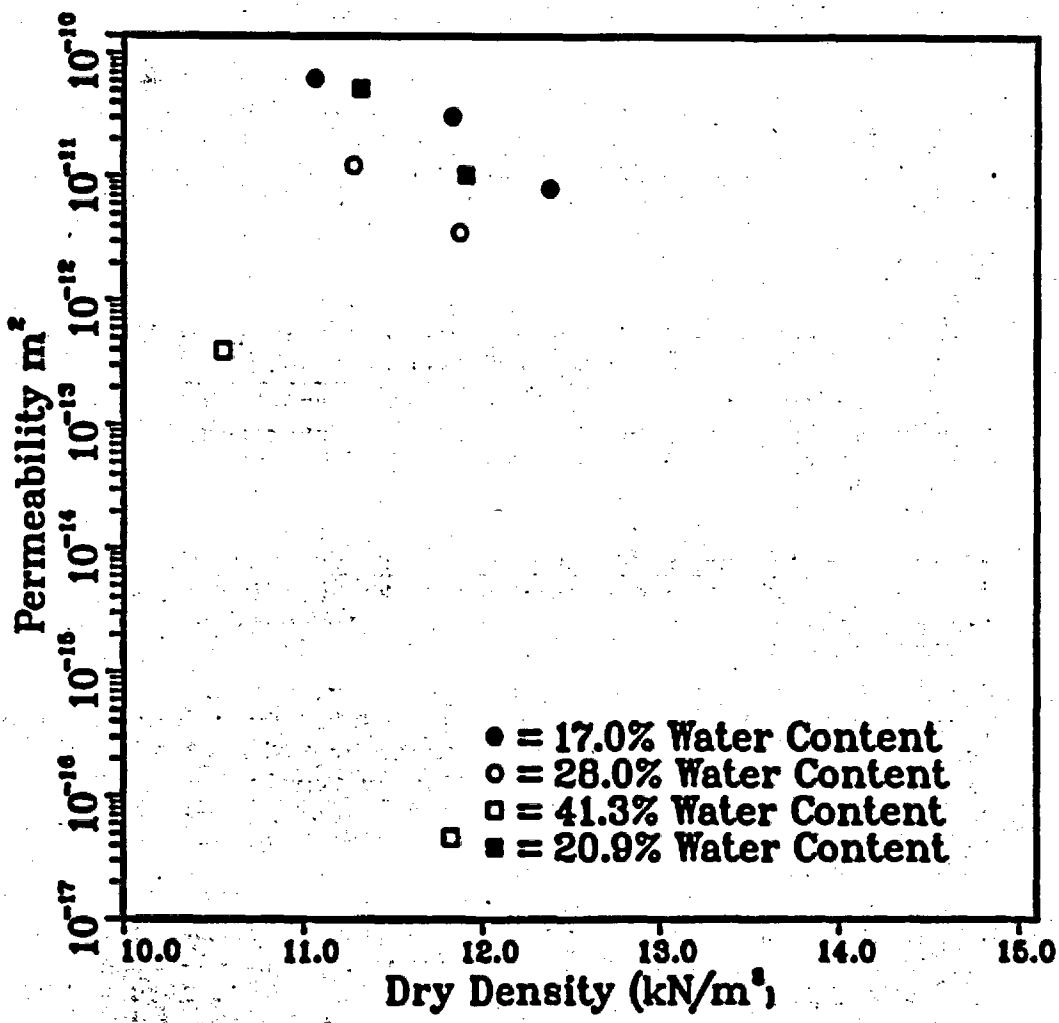

Figure 4.28 Permeability to air vs. dry density for the compacted bentonite samples installed in plexiglass permeameters.

air actually changed the color of the sample from dark grey to a distinctive light gray. To effectively minimize the migration of gaseous radionuclides, highly compacted bentonite plugs at low water content are suggested.

4.4 Swelling Pressure of Bentonite

A device similar to the Soiltest volume change meter (model C-260; Soiltest Catalog, 1983, p. 17) is used to measure the swelling pressure and volume change of bentonite. The device has a capacity for measuring swelling pressure up to 11 MPa. It is intended to run 6 to 8 tests to allow determination of the swelling pressure as a function of dry density.

Figures 4.29 and 4.30 show the swelling pressure and volume change with respect to time for two compacted bentonite samples. The maximum swelling pressure and volume change along with the starting and ending water contents and dry densities are summarized in Table 4.4.

4.5 References

ASTM D698-78, "Standard Test Methods for Moisture-Density Relations of Soils and Soil-Aggregate Mixtures Using 5.5-lb (2.49-kg) Rammer and 12-in (305-mm) Drop," Annual Book of ASTM Standards, Section 4, Construction, Vol. 04.08, Soil and Rock; Building Stones, American Society for Testing and Materials, Philadelphia.

ASTM D4525-85, "Standard Test Method for Permeability of Rocks by Flowing Air," Annual Book of ASTM Standards, Section 4, Construction, Vol. 04.08, Soil and Rock; Building Stones, American Society for Testing and Materials, Philadelphia.

Daemen, J.J.K., K. Fuenkajorn, S. Ouyang, H. Akgun, and R. Armstrong, 1988, "Sealing Boreholes and Shafts in Tuff, Quarterly Progress Report, Sept. 1 - Nov. 30, 1988," Contract NRC-04-86-113, prepared for the U.S. Nuclear Regulatory Commission, by the Department of Mining and Geological Engineering, University of Arizona, Tucson.

Daemen, J.J.K., K. Fuenkajorn, S. Ouyang, H. Akgun, R. Armstrong, D.S. Crouthamel, and C.S. Sharpe, 1989, "Sealing Boreholes and Shafts in Tuff, Quarterly Progress Report, Dec. 1, 1988 - Feb. 28, 1989," Contract NRC-04-86-113, prepared for the U.S. Nuclear Regulatory Commission, by the Department of Mining and Geological Engineering, University of Arizona, Tucson.

Gupta, D.C., M. Nataraja, and J.J.K. Daemen, 1989, "Regulatory Questions and Concerns about Sealing a HLW Repository in an Unsaturated Environment," presented at Workshop on Sealing of Radioactive Waste Repositories, organized by OECD Nuclear Energy Agency and Commission of the European Communities in cooperation with Gesellschaft fur Strahlen-Und Umweltforschung MBH Munchen, Institut fur Tieflagerung, Braunschweig, Federal Republic of Germany, 22-25 May.

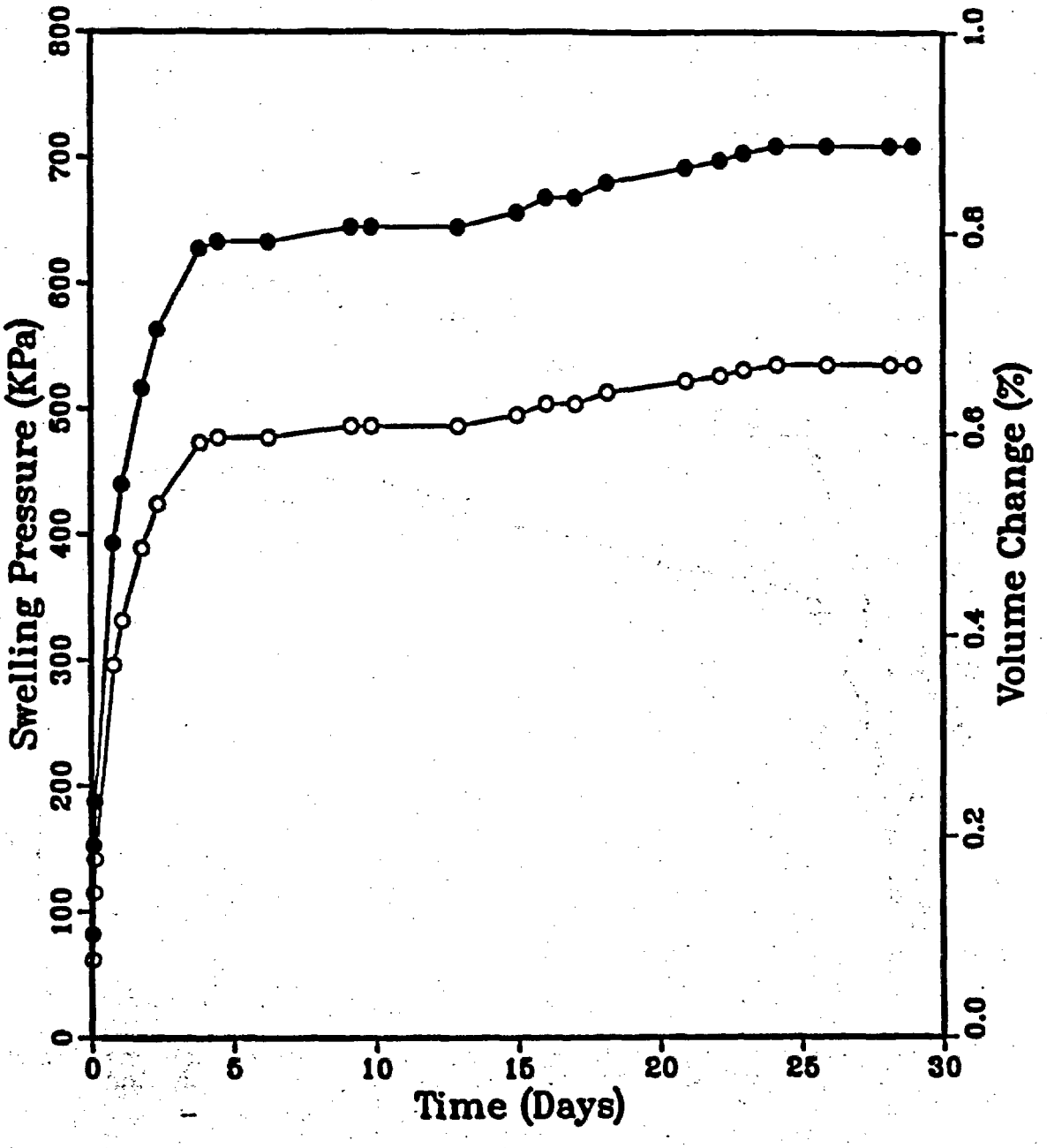

Figure 4.29 Swelling pressure and volume change vs. time for swelling test 1.

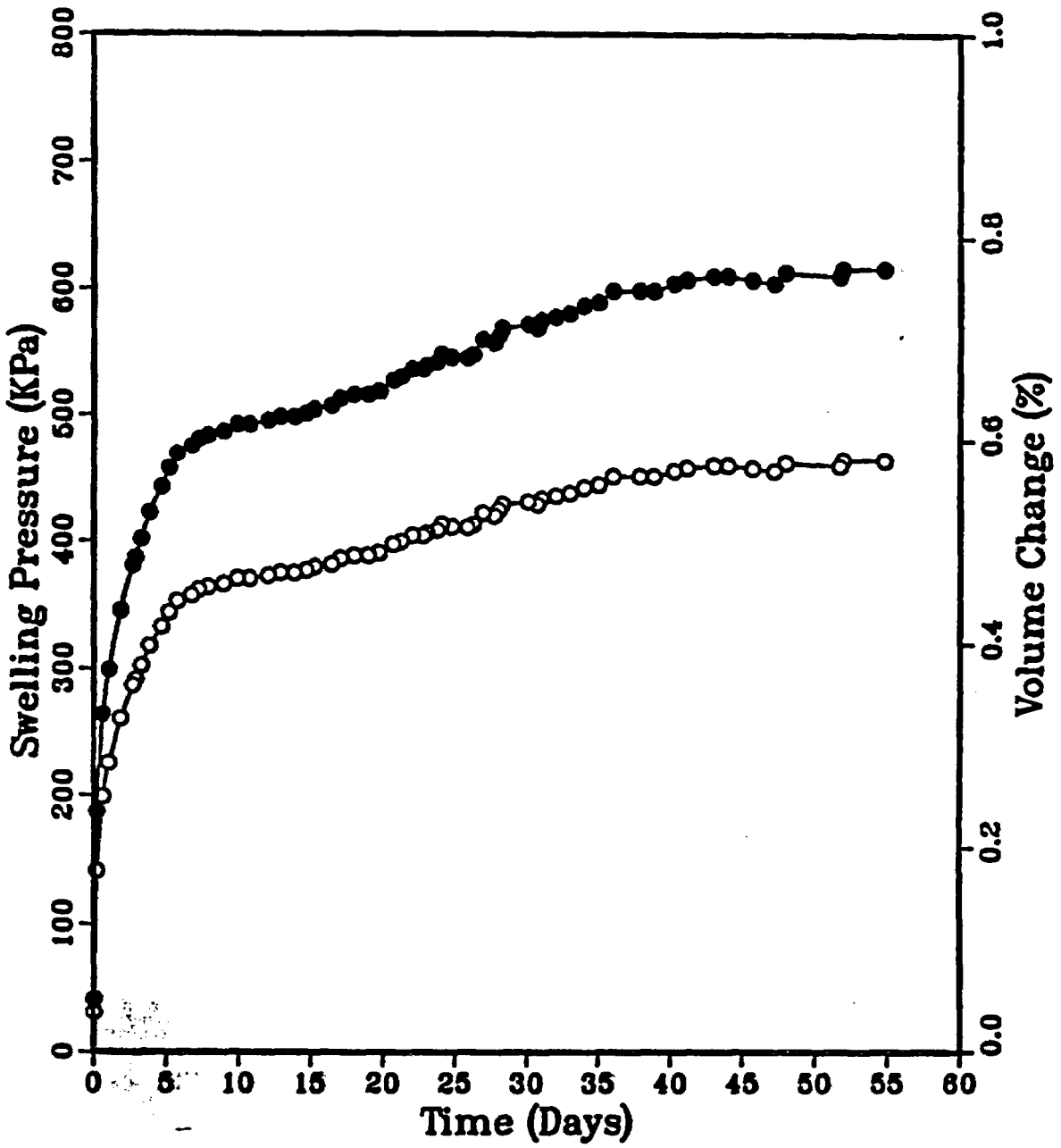

Figure 4.30 Swelling pressure and volume change vs. time for swelling test 2.

Table 4.4 Summary of Bentonite Swelling Pressure Tests

Test Number	Maximum Volume Change (%)	Maximum Swelling Pressure (kPa)	Dry Density (g/cm^3)		Water Content (%)			
						Ending		
			Starting	Ending	Starting	Bottom	Middle	Top
1	0.67	709.4	1.152	1.145	30.52	41.87	-	43.31
2	0.58	615.6	1.210	1.200	17.82	45.60	45.02	50

Head, K.H., 1980, Manual of Soil Laboratory Testing. Volume 1: Soil Classification and Compaction Tests, Engineering Laboratory Equipment Limited, 339 pp.

Lambe, T.W., 1951, Soil Testing for Engineers, John Wiley and Sons, New York, 165 pp.

Pusch, R. and G. Altermark, 1985, "Experience from Preparation and Application of Till/Bentonite Mixtures," Engineering Geology, Vol. 21, pp. 377-382.

Soiltest Catalog, 1983, Soiltest, Inc., Lake Bluff, IL, 407 pp.

U.S.B.P.R., 1962, "Aggregate Gradation for Highways," Bureau of Public Roads, Washington, DC.

Winterkorn, H.F., 1975, "Soil Stabilization," in Foundation Engineering Handbook, H.F. Winterkorn and H.Y. Fang, eds., Van Nostrand Reinhold Co., New York, pp. 312-336.

Yong, R.N., P. Boonsinuk, and G. Wong, 1986, "Formulation of Backfill Material for a Nuclear Fuel Waste Disposal Vault," Canadian Geotechnical Journal, Vol. 23, pp. 216-228.

CHAPTER FIVE

AXIAL STRENGTH OF CEMENT BOREHOLE PLUGS EMPLACED IN TUFF CORES

5.1 Introduction

This chapter presents experimental determinations of the axial bond strength of cementitious borehole plugs in holes in welded tuff cylinders. The bond strength is more easily determined than is the hydraulic bond between such plugs and the rock. Because the permeability of such systems is usually low, its determination requires lengthy experiments. Measuring the bond strength provides a time and cost effective alternative, as well as results that have direct relevance to plug performance.

Axial loads on cement plugs or seals due to gas or water pressures, or due to temperature changes induced subsequent to plug installation generate shear stresses along the plug/rock contact. Deformation of the rock mass, e.g. as a result of waste induced temperature changes, also may load or deform plugs. Stress changes along the rock-plug interface may change the permeability along the interface or along discontinuities along or close to the interface. Under extreme conditions they could cause dislodging or slippage of plugs. Therefore, the interface is a critical element of any seal system.

The objective of this study is to determine the axial strength of cement borehole plugs in tuff cores. The interface strength and deformation are evaluated as a function of borehole size, temperature (up to 90°C) and degree of saturation. The tuff cylinders have inside diameters of 25.4 mm (1 in), 50.8 mm (2 in) or 101.6 mm (4 in), outside diameters of 152.4 mm (6 in) or 187.3 mm (7.375 in), and lengths ranging from 101.6 mm (4 in) to 177.8 mm (7 in). The use of three different inside hole diameters might enable some extrapolation of data from laboratory to field scale [although the 152.4 and 196.9 mm tuff cores used have different stiffnesses (i.e. different wall thickness to inside diameter ratios)]. An analysis which leads to a formulation that allows for the differences in lateral cylinder stiffness, and provides a means for normalizing all results to a common stiffness reference basis is presented. The tuff cores are plugged with Self-Stress II cement plugs having length to diameter ratios of 1.0, in most cases. Daemen et al. (1988b, Appendix 2.A, Ch. 2) give the composition and the procedure for preparing Self-Stress II (SS II) cement borehole plugs. Daemen et al. (1988a, Ch. 5) give the push-out testing program.

Procedures and analyses of push-out tests have been discussed by Stormont and Daemen (1983). Modifications have been implemented for push-out testing on tuff cores with regard to variables measured during testing (i.e. top and bottom cement plug displacement, temperature and degree of saturation of rock cores), and analyses and interpretation of results. Daemen et al. (1988c, pp. 56-105) give derivations of analytical solutions and finite element analysis for borehole plug-rock interaction.

5.2 The Effect of Stiffness on the Bond Strength of Borehole and Shaft Plugs

5.2.1 Introduction

The push-out tests completed to date (i.e. Daemen et al., 1988b,c;1989 and those reported herein) have been performed on tuff cores with three different outside and inside radii: 1) cores with inside radius of 12.7 mm (0.5 in) and outside radius of 76.2 mm (3 in); (2) cores with inside radius of 25.4 mm (1 in) and outside radius of 76.2 mm (3 in); and 3) cores with inside radius of 50.8 mm (2 in) and outside radius of 93.7 mm (3.7 in). These tuff cores have outside to inside radius ratios of 6, 3 and 1.84, respectively. They are plugged with nearly centered Self-Stress II cement plugs having length-to-diameter ratios of 1.0, in most cases. The push-out tests are performed on plugs in unconfined rock cylinders.

The main objective of this section is to investigate analytically the potential influence of cylinder stiffness on the bond strength. The cylinder stiffness can be defined as the ratio of the applied lateral external stress to the outside radial displacement of the cylinder. Additional objectives are to study the effect of lateral external stress and the effect of axial stress applied to the plug on the normal stress across the plug/rock interface, and on the radial displacement along the plug-rock interface. The normal stress and the radial displacement along the plug/rock interface are analyzed as a function of cylinder outside to inside radius ratio, ratio of the Young's modulus of the plug to that of the rock, and Poisson's ratios of the plug and of the rock. The solutions are presented for cases of plane strain and plane stress. The analysis leads to a formulation which allows for the differences in lateral cylinder stiffness, and provides a means for adjusting all results to a common stiffness references basis. Sign conventions are those presented by Jaeger and Cook (1979, pp. 10 and 33-37).

Jeffrey (1980, pp. 18-60) discusses similar problems. Figure 5.1 illustrates the general geometry of a cylindrical inclusion problem which can be specialized to represent a push-out test. Table 5.1 gives definitions of all symbols used.

5.2.2 Influence of Lateral External Stress on Radial Contact Stress

Analyzed in this section is the effect of a lateral external stress (σ_o) applied to the cylinder periphery on the normal stress (σ_i) and radial displacement ($u_{P,C}$) along the plug/rock contact. The objective is to present a formulation that expresses the ratio of the normal stress generated along the plug/rock interface to that of the applied external stress. Results are given as a function of material properties (E_P/E_R, ν_P, ν_R), and for the cylinder radius ratios of 6, 3 and 1.84 used in the push-out tests. All results are adjusted to a common cylinder radius ratio using the assumptions of plane strain and of plane stress.

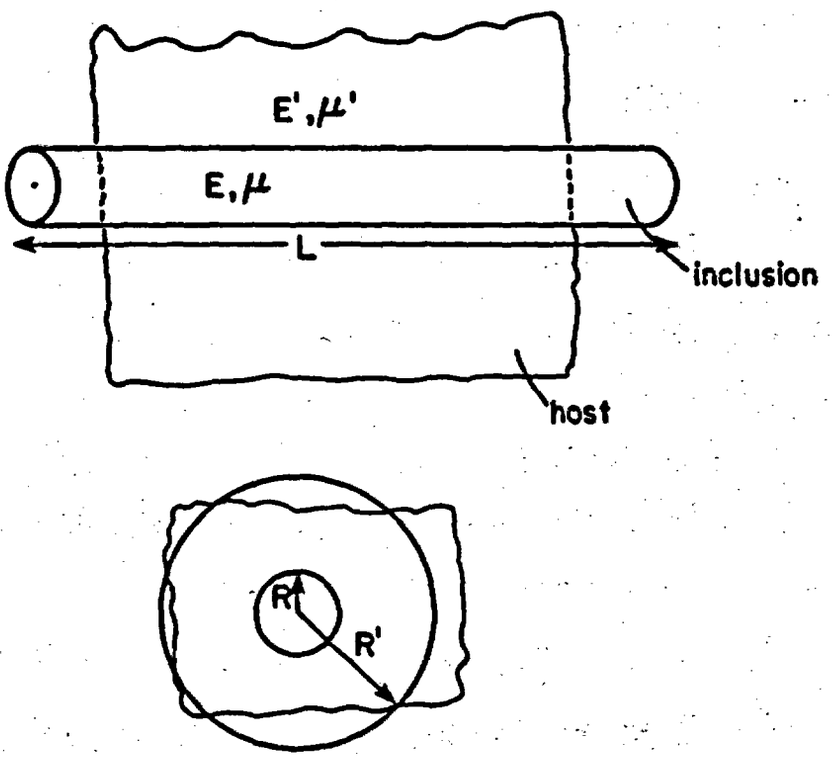

Figure 5.1 Illustration of a cylindrical inclusion problem. Inclusion of radius (R), length (L), Young's modulus (E) and Poisson's ratio (μ) embedded in host of radius (R'), Young's modulus (E') and Poisson's ratio (μ').

Table 5.1 Definition of Symbols Used in Chapter 5

a = plug radius

E, E_p = Young's modulus of plug

E', E_R = Young's modulus of rock

E_p/E_R = modulus ratio

L, L_c = plug length

L_r = length of rock core

P_{po} = axial force applied to the plug

r = radial coordinate

R = rock radius

R/a = cylinder radius ratio

u, v, w = displacement components in the r, θ, and z directions

u_p, u_R = radial displacement of plug and rock

$u_{P,C}$ = radial (inward) displacement of plug due to external stress

$u_{P,Z}$ = radial (outward) displacement of plug due to axial stress

VSF = vertical stress factor

z = distance from initial location of loaded end of plug

α = coefficient used to calculate the interface shear stress distribution in a borehole plug-rock system

λ_R = Lame's constant

ν, ν_p = Poisson's ratio of plug

ν', ν_R = Poisson's ratio of rock

σ_i = radial (normal) stress at plug/rock interface due to an applied external stress

Table 5.1 Terms Used in Chapter 5--Continued

σ_o = applied external stress

σ_{po} = axial stress applied to plug

σ_r, σ_θ, σ_z = normal stress components

σ_r^p, σ_θ^p, σ_z^p = normal stress components in plug

$\sigma_{z,f}^p$ = axial stress at failure

τ_{rz} = vertical shear stress

$\tau_{rz,i}^{av}$, $\tau_{rz,i}$ = average and exponential shear stress along plug-rock interface

$\tau_{rz,i}^{min}$, $\tau_{rz,i}^{max}$ = minimum and maximum exponential interface shear stress

5.2.2.1 Influence of Lateral External Stress on Radial Contact Stress under the Plane Strain Assumption

The radial displacement (u) in a hollow cylinder with an internal radius R_1 and external radius R_2, subjected to a radial stress P_1 at R_1 and P_2 at R_2 (assuming plane strain) is (Jaeger and Cook, 1979, p. 135; Timoshenko, 1956, pp. 205-210):

$$u = \frac{(P_2 R_2^2 - P_1 R_1^2)r}{2(\lambda + G)(R_2^2 - R_1^2)} + \frac{(P_2 - P_1)R_1^2 R_2^2}{2G(R_2^2 - R_1^2)r} \qquad (5.1)$$

where λ, G = Lame constants
r = radial coordinate.

The radial displacement ($u_{R,C}$) in the rock at the plug/rock contact, due to an external stress (σ_o) and an internal stress (σ_i), follows from Eq. (5.1) as:

$$u_{R,C} = \frac{(\sigma_o R^2 - \sigma_i a^2)a}{2(\lambda_R + G_R)(R^2 - a^2)} + \frac{(\sigma_o - \sigma_i)R^2 a}{2G_R(R^2 - a^2)} \qquad (5.2)$$

Substituting the values of the Lame constants (Jaeger and Cook, 1979, p. 111), $\lambda_R = \frac{E_R \nu_R}{(1 + \nu_R)(1 - 2\nu_R)}$ and $G_R = \frac{E_R}{2(1 + \nu_R)}$, yields:

$$u_{R,C} = \frac{(1 + \nu_R)a}{E_R(R^2 - a^2)} [(1 - 2\nu_R)(\sigma_o R^2 - \sigma_i a^2) + (\sigma_o - \sigma_i)R^2] \qquad (5.3)$$

where E_R = Young's modulus of rock
ν_R = Poisson's ratio of rock
R = rock cylinder radius
a = plug radius.

The radial displacement in the plug ($u_{P,C}$) at the plug/rock contact can be calculated from Eq. (5.1) by setting $R_1 = 0$, $R_2 = a$, $P_2 = \sigma_i$, $P_1 = 0$, $r = a$ and by substituting for the Lame parameters. This is the case

of a solid cylinder subjected to a radial stress and maintained in plane strain:

$$u_{P,C} = \frac{(1 + \nu_p)(1 - 2\nu_p)a}{E_p} \sigma_i \qquad (5.4)$$

where E_p = Young's modulus of plug

ν_p = Poisson's ratio of plug

σ_i = radial stress developed along plug/rock contact due to the applied external stress (σ_o)

Equating the rock and plug displacements and solving for the normal stress at the plug/rock contact yields:

$$\sigma_i/\sigma_o = \frac{2(E_p/E_R)(1 + \nu_R)(1 - \nu_R)}{(E_p/E_R)(1 + \nu_R)[(1 - 2\nu_R)(a/R)^2 + 1] + (1 + \nu_p)(1 - 2\nu_p)(1 - (a/R)^2)} \qquad (5.5)$$

The general case of an infinite hollow cylinder, simulating an in-situ rock mass, can be written by substituting $R \to \infty$ into Eq. (5.5):

$$\frac{\sigma_i}{\sigma_o} = \frac{2(E_p/E_R)(1 + \nu_R)(1 - \nu_R)}{(E_p/E_R)(1 + \nu_R) + (1 + \nu_p)(1 - 2\nu_p)} \qquad (5.6)$$

The radial displacement in the plug can be calculated from Eq. (5.3) or (5.4) by substituting for σ_i from Eq. (5.5):

$$u_{P,C}/a = \frac{2(\sigma_o/E_R)(1 + \nu_p)(1 - 2\nu_p)(1 + \nu_R)(1 - \nu_R)}{-(E_p/E_R)(1 + \nu_R)[(1 - 2\nu_R)(a/R)^2 + 1] + (1 + \nu_p)(1 - 2\nu_p)(1 - (a/R)^2)} \qquad (5.7)$$

For an infinite rock mass, Eq. (5.7) can be rewritten by substituting $R \to \infty$ as :

$$\frac{u_{P,C}}{a} = \frac{2(\sigma_o/E_R)(1+\nu_p)(1-2\nu_p)(1+\nu_R)(1-\nu_R)}{(E_p/E_R)(1+\nu_R)+(1+\nu_p)(1-2\nu_p)} \quad (5.8)$$

5.2.2.2 Influence of Lateral External Stress on Radial Contact Stress for Plane Stress Conditions

The solutions for plane strain presented in Section 5.2.2.1 can be converted to the case of plane stress by expressing the plane strain solutions in terms of G and ν, and by replacing ν by $\nu/(1+\nu)$ (Jaeger and Cook, 1979, p. 115).

The radial stress along the plug/rock contact developed due to the applied external stress for the case of plane stress can be derived from Eq. (5.5)) as:

$$\frac{\sigma_i}{\sigma_o} = \frac{2(E_p/E_R)}{(1-\nu_p)(1-(a/R)^2)+(E_p/E_R)[(1+\nu_R)+(1-\nu_R)(a/R)^2]} \quad (5.9)$$

For the case of an infinite rock mass, substituting $R \to \infty$ into Eq. (5.9) yields:

$$\frac{\sigma_i}{\sigma_o} = \frac{2(E_p/E_R)}{(1-\nu_p)+(E_p/E_R)(1+\nu_R)} \quad (5.10)$$

The radial displacement in the plug can be derived from Eq. (5.7) for the case of plane stress:

$$\frac{u_{P,C}}{a} = \frac{2(\sigma_o/E_R)(1-\nu_p)}{(1-\nu_p)(1-(a/R)^2)+(E_p/E_R)[(1+\nu_R)+(1-\nu_R)(a/R)^2]} \quad (5.11)$$

For the case of an infinite rock mass, substituting $R \to \infty$ into Eq. (5.11) yields:

$$\frac{u_{P,C}}{a} = \frac{2(\sigma_o/E_R)(1-\nu_p)}{(1-\nu_p)+(E_p/E_R)(1+\nu_R)} \quad (5.12)$$

5.2.3 Relation Between Normal Stress Across the Plug/Rock Interface and Axial Stress Applied to the Plug

The main objective of this section is to express the ratio of the normal (radial) stress generated along the plug/rock interface to that of an axial stress applied to the plug (σ_{rP}/σ_{po}). Results are given as

a function of cylinder outside to inside radius ratio, ratio of the Young's modulus of the plug to that of the rock and the Poisson's ratio of the plug and rock. All results are adjusted to a common cylinder radius ratio with the assumption of plane strain and plane stress.

A compressive axial stress applied to a plug generates a radial (normal) stress along the plug/rock contact and an outward radial displacement of the plug. The normal stress along the interface is proportional to the axial applied stress on the plug. The radial contact stress can be determined by equating the plug and rock radial displacements along the interface.

The radial displacement in the plug ($u_{P,Z}$) due to an applied axial (compressive) stress (σ_{po}) equals the radial strain times the plug radius (a) (Daemen et al., 1988c, p. 71):

$$u_{P,Z} = \left[\frac{(1 - \nu_p)\sigma_r^p - \nu_p \sigma_z^p}{E_p} \right] a \qquad (5.13)$$

The radial displacement in rock ($u_{R,Z}$) due to an internal stress (σ_r^p) and zero external stress (with the assumption of plane strain) follows from Eq. (5.1) as:

$$u_{R,Z} = - \frac{\sigma_r^p a(1 + \nu_R)}{E_R(R^2 - a^2)} [a^2(1 - 2\nu_R) + R^2] \qquad (5.14)$$

where R = radius of rock cylinder
E_R, ν_R = Young's modulus and Poisson's ratio of rock.

The radial stress σ_r^p across the interface can be determined by equating the plug and rock displacements along the interface:

$$\sigma_r^p = \sigma_z^p \frac{\nu_p (1 - (a/R)^2)}{(1 - \nu_p)(1 - (a/R)^2) + (E_p/E_R)(1 + \nu_R)[(1 - 2\nu_R)(a/R)^2 + 1]} \qquad (5.15)$$

The radial stress along the plug/rock contact due to the axial stress applied to a plug can be derived for the case of plane stress as described in the first paragraph of Section 5.2.2.2. Converting the plane strain solution for the radial rock displacement in Eq. (5.14) into a plane stress solution and equating it to Eq. (5.13) yields:

$$\sigma_r^P = \sigma_z^P \frac{\nu_p (1 - (a/R)^2)}{(1 - \nu_p)(1 - (a/R)^2) + (E_p/E_R)[(1 - \nu_R)(a/R)^2 + (1 + \nu_R)]} \quad (5.16)$$

For the case of an infinite rock mass, substituting $R \to \infty$ into Eqs. (5.15) and (5.16) leads to the solution of the radial stress along the plug/rock contact for cases of both plane strain and plane stress:

$$\sigma_r^P = \sigma_z^P \frac{\nu_p}{(1 - \nu_p) + (E_p/E_R)(1 + \nu_R)]} \quad (5.17)$$

(5.16)

The relation between σ_r^P and σ_z^P can be written as:

$$\sigma_r^P = \sigma_z^P(VSF) \quad (5.18)$$

where VSF is the vertical stress factor. For a plane strain solution, use Eq. (5.15), for a plane stress solution use Eq. (5.16). Eq. (5.17) is used for an infinite rock mass with the assumptions of both plane strain and plane stress.

Daemen et al. (1988c, p. 74, Eq. (5.53)) give the ratio of the normal stress generated along the plug/rock interface to that of the axial stress applied to the plug as:

$$\sigma_r^P/\sigma_{po} = K_2(VSF)$$

where K_2 = [sin hα(L − z)]/(sin hαL), for an axially loaded compressible plug, leading to an exponential stress distribution

$\alpha = [(1 - 2\nu_p(VSF))/((E_p/E_R)(1 + \nu_R)a^2 \ln(R/a))]^{1/2}$

L = plug length

z = distance from initial location of loaded end of plug

VSF = defined by Eq. (5.18)

Definitions of all symbols are given in Table 5.1.

The radial displacement in the plug ($u_{P,Z}$) can be expressed for the case of plane strain by combining Eq. (5.13) or (5.14) into Eqs. (5.15), (5.17) and (5.19) (noting that $u_{P,Z} = u_{R,Z}$):

$$\frac{u_{P,Z}}{a} = - \frac{(\sigma_{po}/E_R)K_2 \nu_p (1 + \nu_R)[(1 - 2\nu_R)(a/R)^2 + 1]}{(1 - \nu_p)(1 - (a/R)^2) + (E_p/E_R)(1 + \nu_R)[(1 - 2\nu_R)(a/R)^2 + 1]} \quad (5.20)$$

where K_2 is defined in Eq. (5.19).

For the case of plane stress, the radial displacement in the plug ($u_{p,z}$) can be obtained in a similar manner (by using Eq. (5.16) instead of (5.15)):

$$\frac{u_{p,z}}{a} = -\frac{(\sigma_{po}/E_R)K_2\nu_p[(1-\nu_R)(a/R)^2 + (1+\nu_R)]}{(1-\nu_p)(1-(a/R)^2) + (E_p/E_R)[(1-\nu_R)(a/R)^2 + (1+\nu_R)]} \quad (5.21)$$

For the case of an infinite rock mass, substituting $R \to \infty$ into Eq. (5.20) or (5.21) leads to the solution of the radial displacement in the plug ($u_{p,z}$) for cases of both plane strain and plane stress:

$$\frac{u_{p,z}}{a} = -\frac{(\sigma_{po}/E_R)K_2\nu_p(1+\nu_R)}{(1-\nu_p) + (E_p/E_R)(1+\nu_R)} \quad (5.22)$$

where K_2 is defined in Eq. (5.19). Definitions of all symbols are given in Table 5.1.

5.2.4 Relations Between Plug/Rock Normal Contact Stress, Applied Axial Plug Stress, and Confining Stress

This section discusses the effect of external stress (σ_o) and axial plug stress (σ_{po}) on the normal stress along the plug/rock contact and on the radial plug displacement. Results are analyzed as a function of different cylinder outside-to-inside radius ratios, plug-to-rock Young's modulus ratios, plug and rock Poisson's ratios and distance along the plug (z/L). Both plane strain and plane stress assumptions are used in the calculations.

The Young's modulus and Poisson's ratio of the tuff are taken as 22,600 ± 5,700 MPa and 0.20 ± 0.03, respectively (Daemen et al., 1988b, p. 36). The cement plug has the properties of System 1 cement (E_p = 7088 ± 702 MPa; ν_p = 0.15 ± 0.06) obtained from Daemen et al. (1983, p. 245). Using the lower and higher bounds for the material properties leads to a negligible deviation of up to ± 0.5% in the calculated σ_i/σ_o values, compared to those calculated by using the average material properties. Hence, throughout this analysis, only the average values of the rock and plug material properties are used (i.e. E_p/E_R = 0.314, ν_p = 0.15, ν_p = 0.20). The two main objectives are to determine the ratio of the normal stress along the plug/rock interface to that of the applied external stress (σ_i/σ_o), and to determine the ratio of the normal stress at the interface to the axial stress applied

to the plug (σ_r^p/σ_{po}). The results are adjusted to a common cylinder radius ratio (i.e. R/a = ∞ or R/a = 6.0) in order to compensate for the different cylinder radius ratios used (i.e. R/a of 6, 3 and 1.84) in push-out tests.

Binnall et al. (1987, pp. 18 and 23) give the average and upper bound values of in-situ horizontal and vertical stresses for four stratigraphic tuff units (Topopah Springs, Calico Hills, Bullfrog, Tram) of the Yucca Mountain site. The ratio of the horizontal stress to the rock Young's modulus (σ_o/E_R) in these stratigraphic locations ranges from 2.4×10^{-4} to 2.31×10^{-3}; the ratio of the vertical stress to rock Young's modulus (σ_{po}/E_R) ranges from 2.5×10^{-4} to 2.66×10^{-3}. The average values of both σ_o/E_R and σ_{po}/E_R are in the neighborhood of 0.001. Therefore, for radial plug displacement calculations, both σ_o/E_R and σ_{po}/E_R will be assumed to be equal to 0.001. The radial stress at the plug/rock contact and the radial plug displacement using the plane stress assumption is generally higher than those calculated with the plane strain assumption, with a deviation usually in the range of 5-7%. Because the difference is small, subsequent presentations and discussions usually are limited to the plane strain configurations.

The ratio of the normal stress along the plug/rock contact to the applied external stress (σ_i/σ_o) increases with increasing Poisson's ratio of the plug and decreasing Poisson's ratio of the rock (Figure 5.2), and increases with increasing plug-to-rock Young's modulus ratio (E_p/E_R) (Figures 5.2 and 5.3). The stress ratio decreases with increasing cylinder radius ratio (R/a) for cylinders of E_p/E_R less than 1.0. The opposite is observed on cylinders with modulus ratios greater than 1.0 (Figure 5.3).

The radial plug displacement due to the applied external stress decreases with increasing modulus ratio. The displacement decreases with increasing cylinder radius ratio for cylinders with modulus ratios less than 1.0 (Figure 5.4). The opposite is observed for cylinders with E_p/E_R greater than 1.0. Table 5.2 summarizes the results for the interface normal stress and displacement due to an applied external stress.

The ratio of the normal stress along the plug/rock contact to the axial stress applied to the plug is plotted as a function of the position along the plug in Figure 5.5. This ratio decreases with increasing modulus ratio, with the highest ratio occurring at the loaded end of the plug (z/L = 0). For a modulus ratio of 0.001, the σ_r^p/σ_{po} ratio drops close to zero after about z/L = 0.45. For E_p/E_R = 1000, σ_r^p/σ_{po} becomes higher than that of E_p/E_R = 0.001 after z/L = 0.45. This can not be shown in Figure 5.5 due to scaling problems, but is presented

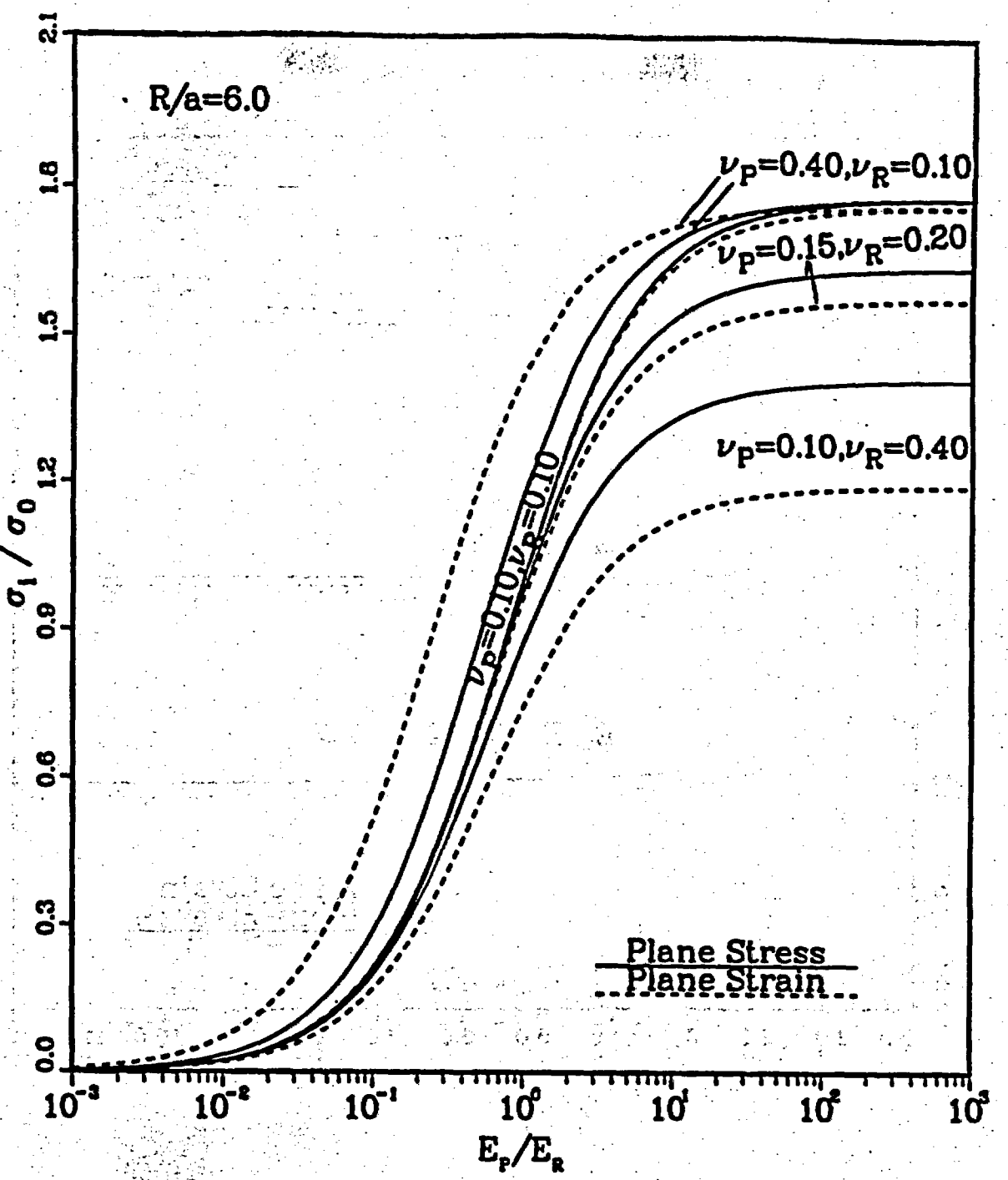

Figure 5.2 Ratio of normal stress along the plug/rock interface to applied external stress (σ_i/σ_o).

E_p/E_R = Young's modulus ratio of plug and rock

ν_p, ν_R = Poisson's ratios of plug and rock

R/a = outside to inside cylinder radius ratio .

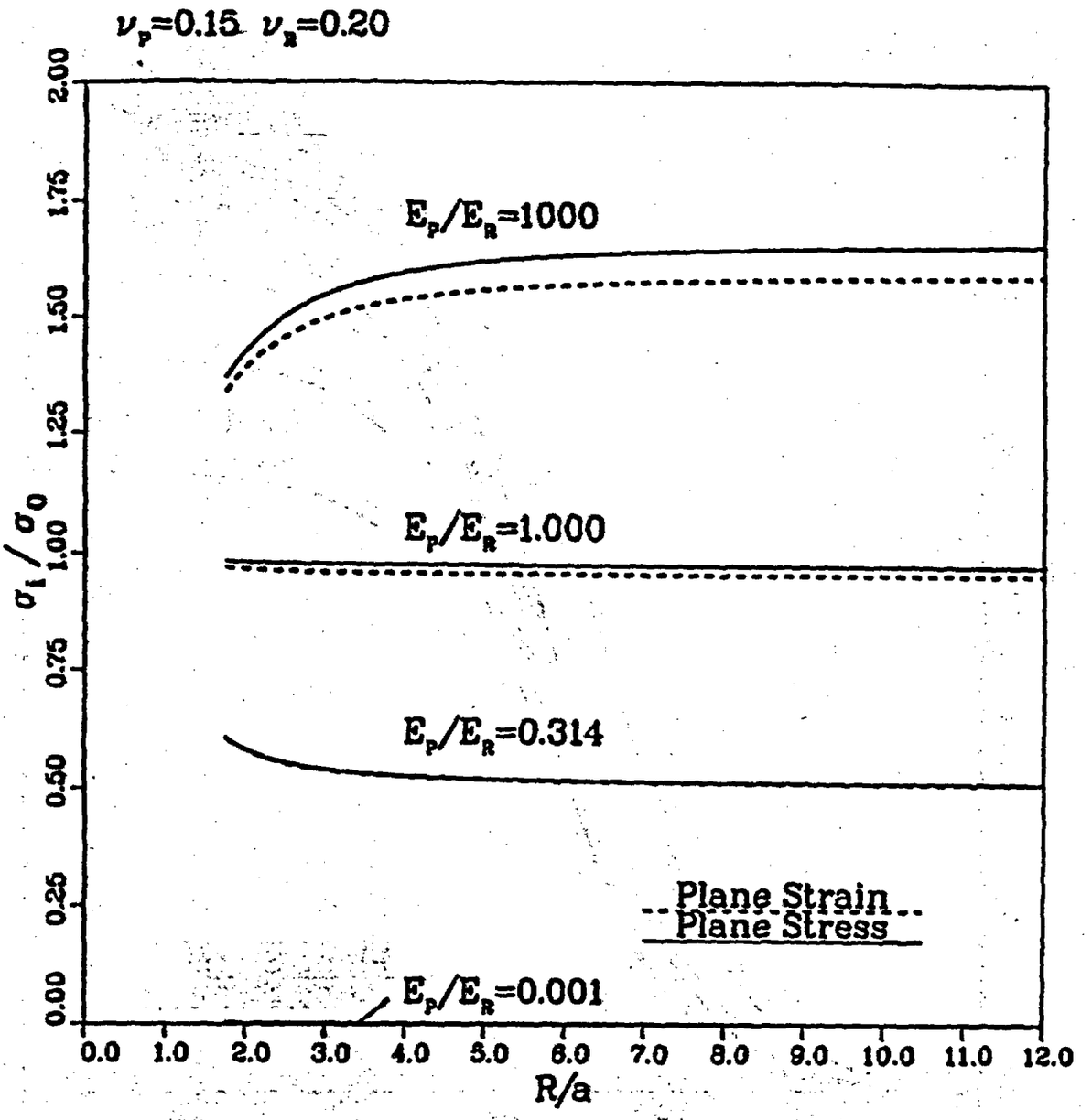

Figure 5.3 Ratio of normal stress along the plug/rock interface to applied external stress (σ_i/σ_o).

E_p/E_R = Young's modulus ratio of plug and rock
ν_p, ν_R = Poisson's ratios of plug and rock
R/a = outside to inside cylinder radius ratio .

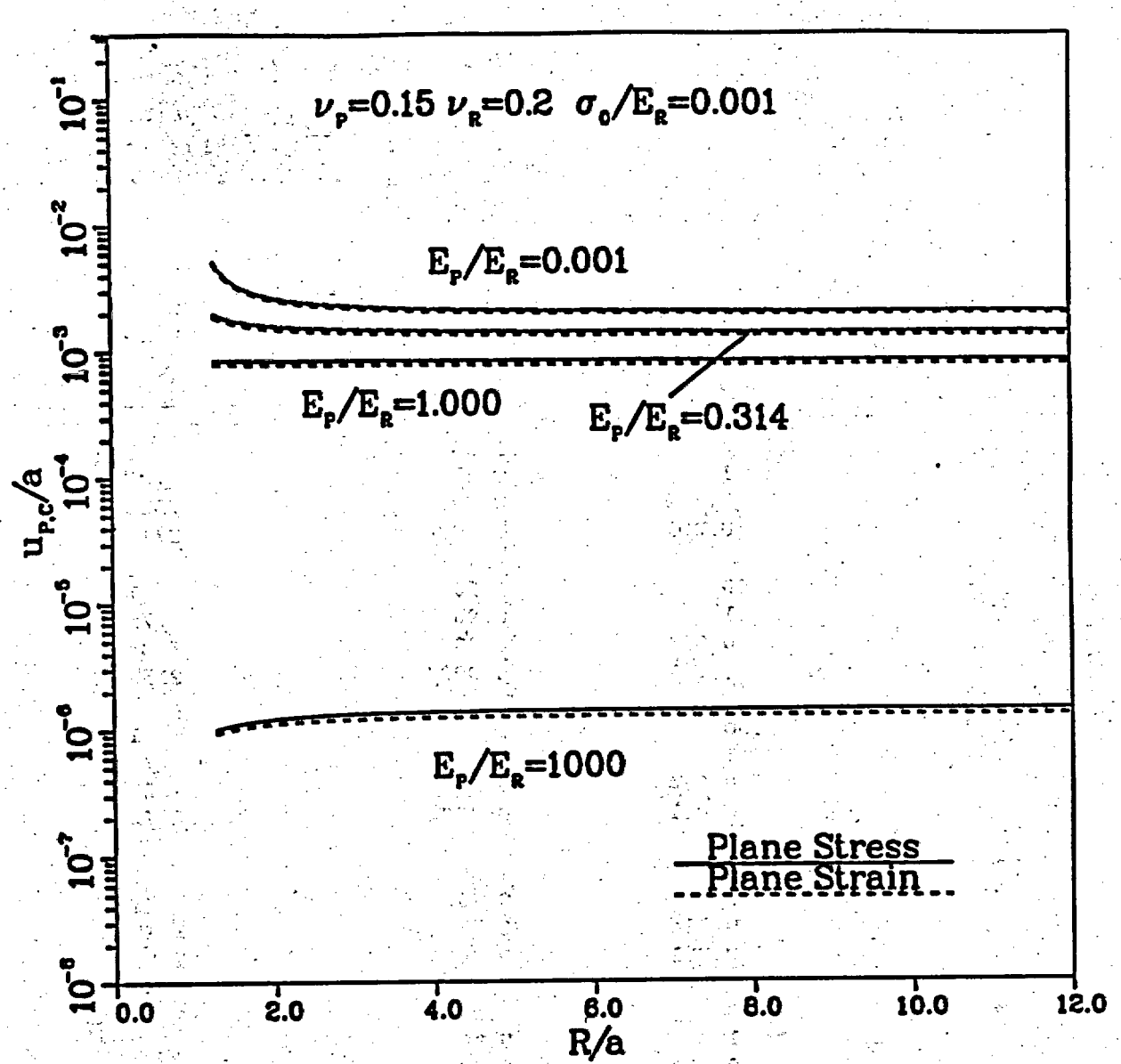

Figure 5.4 Ratio of inward radial plug displacement to plug radius ($u_{P,C}/a$) due to applied external stress (σ_o).

E_p/E_R = Young's modulus ratio of plug and rock
ν_p, ν_R = Poisson's ratios of plug and rock
R/a = outside to inside cylinder radius ratio .

Table 5.2 Effect of External Stress (σ_o) on Normal Stress along the Plug/Rock Contact (σ_i) and on the Inward Radial Plug Displacement ($u_{P,C}$). Results are presented (for the case of plane strain) as a function of different cylinder radius ratios (R/a) and plug-to-rock Young's modulus ratios (E_P/E_R). $\nu_R = 0.20$, $\nu_P = 0.15$, $\sigma_o/E_R = 0.001$. Table 5.1 gives definitions for all symbols used.

Tuff Cylinder Radius Ratio (R/a)	E_P/E_R	σ_i/σ_o	$u_{P,C}/a$ ($\times 10^6$)
1.84	1000	1.36	1.09
	1	0.97	781
	0.314	0.5956	1529
	0.001	0.0034	2713
3.0	1000	1.50	1.21
	1	0.96	775
	0.314	0.5391	1384
	0.001	0.0027	2156
6.0	1000	1.57	1.27
	1	0.96	772
	0.314	0.5168	1326
	0.001	0.0024	1972
10.0	1000	1.59	1.28
	1	0.96	771
	0.314	0.5122	1315
	0.001	0.0024	1937
∞	1000	1.60	1.28
	1	0.96	771
	0.314	0.5097	1308
	0.001	0.0024	1917

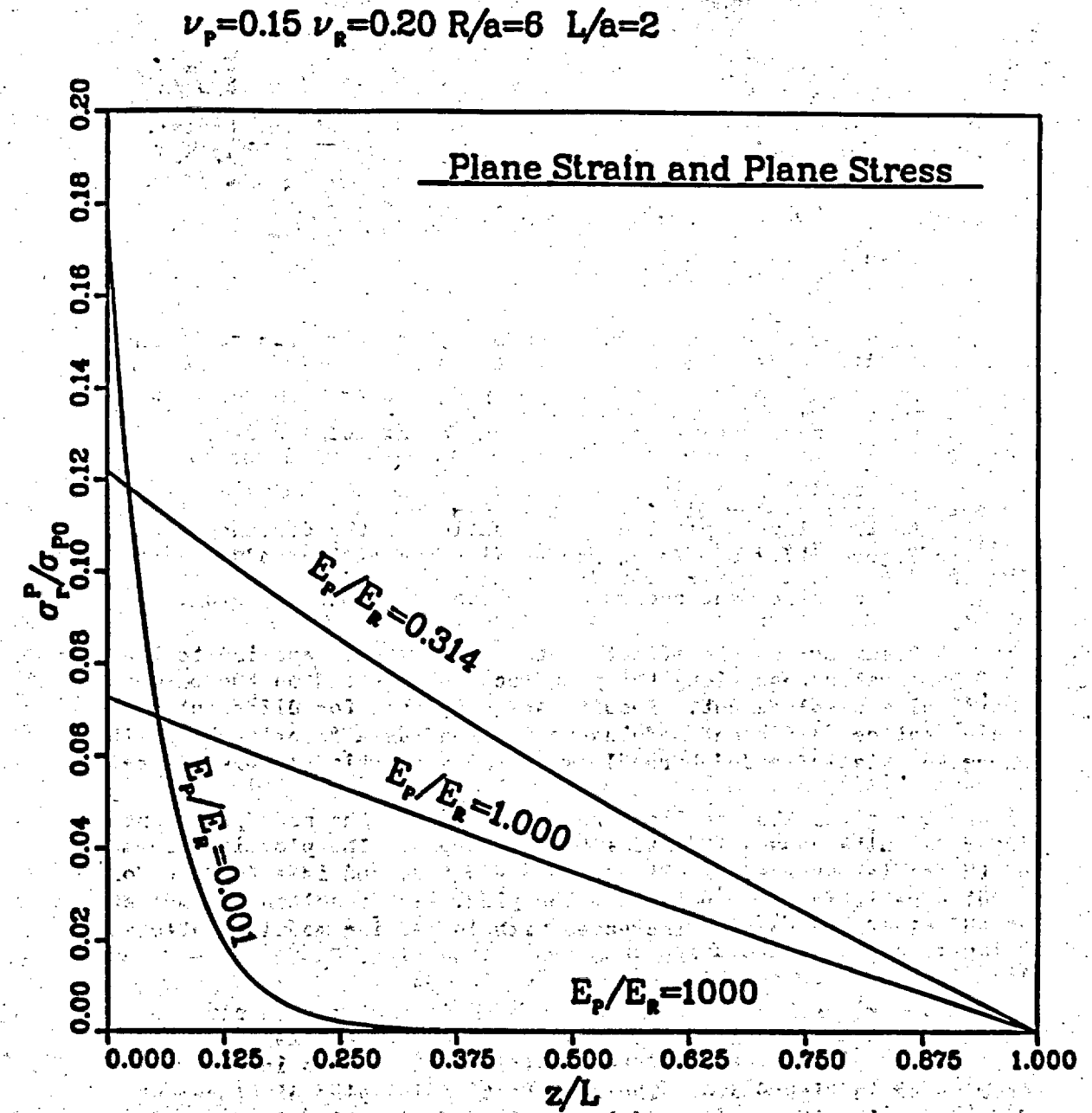

Figure 5.5 Ratio of normal stress along the plug/rock interface to the axial stress applied to the plug (σ_r^p/σ_{po}).

E_p/E_R = Young's modulus ratio of plug and rock
z/L = distance along the axially loaded plug.

in Table 5.3. The reason for the curve of $E_p/E_R = 0.001$ giving the highest σ_r^p/σ_{po} at the loaded end of the plug and the lowest σ_r^p/σ_{po} after $z/L = 0.20$ is the value of the α-coefficient in Eq. (5.19). The values of α for modulus ratios of 0.001, 0.314, 1.0 and 1000 are 20.99. 1.195, 0.675 and 0.022, respectively. Inserting $\alpha = 20.99$ into Eq. (5.19) for $E_p/E_R = 0.001$ leads to the highest σ_r^p/σ_{po} at $z/L = 0$ and lowest σ_r^p/σ_{po} after $z/L = 0.20$.

Figure 5.6 gives σ_r^p/σ_{po} as a function of cylinder radius ratio and modulus ratio at the loaded end of the plug. σ_r^p/σ_{po} increases with increasing cylinder radius ratio and decreasing modulus ratio.

The outward radial plug displacement ($u_{p,z}$) due to the axial stress applied to the plug is plotted as a function of the distance along the plug in Figure 5.7. $u_{p,z}/a$ decreases with increasing modulus ratio. The highest displacement occurs at the loaded end of the plug.

Table 5.3 summarizes the effect of the axial stress applied to the plug on the normal stress along the plug/rock contact and on the outward radial plug displacement. Results are presented for different cylinder radius ratios, different modulus ratios, and as a function of position along an axially loaded borehole with the assumption of plane strain.

Figure 5.8 gives the resultant radial stress at the rock/plug contact due to simultaneous axial and external stress. The plot is a summation of the radial stresses in Figures 5.3 and 5.5, and is a function of modulus ratio and distance along the plug. The resultant normal stress at the plug/rock contact increases with increasing modulus ratio and slightly decreases away from the top of the plug.

Figure 5.9 gives a plot of the resultant (inward) radial plug displacement due to the combined effect of axial and lateral loading. The plot is a subtraction of the radial displacements in Figure 5.7 from those in Figure 5.4. The resultant radial plug displacement decreases with increasing modulus ratio and slightly increases away from the top of the plug.

Table 5.4 summarizes the resultant normal stress at the plug/rock contact and the resultant (inward) radial plug displacement due to the effect of axial and lateral loading. Results are presented for different cylinder radius ratios, different modulus ratios, and as a function of the distance along a borehole plug, with the assumption of plane strain. In Table 5.4 the Poisson's ratio of the plug and the rock are 0.15 and 0.20, respectively.

Table 5.3 Effect of Axial Stress Applied to Plug (σ_{po}) on Normal Stress along the Plug/Rock Contact (σ_r^p) and on the Outward Radial Plug Displacement ($u_{P,Z}$). Results are presented (for the case of plane strain) as a function of cylinder radius ratio (R/a), plug-to-rock Young's modulus ratio (E_p/E_R), and distance along an axially loaded borehole plug (z/L). ν_R = 0.20, ν_P = 0.15, σ_{po}/E_R = 0.001. Table 5.1 gives definitions for all symbols used.

Tuff Cylinder Radius Ratio (R/a)	E_p/E_R	σ_r^p/σ_{po} z = 0	σ_r^p/σ_{po} z = L/4	σ_r^p/σ_{po} z = L/2	$u_{P,Z}/a$ (x 10^6) z = 0	$u_{P,Z}/a$ (x 10^6) z = L/4	$u_{P,Z}/a$ (x 10^6) z = L/2
1.84	1000	7.5×10^{-5}	5.6×10^{-5}	3.8×10^{-5}	0.15	0.11	7.49×10^{-2}
	1	0.0526	0.0289	0.0151	105	58	30
	0.314	0.1015	0.0363	0.0128	203	73	26
	0.001	0.1761	3×10^{-9}	4.5×10^{-17}	352	5.6×10^{-6}	8.9×10^{-14}
3.0	1000	1.04×10^{-4}	7.8×10^{-5}	4.3×10^{-5}	0.15	0.11	7.49×10^{-2}
	1	0.0655	0.0406	0.0235	94	58.5	34
	0.314	0.1152	0.0532	0.0239	166	77	34
	0.001	0.1762	2.7×10^{-7}	4×10^{-13}	254	3.8×10^{-4}	5.8×10^{-10}
6.0	1000	1.2×10^{-4}	9×10^{-5}	6×10^{-5}	0.15	0.11	7.49×10^{-2}
	1	0.0713	0.0473	0.0228	89	59	36
	0.314	0.1206	0.0651	0.0334	151	82	42
	0.001	0.1762	4.9×10^{-6}	1.4×10^{-10}	221	6.1×10^{-3}	1.7×10^{-7}

Table 5.3 Effect of Axial Stress Applied to Plug (σ_{po}) on Normal Stress along the Plug/Rock Contact (σ_r^p) and on the Outward Radial Plug Displacement ($u_{p,z}$)--Continued

Tuff Cylinder Radius Ratio (R/a)	E_p/E_R	σ_r^p/σ_{po} z = 0	z = L/4	z = L/2	$u_{p,z}/a$ (x 10^6) z = 0	z = L/4	z = L/2
10.0	1000	1.23×10^{-4}	9.2×10^{-5}	6.2×10^{-5}	0.15	0.11	7.5×10^{-2}
	1	0.0725	0.0494	0.0307	88	60	37
	0.314	0.1217	0.0698	0.0378	148	85	46
	0.001	0.1762	1.7×10^{-5}	1.6×10^{-9}	215	2.1×10^{-2}	2×10^{-6}
∞	1000	1.26×10^{-4}	9.5×10^{-5}	6.5×10^{-5}	0.15	0.11	7.5×10^{-2}
	1	0.0732	0.0549	0.0366	87.8	66	44
	0.314	0.1223	0.0917	0.0611	147	110	73
	0.001	0.1762	0.1108	0.0646	212	133	78

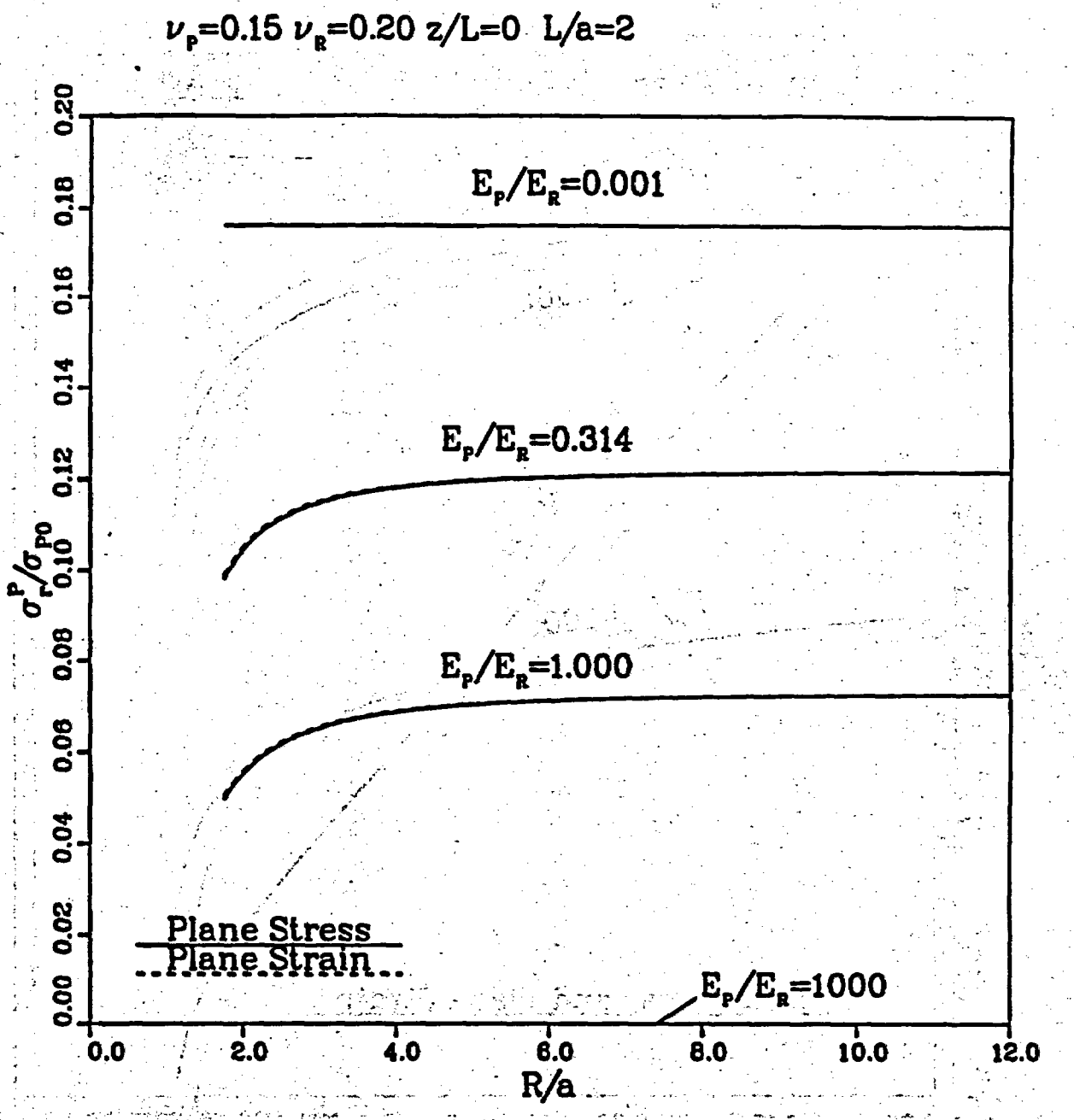

Figure 5.6 Ratio of normal stress along the plug/rock interface to the axial stress applied to the plug (σ_r^P/σ_{po}). σ_r^P/σ_{po} values are for the loaded end of plug (z/L = 0).

E_p/E_R = Young's modulus ratio of plug and rock
R/a = cylinder radius ratio.

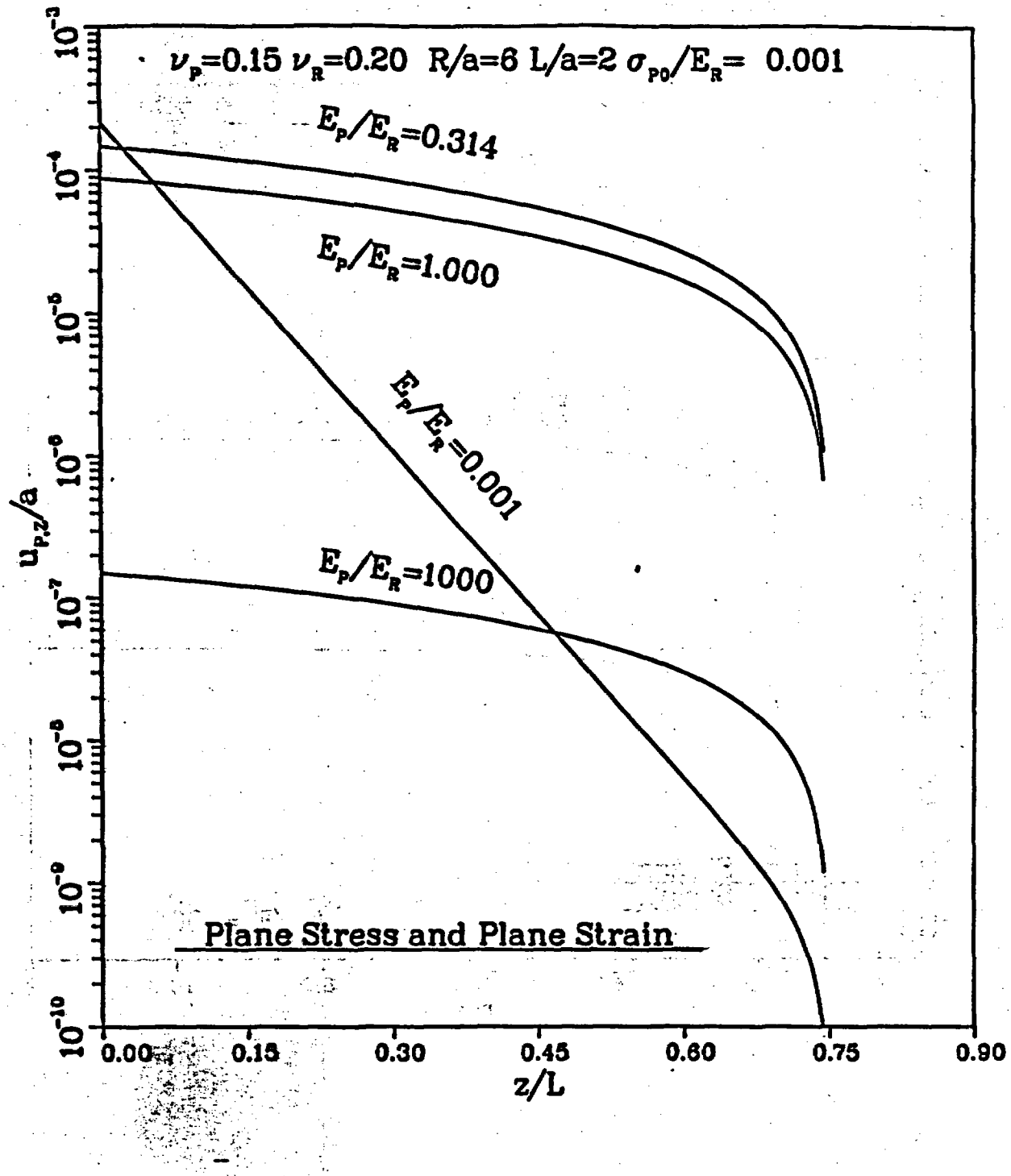

Figure 5.7 Ratio of outward radial plug displacement to the plug radius ($u_{P,Z}/a$) due to the applied axial stress to the plug (σ_{po}).

E_P/E_R = Young's modulus ratio of plug and rock
z/L = distance along the axially loaded plug.
Table 5.1 gives definitions of all symbols used.

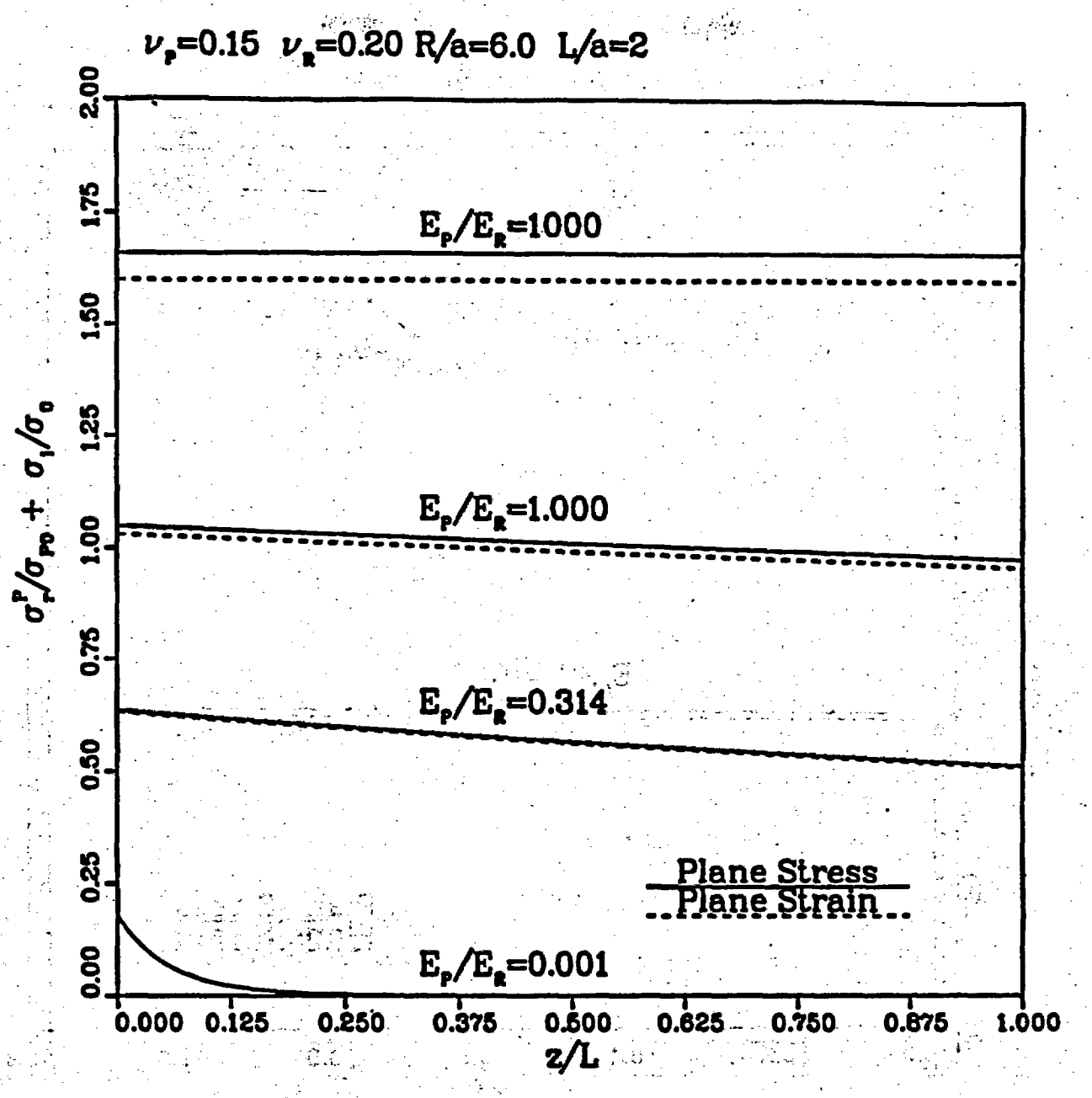

Figure 5.8 Radial stress ($\sigma_r^p/\sigma_{po} + \sigma_i/\sigma_o$) generated along the plug/rock contact due to the applied axial stress to the plug (σ_{po}) and external stress (σ_o).

E_p/E_R = Young's modulus ratio of plug and rock
z/L = distance along the axially loaded plug.

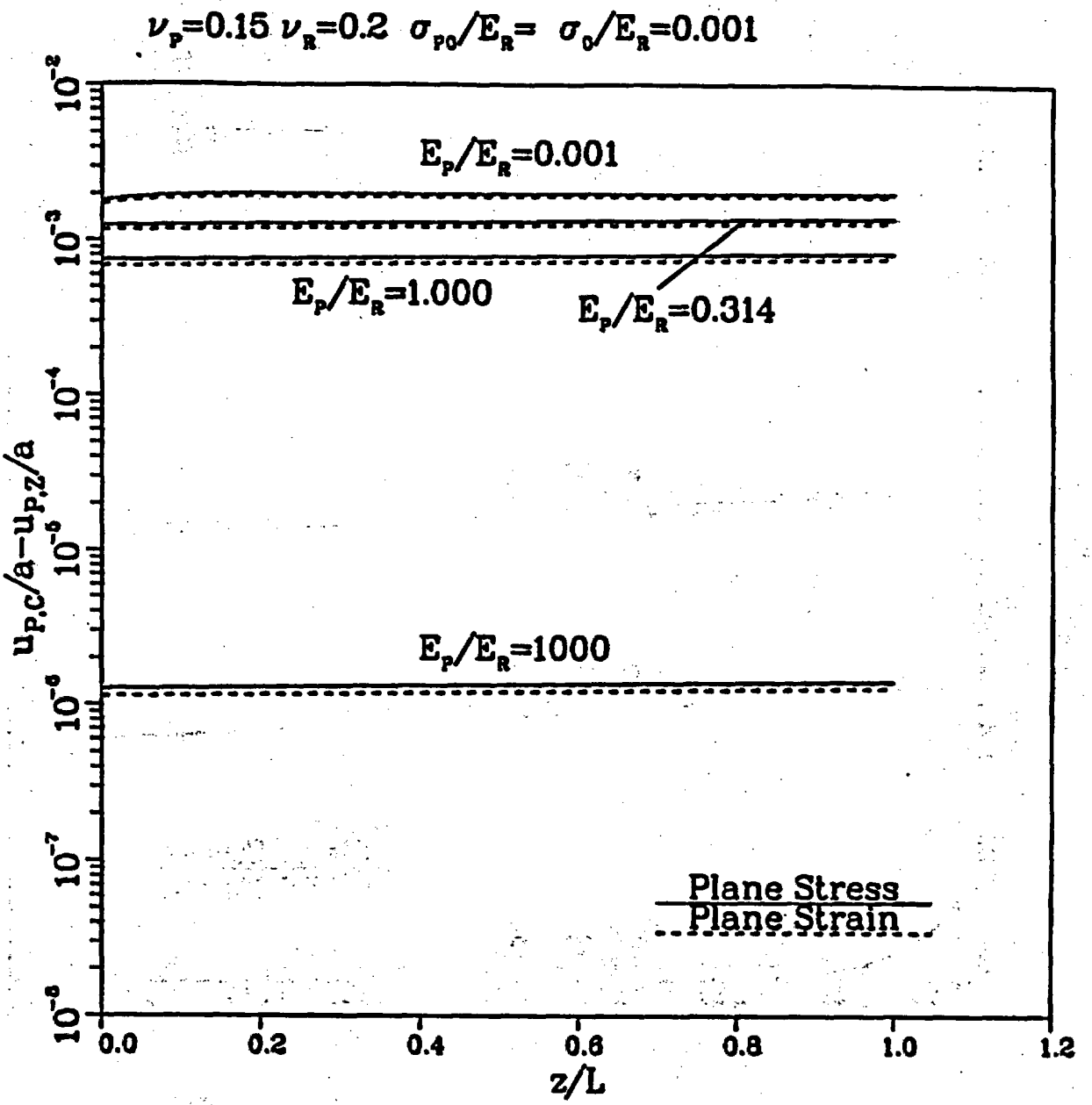

Figure 5.9 Ratio of the (inward) radial plug displacement to the plug radius ($u_{P,C}/a - u_{P,Z}/a$) due to the applied axial stress to the plug (σ_{po}) and external stress (σ_o).

E_P/E_R = Young's modulus ratio of plug and rock
z/L = distance along the axially loaded plug.
Table 5.1 gives definitions of all symbols used.

Table 5.4 The Resultant Radial (normal) Stress at Plug/Rock Contact and Radial (inward) Plug Displacement due to Axial and External Stress. Results are presented (for the case of plane strain) as a function of cylinder radius ratio (R/a), plug-to-rock Young's modulus ratio (E_p/E_R), and distance along an axially loaded borehole plug (z/L). $\nu_R = 0.20$, $\nu_P = 0.15$, $\sigma_{po}/E_R = \sigma_o/E_R = 0.001$. Table 5.1 gives definitions for all symbols used.

Tuff Cylinder Radius Ratio (R/a)	E_p/E_R	Resultant Radial Stress at Plug/Rock Contact $(\sigma_i/\sigma_o + \sigma_r^P/\sigma_{po})$ z = 0	z = L/2	z = L	Resultant (inward) Radial Plug Displacement $u_{P,C}/a - u_{P,Z}/a$ (x 10^6) z = 0	z = L/2	z = L
1.84	1000	1.3601	1.3601	1.36	0.94	1.015	1.09
	1	1.0226	0.9851	0.97	676	751	781
	0.314	0.7015	0.6128	0.60	1326	1503	1529
	0.001	0.1795	0.0034	0.0034	2361	2713	2713
3.0	1000	1.5001	1.5001	1.50	1.06	1.14	1.21
	1	1.0255	0.9835	0.96	681	741	775
	0.314	0.6552	0.5639	0.54	1218	1350	1384
	0.001	0.1789	0.0027	0.0027	1902	2156	2156
6.0	1000	1.5701	1.5701	1.57	1.12	1.20	1.27
	1	1.0313	0.9888	0.96	683	736	772
	0.314	0.6406	0.5534	0.52	1175	1284	1326
	0.001	0.1786	0.0024	0.0024	1751	1972	1972
10.0	1000	1.5901	1.5901	1.59	1.14	1.21	1.30
	1	1.0325	0.9907	0.96	683	734	771
	0.314	0.6317	0.5478	0.51	1167	1278	1315
	0.001	0.1786	0.0024	0.0024	1722	1937	1937

Table 5.4 The Resultant Radial (normal) Stress at Plug/Rock Contact and Radial (inward) Plug Displacement due to Axial and External Stress--Continued

Tuff Cylinder Radius Ratio (R/a)	E_p/E_R	Resultant Radial Stress at Plug/Rock Contact $(\sigma_i/\sigma_o + \sigma_r^p/\sigma_{po})$ z = 0	z = L/2	z = L	Resultant (inward) Radial Plug Displacement $u_{p,c}/a - u_{p,z}/a$ (x 10^6) z = 0	z = L/2	z = L
∞	1000	1.6001	1.6001	1.60	1.14	1.21	1.28
	1	1.0332	0.9966	0.96	683	727	771
	0.314	0.6323	0.5711	0.51	1161	1235	1308
	0.001	0.1786	0.067	0.0024	1705	1839	1917

5.2.5 Normalized Radial Interface Stresses

The ratio of the normal stress along the plug/rock contact to the applied lateral stress for a cylinder with a radius ratio of 6 is only up to 1.39% more than that for a radius ratio of infinity. Therefore, it can be assumed that a radius ratio of 6 represents an in-situ rock mass (i.e. infinite conditions). The curve for a modulus ratio of 0.314 (Figure 5.3 and Table 5.2) represents a push-out specimen. Inspecting this curve shows that a tuff cylinder with a radius ratio of 1.84 (corresponding to a 101.6 mm (4") plug in a 187.3 mm rock cylinder) shows a 16.85% higher σ_i/σ_o than a cylinder with an R/a of infinity, and a 15.25% higher σ_i/σ_o than a cylinder with an R/a of 6.0 (corresponding to a 25.4 mm (1") plug in a 152.4 mm diameter cylinder) (Table 5.2). Hence, cylinders with different radius ratios have different σ_i/σ_o ratios along their plug/rock contacts, which should be normalized to a common cylinder ratio for assessment of size effects.

The interface radial stress due to an applied external stress can be adjusted to a common radius ratio (or common stiffness) as follows:

$$\sigma_{o\ corrected} = I_c \sigma_o \qquad (5.23)$$

where I_c = correction factor =

$$\frac{(\sigma_i/\sigma_o) \text{ acting on the sample with the desired radius ratio}}{(\sigma_i/\sigma_o) \text{ acting on the sample to be adjusted}}$$

σ_o = external stress applied to the sample

$\sigma_{o\ corrected}$ = corrected (normalized) external stress.

The external stress applied to the push-out cylinders can be adjusted to a radius ratio of 6.0 (representing a 1" push-out specimen) by using a correction factor (I_c) of 0.868 for the samples with an R/a of 1.84 (representing a 4" push-out cylinder) and 0.959 for samples with an R/a of 3.0 (representing a 2" push-out cylinder). Adjustment to an infinite radius ratio leads to correction factors (I_c) of 0.986, 0.946 and 0.856, for the 1", 2" and 4" push-out cylinders, respectively (Table 5.2).

The contact (radial) stress due to an applied axial stress (at z/L = 0) for a cylinder with a radius ratio of 6 is only up to 1.39% less than that for a radius ratio of infinity. Inspecting the values for a push-out specimen (i.e. E_p/E_R = 0.314; Table 5.3) shows that a tuff cylinder with R/a = 1.84 (representing a 101.6 mm (4") plug) shows a 20.49% lower σ_r^p/σ_{po} than a cylinder with an R/a of infinity and an

18.82% lower σ_r^p/σ_{po} than a cylinder with an R/a of 6.0 (corresponding to a 25.4 mm (1") push-out specimen).

The interface contact stress due to an axial stress applied on the plug can be adjusted to a common radius ratio (or common stiffness) as follows:

$$\sigma_{po\ corrected} = I_z \sigma_{po} \tag{5.24}$$

where I_z = correction factor =

$$\frac{(\sigma_r^p/\sigma_{po}) \text{ acting on the sample with the desired radius ratio}}{(\sigma_r^p/\sigma_{po}) \text{ acting on the sample to be adjusted}}$$

σ_{po} = axial (compressive) stress applied to the plug

$\sigma_{po\ corrected}$ = corrected (adjusted) axial stress.

The axial stress applied to the plugs of the push-out cylinders can be adjusted to a radius ratio of 6.0 (corresponding to a 25.4 mm push-out cylinder) by using a correction factor of 1.1882 for the samples with an R/a of 1.84 (corresponding to a 101.6 mm push-out cylinder) and 1.0469 for samples with an R/a of 3.0 (corresponding to a 50.8 mm push-out cylinder). Adjustment to an infinite radius ratio leads to correction factors of 1.0141, 1.062 and 1.205 for the 25.4, 50.8 and 101.6 mm cylinders (Table 5.3).

5.3 Push-Out Tests

5.3.1 Introduction

Figure 5.10 shows the push-out test arrangement. A cylindrical steel rod is used to apply an axial load to a cement plug. Daemen et al. (1988b, pp. 109-111; 1988c, Ch. 5) give a detailed description of the test set-up, as well as of sample preparation, storage and curing conditions*. Daemen et al. (1988b, Apps. 5.A and 5.B, pp. 157-177) give the detailed procedures for push-out testing and for determining the water content (w) and degrees of saturation (S) of push-out

*It was originally proposed (e.g. in Daemen et al., 1988b, p. 110) to store the ambient relatively dry samples at 20-45% r.h. (relative humidity) and at 36°C in the environmental chamber. Some ambient relatively dry samples push-out tested within this period are cured and tested in room conditions (24 ± 2°C, 36 ± 2% r.h.). This is done to allow the use of the environmental chamber for partially saturated samples.

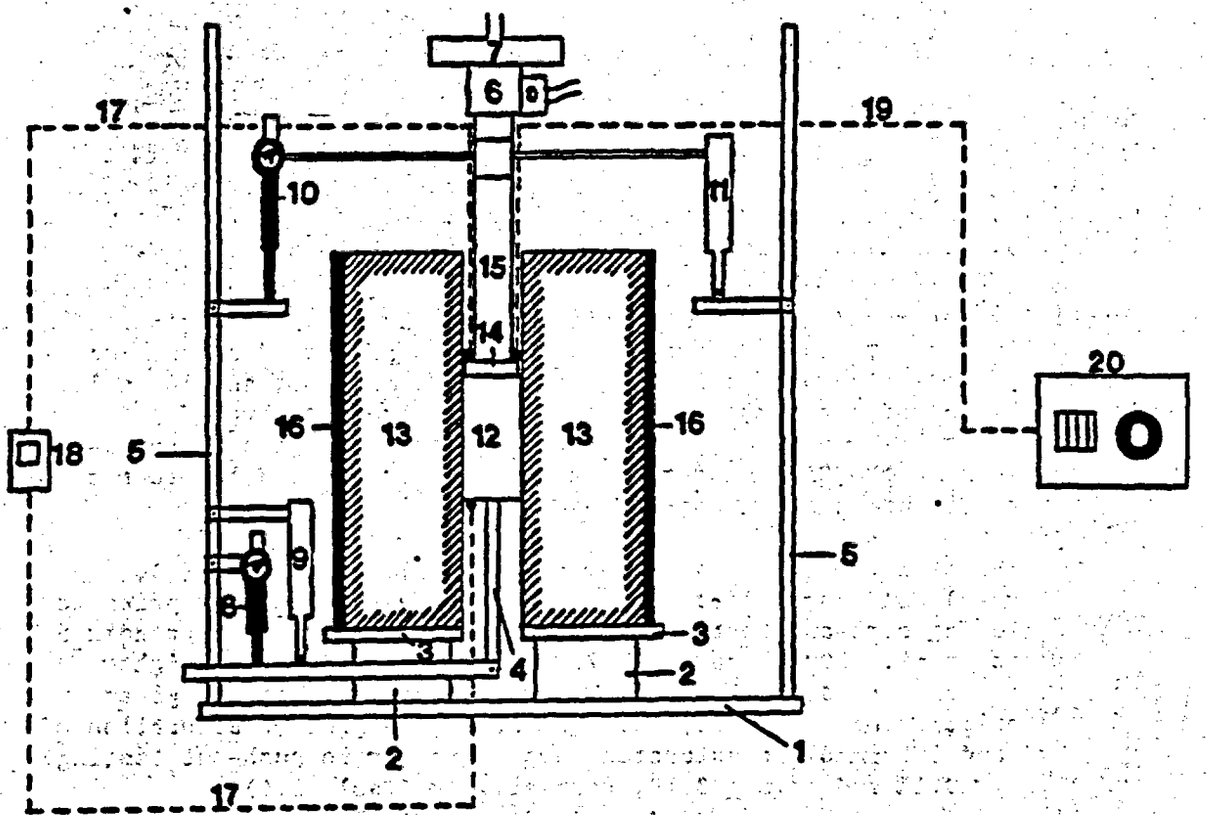

Not to scale

1. Cylindrical steel plate
2. Circular steel plate with a slit
3. Square steel plate
4. Section for bottom displacement transfer
5. Vertical steel bars
6. Load cell
7. Loading platen
8,10. Bottom and top dial gages
9,11. Bottom and top LVDT's
12. Cement plug
13. Rock sample
14. Steel cylinder
15. Axial bar
16. Steel pipe with heating tape wrapped around
17. Thermocouple sensor and wire
18. Digital thermometer
19. Heater probe and wire
20. Heater controller

Figure 5.10 Schematic drawing of push-out test set-up.

specimens. Daemen et al. (1988b, p. 110) gives the procedure for numbering push-out specimens.

5.3.2 Push-Out Test Results and Discussion of Results

Push-out tests have been performed on 16 Apache Leap tuff cylinders. The cylinders have inside diameters of 25.4 mm (1 in), 50.8 mm (2 in) and 101.6 mm (4 in), outside diameters of 152.4 mm (6 in) and 187.3 mm (7.375 in), and lengths ranging from 106.7 mm (4.2 in) to 228.9 mm (9.01 in). The tuff cylinders are plugged with centered Self-Stress II cement plugs having length to diameter ratios of approximately 1.0. The plugged cylinders are cured for eight days at relatively dry or partially saturated conditions. Figure 5.11 gives the dimensions of the cylinders. Three push-out tests have been performed on specimens with 25.4 mm inside diameter (I.D.), 3 on 50.8 mm I.D., and 10 on 101.6 mm I.D. Nine of the samples are cured and tested at elevated temperatures. The 50.8 mm (2 in) inside diameter samples are prepared by over-coring the 25.4 mm samples after they are tested in order to reduce sample preparation requirements.

The degree of saturation (S), water content (w), void ratio (e), porosity (n) and density (ρ) of the Apache Leap tuff samples prior to and following push-out testing are determined according to Appendix 5.B in Daemen et al., 1988b, pp. 166-177. Table 5.5 gives the weight parameters used to determine the above variables. Table 5.6 gives characteristics of each specimen. The average degree of saturation of the low and intermediate saturated samples (prior to push-out testing) is 31.6 $\pm$ 19.1% and 53.8 $\pm$ 3.7%, respectively (Table 5.6).

Table 5.7 presents the axial stress, plug length, and average and exponential shear stresses at failure. The average shear stresses along the interface are calculated from Daemen et al. (1989, p. 103, Eq. (5.1)). The extreme exponential shear stresses are calculated from Daemen et al. (1989, p. 103, Eq. (5.2)). The maximum and minimum exponential shear stresses are the shear stresses at the loaded end ($z = 0$) and at the unloaded end ($z = L_c$) of the plug, respectively.

The plugs fail at axial stress, uniform shear stress, and maximum exponential shear stress ranges of 11.0 to 35.6 MPa, 2.15 to 7.57 MPa, and 11.25 to 21.45 MPa, respectively.

None of the rock cylinders with a 25.4 and 50.80 mm diameter hole split in tension during push-out testing (Table 5.3). Six of the 101.6 mm I.D. cylinders show tensile fracturing and splitting. None of the cylinders that show tensile splitting have fractures running through the cement plugs. This suggests that the failure mechanism is fundamentally different from that induced by cement swelling itself, e.g. as observed by Akgun and Daemen (1986, pp. 39-68). In all probability, the tensile failure of the rock cylinders is due to the lateral strain induced in the cement plug by the axial load, and transferred to the rock cylinder as an internal stress.

Tables 5.8 through 5.10 give the mean axial stress, mean average shear stress, and mean maximum exponential shear stress at failure. The data includes results of the 16 push-out tests performed this quarter

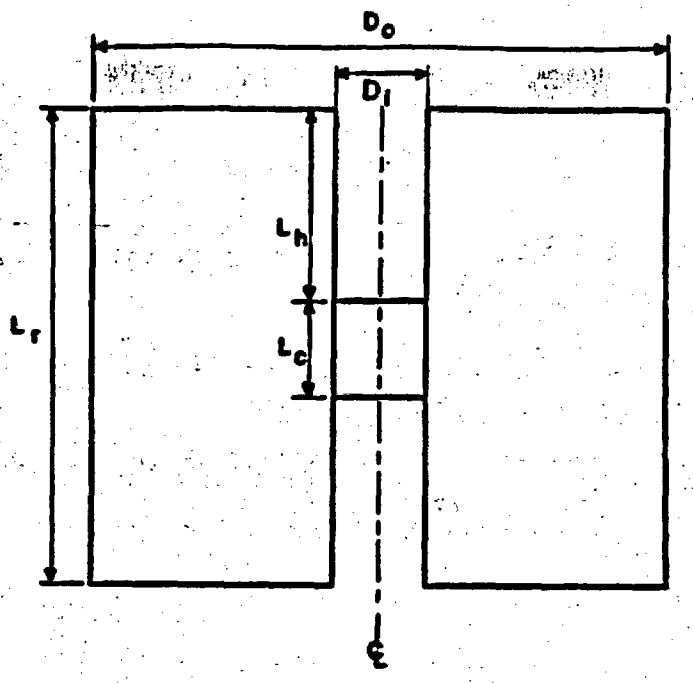

Apache Leap Tuff Specimen	L_r (mm)	L_h (mm)	L_c (mm)
APA5-6-1-AMB-RD-3-PO2-SSII[a]	139.5	66.5	29.7
APA2-6-1-AMB-RD-1-PO1-SSII[a]	132.5	63.8	30.2
APD-6-1-AMB-RD-1-PO3-SSII[a]	129.8	53.9	30.3
APJ-8-4-36-RD-4-PO1-SSII[c]	131.5	13.6	93.9
APA5-6-2-36-RD-4-PO3-SSII[b]	113.0	25.2	50.2
AP113-6-2-36-RD-2-PO1-SSII[b]	130.3	41.5	47.0
APD-6-2-36-RD-2-PO1-SSII[b]	106.7	19.8	53.6
APA6-8-4-36-RD-1-PO2-SSII[c]	118.3	11.3	80.7
API-8-4-36-RD-1-PO1-SSII[c]	168.8	27.2	102.0
APM-8-4-AMB-RD-2-Po1-SSII[c]	170.1	15.8	93.6
APJ-8-4-AMB-PS-3-PO1-SSII[c]	159.0	16.5	99.1
APM-8-4-AMB-PS-6-PO1-SSII[c]	213.2	92.0	97.9
APM-8-4-AMB-RD-1-PO1-SSII[c]	199.0	42.6	97.5
APA-8-4-66-PS-4-PO1-SSII[c]	210.7	40.5	129.5
APM-8-4-66-PS-5-PO1-SSII[c]	198.5	56.3	101.5
APA-8-4-44-PS-5-PO1-SSII[c]	228.9	57.4	103.6

Figure 5.11 Dimensions of the Apache Leap tuff cylinders used for push-out tests.

Figure 5.11 NOTES

NOTES:

[a]Samples with inside diameters (D_i) of 25.4 mm (1 in) and outside diameters (D_o) of 152.4 mm (6 in).

[b]Samples with inside diameters (D_i) of 50.8 mm (2 in) and outside diameters (D_o) of 152.4 mm (6 in).

[c]Samples with inside diameters (D_i) of 101.6 mm (4 in) and outside diameters (D_o) of 187.3 mm (7.375 in).

Figure 5.11 Dimensions of the Apache Leap tuff cylinders used for push-out tests.--Continued

Table 5.5 Weight Parameters of Apache Leap Tuff Specimens Prior to and Following Push-Out Testing. The parameters are used to determine the degree of saturation, water content, void ratio, porosity, and density of push-out specimens. Detailed procedure for the determination of degree of saturation, void ratio, etc., is given in Appendix 5.B of Daemen et al. (1988b).

Apache Leap Tuff Sample	W1[a] (g)	W2[b] (g)	W3[c] (g)	W4[d] (g)	W5[e] (g)
APA5-6-1-AMB-RD-3-P02-SSII	5828	5844	5873	5881	5865
APA2-6-1-AMB-RD-1-P01-SSII	5624	5640	5669	5679	5662
APD-6-1-AMB-RD-1-P03-SSII	5166	5183	5212	5224	5209
APJ-8-4-36-RD-4-P01-SSII	5668	5910	7386	7348	7105
APA5-6-2-36-RD-4-P03-SSII	4289	4364	4557	4576	4501
AP113-6-2-36-RD-2-P01-SSII	4953	5028	5208	5211	5134
APD-6-2-36-RD-2-P01-SSII	3833	3906	4104	4210	4044
APA6-8-4-36-RD-1-P02-SSII	4922	5172	6496	6448	6196
API-8-4-36-RD-1-P01-SSII	7916	8343	9944	9900	9473
APM-8-4-AMB-RD-2-P01-SSII	7334	7762	9250	9244	8815
APJ-8-4-AMB-PS-3-P01-SSII	6883	7309	8858	8927	8499
APM-8-4-AMB-PS-6-P01-SSII	9168	9414	10948	11048	10803
APM-8-4-AMB-RD-1-P01-SSII	8524	8952	10513	10512	10085
APA-8-4-66-PS-4-P01-SSII	8671	9095	10750	10898	10453
APM-8-4-66-PS-5-P01-SSII	8540	8961	10558	10654	10229
APA-8-4-44-PS-5-P01-SSII	9553	9978	11613	11753	11325

Table 5.5 NOTES

NOTES:

[a] W1 = weight of the dry specimen (g)

[b] W2 = weight of the dry specimen + rubber stopper + moisture (g)

[c] W3 = W2 + weight of the cement slurry (g)

[d] W4 = weight of the specimen after it has been left underwater or in the environmental chamber (at desired temperature and relative humidity) or at room conditions (24 ± 2°C, 36 ± 2% r.h.) for 8 days

[e] W5 = weight of the specimen following push-out testing.

Table 5.6 The Degree of Saturation, Water Content, Void Ratio, Porosity, and Density of Apache Leap Tuff Specimens Prior to and Following Push-Out Testing. Detailed procedure for the determination of the degree of saturation, water content, etc., is given in Appendix 5.B of Daemen et al. (1988b).

Apache Leap Tuff Sample	S_p^1 (%)	S_f^1 (%)	w_p^2 (%)	w_f^2 (%)	e_p^3 (%)	e_f^3 (%)	n_p^4 (%)	n_f^4 (%)	ρ_p^5 (g/cc)	ρ_f^5 (g/cc)
APA5-6-1-AMB-RD-3-P02-SSII	6.78	6.78	0.29	0.29	0.11	0.11	10.1	10.1	2.36	2.36
APA2-6-1-AMB-RD-1-P01-SSII	9.35	8.85	0.34	0.32	0.09	0.09	8.6	8.6	2.40	2.39
APD-6-1-AMB-RD-1-P03-SSII	6.95	6.95	0.44	0.44	0.17	0.17	14.3	14.3	2.25	2.25
APJ-8-4-36-RD-4-P01-SSII	49.83	49.59	6.40	6.37	0.34	0.34	25.6	25.6	2.19	2.12
APA5-6-2-36-RD-4-P03-SSII	31.65	31.65	1.79	1.79	0.15	0.15	12.9	12.9	2.36	2.32
AP113-6-2-36-RD-2-P01-SSII	22.14	21.03	1.18	1.12	0.14	0.14	12.3	12.3	2.36	2.32
APD-6-2-36-RD-2-P01-SSII	23.98	23.06	1.96	1.88	0.21	0.21	17.6	17.6	2.24	2.20
APA6-8-4-36-RD-1-P02-SSII	44.14	43.65	6.36	6.29	0.39	0.39	27.8	27.8	2.14	2.05
API-8-4-36-RD-1-P01-SSII	60.99	60.58	5.12	5.09	0.22	0.22	18.3	18.3	2.39	2.29
APM-8-4-AMB-RD-2-P01-SSII	47.43	47.33	5.52	5.51	0.31	0.31	23.7	23.7	2.25	2.14
APJ-8-4-AMB-PS-3-P01-SSII	58.78	58.46	7.02	6.99	0.32	0.32	24.2	24.2	2.27	2.16
APM-8-4-AMB-PS-6-P01-SSII	52.46	52.01	5.75	5.71	0.29	0.29	22.5	22.5	2.22	2.17
APM-8-4-AMB-RD-1-P01-SSII	44.67	44.49	5.13	5.11	0.30	0.30	23.4	23.4	2.23	2.14
APA-8-4-66-PS-4-P01-SSII	51.34	49.64	6.84	6.61	0.35	0.35	26.1	26.1	2.18	2.09
APM-8-4-66-PS-5-P01-SSII	56.30	55.83	6.22	6.17	0.29	0.29	22.7	22.7	2.27	2.18
APA-8-4-44-PS-5-P01-SSII	49.93	49.62	6.14	6.10	0.33	0.33	24.6	24.6	2.20	2.12

Table 5.6 NOTES

NOTES:

[1] S_p and S_f: degree of saturation of push-out specimen prior to and following push-out test, respectively.

[2] w_p and w_f: water content of push-out specimen prior to and following push-out test, respectively.

[3] e_p and e_f: void ratio of push-out specimen prior to and following push-out test, respectively.

[4] n_p and n_f: porosity of push-out specimen prior to and following push-out test, respectively.

[5] ρ_p and ρ_f: density of push-out specimen prior to and following push-out test, respectively.

Table 5.7 Axial Stress at Failure, Plug Length, and Average and Exponential Extreme Shear Stresses at Failure for Apache Leap Tuff Samples. The maximum exponential shear stress occurs at the loaded end ($z = 0$) of the cement plug. The minimum exponential shear stress occurs at the bottom ($z = L_c$) of the cement plug.

Apache Leap Tuff Specimen	Axial Stress ($\sigma^{p}_{z,f}$) at Failure (MPa)	Plug Length (L_c) (mm)	Average* Interface Shear Stress ($\tau^{av}_{rz,i}$) at Failure (MPa)	Exponential** Extreme Shear Stress ($\tau_{rz,i}$) at Failure (MPa) $z = 0$	$z = L_c$
APA5-6-1-AMB-RD-3-PO2-SSII	35.5	29.7	7.57	21.36	2.59
APA2-6-1-AMB-RD-1-PO1-SSII	35.1	30.2	7.38	21.13	2.45
APD-6-1-AMB-RD-1-PO3-SSII	35.6	30.3	7.47	21.45	2.47
APJ-8-4-36-RD-4-PO1-SSII[a]	15.5	93.9	4.19	15.88	0.72
APA5-6-2-36-RD-4-PO3-SSII	24.4	50.2	6.16	18.70	1.82
AP113-6-2-36-RD-2-PO1-SSII	22.0	47.0	5.95	16.95	2.00
APD-6-2-36-RD-2-PO1-SSII	21.8	53.6	5.16	16.72	1.32
APA6-8-4-36-RD-1-PO2-SSII[b]	11.0	80.7	3.45	11.29	0.87
API-8-4-36-RD-1-PO1-SSII[a]	15.1	102.0	3.76	15.48	0.50
APM-8-4-AMB-RD-2-PO1-SSII[a]	13.7	93.6	3.72	14.08	0.64
APJ-8-4-AMB-PS-3-PO1-SSII	19.2	99.1	4.92	19.70	0.72
APM-8-4-AMB-PS-6-PO1-SSII	16.7	97.9	4.34	17.17	0.66

Table 5.7 Axial Stress at Failure, Plug Length, and Average and Exponential Extreme Shear Stresses at Failure for Apache Leap Tuff Samples.--Continued

Apache Leap Tuff Specimen	Axial Stress ($\sigma^{P}_{z,f}$) at Failure (MPa)	Plug Length (L_c) (mm)	Average* Interface Shear Stress ($\tau^{av}_{rz,i}$) at Failure (MPa)	Exponential** Extreme Shear Stress ($\tau_{rz,i}$) at Failure (MPa)	
				$z = 0$	$z = L_c$
APM-8-4-36-RD-1-PO1-SSII	14.5	97.5	3.79	14.92	0.58
APA-8-4-66-PS-4-PO1-SSII[a]	11.0	129.5	2.15	11.25	0.12
APM-8-4-66-PS-5-PO1-SSII	13.3	101.5	3.32	13.62	0.45
APA-8-4-44-PS-5-PO1-SSII[a]	20.6	103.6	5.05	21.11	0.65

NOTES:

*Calculated from Daemen et al. (1989, p. 103, eq. (5.1)).

**Calculated from Daemen et al. (1989, p. 103, eq. (5.2)) for the case of plane strain.

[a]Sample shows tensile fracturing (following push-out testing).

[b]Sample shows tensile splitting (following push-out testing).

Table 5.8 Axial Stress at Failure on Cement Plugs in Apache Leap Tuff Cylinders. In parentheses are given the number of samples tested. Data for the 16 push-out tests performed in this quarter, combined with the 85 push-out tests reported previously (Daemen et al, 1988b,c; 1989).

Apache Leap Tuff Specimen		Mean Axial Stress ($\bar{\sigma}^{P}_{z,f}$) at Failure ± St. Dev. (MPa)		
	Curing and	Specimen I.D.		
Saturation	Test Temp.	25.4 mm	50.8 mm	101.6 mm
Highly saturated	Ambient*	35.2 ± 4.4 (6)	22.7 ± 5.5 (3)	14.9 ± 1.7 (3)
	45°C	41.3 ± 4.0 (5)	21.7 ± 5.9 (3)	16.2 ± 1.3 (3)
	70°C	29.5 ± 5.1 (4)	21.6 ± 4.3 (3)	13.1 ± 3.7 (3)
	90°C	13.3 ± 4.1 (3)	10.2 ± 3.4 (4)	6.5 ± 2.1 (3)
Partially saturated	Ambient*	34.6 ± 6.4 (7)	26.4 ± 8.1 (5)	11.9 ± 4.4 (3)
	44°C	45.3 ± 9.4 (5)	20.1 ± 3.9 (4)	14.8 ± 5.1 (3)
	65-70°C	40.9 ± 10.9 (3)	24.3 ± 6.0 (3)	12.9 ± 1.7 (3)
Relatively dry	Ambient**	35.4 ± 0.3 (3)	26.3 ± 4.4 (3)	14.6 ± 0.9 (3)
	36°C	27 ± 6.7 (7)	22.7 ± 1.5 (3)	13.9 ± 2.5 (3)

*Ambient = 24 ± 2°C

**Samples cured at room conditions (i.e. not in environmental chamber) at 24 ± 2°C, 36 ± 2% r.h.

Table 5.9 Bond Strengths of Cement Plugs in Apache Leap Tuff Cylinders. Numbers in parentheses are the number of tests. Data for the 16 tests performed this quarter, combined with the 85 tests performed previously (Daemen et al, 1988b,c; 1989).

Apache Leap Tuff Specimen		Mean Average Shear Stress ($\bar{\tau}^{av}_{rz,i}$) at Failure ± St. Dev. (MPa)		
		Specimen I.D.		
Saturation	Curing and Test Temp.	25.4 mm	50.8 mm	101.6 mm
Highly saturated	Ambient*	7.3 ± 1.0 (6)	6.3 ± 1.9 (3)	3.9 ± 0.7 (3)
	45°C	8.6 ± 0.9 (5)	6.5 ± 2.1 (3)	4.3 ± 0.6 (3)
	70°C	6.6 ± 1.2 (4)	5.6 ± 0.9 (3)	3.3 ± 0.9 (3)
	90°C	3.7 ± 0.7 (3)	2.7 ± 1.0 (4)	1.6 ± 0.4 (3)
Partially saturated	Ambient*	7.6 ± 1.0 (7)	6.6 ± 2.0 (5)	3.8 ± 1.6 (3)
	44°C	9.3 ± 2.4 (5)	5.2 ± 0.7 (4)	3.7 ± 1.2 (3)
	65-70°C	8.5 ± 2.5 (3)	6.0 ± 1.2 (3)	3.0 ± 0.8 (3)
Relatively dry	Ambient**	7.5 ± 0.1 (3)	6.6 ± 1.1 (3)	3.8 ± 0.1 (3)
	36°C	5.6 ± 1.2 (7)	5.4 ± 0.5 (3)	3.8 ± 0.4 (3)

*Ambient = 24 ± 2°C

**Samples cured at room conditions (i.e. not in environmental chamber) at 24 ± 2°C, 36 ± 2% r.h.

Table 5.10 Mean Maximum Exponential Shear Stress at Failure along Cement-Rock Interface for Apache Leap Tuff Push-out Tests. In parentheses are given the number of tests. Data for the 16 tests performed this period, combined with the 85 tests performed previously (Daemen et al, 1988b,c; 1989).

Apache Leap Tuff Specimen		Mean Maximum Exponential Shear Stress at Failure $(\overline{\tau^{max}_{rz,i}})$ ± St. Dev. (MPa)		
		Specimen I.D.		
Saturation	Curing and Test Temp.	25.4 mm	50.8 mm	101.6 mm
Highly saturated	Ambient*	22.6 ± 3.5 (6)	18.0 ± 4.1 (3)	15.0 ± 1.7 (3)
	45°C	28.1 ± 2.7 (5)	16.9 ± 4.4 (3)	16.3 ± 1.2 (3)
	70°C	19.6 ± 4.2 (4)	12.1 ± 1.7 (3)	13.1 ± 3.6 (3)
	90°C	10.7 ± 2.2 (3)	7.8 ± 2.7 (4)	6.5 ± 2.1 (3)
Partially saturated	Ambient*	21.6 ± 3.5 (7)	21.5 ± 7.9 (5)	15.0 ± 6.2 (3)
	44°C	27.2 ± 5.7 (5)	15.4 ± 3.0 (4)	15.1 ± 5.4 (3)
	65-70°C	24.6 ± 6.5 (3)	18.6 ± 4.5 (3)	13.1 ± 1.6 (3)
Relatively dry	Ambient**	21.3 ± 0.2 (3)	20.2 ± 3.4 (3)	14.9 ± 0.8 (3)
	36°C	16.2 ± 4.0 (7)	15.5 ± 1.1 (3)	14.2 ± 2.5 (3)

*Ambient = 24 ± 2°C

**Samples cured at room conditions (i.e. not in environmental chamber) at 24 ± 2°C, 36 ± 2% r.h.

combined with the 85 push-out tests performed in previous quarters (Daemen et al., 1988b,c; 1989). The bond strength of the 25.4, 50.8 and 101.6 mm most highly saturated samples show a moderate increase in going from ambient temperature (24 ± 2°C) to 45°C and then a substantial decrease from 45°C to 90°C (Table 5.9). There is no discernible difference between the bond strengths of highly and intermediately saturated samples. The axial stress at failure and bond strength decrease with increasing plug diameter.

The relatively dry 25.4 mm samples cured and tested at 36°C show lower mean strength than the more saturated samples (Tables 5.8 through 5.10). This parallels conclusions from previous studies (e.g. Daemen et al., 1985, pp. 338-360; Adisoma and Daemen, 1988). A common observation in these previous studies is that if the push-out samples are allowed to dry out, their cement plugs show significant shrinkage and drastic strength reduction after moderately long periods of time (e.g. more than 2 years). The relatively dry 50.8 and 101.6 mm samples cured and tested at ambient conditions (24 ± 2°C, 36 ± 2% r.h.) show comparable strength measures to the more saturated samples (Tables 5.8 through 5.10). This is most probably because these samples are cured and tested at room conditions (24 ± 2°C, 36 ± 2% r.h.) with a film of water in their top boreholes during the initial 3 to 5 days of cement curing. The relatively dry samples tested in the environmental chamber at 36°C, 45% r.h. have their free water (on the top specimen boreholes) evaporated within one day after the samples are placed in the environmental chamber. This might be the reason for the relatively dry samples cured in the environmental chamber giving lower strength measures than those cured in room conditions (Tables 5.8 through 5.10).

5.4 Summary

This chapter analyzes the influence of cylinder stiffness on the plug/rock interface normal stress during push-out tests. Increasing normal contact stress presumably increases the shear strength of the interface. The normal stress along the plug/rock contact due to an applied lateral stress increases with increasing modulus ratio, increasing cylinder radius ratio (for modulus ratios greater than 1.0; the opposite is observed on cylinders with modulus ratios less than 1.0), and with increasing Poisson's ratio of the plug. The (inward) radial displacement due to an external radial compressive stress decreases with increasing modulus ratio and is inversely proportional to the normal stress developed along the plug/rock interface.

The normal stress at the plug/rock contact due to an axial stress applied to the plug increases with increasing cylinder radius ratio and decreasing modulus ratio. The (outward) radial displacement due to an axial stress is directly proportional to the normal stress developed along the plug/rock contact.

The bond strength of the 25.4, 50.8 and 101.6 mm highly saturated samples show a moderate increase in going from ambient temperature to 45°C and then show a substantial decrease from 45 to 90°C. The partially and highly saturated samples show comparable bond strengths. The relatively dry samples cured and tested at 36°C show lower mean

bond strength than the highly saturated samples. The axial stress at failure and bond strength decrease with increasing plug diameter.

5.5 References

Adisoma, G. and J.J.K. Daemen, 1988, "Experimental Assessment of the Influence of Dynamic Loading on the Permeability of Wet and of Dried Cement Borehole Seals," NUREG/CR-5129, prepared for Division of Engineering, Office of Nuclear Regulatory Research, U.S. Nuclear Regulatory Commission, by the Department of Mining and Geological Engineering, University of Arizona, Tucson.

Akgun, H. and J.J.K. Daemen, 1986, "Size Influence on the Sealing Performance of Cementitious Borehole Plugs," NUREG/CR-4738, prepared for Division of Engineering Safety, Office of Nuclear Regulatory Research, U.S. Nuclear Regulatory Commission, by the Department of Mining and Geological Engineering, University of Arizona, Tucson.

Binnall, E.P., S.M. Benson, L. Tsao, H.A. Wollenberg, T.K. Takunaga, and E.B. Didwall, 1987, "Critical Parameters for a High-Level Waste Repository, Vol. 2: Tuff," NUREG/CR-4161, prepared for the U.S. Nuclear Regulatory Commission, Division of Engineering, Office of Nuclear Regulatory Research, by the Lawrence Livermore National Laboratory, P.O. Box 808, Livermore, CA.

Daemen, J.J.K., J.C. Stormont, N.I. Colburn, D.L. South, S.A. Dischler K. Fuenkajorn, W.B. Greer, G.S. Adisoma, D.E. Miles, B. Kousari, and J. Bertuca, 1983, "Annual Report, Rock Mass Sealing, June 1, 1982 - May 31, 1983," NUREG/CR-3473, prepared for the U.S. Nuclear Regulatory Commission, Office of Nuclear Regulatory Research, Division of Health, Siting and Waste Management, by the Department of Mining and Geological Engineering, University of Arizona, Tucson.

Daemen, J.J.K., W.B. Greer, G.S. Adisoma, K. Fuenkajorn, W.D. Sawyer, Jr., A. Yazdandoost, H. Akgun, and B. Kousari, 1985, "Annual Report, Rock Mass Sealing, June 1, 1983 - May 31, 1984," NUREG/CR-4174, prepared for the U.S. Nuclear Regulatory Commission, Office of Nuclear Regulatory Research, Division of Radiation Programs and Earth Sciences, by the Department of Mining and Geological Engineering, University of Arizona, Tucson.

Daemen, J.J.K., K. Fuenkajorn, S. Ouyang, and H. Akgun, 1988a, "Sealing of Boreholes and Shafts in Tuff: Quarterly Progress Report, March 1 - May 31, 1988," Contract NRC-04-86-113, prepared for the U.S. Nuclear Regulatory Commission, Office of Nuclear Regulatory Research, Division of Engineering, by the Department of Mining and Geological Engineering, University of Arizona, Tucson.

Daemen, J.J.K., K. Fuenkajorn, S. Ouyang, H. Akgun and R. Armstrong, 1988b, "Sealing of Boreholes and Shafts in Tuff: Quarterly Progress Report, June 1 - August 31, 1988," Contract NRC-04-86-113, prepared for the U.S. Nuclear Regulatory Commission, Office of Nuclear Regulatory Research, Division of Engineering, by the Department of Mining and Geological Engineering, University of Arizona, Tucson.

Daemen, J.J.K., K. Fuenkajorn, S. Ouyang, H. Akgun and R. Armstrong, 1988c, "Sealing of Boreholes and Shafts in Tuff: Quarterly Progress Report, Sept. 1 - Nov. 30, 1988," Contract NRC-04-86-113, prepared for the U.S. Nuclear Regulatory Commission, Office of Nuclear Regulatory Research, Division of Engineering, by the Department of Mining and Geological Engineering, University of Arizona, Tucson.

Daemen, J.J.K., K. Fuenkajorn, S. Ouyang, H. Akgun, R. Armstrong, D.R. Crouthamel, and C.J. Sharpe, 1989, "Sealing of Boreholes and Shafts in Tuff: Quarterly Progress Report, Dec. 1, 1988 - Feb. 28, 1989," Contract NRC-04-86-113, prepared for the U.S. Nuclear Regulatory Commission, Office of Nuclear Regulatory Research, Division of Engineering, by the Department of Mining and Geological Engineering, University of Arizona, Tucson.

Jaeger, J.C. and N.G.W. Cook, 1979, Fundamentals of Rock Mechanics, Third Edition, Chapman and Hall, London, John Wiley & Sons, Inc., N.Y.

Jeffrey, R.G. and J.J.K. Daemen, 1980, "Shaft and Borehole Plug-Rock Mechanical Interaction," Topical Report to the U.S. Nuclear Regulatory Commission, Contract No. NRC-04-78-271, by the Department of Mining and Geological Engineering, University of Arizona, Tucson.

Stormont, J.C. and J.J.K. Daemen, 1983, "Axial Strength of Cement Plugs in Granite and Basalt," NUREG/CR-3594, prepared for the U.S. Nuclear Regulatory Commission, Office of Nuclear Regulatory Research, Division of Health, Siting, and Waste Management, by the Department of Mining and Geological Engineering, University of Arizona, Tucson.

CHAPTER SIX

FRACTURE SEALING

6.1 Introduction

Fractures in the rock mass surrounding a repository may provide preferential flowpaths for the inflow of groundwater and for the outflow of air, potentially containing gaseous radionuclides. In order to reduce their permeability, such cracks may have to be sealed. The likelihood that extensive or at least local grouting will be required as part of repository sealing has been noted in numerous publications addressing high level waste repository closing (e.g. Koplick et al., 1979; Kelsall et al., 1983, 1985a,b,c). The most explicit and detailed use of fracture grouting for repository sealing probably is given in the conceptual seal designs for the Nevada Nuclear Waste Storage Investigations Project (Fernandez and Freshley, 1984; Fernandez, 1985).

The objective of the work described in this chapter is to determine the effectiveness of fracture sealing (grouting) in welded tuff. Daemen et al. (1988a, Ch. 6) give the detailed work plan and test schedule. Apache Leap tuff (brown unit), A-Mountain tuff and Topopah Springs tuff have been used for preparing rock samples. Daemen et al. (1988b, Ch. 6) describe sample preparation and test procedure.

Experimental work includes measurement of permeability of intact rock and of fractures under ranges of normal stresses and injection pressures, determination and characterization of fracture roughness, injection of grout into the fractures, and testing the permeability of grouted fractures. The effectiveness of grouting is evaluated in terms of the permeability reduction resulting from fracture grouting. Analysis of the results includes study of the effects of normal stress, injection pressure, fracture roughness and grout formulations on sealing effectiveness.

6.2 Permeability of Tuff Cylinders

In this quarterly period the permeability of intact tuff sample AP7-1-6-FG4 and the permeability of a tension-induced fracture (sample AP30-1-6-FG11) have been measured.

The permeability of sample AP7-1-6-FG4 ranged from 1×10^{-7} to 3×10^{-10} cm/s. This sample developed a vertical tension crack under 5 MPa normal stress and 3 MPa injection pressure. At this point the flow increased dramatically. Measurements made earlier on intact Apache Leap tuff samples showed values of around 1×10^{-9} cm/s. Figure 6.1 shows the effect of normal stress on permeability. The greatest reduction in flow occurs at low normal stress. Sample FG4 was tested using a pressure intensifier instead of a failing head permeameter due to the low flow rate.

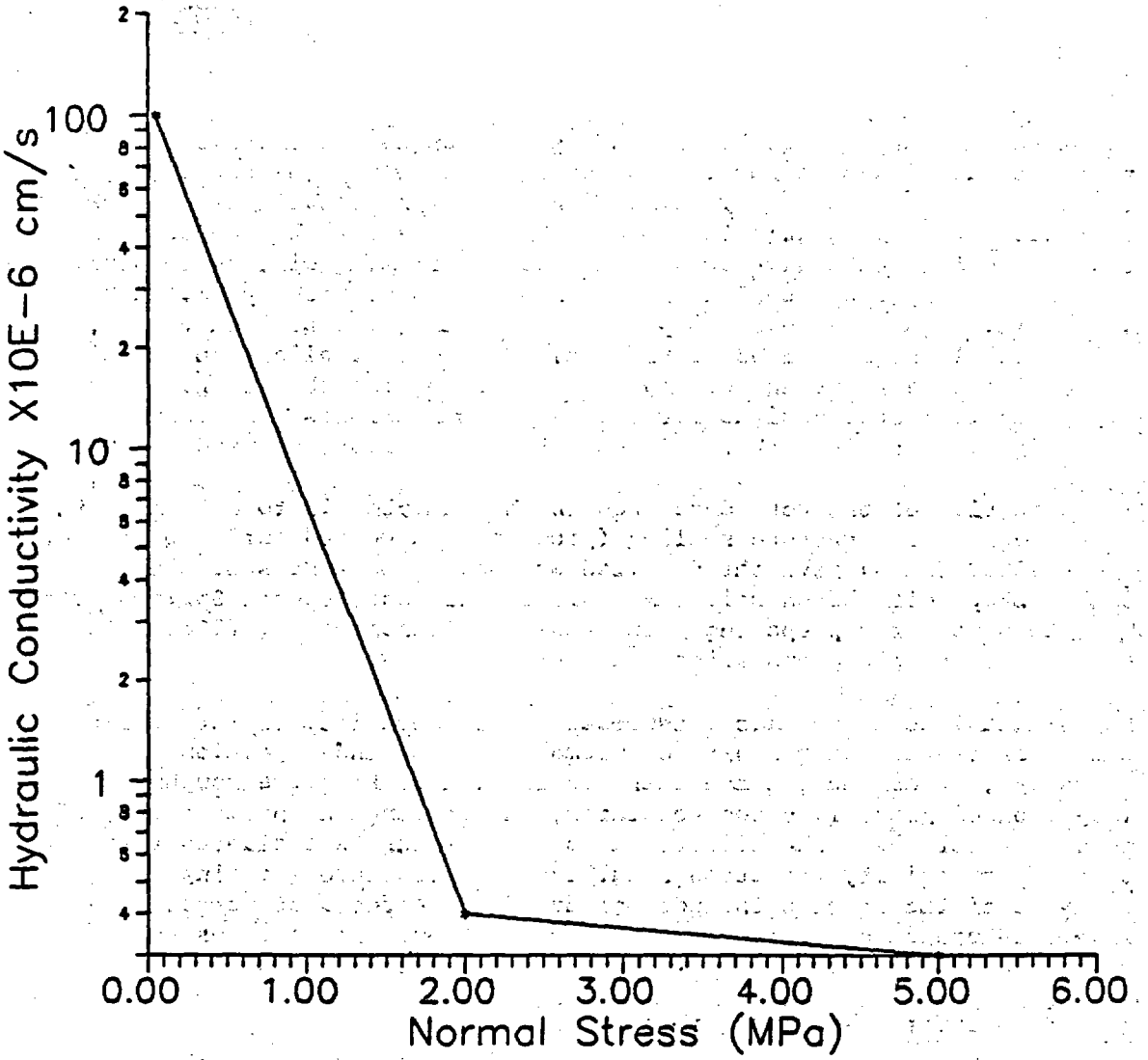

Figure 6.1 Hydraulic conductivity of intact welded tuff sample AP7-1-6-FC4 as a function of normal stress. Each data point represents the average of at least two test runs for each normal stress.

A gas-over-water pressure intensifier (Fuenkajorn and Daemen, 1986, Appendix C) supplies a steady-state flow to the sample at a specified injection pressure. The volume of water injected along with the injection time and pressure are used to calculate the permeability. Due to problems encountered in testing sample FG4, injection pressures will be limited to 0.1 to 1.0 MPa. Flow tests are continued at each normal stress until a uniform flow rate is achieved. The water level around the outside of the sample is always kept above the fracture.

Fracture permeability testing of sample FG11 was accomplished using a falling head permeameter. Results show permeabilities of around 2 x 10^{-4} cm/s at 10 MPa, which compares well with testing of sample AP21-3-6-FG1 (Daemen et al., 1989, p. 133). Permeabilities are measured under normal stresses of 0.05, 2, 5, 8, and 10 MPa. The sample is loaded, unloaded and reloaded without interrupting the flow. Figure 6.2 shows the permeability reduction with normal stress and the ultimately resulting hysteresis. This reduction in flow is presumably due to fracture deformation and some reduction due to the closing of pore spaces and preexisting microfractures as the sample is first loaded. Schaffer and Daemen (1987, p. 91) report similar behavior. A slight irreversible decrease in permeability occurs after the first loading/unloading cycle. The very small magnitude of the residual permeability change suggests that only very limited permanent deformation of asperities occurs.

Figure 6.3 shows the calculated fracture aperture as a function of normal stress. Daemen et al. (1988a, Ch. 6, App. 6.A) give the test method and method of calculation. Identifying the width of the aperture is of key importance in selecting appropriate grouting parameters such as injection pressure, grout viscosity, and grout constituents.

6.3 Characterization of Grout Formulations

Prior to fracture grouting, grout formulations must be characterized to help choose suitable components that will perform adequately given certain fundamental parameters such as viscosity, injection pressure, aperture, maximum particle size, and strength.

An ideal grout would have the viscosity of water and the strength of concrete, not to mention being impermeable, durable, and nontoxic. No such products are available, making it necessary to select key parameters such as a water-to-solids ratio that will provide "pumpability" of the cementitious slurry along with a viscosity that will suspend the heavier particles to allow a more homogeneous mixture to be emplaced throughout the fracture. Increasing the viscosity of a slurry by lowering the water-to-solids ratio is desirable to achieve adequate strength and impermeability up to the point where the thickest consistency is found that will penetrate cracks at given pressures (Kennedy, 1958, p. 1731-1). Grouts with high viscosities are harder to pump, requiring higher pressures and pumping time (Herndon et al., 1976, pp. 20-23). Cement grouts with low viscosities may promote finger-like flows along paths of least resistance and little penetration into finer interconnecting fractures and larger rock pores. This is presumably due to the grouts' lack of body.

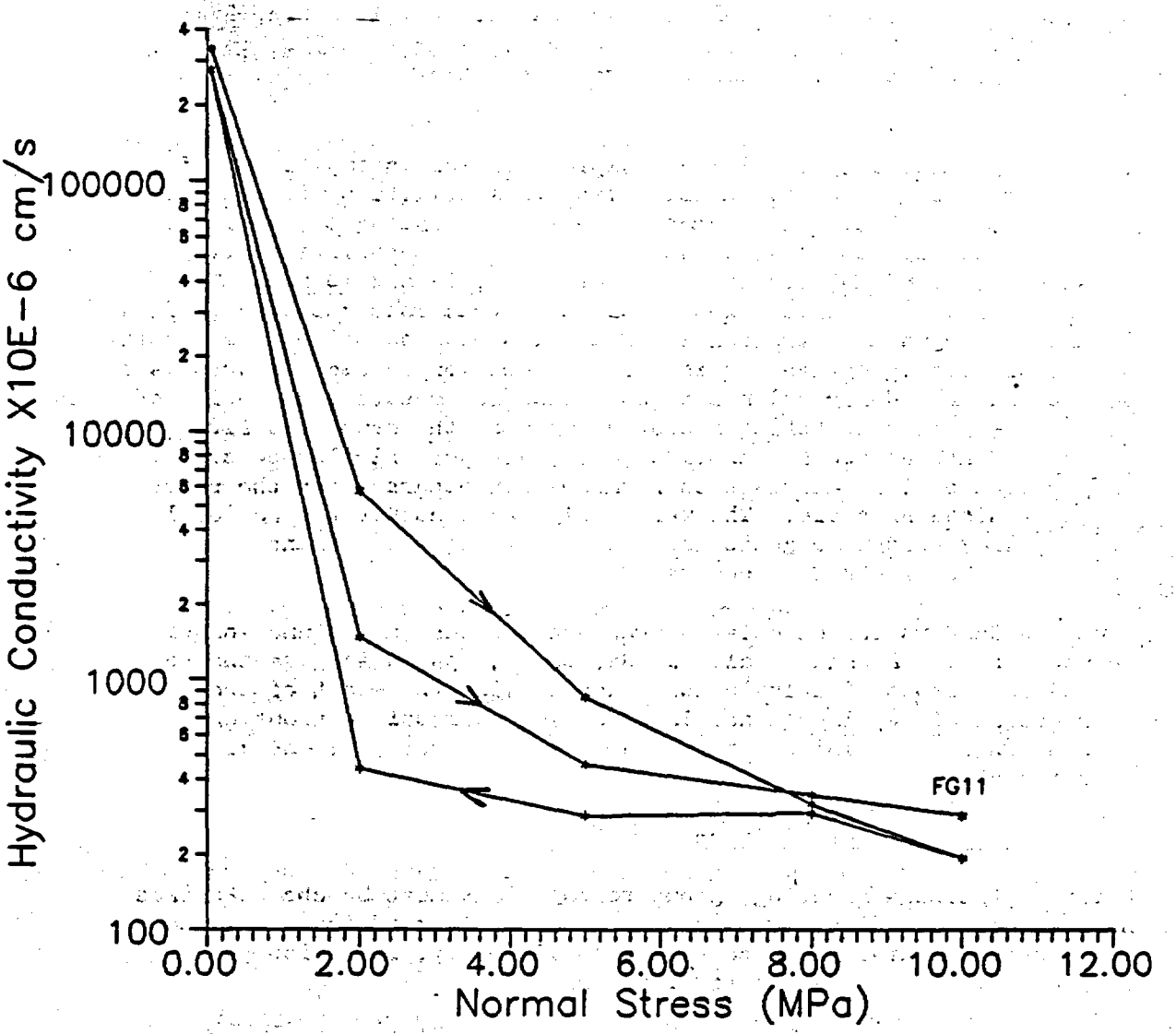

Figure 6.2 Hydraulic conductivity of tension-induced fracture as a function of normal stress for Apache Leap tuff sample AP30-1-6-FG11. Each data point represents the average of at least four test runs for each normal stress. Arrows indicate the loading, unloading and reloading sequence.

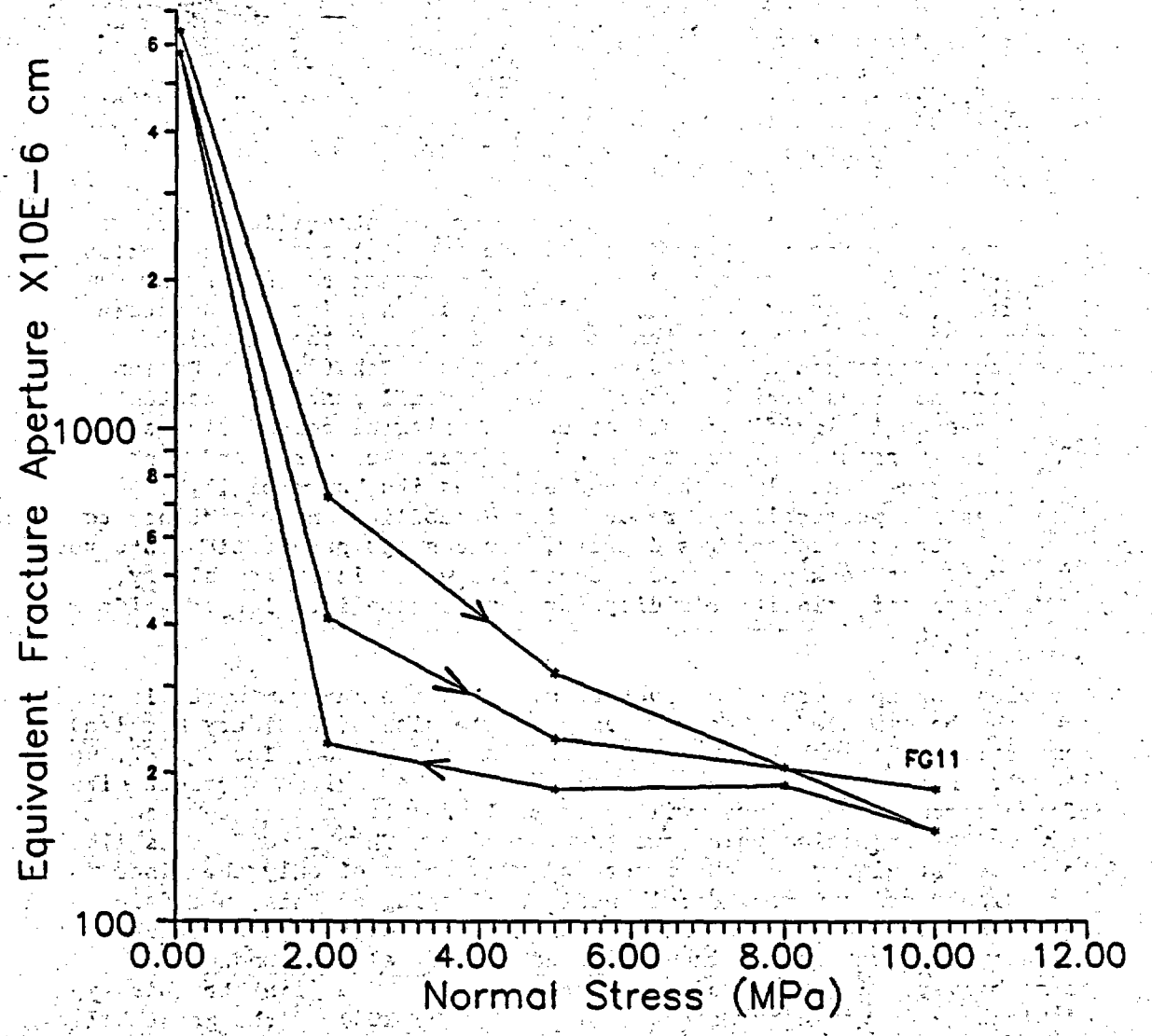

Figure 6.3 Fracture aperture as a function of normal stress for Apache Leap tuff sample AP30-1-6-FG11. Each data point represents the average of at least four test runs for each normal stress. The sample is loaded, unloaded and reloaded.

The water content of cementitious grouts must be limited in order for the slurry to be termed stable and have the potential to achieve its full strength. A slurry is termed stable if it bleeds less than 5% in two hours (Shannon and Wilson, Inc., 1987, pp. 14-15). Bleed capacity is obtained by dividing the water loss by the initial slurry volume. A measure of viscosity and stability referenced by Cambeford (1977, p. 64) is the Marsh flow cone. The time required for a fixed volume of slurry to pass through the cone is measured. A stable grout will pass through in 35 to 40 seconds. Excessive bleed water not only indicates instability, but may also stifle bonding of the grout on the upper surface of a fracture (Kennedy, 1958).

Bentonite, a colloidal additive prepared from montmorillonite clays reduces bleed water and therefore increases stability. Flocculation of bentonite in a water-cement slurry prevents sedimentation of the cement particles (Schaffer and Daemen, 1987, p. 41). A major disadvantage reported by Deere (1982) is that bentonite reduces the uniaxial compressive strength of a hardened grout mix. Schaffer and Daemen reference numerous articles stating that a small bentonite content (2-3%) has an insignificant effect on the uniaxial compressive strength of the cured grout. Bentonite in cement decreases early and final strength, gives the slurry body and enhances its "pumpability", decreases its permeability, reduces its durability and resistance to chemical attack, reduces its density, reduces its penetration into very small voids or rock pores, and reduces its water loss from slurry, which helps maintain its fluidity for penetration into larger voids (Smith, 1976).

The width or aperture of a fracture dictates the maximum particle size that can be emplaced. The maximum particle size of ordinary Portland cement is 0.004 inch (0.00016 mm) (Shannon and Wilson, Inc., 1987, pp. 14-15). Fractures with apertures less than the maximum particle size of the cementitious slurry will presumably result in an interface between the injection point and the fracture. This interface is likely to cause "straining" of the grout and admittance of only the finer ingredients or even more detrimental, a clogging of this interface zone. A fracture that is clogged at this port will show a reduced permeability that is not indicative of the actual surrounding permeability. A measure of the susceptibility of a joint to this type of blockage is given by Mitchell (1970, pp. 73-109) as the groutability ratio, which is defined as the aperture divided by the maximum particle size. For successful grouting the groutability ratio should be greater than three. High injection pressures can dilate a fracture and allow greater particle sizes to be admitted. Injection pressures greater than the in-situ normal stresses on the fracture can cause hydraulic fracturing, ground heaving and crack propagation resulting in greater hydraulic conductivity.

The cement used in this experiment is Self-Stress II (SSII) cement composed of Ideal Type I/II Portland cement provided by Dowell Schlumberger. 1% D65 (a dispersant) and 10% D53 (an expansive agent) have been added to the SSII cement at the factory. American Colloid C/S granular bentonite is added in amounts ranging from 2 to 5% in respect to the weight of cement. Mixing is performed according to the

API specification No. 10 (American Petroleum Institute, 1986, pp. 14-19) with two modifications: bentonite is added to 15% of the water to be used and allowed to hydrate two hours prior to blending (Deere, 1982), and blending is done for one additional minute to aid in mixing (Daemen et al., 1988a, App. 2.A).

Four grout formulations have been selected. Mix number 1 has a water-to-solids (w/s) ratio of 0.45 with 2% bentonite by weight of cement. Mix number 2 has a w/s ratio of 0.55 with 3% bentonite. Mix 3 has a w/s ratio of 0.65 with 5% bentonite. Mix number 4 has a w/s ratio of 0.45 consisting completely of SSII cement. Water-to-solids ratios have been chosen to provide stable mixes and to achieve adequate grout penetration. Density, viscosity, bleed capacity, strength, and permeability are measured in the laboratory.

6.4 Characterization of Fracture Surfaces

Fracture surfaces are characterized by their roughness or height of asperities, surface waviness, orientation, aperture, and contact area or flow paths of high resistance. In terms of groutability, rough surfaces substantially increase the minimum water-cement ratio needed to allow flow (Schaffer and Daemen, p. 51). Shannon and Wilson state (1987, p. 14-15) that fracture roughness has a significant influence on the radius of penetration of the grout due primarily to the increased travel distance required by the grout's tortuous path and the associated pressure drop.

Welded tuff samples have fractures perpendicular to the applied stress and generally are planar. Fracture apertures are calculated from the measured permeabilities, because the apertures of these tight fractures are hard to measure directly. The roughness and contact areas are measured with a profilometer. Profiles of a surface are obtained by trolleying a probe assembly along a pair of horizontal steel rods and lowering the probe to contact the sample according to a specified sample interval (Farrington, 1983). A profile record is generated by a data acquisition system and reduced to provide profiles of both surfaces that may be overlayed to produce the difference between matched grids and aperture distributions.

6.5 References

American Petroleum Institute, 1986, Specifications for Materials and Testing for Well Cements, 3rd Edition, American Petroleum Institute, Productions Dept., Dallas, TX.

Cambeford, H., 1977, "The Principles and Applications of Grouting," Q. Jl. Engrg. Geol., Vol. 10, p. 57-95.

Daemen, J.J.K., K. Fuenkajorn, S. Ouyang, H. Akgun, and R. Armstrong, 1988a, "Sealing of Boreholes and Shafts in Tuff: Quarterly Progress Report, June 1 - August 31, 1988," Contract NRC-04-86-113, prepared for the U.S. Nuclear Regulatory Commission, by the Department of Mining and Geological Engineering, University of Arizona, Tucson.

Daemen, J.J.K., K. Fuenkajorn, S. Ouyang, H. Akgun, and R. Armstrong, 1988b, "Sealing of Boreholes and Shafts in Tuff: Quarterly Progress Report, Sept. 1 - Nov. 30, 1988," Contract NRC-04-86-113, prepared for the U.S. Nuclear Regulatory Commission, by the Department of Mining and Geological Engineering, University of Arizona, Tucson.

Daemen, J.J.K., K. Fuenkajorn, S. Ouyang, H. Akgun, R. Armstrong, D.S. Crouthamel, and C.J. Sharpe, 1989, "Sealing of Boreholes and Shafts in Tuff: Quarterly Progress Report, Dec. 1, 1988 - Feb. 28, 1989," Contract NRC-04-86-113, prepared for the U.S. Nuclear Regulatory Commission, by the Department of Mining and Geological Engineering, University of Arizona, Tucson.

Deere, D.U., 1982, "Cement-Bentonite Grouting for Dams," Grouting in Geotechnical Engineering, W.H. Baker, ed., Proceedings of the Conference on Feb. 10-12, New Orleans, LA, pp. 279-300. Published by American Society of Civil Engineers, New York.

Farrington, J.J., 1984, "On the Characterization of Rock Joint Roughness," Master's Thesis, University of Colorado at Boulder.

Fernandez, J.A., 1985, "Repository Sealing Plan for the Nevada Nuclear Waste Storage Investigations Project Fiscal Years 1984 Through 1990," Sandia Report SAND 84-0910. Prepared by Sandia National Laboratories, Albuquerque, New Mexico 87185.

Fernandez, J.A. and M.D. Freshley, 1984, "Repository Sealing Concepts for the Nevada Nuclear Waste Storage Investigations Project," SAND 83-1778. Prepared by Sandia National Laboratories, Albuquerque, New Mexico 87185.

Fuenkajorn, K. and J.J.K. Daemen, 1986, "Experimental Assessment of Borehole Wall Drilling Damage in Basaltic Rocks," NUREG/CR-4541, prepared for the U.S. Nuclear Regulatory Commission, by the Department of Mining and Geological Engineering, University of Arizona, Tucson.

Herndon, J. and T. Lenahan, 1976, "Grouting in Soils, Vol. 2. Design and Operations Manual," prepared for Federal Highway Administration, by Haliburton Services, Duncan, OK.

Kelsall, P.C., W.E. Coons, and D. Meyer, 1983, "Repository Sealing Program Plan: Repository in Salt," ONWI-414, prepared by D'Appolonia Consulting Engineers, Inc., for Office of Nuclear Waste Isolation, Battelle Memorial Institute, Columbus, Ohio.

Kelsall, P.C., J.B. Case, D. Meyer, J.G. Franzone, and W.E. Coons, 1985a, "Schematic Designs for Penetration Seals for a Repository in Richton Dome," BMI/ONWI-562, prepared by IT Corporation for Office of Nuclear Waste Isolation, Battelle Memorial Institute, Columbus, Ohio. December.

Kelsall, P.C., D. Meyer, J.B. Case, and W.E. Coons, 1985b, "Schematic Designs for Penetration Seals for a Repository in the Paradox Basin," BMI/ONWI-563, prepared by IT Corporation for Office of Nuclear Waste Isolation, Battelle Memorial Institute, Columbus, Ohio. December.

Kelsall, P.C., J.B. Case, W.E. Coons, J.G. Franzone, and D. Meyer, 1985c, "Schematic Designs for Penetration Seals for a Repository in the Permian Basin," BMI/ONWI-564, prepared by IT Corporation for Office of Nuclear Waste Isolation, Battelle Memorial Institute, Columbus, Ohio. December.

Kennedy, T.B., 1958, "Pressure Grouting Fine Fissures," Paper 1731 in Journal of Soil Mechanics and Foundations Division, Proceedings of the American Society of Civil Engineers, Vol. 84, No. SM 3, August.

Koplick, C.M., D.L. Pentz, and R. Talbot, 1979, "Information Base for Waste Repository Design, Vol. 7, Executive Summary," NUREG/CR-0495. Prepared for U.S. Nuclear Regulatory Commission, Division of Waste Management, Office of Nuclear Material Safety and Safeguards, by the Analytical Sciences Corporation, Reading, Massachusetts, NTIS: PB 293407.

Mitchell, J.K., 1970, "In-Place Treatment of Foundation Soils," Journal of Soil Mechanics and Foundation Division, ASCE, Vol. 1, January, pp. 73-109, New York.

Schaffer, A. and J.J.K. Daemen, 1987, "Experimental Assessment of the Sealing Effectiveness of Rock Fracture Grouting," NUREG/CR-4541, prepared for the U.S. Nuclear Regulatory Commission, by the Department of Mining and Geological Engineering, University of Arizona, Tucson.

Shannon and Wilson, Inc., 1987, "Cement Grout Flow Behavior in Fractured Rock," for the Bureau of Reclamation, Denver, CO, and the Army Corps of Engineers, Omaha, NE.

Smith, D.K., 1976, Cementing, American Institute of Mining, Metallurgical and Petroleum Engineers, Inc., 2nd Printing, 184 pp.

CHAPTER SEVEN

BOREHOLE STABILITY TESTING

7.1 Introduction

The stability of boreholes, or more generally of underground openings (i.e. including shafts, ramps, drifts, etc.) at locations where seals are to be emplaced is an integral part of sealing design. Excessive deformations of the rock mass surrounding seals could negate the effectiveness of seals. Two aspects of concern in this regard are the effect of seal swelling on the surrounding rock and the effect of compressive stress fields and the stress concentrations that result around a borehole. The stability and deformation of boreholes in tuff will be studied by means of internal and external pressurization tests.

7.2 Borehole Deformation and Stability Tests: External Loading

The purpose of this section is to evaluate the stability and deformation of a circular hole in a tuff specimen subjected to various external boundary load conditions. The experimental work involves polyaxial, uniaxial and triaxial borehole stability tests. The applied differential stresses and confining pressures are selected to represent approximately the most severe stress conditions likely at the Yucca Mountain repository site. Daemen et al. (1988a, Ch. 7, pp. 40-42) give the work plan and test sequence. Daemen et al. (1988b, Section 4.2, Appendices 7.A, 7.B and 7.C) give sample specifications and test procedures. Preliminary testing was performed to evaluate the strain gage installation and to maximize the information obtained from each sample, given the expensive and time-consuming sample preparation and gage installation. The load was held constant at each step just long enough to take readings on each of eight channels, about 15 seconds. After taking measurements at the highest stress, the stress was reduced to zero and readings taken. This allows measurement of residual strain in the sample, as well as of the unloading stiffness of the sample. Topopah Springs tuff was used for preparing the polyaxial samples. As before, no samples have experienced failure under stresses specified in the work plan. Overstressing, as compared to the in-situ stress state, will be required in order to induce failure.

7.3 Experimental Results

Two polyaxial borehole stability samples, TPS-PX1 and TPS-PX2, of Topopah Spring tuff have been prepared for testing. Preliminary testing has been performed on TPS-PX1. The sample was tested in uniaxial and biaxial stress normal to the hole axis (Figure 7.1). Table 7.1 gives the X and/or Y stress and strain measurements for lateral (circumferential) and axial (longitudinal) gages at four locations around the borehole (Figure 7.1). Readings were taken at five stresses, which are in the range of stresses scheduled in the workplan, cited above. No failure occurred at maximum stresses used in

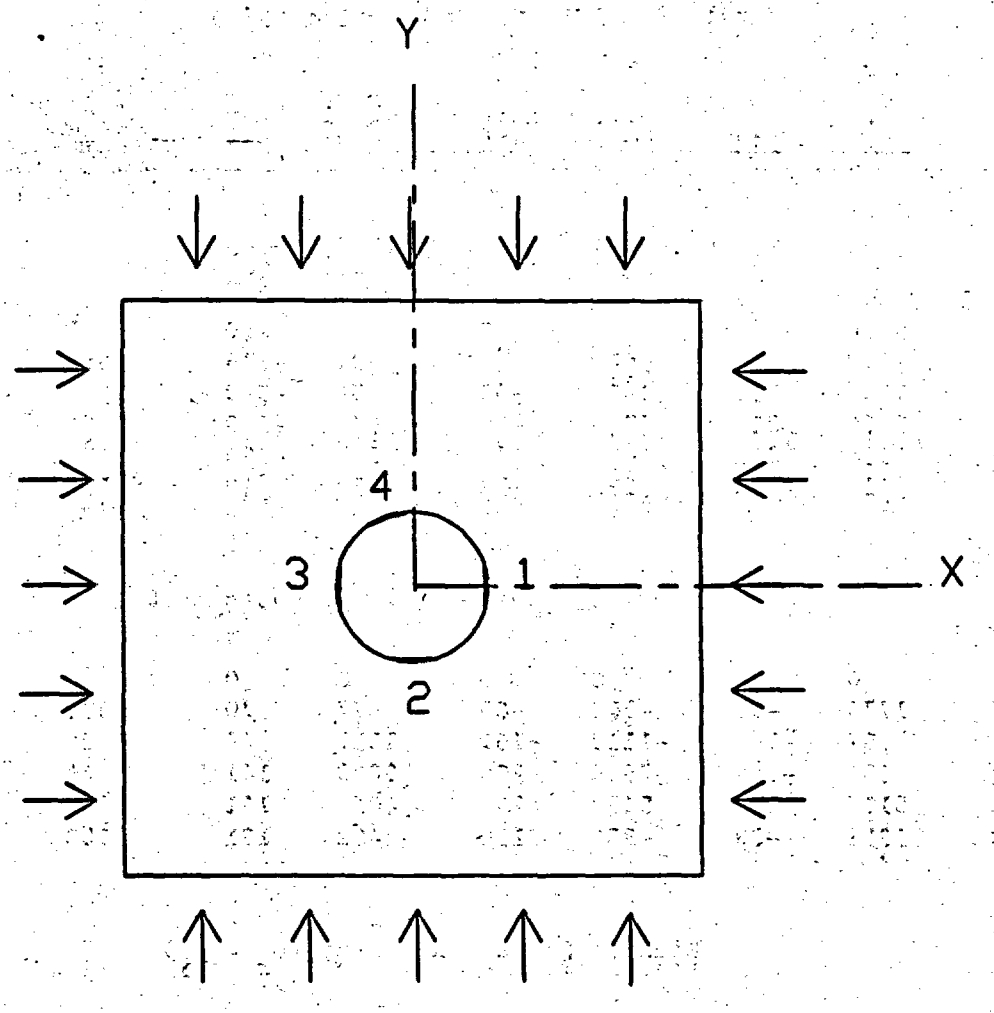

Figure 7.1 Orientation and location of strain gages with respect to loading direction (x and y). 1, 2, 3 and 4 represent strain gages. 10 x 10 x 20 cm block sample with 25 mm diameter coaxial hole.

Table 7.1 Results of Biaxial Borehole Deformation and Stability Tests: Sample TPS-PX1 (Topopah Spring Tuff)

	Strain (microstrains)							
	1LAT*	1AX	2LAT	2AX	3LAT	3AX	4LAT	4AX
σ_x (MPa)	Uniaxial State - X Direction ($\sigma_y = 0$)							
0.00	0	0	0	0	0	0	0	0
4.83	-398	-119	669	8	-391	-146	589	-33
10.00	-1003	-305	1404	-43	-954	-349	1208	-110
15.17	-2489	310	2943	-29	-634	-269	2506	-126
19.99	-4145	361	4081	-48	-587	-394	3422	-163
0.00	413	395	221	12	-152	19	231	-16
σ_y (MPa)	Uniaxial State - Y Direction ($\sigma_x = 0$)							
0.00	0	0	0	0	0	0	0	0
4.83	1775	-98	-502	-83	877	70	-380	-40
10.00	2667	-144	-1118	-161	1617	68	-625	-95
15.17	4081	-155	-7545	-298	3008	141	46	-70
19.99	5117	-180	-5482	-268	4053	161	137	-86
0.00	1251	-88	-386	150	482	131	-108	19
σ_x, σ_y (MPa)	Biaxial State - XY Plane ($\sigma_x = \sigma_y$)							
0.00	0	0	0	0	0	0	0	0
4.83	385	-107	-1853	-114	202	-48	472	-60
10.00	765	-202	-2429	-200	499	-117	876	-134
15.17	1123	-288	-2838	-279	815	-183	1256	-195
19.99	1443	-368	-3181	-352	1095	-250	1586	-249

*1,2,3,4 = strain gage number (Figure 7.1)
LAT = measured lateral strain
AX = measured axial strain

the preliminary testing. Figures 7.2 through 7.4 give the lateral strains as a function of applied stress. The strains show considerable inconsistency, e.g. lack of symmetry. Possible causes for the inconsistencies are under investigation.

7.4 References

Daemen, J.J.K., K. Fuenkajorn, S. Ouyang, and H. Akgun, 1988a, "Sealing of Boreholes and Shafts in Tuff: Quarterly Progress Report, March 1 - May 31, 1988," Contract NRC-04-86-113, prepared for the U.S. Nuclear Regulatory Commission, Office of Nuclear Regulatory Research, Division of Engineering, by the Department of Mining and Geological Engineering, University of Arizona, Tucson.

Daemen, J.J.K., K. Fuenkajorn, S. Ouyang, H. Akgun, and R. Armstrong, 1988b, "Sealing of Boreholes and Shafts in Tuff: Quarterly Progress Report, June 1 - Aug. 31, 1988," Contract NRC-04-86-113, prepared for the U.S. Nuclear Regulatory Commission, Office of Nuclear Regulatory Research, Division of Engineering, by the Department of Mining and Geological Engineering, University of Arizona, Tucson.

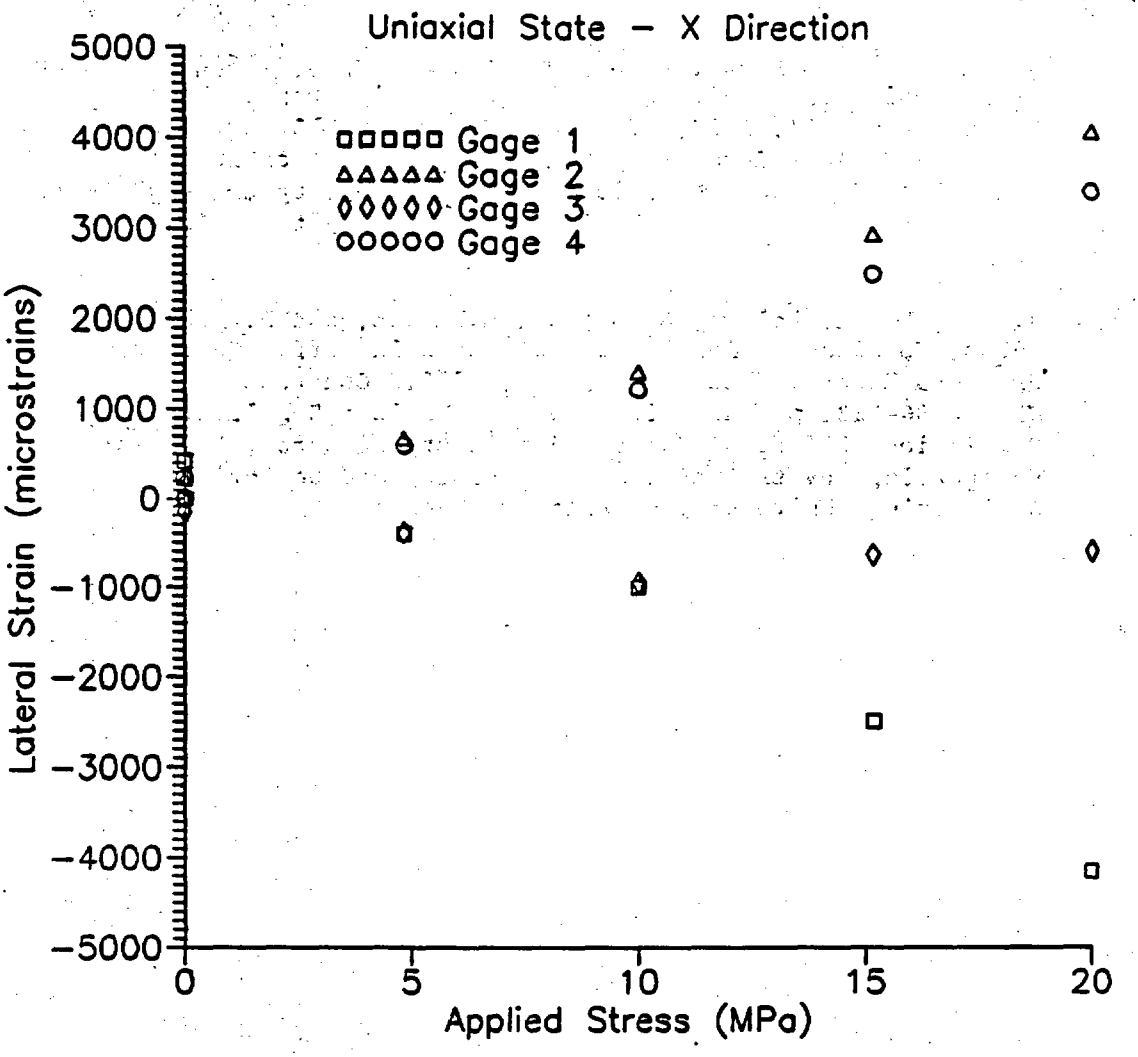

Figure 7.2 Results of sample TPS-PX1, $\sigma_y = 0$, σ_x increases from 0 to 20 MPa. Lateral strain as a function of applied stress (σ_x).

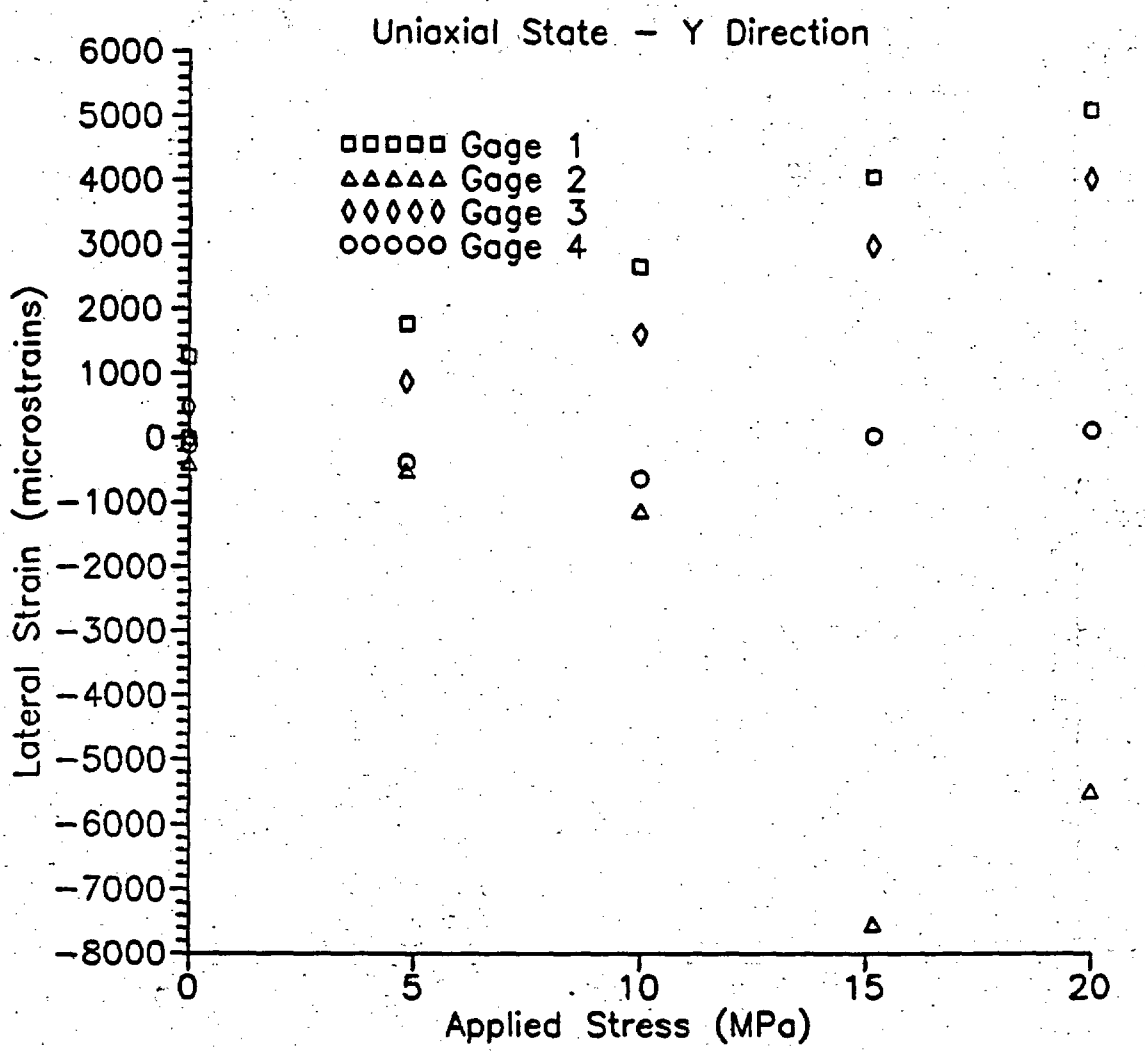

Figure 7.3 Results of sample TPS-PX1, $\sigma_y = 0$, σ_x increases from 0 to 20 MPa. Lateral strain as a function of applied stress (σ_y).

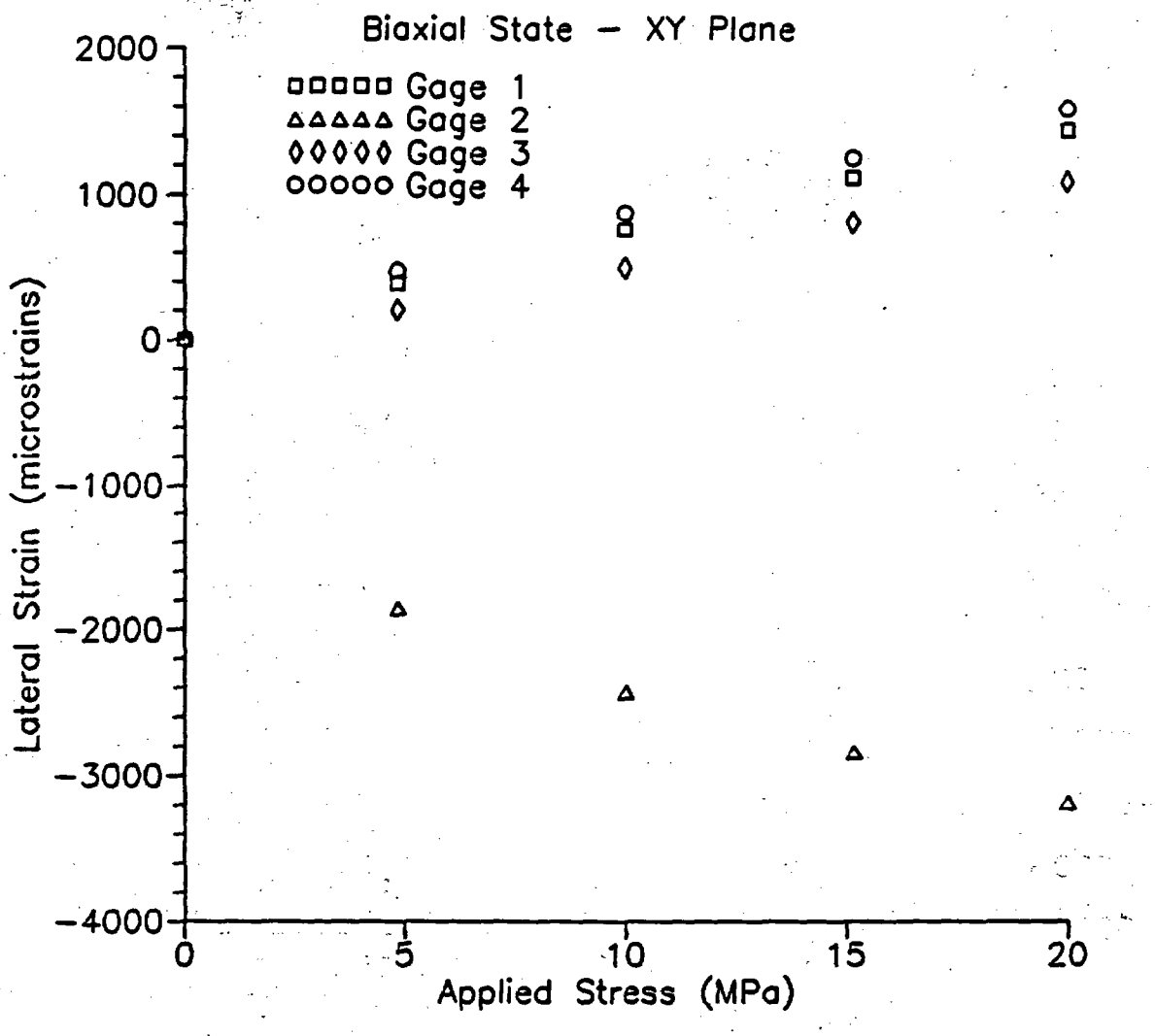

Figure 7.4 Uniform lateral stress ($\sigma_x = \sigma_y$). Lateral strains as a function of applied stress.

CHAPTER EIGHT

FIELD TESTING

8.1 Introduction

The purpose of field testing is to assess the performance of borehole plugs under in-situ conditions, in particular as affected by field emplacement. The tests will be conducted in Apache Leap tuff, near Superior, Arizona. Evans (1983) and Vogt (1988) describe the geology of the area and the rock. The sealing materials to be considered for in-situ testing are cement, bentonite and bentonite/crushed tuff mixtures. Rock from the field site has been collected for laboratory testing.

This chapter describes drilling of three vertical holes, in-situ rock permeability obtained from packer testing, and method to test the plug installation.

8.2 Packer Testing of Inclined Holes

Constant pressure (steady-state flow) and falling head packer tests using a straddle packer system were conducted on the inclined holes of all three sites to aid in locating the vertical boreholes and plugs and to obtain an estimate of the hydraulic conductivity of the rock. Analysis of the tests is in terms of hydraulic conductivity calculated using Darcy's law, based on the assumption of a homogeneous, isotropic porous medium.

8.2.1 Test Method

Both the constant pressure injection tests and the falling head tests use straddle packers to isolate a borehole test interval (Figure 8.1). The test interval is fixed at 37 cm between the upper and lower packer assembly and is lowered to the depth at which the interval to be tested will be isolated when the packers are inflated. The lower packer is inflated to the desired pressure and allowed sufficient time (about 10 minutes) to equilibrate. Water is then piped down the borehole to fill the interval to be tested. The upper packer is then inflated to the desired pressure and allowed to equilibrate. Some excess water is introduced into the interval before upper packer inflation. As the packer inflates, this water is forced up the open injection line under pressure.

If the test interval consists of relatively intact rock, the injection pressure will stabilize, allowing use of the steady-state injection system. If fractures are present in the test interval, allowing water to quickly flow out of the test interval, the falling head system is implemented to measure the hydraulic conductivity of the interval.

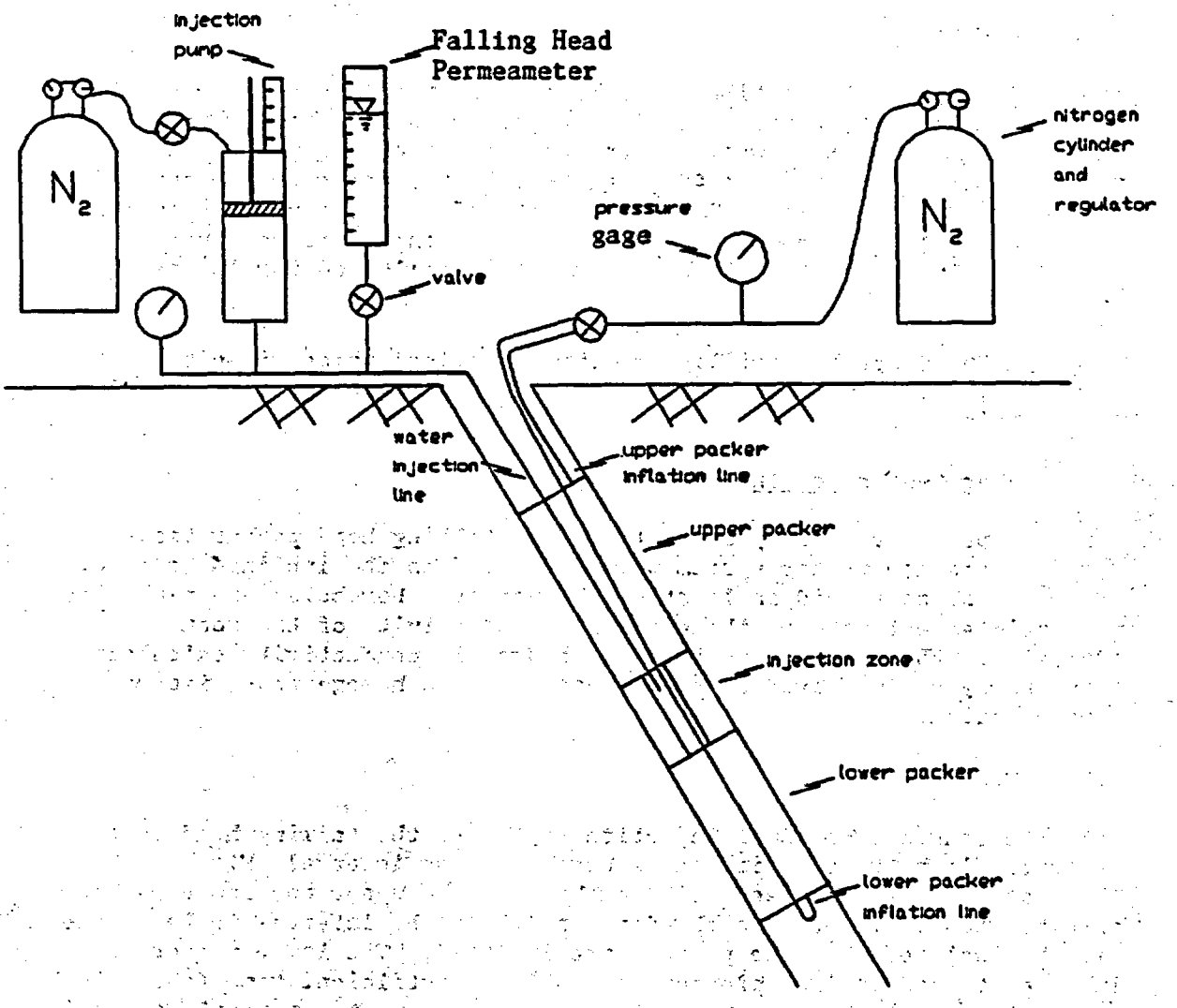

Figure 8.1 Straddle packer system used to measure rock permeability around inclined holes. The system allows both steady-state flow (constant injection pressure) and falling head permeameter tests to be performed.

The packers are inflated to pressures from 0.7 to 1.4 MPa. Injection pressures range from 0.14 to 0.56 MPa. To prevent leakage at the packer and borehole interface, the injection pressure is always kept lower than half the packer pressure. Test duration for each interval ranges from 20 to 50 minutes. The amount of water flow (either by constant pressure or by falling head) is recorded every 30 seconds. For each interval, the test is terminated after a constant flow rate has been observed.

The permeability of the rock is calculated by assuming that the flow into the rock around the hole is laminar, all connective voids are filled with water, and that Darcy's law is valid. For steady-state flow tests, the hydraulic conductivity (k) of the test interval is calculated using an equation modified from Bear (1979, pp. 305-306):

$$k = \frac{Q \ln(R_o/R_i)}{2\pi L_H \Delta h} \quad \text{(cm/s)} \qquad (8.1)$$

where Q = flow rate in cm^3/s
R_i = radius of the borehole in cm (= 2.86 cm)
R_o radius of the saturated test zone in cm (assumed to equal $2L_H$)
L_H = length of the test interval in cm (= 37 cm)
Δh = applied water head in cm.

For falling head tests, the hydraulic conductivity (k) of the rock is calculated from an equation derived from Bear (1979, pp. 305-306) and Freeze and Cherry (1979, p. 336):

$$k = \frac{a \ln(R_o/R_i) \ln(h_o/h_i)}{2\pi L_H (t_i - t_o)} \quad \text{(cm/s)} \qquad (8.2)$$

where a = cross-sectional area of the falling head permeameter (= 5.03 cm^2)
R_o = radius of the saturated test zone in cm (assumed to equal $2L_H$)
R_i = radius of the borehole in cm (= 2.86 cm)
L_H = length of the test interval in cm (= 37 cm)
$t_i - t_o$ = time between readings
h_o = initial height of water from the tank to the center of test interval at time t_o
h_i = height of water from the tank to the center of the test interval at time t_i

8.2.2 Test Results

Figures 8.2 through 8.4 give the calculated hydraulic conductivity as a function of hole length of locations A, B and C, respectively. Two distinct hydraulic conductivities are observed: $k = 10^{-5}$ to 10^{-4} cm/s probably represents a lower bound estimate of the fracture zone permeability, and $k \leq 1.9 \times 10^{-8}$ cm/s represents the intact rock permeability.

Falling head tests indicate that nearly all of the fractured zones in the inclined boreholes have a measured hydraulic conductivity (k) on the order of 10^{-5} cm/s (Figures 8.2 through 8.4). With the lower packer deflated and the injection water allowed to flow past the lower packer, the hydraulic conductivity of the system ranges from 8.0×10^{-4} to 1.0×10^{-5} cm/s. This indicates that in some highly fractured zones of the borehole, the injected water flows out of the test interval nearly as fast as the system can provide. In less fractured zones, the magnitude of flow out of the test interval decreases and can be calculated if it is less than the output flow of the injection system.

For steady-state tests, the accuracy of the injection system and test duration limit the minimum measurable hydraulic conductivity, which is 1.9×10^{-8} cm/s. Therefore, when intact zones are encountered in the borehole, and the flow into the injection zone is less than can be measured, the hydraulic conductivity of that test interval is considered less than 1.9×10^{-8} cm/s.

For inclined hole A, the intact rock is found at a depth from 470 to 520 cm. The hydraulic conductivity of this zone is less than 1.9×10^{-8} cm/s. The intact zones are found in inclined hole B at depths from 200 to 220 cm and from 320 to 400 cm. For inclined hole C, the intact rock (i.e. $k < 1.9 \times 10^{-8}$ cm/s) is found at a depth from 420 to 620 cm. Correlation of the permeability results with the core obtained from the inclined holes is uncertain due to extensive breakage of the core caused by drilling.

8.3 Drilling of 150 mm Diameter Vertical Holes

Six inch (150 mm) diameter vertical holes have been drilled at locations A, B and C. Each hole is located so as to intersect a previously drilled inclined hole (Daemen et al., 1989, Ch. 8) at a depth of approximately 5 to 6 meters. The drilling was commenced on April 11, 1989, and was completed on April 22. The work was performed by the Boyles Bros. Drilling Co.

The location of the vertical hole to be drilled is determined by the information obtained from inclined holes (core log and flow test results) and by the rock quality appearing on the cliff and ground surfaces. The position and orientation of the drill rig mounted on a

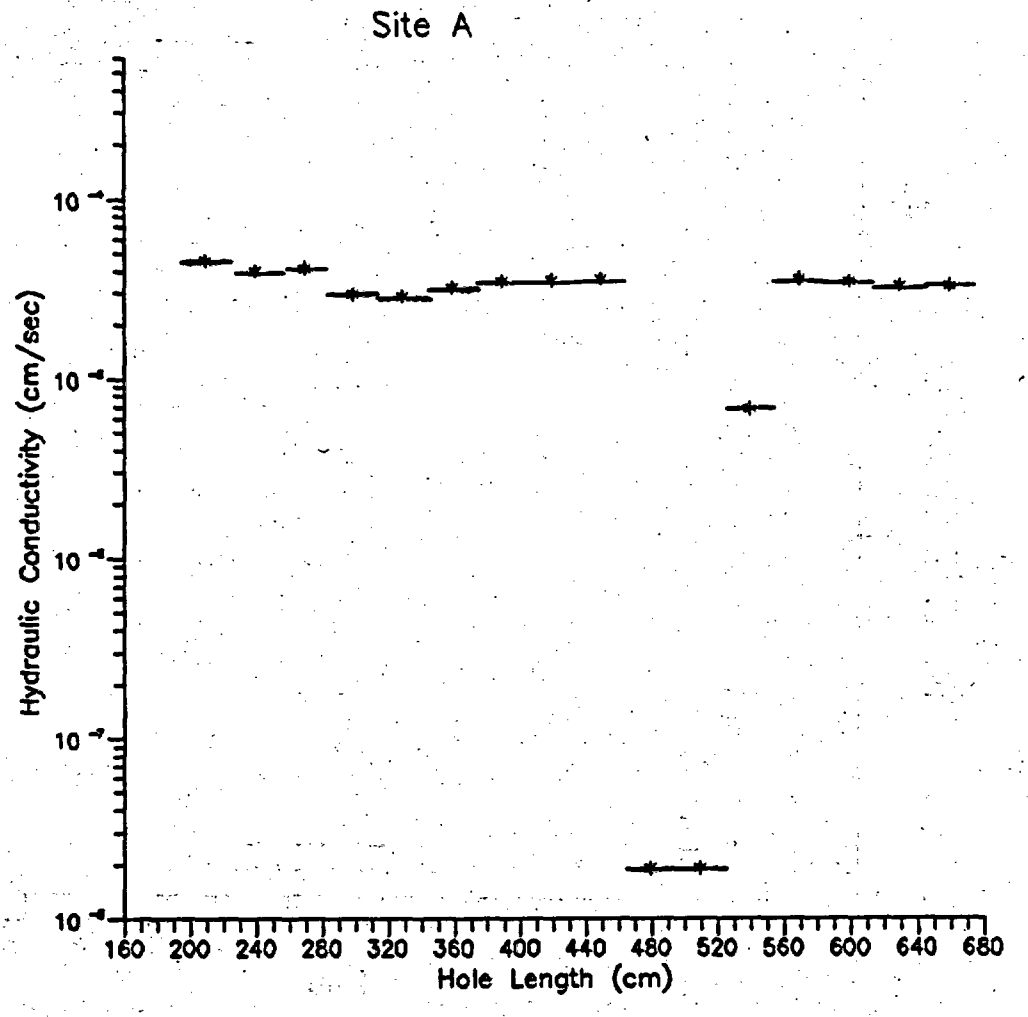

Figure 8.2 Test results of inclined hole A. Hydraulic conductivity as a function of hole length. Low permeability rock (intact rock) is observed at a depth from 470 to 520 cm. Minimum hydraulic conductivity measurable by the system = 1.900 x 10^{-8} cm/sec. Maximum hydraulic conductivity measurable by the system = 0.800 to 1.0 x 10^{-5} cm/sec.

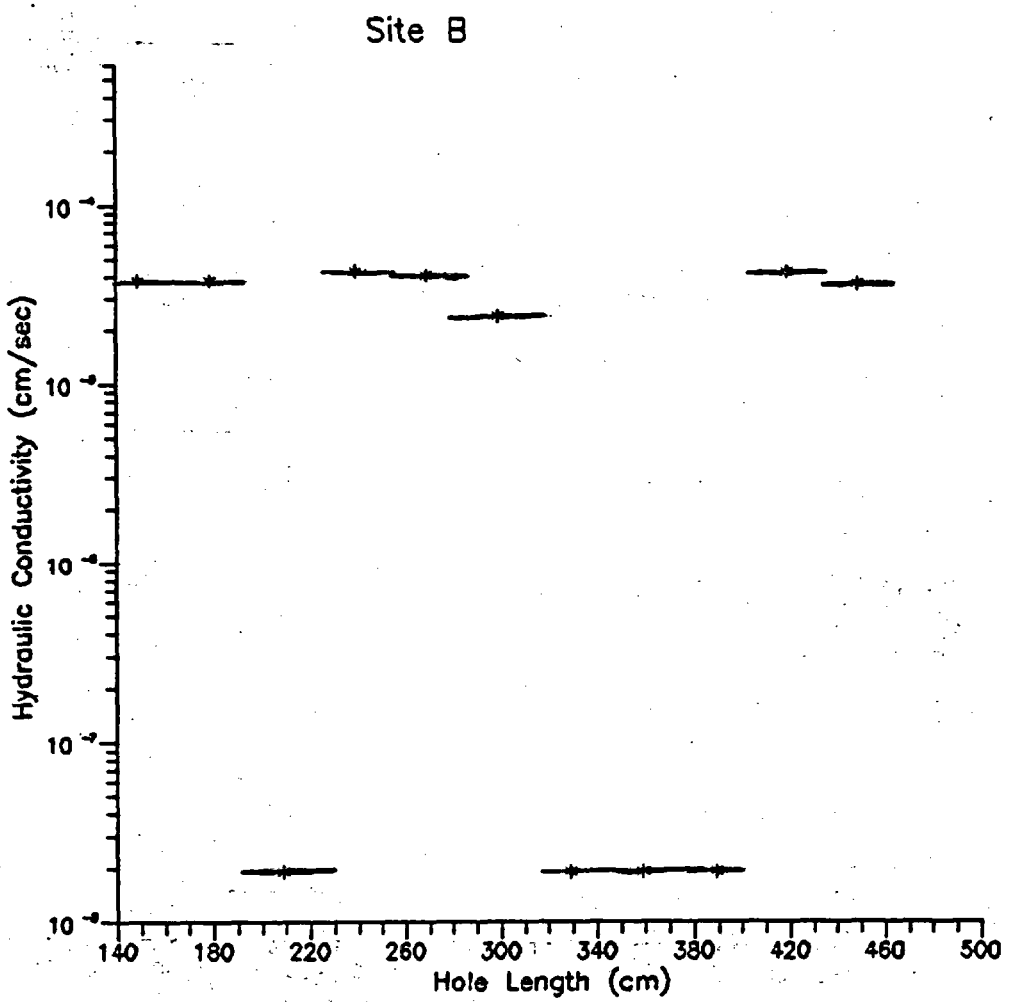

Figure 8.3 Test results of inclined hole B. Hydraulic conductivity as a function of hole length. Low permeability rock (presumably intact) is observed at depths from 200 to 220 cm and 320 to 400 cm. Minimum hydraulic conductivity measurable by the system = 1.900×10^{-8} cm/sec. Maximum hydraulic conductivity measurable by the system = 0.800 to 1.0×10^{-5} cm/sec.

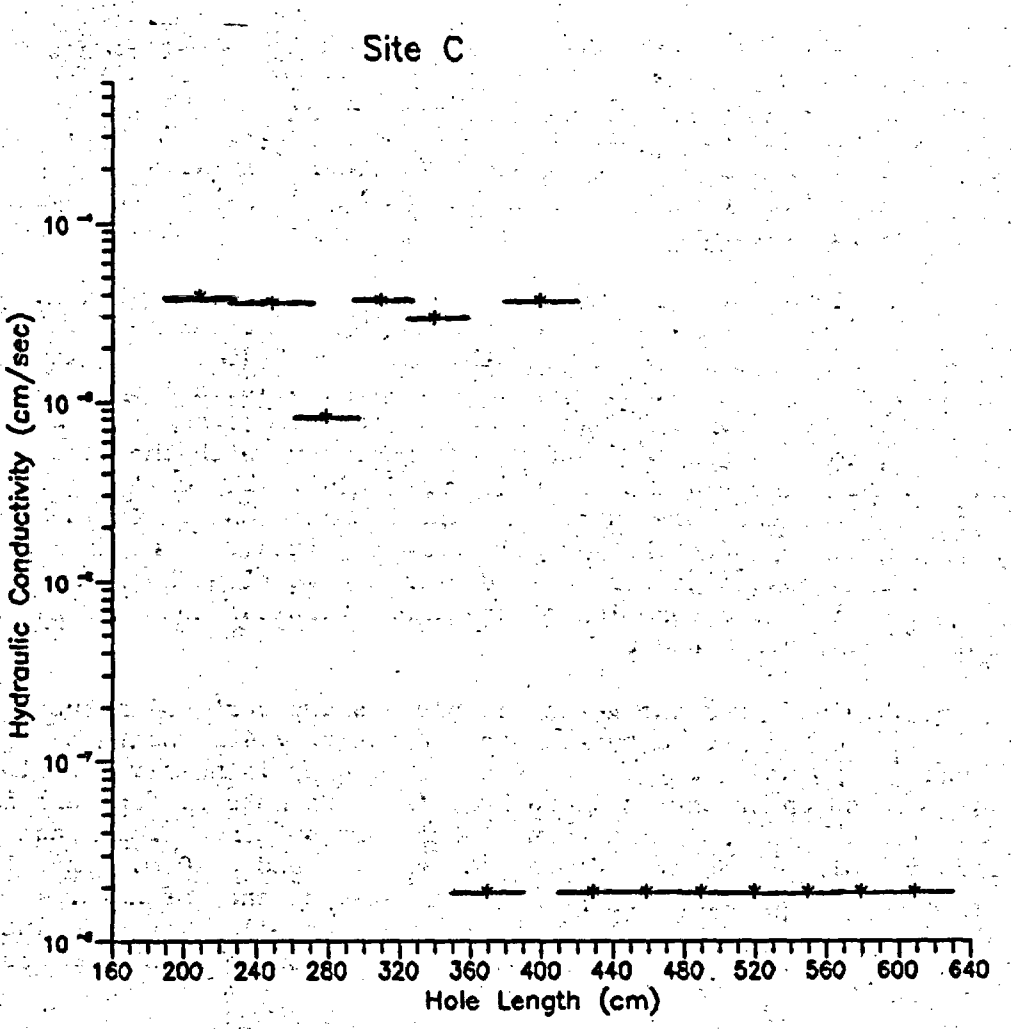

Figure 8.4 Test results of inclined hole C. Hydraulic conductivity as a function of hole length. Low permeability rock (intact rock) is observed at a depth from 350 to 620 cm. Minimum hydraulic conductivity measurable by the system = 1.900 x 10^{-8} cm/sec. Maximum hydraulic conductivity measurable by the system = 0.800 to 1.0 x 10^{-5} cm/sec.

6-ton truck are specified by using a theodolite (Figure 8.5). Daemen et al. (1989, Ch. 8) describe a method to locate the vertical hole to be drilled by intersecting the inclined hole. After the drill rig is aligned, the truck is stabilized using hydraulic jacks.

A 178 mm diameter thin wall diamond impregnated bit mounted on a 5-cm diameter drill rod is used to drill through concrete and rock to a depth of approximately 1.3 m. Fresh water is used as the drilling fluid. The core is then removed. A 175 mm OD, 162 mm ID steel casing about 2 m long is placed in the hole. The casing is stabilized by pouring cement into the gap between the hole and casing. The cement is cured for about 10 hours.

A 150 mm OD, 100 mm ID diamond impregnated bit (Figure 8.6) mounted on a 2.74 m long core barrel is used to drill the vertical hole below the case hole. Fresh water is used as the drilling fluid. The rate of bit penetration varies from 15 to 100 cm/hr. The rotational speed of the drill bit is about 100 rpm. The core is recovered every 1 to 2 m of bit penetration. Figure 8.7 shows core recovered with the core barrel. Nominal core diameter is 100 mm (4 in). The drilling is terminated after the hole intersects the inclined hole. Table 8.1 gives the geometry of each test site hole combination. Figures 8.8 through 8.10 show the core recovered from the vertical holes A, B and C, respectively. The core log of the three vertical holes is given in Appendices 8.A, 8.B and 8.C.

The core obtained from the vertical hole A shows vertical natural fractures from the ground surface to a depth of 7.6 m (near the intersection point). The trend of the fractures is nearly parallel to the dip direction of the inclined hole (A). No natural fracture is found below the intersection point. The core obtained from location B breaks in small pieces at a depth between 2.44 and 6.10 m. This is probably due to the drilling process and the presence of natural fractures. The vertical hole C (inside the tunnel) gives good intact core throughout the hole length. Only a few natural fractures are observed.

8.4 Video Logging of Vertical Holes

Borehole video logging was performed in order to investigate the characteristics of the rock on the wall of vertical holes and to select a location at which to place the plug. The work was performed on May 19, 1989 by "Well Scan Inc." A 76 mm OD color camera (Wellcam, WC-9941) with headlight is lowered into the hole using a steel cable. The borehole image is monitored using a control unit (WC-9541) and is simultaneously recorded by a videocassette recorder. A rope is lowered into the borehole to provide a reference orientation inside the hole. The depth of the camera is measured from the encoder at the cable reel.

The investigation is made from the top end of the casing to the bottom of the borehole. The observations agree well with the core log. The vertical hole C seems to be the best (i.e. less fractured) for seal testing purpose. Holes A and B show highly fractured rock. Most fractures are nearly vertical.

Figure 8.5 The drill is positioned and oriented. Theodolite used to precisely measure the drill orientation.

Figure 8.6 Six-inch OD thick wall diamond impregnated bit used in drilling of vertical holes. The bit is mounted on the bottom end of the 9-ft long core barrel.

Figure 8.7 Core recovered by using core barrel after each run.

Table 8.1 Length of Vertical Holes and Inclined Holes at Locations A, B and C

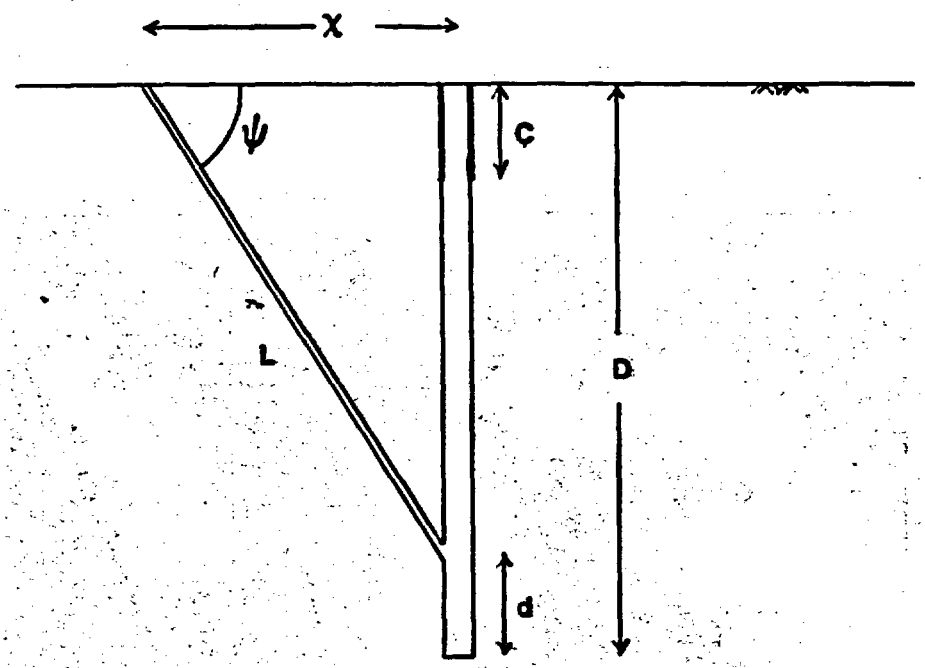

D = total depth of vertical hole
d = length of vertical hole below intersection point
c = length of casing
L = length of inclined hole
x = horizonal distance between vertical and inclined holes
ψ = dip angle of inclined hole
θ = dip direction of inclined hole

Location	D (m)	d (m)	c (m)	L (m)	x (m)	ψ	θ
A	7.47	1.68	1.47	8.84	4.72	57°38'	S 10° W
B	6.71	1.83	1.30	7.48	4.57	52°18'	N 88° W
C	6.22	0.74	1.12	7.01	4.11	52°45'	N 80° E

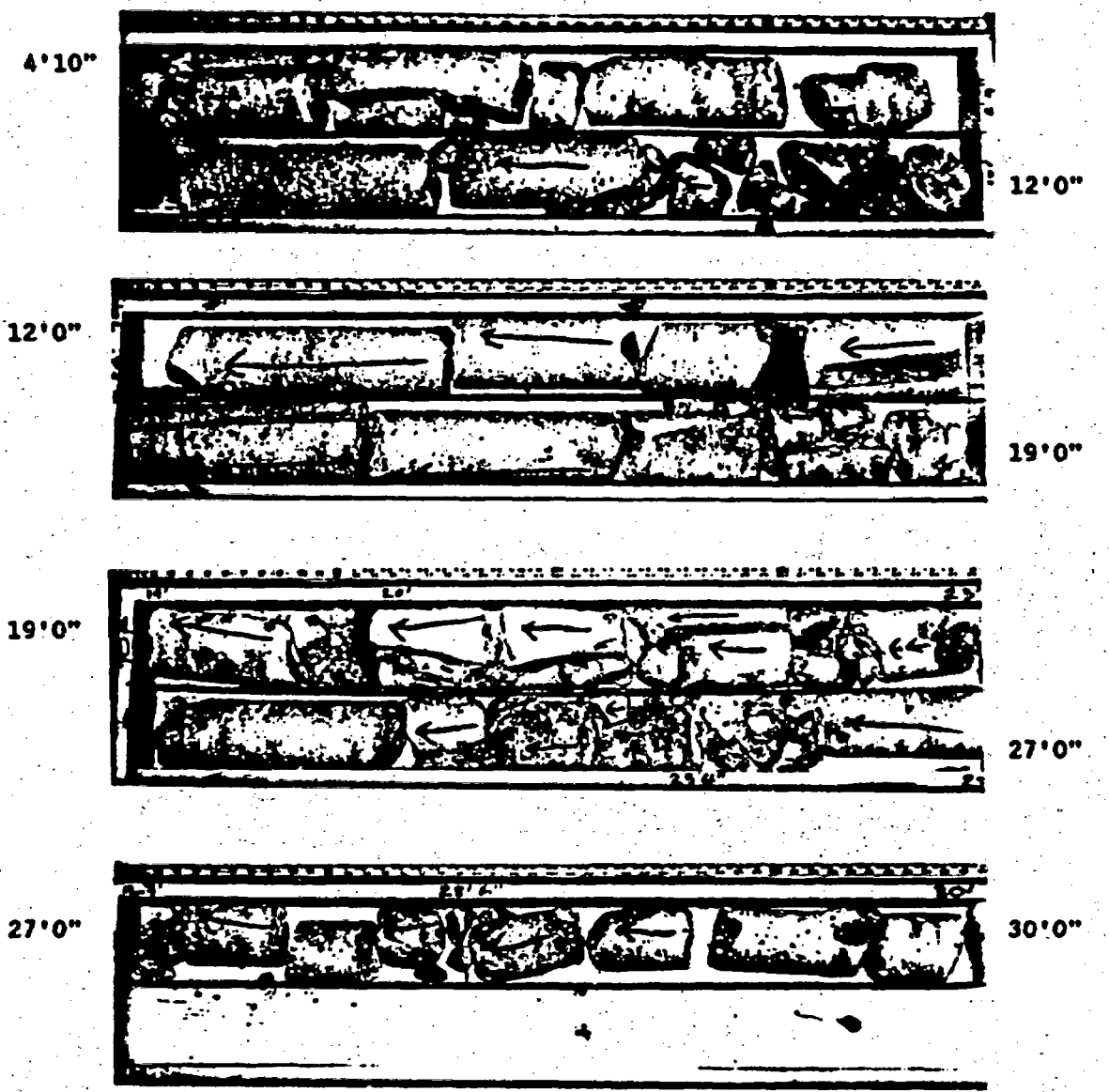

Figure 8.8 100 mm diameter core drilled from location A.

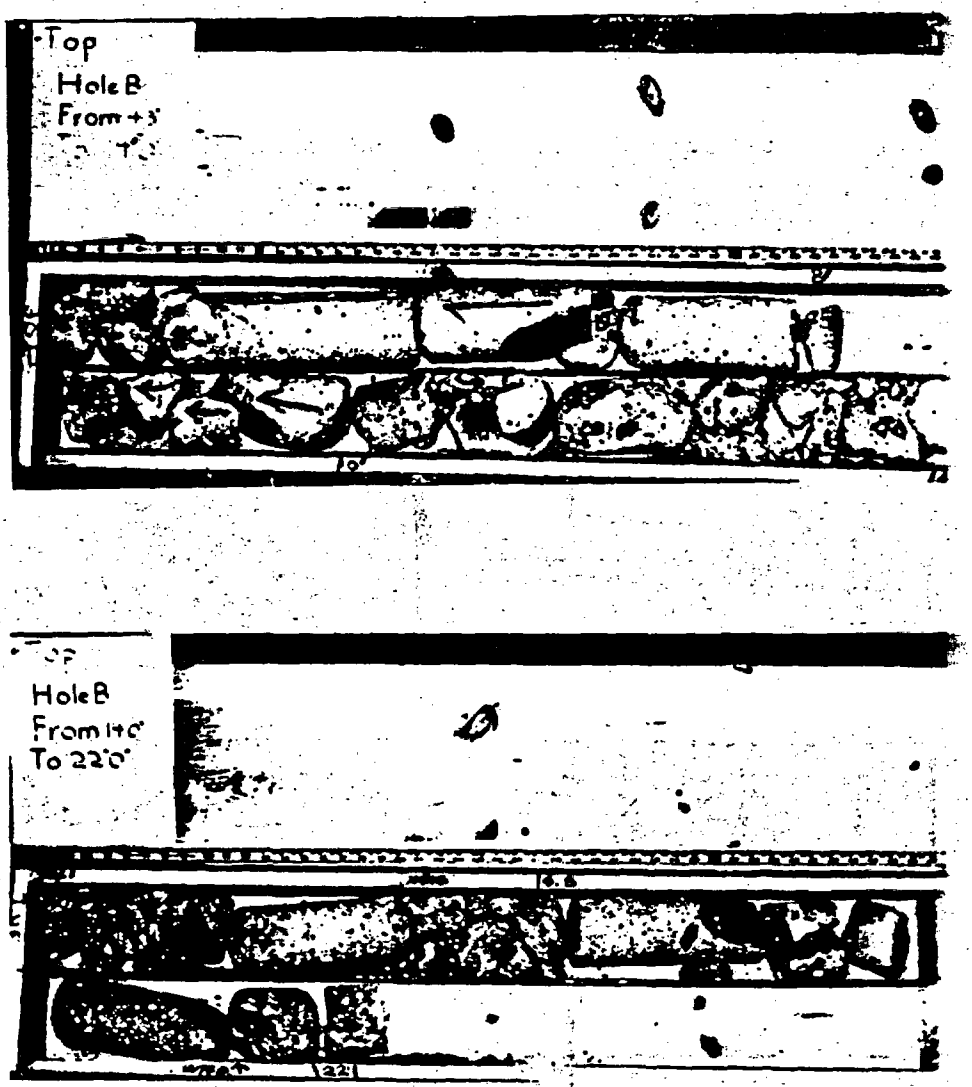

Figure 8.9 100 mm diameter core drilled at location B.

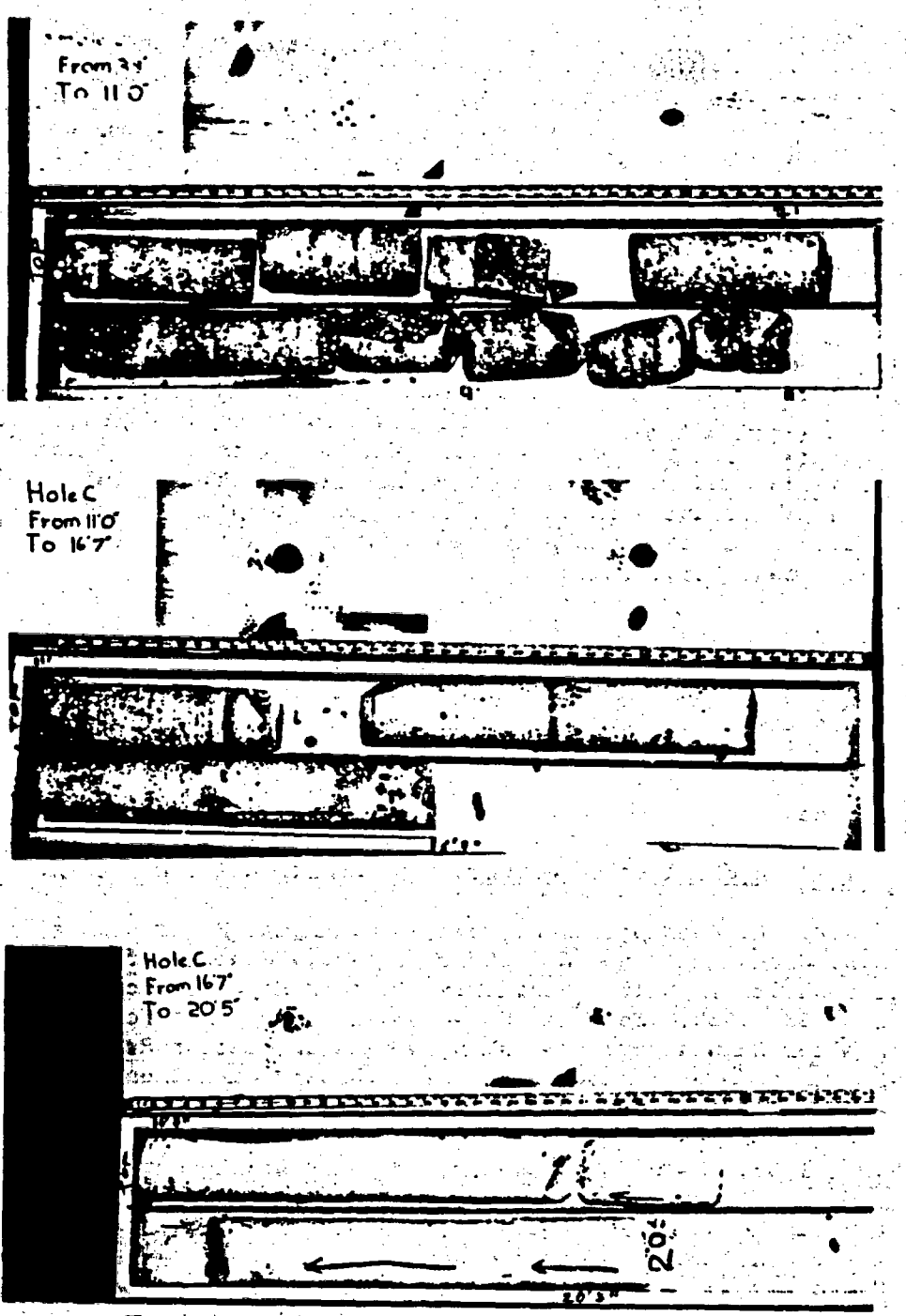

Figure 8.10 100 mm diameter core drilled at location C.

8.5 Joint Orientation Measurement

Daemen et al. (1989, Ch. 8, Section 8.4) give the method and results of joint orientation measurement at the field site near Superior, Arizona. An error was made in plotting the poles of the joint planes on a stereographic projection (Daemen et al., 1989, Figs. 8.8 and 8.9, pp. 169-70). Figure 8.11 gives the correct normals to joint planes and their contours. Four joint sets are recognized: N 270°/vertical, N 300°/vertical, N 240°/vertical, and N 250°/10°

8.6 Future Plans

Straddle packer tests will be performed on vertical holes to obtain information about the rock and fracture permeabilities. A full-scale laboratory model will be made to simulate vertical and inclined holes at location C (inside the tunnel). The model will be used to try out the plug installation procedure. Clear plastic tubes will be used to simulate vertical and inclined holes at the intersection point. This allows visual observation on the uniformity of the plug (cement), injection zone underneath the plug, and on the location of the injection and collection tubes.

The flow measuring system for in-situ permeability testing will be improved in order to assure that lower hydraulic conductivities can be measured reliably. Not much effort will be devoted to improve the resolution in the upper permeability range, as these results are of limited interest to us.

8.7 References

Bear, J., 1979, Hydraulics of Groundwater, McGraw-Hill, New York.

Daemen, J.J.K., K. Fuenkajorn, S. Ouyang, H. Akgun, R. Armstrong, D.S. Crouthamel, and C.J. Sharpe, 1989, "Sealing of Boreholes and Shafts in Salt: Quarterly Progress Report, Dec. 1, 1988 - Feb. 28, 1989," Contract NRC-04-86-113, prepared for the U.S. Nuclear Regulatory Commission, Office of Nuclear Regulatory Research, Division of Engineering, by the Department of Mining and Geological Engineering, University of Arizona, Tucson.

Evans, D.D., 1983, "Welded Tuff Characteristics at the Nevada Test Site and Near Superior, Arizona," Technical Report prepared for U.S. Nuclear Regulatory Commission, Division of Health, Siting and Waste Management, Office of Research, by the Department of Hydrology and Water Resources, University of Arizona, Tucson.

Freeze, R.A., and J.A. Cherry, 1979, Groundwater, Prentice-Hall, New Jersey.

Vogt, G.T., 1988, "Porosity, Pore-Size Distribution and Pore Subsurface Area of the Apache Leap Tuff Near Superior, Arizona, Using Mercury Porosimeter," Master's Thesis, University of Arizona, Tucson.

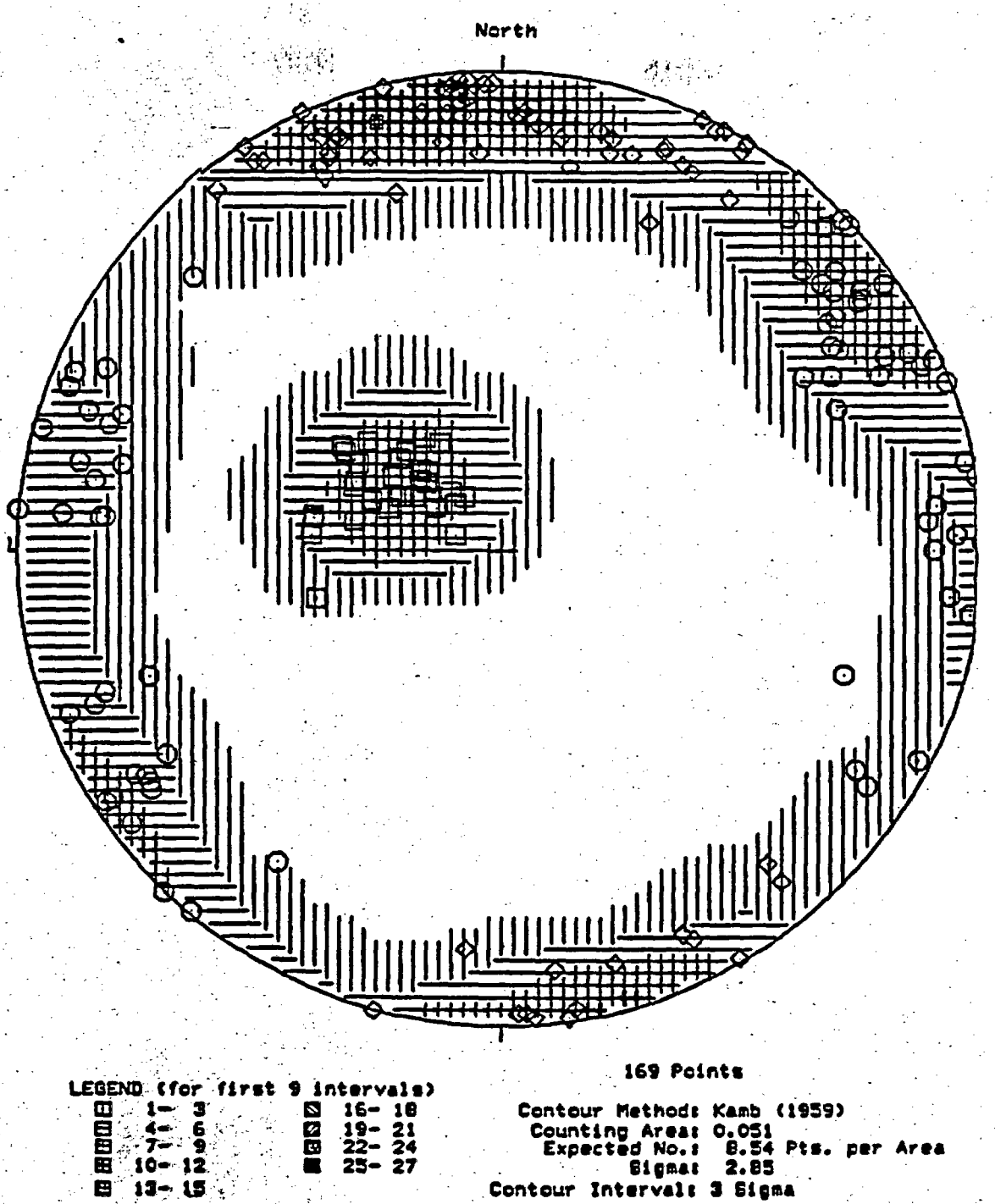

Figure 8.11 Stereographic projection of the poles of the joint planes.

APPENDIX 8.A

DRILLING LOG OF VERTICAL HOLE AT LOCATION A

Hole No. A

DRILLING LOG	DIVISION Rock Mechanics Labs.	INSTALLATION	SHEET One OF 2 SHEETS

1. PROJECT: UA/NRC-04-86-113
2. LOCATION (Coordinates or Station): SUPERIOR, ARIZONA
3. DRILLING AGENCY: Boyles Bros. Drilling Co.
4. HOLE NO. (As shown on drawing title and file number): A EAST of Tunnel
5. NAME OF DRILLER: K. HIRCHI
6. DIRECTION OF HOLE: ☑ VERTICAL ☐ INCLINED _____ DEG. FROM VERT.
7. THICKNESS OF OVERBURDEN: 4' 10"
8. DEPTH DRILLED INTO ROCK: 25' 2"
9. TOTAL DEPTH OF HOLE: 30'
10. SIZE AND TYPE OF BIT: 6" dia. diamond
11. DATUM FOR ELEVATION SHOWN (TBM or MSL):
12. MANUFACTURER'S DESIGNATION OF DRILL: CHRISTENSEN
13. TOTAL NO. OF OVER-BURDEN SAMPLES TAKEN: DISTURBED ✓ UNDISTURBED
14. TOTAL NUMBER CORE BOXES: 4
15. ELEVATION GROUND WATER: —
16. DATE HOLE: STARTED 4-11-89 COMPLETED 4-13-89
17. ELEVATION TOP OF HOLE: 3600 ft
18. TOTAL CORE RECOVERY FOR BORING: 99 %
19. SIGNATURE OF INSPECTOR: K. Fuenleyoni

ELEVATION a	DEPTH ft b	LEGEND c	CLASSIFICATION OF MATERIALS (Description) d	% CORE RECOVERY e	BOX OR SAMPLE NO. f	REMARKS (Drilling time, water loss, depth of weathering, etc., if significant) g
3600' above sea level	1'	6.5" dia. O.D. steel CASING	7" dia. core of concrete. Broken Fresh welded Tuff Rock fill, gravel, sand	50%		Use 7" OD thin wall impregnated diamond bit. Drill with water 7" dia. hole 4' 10" deep sink casing, stabilize with concrete, No water lost.
	2'					
	3'					
	4'					
	4' 10"		Broken, highly fractured			wait 24 hrs
	5'		All frac. NF, nearly vertical & horiz. Iron ox. stain Fresh Welded Tuff	RUN NO. 1 100%	Box No. 1	Use 6" OD Thick wall diamond bit, 9' long core barrel, obtain 6" Dia. hole & 4" dia. core. Water lost 25%. April 12
	6'					
	7'					
	8' 4"		Total Core length 3' 6"			
	9'		All NF. horiz. & nearly Vertic. — No core lost. Fresh welded Tuff- Five layers normal to core axis, Inclusions	RUN NO. 2 100%		Water lost 25%
	10'					
	11'					
	12'		Broken core			

ELEVATION a	DEPTH ft b	LEGEND c	CLASSIFICATION OF MATERIALS (Description) d	% CORE RECOVERY e	BOX OR SAMPLE NO. f	REMARKS (Drilling time, water loss, depth of weathering, etc., if significant) g
	13'		Horiz. Fractures NF	RUN NO. 3	Box No. 2	Water lost 25%
			NF Fresh welded Tuff			
	14'		NF Core length 2'7"	89%		
	15'		NF Core lost 4"			
	16'		Fresh welded Tuff NF	RUN NO. 4		Water flow out at inclined hole water lost 50%-75%
			Vertical			
	17'		NF	100%		
	18'		NF			
	19'		Broken rock 10" NO core lost			
	19		7" Fresh welded Tuff	RUN	Box	Water lost 50%
	20'		All NF. Frac. in vertical and horiz. with Fe2O3 stain Reddish brown	NO. 5	No. 3	flow to inclined hole and fractures
	21'			100%		
	22'		NF. Broken Rock 3"			
	23'		NO CORE lost			
			NO Fracture Fresh welded Tuff	RUN NO. 6		Water lost 100% flow to inclined hole
	24'		NF.	100%		
			NF			
	25' 9"		NF NO CORE LOST			
	26'		Broken Rock Fresh welded Tuff. IF	RUN NO. 7		Water lost 100% flow to inclined hole
			Intact Core	100%		
	27'		NO CORE LOST			
			Broken Rock	RUN NO. 8	Box No. 4	Water lost 100% flow to inclined hole
	28'		NF.	100%		
			NO CORE LOST			
	29'		Broken rock Fresh welded Tuff	RUN NO. 9		Water lost 100% flow to inclined hole
			NF. frac. have Iron oxide stain.	100%		
	30'		NF. NO CORE LOST			Drilling Terminated
						Hole is flushed with fresh water (1000 gal) 15 minutes.

(A)

APPENDIX 8.B

DRILLING LOG OF VERTICAL HOLE AT LOCATION B

Hole No. B

DRILLING LOG	DIVISION Rock Mechanics Lab.	INSTALLATION	SHEET ONE OF 2 SHEETS

1. PROJECT: UA/NRC - 04-86-113
2. LOCATION (Coordinates or Station): SUPERIOR, ARIZONA
3. DRILLING AGENCY: Boyles Bros. Drilling Co.
4. HOLE NO. (As shown on drawing title and file number): B west of Tunnel.
5. NAME OF DRILLER: K. Hirchi
6. DIRECTION OF HOLE: ☑ VERTICAL ☐ INCLINED _____ DEG. FROM VERT.
7. THICKNESS OF OVERBURDEN: 4' 3"
8. DEPTH DRILLED INTO ROCK: 17'9"
9. TOTAL DEPTH OF HOLE: 22'
10. SIZE AND TYPE OF BIT: 6" O.D. Diamond
11. DATUM FOR ELEVATION SHOWN (TBM or MSL):
12. MANUFACTURER'S DESIGNATION OF DRILL: CHRISTENSEN
13. TOTAL NO. OF OVER-BURDEN SAMPLES TAKEN: DISTURBED ✓ UNDISTURBED
14. TOTAL NUMBER CORE BOXES: 2
15. ELEVATION GROUND WATER: –
16. DATE HOLE: STARTED 4-19-89 COMPLETED 4-21-89
17. ELEVATION TOP OF HOLE: 3600 ft
18. TOTAL CORE RECOVERY FOR BORING: 91 %
19. SIGNATURE OF INSPECTOR: K. Fierbyon.

ELEVATION a	DEPTH ft b	LEGEND c	CLASSIFICATION OF MATERIALS (Description) d	% CORE RECOVERY e	BOX OR SAMPLE NO. f	REMARKS (Drilling time, water loss, depth of weathering, etc., if significant) g
3600' above sea level	1' 2' 3' 4' 3"	6.5" dia. OD steel casing	Broken Concrete + Rock Fresh Welded Tuff NO CORE, gravel sand			use 7" Thin wall impregnated diamond bit. 7" dia. hole 4' 3" deep. place casing stabilize with concrete No wate lost wait 24 hours
	5' 6' 7' 8'	NF NF NF	6" Broken due to drilling 13" Fresh welded Tuff + flow layers, inclusions 13" Broken due to Natural Fractures, Fe oxide stain core lost 10"	RUN NO. 1 78%	BOX NO. 1	No water lost use 6" Thick wall bit, 9' long core barrel produce 6" dia. hole & 4" dia. core take 1:30 hrs 4-20-89 10:30 AM
	9' 10'	14"	Broken core due to NF. Fresh welded Tuff Core lost 10"	RUN NO. 2 58%		4-21-89 All wate lost 12:00 PM

(HOLE NO. B)

ELEVATION a	DEPTH ft b	LEGEND c	CLASSIFICATION OF MATERIALS (Description) d	% CORE RECOVERY e	BOX OR SAMPLE NO. f	REMARKS (Drilling time, water loss, depth of weathering, etc., if significant) g
	11'		Broken Rock: Fresh welded Tuff	RUN		All water lost
			NF.	NO. 3		
	12'			100 %		
	13'					
	14'		NF ? No core lost			
			Broken Rock due to drilling and Natural Fracture.	RUN	Box	All water lost
	15'		NF & IF	NO. 4	NO. 2	
			Intact 13"			
	16'		NF	100 %		
			Broken rock: Highly Fracturing			
	17'					
			Intact.			
	18'					
	19' 8"		Broken core due to NF.	RUN	Box	
				NO. 5	NO. 2	All water lost
	19'		Broken core due to drilling & NF			Hole intersect inclined.
			NF	100%		hole at ≈ 21'6" deep.
	20'					
			Intact			4-21-89.
	21'		F			
		X	intersect			Drilling is terminated
	22'		Intact			
			-			Hole is flushed with Freshest water for 15 min (1000 gal)

APPENDIX 8.C

DRILLING LOG OF VERTICAL HOLE AT LOCATION C

Hole No. C

DRILLING LOG	DIVISION: ROCK MECHANICS LAB.	INSTALLATION	SHEET ONE OF 2 SHEETS

1. PROJECT: UA-NRC-04-86-113	10. SIZE AND TYPE OF BIT: 6" dia. Thick wall Diamond
2. LOCATION (Coordinates or Station): SUPERIOR, ARIZONA	11. DATUM FOR ELEVATION SHOWN (TBM or MSL): 3600 ft above sea level at 0' depth
3. DRILLING AGENCY: BOYLES BROS. DRILLING CO.	12. MANUFACTURER'S DESIGNATION OF DRILL: CHRISTENSEN
4. HOLE NO. (As shown on drawing title and file number): C (inside tunnel)	13. TOTAL NO. OF OVER-BURDEN SAMPLES TAKEN: DISTURBED ✓ / UNDISTURBED
5. NAME OF DRILLER: HIRCHI + RILEY	14. TOTAL NUMBER CORE BOXES: 3
6. DIRECTION OF HOLE: ☑ VERTICAL ☐ INCLINED _____ DEG. FROM VERT.	15. ELEVATION GROUND WATER: —
7. THICKNESS OF OVERBURDEN: 1'	16. DATE HOLE: STARTED 4-14-89 / COMPLETED 4-17-89
8. DEPTH DRILLED INTO ROCK: 19' 5"	17. ELEVATION TOP OF HOLE: 3600 ft
9. TOTAL DEPTH OF HOLE: 20' 5"	18. TOTAL CORE RECOVERY FOR BORING: 92 %
	19. SIGNATURE OF INSPECTOR: K. Ewenhjem.

ELEVATION a	DEPTH ft b	LEGEND c	CLASSIFICATION OF MATERIALS (Description) d	% CORE RECOVERY e	BOX OR SAMPLE NO. f	REMARKS (Drilling time, water loss, depth of weathering, etc., if significant) g
3600' above sea level	1' / 2' / 3' 8"	6 5/8" OD. CASING	Broken Rock, Fresh Welded Tuff, gravel. Highly Fracturing (natural + blasting induced) Reddish brown	NO CORE		USE 7" OD. thin wall impregnated bit, drill with water. 7" dia. Hole sink casing + stabilize with concrete NO water lost
	4' / 5' / 6'		11" NF — Fresh welded Tuff with horiz. Natural Fract. 9" NF / IF (3hrs drill)	RUN NO. 1 100%	BOX NO. 1	USE 6" DD. Thick wall Diamond bit, drill with water, obtain 6" dia. hole and 4" dia. core NO water lost, 9' CORE BARREL
	7'		1" IF — Intact core, FWT, reddish brown (3hrs drill)	RUN NO. 2 100%		NO water lost
	8' / 9'		15" IF — horiz. Induced Fract. Fresh welded Tuff with Indosions. Flow layers 7" normal to core axis core lost 2"	RUN NO. 3 92%		NO water lost April 16
	10' / 11'		6" IF — natural Fract. 4" NF / 3" IF — Inclined to core axis Fresh welded Tuff core lost 7"	RUN NO. 4 71%		NO water lost April 17

(HOLE NO. C)

ELEVATION a	DEPTH b	LEGEND c	CLASSIFICATION OF MATERIALS (Description) d	% CORE RECOVERY e	BOX OR SAMPLE NO. f	REMARKS (Drilling time, water loss, depth of weathering, etc., if significant) g
	12'		14" Intact core. No natural Fractures. Fresh welded Tuff. Core broken by drilling and recovery process.	RUN NO. 5 90%	Box NO. 2	No water lost
	13'	IF				
	14'	IF				
	15'		23"			
	16'					
	16'2"	IF	core lost 7"			April 17
	17'	IF	Fresh Welded Tuff; Reddish brown	RUN NO. 6 100%	Box NO. 3	All water lost
	18'	X	Intersect inclined hole			Intersect inclined hole at 18' depth
	19'	NF	2'1" Intact core. NO CORE LOST			April 17 ; 17:00 PM Drilling terminated
	20'					
	20'5"					Hole is flushed with fresh water (1,000 gal) for 12 minutes.